Connecting hyperbolic invariant manifolds at variations of the Poincaré section orientation

A numerical investigation into novel transfer solutions connecting collinear periodic libration point orbits through their associated manifold structures

by:

K. Langemeijer

TUDelft

This page is intentionally left blank.

Connecting hyperbolic invariant manifolds at variations of the Poincaré section orientation

A numerical investigation into novel transfer solutions connecting collinear periodic libration point orbits through their associated manifold structures

by:

K. Langemeijer

to obtain the degree of Master of Science

at the Delft University of Technology,

to be defended publicly on Friday January 19, 2018 at 14:00.

Cover image: Near-heteroclinic connection between vertical Lyapunov orbits in the Earth-Moon system at a variation of the Poincaré section orientation.

Student number: 4165209
Project duration: July 3, 2018 – January 19, 2018

TU Delft thesis committee:

Ir. K.J. Cowan MBA	*Astrodynamics and Space Missions, Lecturer*	Supervisor
Prof. dr. ir. P.N.A.M. Visser	*Astrodynamics and Space Missions, Professor*	Chair
Ir. P.P. Sundaramoorthy	*Space Systems Engineering, Researcher*	Independent examiner
Dr. ir. D. Dirkx	*Astrodynamics and Space Missions, Assistant professor*	Additional examiner

An electronic version of this thesis is available at `http://repository.tudelft.nl/`.

TUDelft

This page is intentionally left blank.

Preface

The elegance of the circular restricted three-body problem is easily mistaken for simplicity, yet this system is known to possess some of the most complex dynamic behaviour. Throughout history, many of the greatest mathematical minds have been intrigued by this subject and have developed novel theories in an attempt to solve it. Although these methods have revolutionised the natural sciences, even these efforts have proven to be unable to capture the full complexity of this system. In more recent efforts, the emphasis has shifted from a fully analytic approach to the adoption of numerical methods. This exotic combination of mathematical intricacies and programming have inspired me to pursue the discovery of novel insights into these transfer phenomena while laying a basis for future research by contributing to the TU Delft Astrodynamic Toolbox.

K. Langemeijer
Delft, January 2018

This page is intentionally left blank.

Abstract

The three-body problem (3BP) formulated by I. Newton has inspired many great mathematicians like L. Euler (1707-1783), J.L. Lagrange (1736-1813), K.G.J. Jacobi (1804-1851), W.R. Hamilton (1805-1865) and J.H. Poincaré (1854-1912) to develop mathematical studies, methods and theories in an attempt to solve this problem. Although these concepts have been crucial to the advancement of the natural sciences, a closed form solution has yet to be found. To aid in solving this problem, a restricted form of the 3BP has been formulated in which the mass of the two primaries greatly exceeds the mass of the third body. Known as the *circular restricted three-body problem*, this system gives rise to three collinear and two equilateral equilibria referred to as libration points. These locations are surrounded by various families of periodic libration point orbits. The corresponding exotic trajectories are highly non-Keplerian which offer desirable characteristics that have revolutionised space mission design. Crucial to this effort has been the theory on hyperbolic invariant manifolds. These topological structures asymptotically arrive at (stable) or depart from (unstable) a selected target orbit by exploiting the natural dynamics of the system. A connection which joins stable and unstable manifold trajectories with no discrepancy in state space, constitutes to a free (natural) transfer mechanism. In the case that two different equilibria are connected, this path is called a *heteroclinic connection*. The potential existence of these solutions are of significant scientific interest and are known to exist in the planar case. In this research, the current theory is extended by providing a comprehensive understanding of the phase space of the (spatial) *vertical Lyapunov* (V-L) orbits and their associated manifolds including the potential existence of heteroclinic connections in the Earth-Moon system.

The transition from the planar to the spatial case is associated with a rapid increase in complexity. To reduce the order of the problem, the two hyperbolic manifolds which are to be connected are integrated until they intersect a plane called a *Poincaré section*. These stopping conditions form a $N-1$-dimensional subset of the phase space. A completely new effort is aimed at investigating the influence of the orientation of this section on the state vector discrepancy that arises from the connection of hyperbolic manifolds emanating from collinear libration points L_1 and L_2. The aim of this study is to reveal novel transfer trajectories outside the solution space confined by the traditional locations and orientations of the Poincaré section.

The path towards creating these insights consist of three stages, all of which employ a variety of numerical methods. As these steps are sequential, the individual chapters of this thesis cannot be considered as stand-alone work. First of all, the target orbits are generated through the refinement (*Differential Correction*) and extension (*Numerical Continuation*) of analytic approximations based on *Perturbation Theory*. The families of horizontal Lyapunov (H-L), halo, axial, and V-L are analysed to provide an overview of the range of possible solutions. The periodicity of each orbit is verified numerically and the trajectory is validated by studying the so-called *monodromy matrix*. Secondly, the manifolds are constructed using the eigenspace of this fundamental matrix. Once more a high level of generality is achieved, this time by analysing the sets of manifolds associated with three different families of target orbits at three distinct energy levels. Each member of each manifold is verified through studying deviations in the Jacobi's constant, and validated by using symmetries. Lastly, the stopping conditions for integration of these hyperbolic trajectories are varied to analyse the sensitivity with respect to the orientation of the Poincaré section.

This research has revealed that the most optimal connections for V-L orbits are found <u>outside</u> of the traditional stopping conditions. The ramifications of this behaviour are extensive and are observed to arise from the fact that these hyperbolic trajectories curve behind the Moon. Moreover, the orthographic projections display interesting differences in global stability. The manifolds associated with the V-L family retain their shape, whereas those corresponding to the H-L and halo families behave in a chaotic way over time. This enables an accurate approximation over extended integration periods. In addition, the V-L orbits have revealed the largest eigenvalue moduli across all families in both equilibria which indicate a minimum time to unwind from the target orbit. In conclusion, these insights provide a fresh perspective on the range of possible solutions and phenomena that can be further explored. Moreover, new techniques have been employed to ensure the mathematical validity of libration point orbits and their hyperbolic invariant manifolds. As these structures are inherently difficult to verify, this effort forms a valuable contribution to the TU Delft Astrodynamic Toolbox (C++) for future research.

This page is intentionally left blank.

Contents

List of Figures

This page is intentionally left blank.

List of Tables

This page is intentionally left blank.

Nomenclature

List of acronyms

Acronym	Definition	Chapter
API	Application programming interface	*4*
CR3BP	Circular restricted three-body problem	*1 - 4, 7, A*
DC	Differential correction	*3, 4, C*
DST	Dynamical systems theory	*2, 5*
EM	Earth-Moon	*1 - 8, A - C*
EOM	Equations of motion	*1 - 3, 5*
H-L	Horizontal Lyapunov	*1 - 8, A - C*
IVP	Initial value problem	*2*
LEO	Low Earth orbit	*6*
l.p.o.	Libration point orbit	*1, 4, 7*
NC	Numerical continuation	*3, 4, B*
ODE	Ordinary differential equation	*2, 3, A*
OpenMP	Open multi-processing	*4, B*
RK78	Runge-Kutta-Fehlberg 7(8)	*2 - 8, A - C*
SPM	State propagation matrix	*3*
STM	State transition matrix	*3 - 6*
TPBVP	Two-point boundary value problem	*2*
Tudat	TU Delft Astrodynamics Toolbox	*1, 8, B*
V-L	Vertical Lyapunov	*1 - 8, A - C*
V&V	Verification and validation	*3 - 6*

List of symbols

Symbol	Description	Equation
$\lvert a \rvert$, $\lVert a \rVert$, $\hat{a}$, $\dot{a}$, $\ddot{a}$	Absolute value, norm, estimate, time derivative, second derivative w.r.t. time of a	*2.1 - 2.3, 3.17, 3.19 - 3.24, 3.27, 3.38, 3.39, 5.2, 5.6, B.7*
$\approx$, $\neq$, $:=$, $\mapsto$	Approximately equal, not equal to, is defined as, maps to	*2.11, 2.12, 2.21, 2.25, 3.10, 3.20 - 3.24, 3.32 - 3.34, 7.2 - 7.4, B.8*
$\mathbf{A}(t)$	State propagation matrix	*2.15, 2.20*
A_x, A_z	In-plane (xy) or out-of-plane (z) amplitude	*3.1 - 3.6, 3.17*
a_{rj}	Internal weight at stage r for RK78	*B.2, B.3, B.6*
β	Base for floating point numbers	*A.3*
b_r, $\hat{b}_r$	External weights at stage r for the seventh and eight-order estimate in RK78	*B.4 - B.6*
C	Jacobi's constant	*2.10, 4.1*
c_r	Node at stage c for RK78	*B.2, B.3, B.6*
$\cup$, $\cap$	Union/intersection of sets	*7.1*
D	Differential operator	*2.12 - 2.14*
Δ	Correction factor	*3.10, 3.15, 3.17*
Δ_n	Difference in state at NC-step n	*3.28, 3.30*
δ	Finite difference	*2.14, 3.21 - 3.24*
δ_n	Switching function	*3.1 - 3.6*
$e(h_i)$	Local truncation error of integration step (h_i)	*B.7, B.8*
ϵ	Eigenvector offset from periodic orbit	*5.6*

1

Introduction

Invariant manifold theory has proven to yield low-energy spacecraft trajectories, crucial to the feasibility of today's and future space missions. This research project is dedicated to creating a decisive step in the generation, verification and analysis of these manifold structures. In this way, this report forms a theoretical basis for anyone willing to adopt manifolds in space mission design. This chapter provides a critical discussion of the relevant heritage and the current scientific gap that it poses. Consecutively, the research framework is introduced which gives a detailed outline of the question, aims and objectives that have to be addressed when bridging this gap. Lastly, the outline of this document is presented.

1.1. Scientific gap and research motivation

To illustrate the relevance and potential impact of the outcome of this study, this project is put into perspective by discussing the exceptional research leading up to this point.

1.1.1. Heritage of libration point orbits and invariant manifolds

The three-body problem (3BP) formulated by I. Newton has inspired many great mathematicians like L. Euler (1707-1783), J.L. Lagrange (1736-1813), K.G.J. Jacobi (1804-1851), W.R. Hamilton (1805-1865) and J.H. Poincaré (1854-1912) to develop mathematical studies, methods and theories in an attempt to solve this problem. Although these concepts have been crucial to the advancement of the natural sciences, an analytic solution to the general problem has yet to be found. To aid in solving this problem, a restricted form of the 3BP has been formulated in which the mass of the two primaries greatly exceeds the mass of the third body. The so-called *circular restricted three-body* (CR3BP) has been intensely studied in an attempt to gain further understanding of the more complex 3BP.

After the discovery of the three collinear and two equilateral equilibrium points, by L. Euler (1767) and J.L. Lagrange (1772) respectively, the periodic solutions surrounding these libration points have been of great interest. Most profoundly has been the effort by J.H. Poincaré, who's research into the dynamical stability of systems has formed the basis for *Dynamical Systems Theory* (DST).

In more recent history, both analytic and numerical approaches have been aimed at finding global solutions to the CR3BP. Crucial to this effort has been the theory on invariant manifold structures of the collinear libration points, which *"provide the framework for understanding transport phenomena from a geometric point of view"* [Koon et al., 2009]. The trajectories arising from this framework exploit the natural dynamics of the system to yield low-energy trajectories to complex and highly non-Keplerian orbits, as required by recent space missions. The first mission to exploit these *libration point orbits* (l.p.o.) was the revolutionary International Sun-Earth Explorer (ISEE-3) [Dunhan and Farquhar, 2003]. Together with its successor, the Solar and Heliospheric Observatory (SOHO), they produced the first measurements of the phenomenon currently known as space weather [Farquhar, 2001]. The ground-breaking research facilitated by these missions has cemented the scientific relevance of the desirable characteristics that these exotic orbits have to offer.

1

1.1.2. Current research gap

Prior approaches to computing manifolds have been mostly aimed at two types of target orbits: *horizontal Lyapunov* (H-L) and *halo*. Renowned for their simplicity and communication characteristics respectively, these investigations have been driven by past practical needs [Farquhar et al., 2004].[1] As stated in [Howell et al., 1997], "successful and efficient design of mission options will require new perspectives and a more complete understanding of the solution space is imperative." In this way, this research is focused on another type of libration point orbits: the *vertical Lyapunov* (V-L) family. Also designated as figure-eight or near-vertical orbits, potential future missions for this out-of-plane motion are vast and range from lunar south pole coverage to radio astronomy to be performed in the Moon's eclipse [Grebow et al., 2008][Dekens et al., 2014].[2]

The goal of this research is to bridge multiple scientific gaps identified in literature. First and foremost, the scope of invariant manifolds will be extended to this different type of l.p.o.: the V-L family. Extending the current manifold theory to this type of orbit is expected to yield insights into the feasibility of heteroclinic manifold connections. In recent efforts by [Haapala, 2014], this type of natural connection which combines manifolds originating from orbits around L_1 and L_2 respectively, has only been exposed for the H-L and halo families in the Earth-Moon (EM) system. In addition, a completely new effort will be aimed at investigating the sensitivity of the state vector discrepancy at the position of manifold connection with respect to the orientation of the Poincaré section. The aim of this study is to reveal novel transfer solutions outside the solution space confined by the traditional locations and orientations of the Poincaré sections. The outcome of this combined research can give rise to a completely new set of trajectories, opening doors for a wider range of scientific missions previously unattainable.

Research gap: *Comprehensive understanding of the phase space of hyperbolic invariant manifolds emanating from vertical Lyapunov orbits including the potential existence of heteroclinic connections in the Earth-Moon system*

Apart from the research gap stated above, this research aims to address another need: ballistic manifold verification. Analogous to the impression of the CR3BP, manifold structures can be considered as very elegant and thereby may give the false impression of simplicity. A more thorough analysis of these trajectories show that both numerous scientific methods as well as technical knowledge of the numerical approximation is involved. Inaccuracies in any of the steps of both aspects will lead to untrustworthy results. Due to scale of these topological structures, general verification techniques like visual inspection are considered to be unfit. Hence, a novel technique for verification is proposed to resolve this issue.

1.1.3. Rationale for variations in orientation of the phase portrait

The rationale behind investigating the sensitivity of manifold connections with respect to the orientation of the Poincaré section can be attributed to the continuous nature of the solution space for this *autonomous Hamiltonian system*. This property has two main effects. Firstly, slight variations in the orientation of the Poincaré section are expected to yield solutions close to the nominal case. Reason for this is the absence of discontinuities and moderate gradient at distance from the two primaries. Secondly, the leading researchers in this field adopt gradient-based techniques for optimisation [Gómez et al., 2001a][Gómez et al., 2001b]. These methods have proven to yield rapid and robust convergence to local optima, thereby providing efficient solutions. Potential drawbacks of this approach includes the omission of other more optimal solutions, located far from the initial guess. In this way, this research may lead to novel and more optimal solutions by providing unconventional guesses at large deviations in Poincaré section orientation far from the nominal case.

---

[1] The main drawback of these types of orbits are the restricted domain of motion for the planar Lyapunov, and the very broad lateral amplitude for the halo orbit. The latter forms a significant increase in costs of space missions as it requires orientable antennas [Jorba and Masdemont, 1996].

[2] Please note that the out-of-plane motion is associated with the z-direction, as described in the nomenclature.

1.2. Research framework definition

This research project aspires to close the scientific gap described in Section 1.1.2, which can be sculpted into a set of research questions and objectives. Each sub-component of this framework is aimed at solving a piece of the puzzle and together form the answer to the main research question to be solved in reaching the project goal.

1.2.1. Research questions

The main scientific question is the internal aim of the research. The answer to this question and the corresponding sub-questions will provide the exact knowledge required for achieving the research objectives:

Research Question: *What is the influence of the orientation of the Poincaré section on the state vector discrepancy that arises from the connection of hyperbolic invariant manifolds emanating from Earth-Moon collinear libration points L_1 and L_2 in search of near-heteroclinic connections, after expanding the scope from the planar to the spatial case?*

To aid in answering this main question, three sub-questions are formulated:

Sub-question 1: How can the hyperbolic invariant manifolds for the doubly symmetric vertical Lyapunov orbits be constructed?

(a) Are any characteristics of the target orbit inherited by the stable and unstable manifolds? *Ch. 4*
(b) In this way, are there limitations associated to members of the family in which chaotic behaviour within the hyperbolic manifold appears? *Ch. 6*
(c) How can the trajectories that numerically approximate these topological structures be verified for their mathematical fidelity? *Ch. 5*

Sub-question 2: How do the geometry and stability characteristics of the unstable and stable manifolds change for a range of energy levels?

(a) Is this behaviour similar for a variety of types of orbits? *Ch. 6*
(b) Can the observed dynamical behaviour be formulated into a general rule for a specific mass parameter? *Ch. 6*

Sub-question 3: Do the hyperbolic manifolds emanating from different type of orbits at the collinear libration points L_1, L_2 join in phase space at the four predefined Poincaré sections for similar energy levels?

(a) Is it possible to find natural connections ($\Delta V = 0$) when attempting to join the unstable and stable trajectories from L_1 and L_2 respectively at $U_{2,3}$ to form a heteroclinic connection? *Ch. 7*
(b) Can changing the orientation of the Poincaré section yield improved solutions in terms of ΔV through enhanced state vector alignment? *Ch. 7*
(c) How can a near-heteroclinic connection be refined to a more optimal solution in terms of minimum position and velocity discrepancy at the connection of hyperbolic trajectories? *Ch. 8*

This set of research questions form the plan of attack on the road to achieving the project goal. This objective also consists of tangible sub-goals, which are vital to the success of the proposed research.

1.2.2. Research objectives

The proposed contribution of this research to solving problems outside the research itself is the external aim of this research. The set of goals are categorised based on either a scientific or technical foundation:

Research Objective: *To expand the current invariant manifold theory by analysing the phase space of hyperbolic manifolds emanating from vertical Lyapunov orbits for various energy levels.*

Sub-objective 1: Assess whether pure heteroclinic connections between vertical Lyapunov orbits might exist in the Earth-Moon system. *Ch. 7*

Sub-objective 2: Develop a novel verification technique for ballistic manifold trajectories to ensure the mathematical precision of the numerical approximation. *Ch. 5*

Sub-objective 3: Evaluate how the connection between manifolds changes for different orientations of the Poincaré section by changing these parameters one-vector-at-a-time. *Ch. 7*

Sub-objective 4: Lay the foundation for future manifold related research using the *TU Delft Astrodynamic Toolbox* (Tudat) by developing a set of generalised tools for the construction and verification of hyperbolic invariant manifolds emanating from periodic collinear libration point orbits including the generation of families of horizontal Lyapunov, vertical Lyapunov and halo orbits using semi-analytic methods for an initial guess. *Ch. 3, 5*

Sub-objective 5: To establish and resolve the challenges of using an explicit variable step-size Runge-Kutta method in the quest for an accurate numerical approximation of periodic libration point orbits and their (un)stable subspace. *Ch. 3, 5*

Sub-objective 6: Provide insight into the dynamic behaviour and phase space of periodic libration point orbits and their hyperbolic invariant manifolds by producing animations and orthographic projections. *Ch. 4, 6, 7*

1.2.3. Report structure

Before one can commence with answering these questions, multiple steps have to be outlined in this report. Firstly, Chapter 2 discusses a detailed review of state of the art literature produced by the most renowned academics in this field. Based on this current knowledge, Chapter 3 formulates the chosen numerical approach to orbit generation followed by the analysis and critical discussion of these results in Chapter 4. Paired with the theory on invariant manifold theory in Chapter 5 and the corresponding detailed interpretation and verification of these structures in Chapter 6, this forms the new software foundation for future DST research in the CR3BP using Tudat. Chapter 7 focuses on the novel effort towards connecting manifolds and its sensitivity with respect to the orientation of the Poincaré section. This research is concluded in Chapter 8 by addressing the impact of this research including answers to the research questions and presenting proposals for future research. Additional information aiding in the understanding and replicating of the presented work is presented in the appendices, including the used parameters and constants in Appendix A and numerical settings in Appendix B.[3]

---

[3]Please note that each chapter should not be viewed as stand-alone work, since each endeavour builds upaon the previous efforts.

2

Dynamical systems theory in the CR3BP

This research concerns invariant manifold theory, which lies within the greater research field of DST and touches upon *bifurcation and Floquet theory* of linear and nonlinear autonomous dynamical systems. The scope is confined to studying the behaviour of the *continuous Hamiltonian system* in the CR3BP. This section provides a critical discussion of the relevant theory and techniques employed throughout this thesis. A foundation for the understanding of the behaviour and characteristics of this complex system, which is critical to the correct interpretation of the generated results. Firstly, the differential equations governing the CR3BP are discussed along with their convenient equilibria and symmetries. Secondly, a technique for nonlinear differential systems is introduced to propagate, refine, analyse and verify the orbits and manifolds. Lastly, the main types of libration point orbits and their interrelations are revealed to give a glimpse of the solution space of periodic motion.

2.1. Circular restricted three body problem

The basis of this problem lies within the CR3BP and aims to exploit the natural gravity gradient to provide transfer mechanisms. As the scope is confined to the ballistic case, the differential equations presented in this section dictate all motion presented in the results.

2.1.1. Dynamical model arising from the pseudo-potential

The force field in the CR3BP is fully determined by the two primary bodies P_1 and P_2 shown in Figure 2.1, which orbit in a rotating motion around their joint center of gravity. Due to this constant circular motion, a rotating reference frame can be set with the x-axis extending to both primaries, the z-axis in the direction of the angular momentum and the y-axis complying with the right-hand convention.
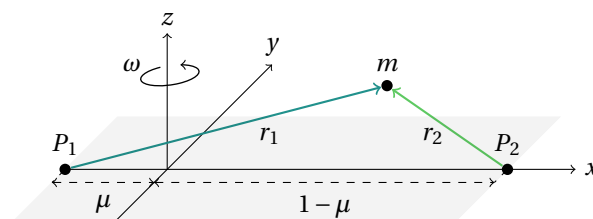
Figure 2.1: *Rotating (synodic) coordinate system of the circular restricted three-body problem.*

The third body with negligible mass m is subjected to Newton's law of universal gravitation exerted by bodies P_1 and P_2. Converting the corresponding accelerations from the inertial to the rotating reference (as shown in Figure 2.1) introduces Coriolis and centrifugal accelerations as apparent forces. Equations 2.1 through 2.3 reveal the set of three second-order differential equations constituting to the equations of motion (EOM).

5

$$\ddot{x} - 2\dot{y} = x - \frac{1-\mu}{r_1^3}(\mu + x) + \frac{\mu}{r_2^3}(1 - \mu - x) \tag{2.1}$$

$$\ddot{y} + 2\dot{x} = y - \frac{1-\mu}{r_1^3}y \qquad\quad - \frac{\mu}{r_2^3}y \tag{2.2}$$

$$\ddot{z} \quad = \quad -\frac{1-\mu}{r_1^3}z \qquad\quad - \frac{\mu}{r_2^3}z \tag{2.3}$$

Firstly, it is important to note that the out-of-plane motion (z-direction) is simply harmonic whereas the in-plane motion (xy-direction) is coupled. The second essential insight into this dynamical model is the absence of an explicit dependence on time, as the relative position of the two primaries remains unchanged. This constitutes to a non-central conservative force field with can be expressed as the potential shown in Equation 2.4. This function encompasses both the centrifugal and gravitational forces.

$$\Omega = \frac{1}{2}\left(x^2 + y^2\right) + \frac{1-\mu}{r_1} + \frac{\mu}{r_2} \tag{2.4}$$

Interestingly, the right-hand side of Equations 2.1 through 2.3 can be represented by the partial derivatives of the potential with respect to the three orthogonal directions x, y, z respectively. The function Ω is referred to as the pseudo-potential as it only accounts for the gravitational and centrifugal forces which are dependent on the position and mass parameter. To fully determine the dynamics of the particle, the Coriolis force has to be included and is expressed by the ± 2 terms on the left-hand side of Equations 2.1 and 2.2 as a function of the velocity components. [1]

2.1.2. Equilibria, symmetries and image trajectories

The pseudo-potential presented in Equation 2.4 gives rise to the five equilibrium points shown in Figure 2.2. Please note that for the sake of completeness, also the two equilateral points L_4 and L_5 are shown whereas the scope of this research is confined to the collinear points L_1 and L_2.
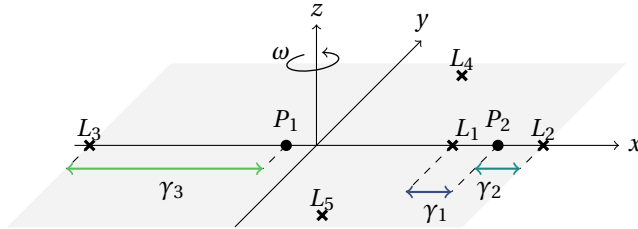
Figure 2.2: *Location of the three collinear and two equilateral libration points in the rotating (synodic) coordinate system.*

At these libration points, the partial derivatives of the pseudo-potential equal zero as shown in Equation 2.5.

$$\Omega_x = \Omega_y = \Omega_z = 0 \tag{2.5}$$

The spatial distribution of equilateral points L_4 and L_5 in Figure 2.2 already provide evidence of the axially-symmetric gravitational structure of this dynamical system. In combination with the "linear homogeneous structure of the Corliolis acceleration terms," the symmetrical properties of the equations of motion is captured in the theory on image trajectories presented in [Miele, 2010]. This theorem provides a powerful tool for the computation and verification of ballistic manifolds. According to this theory, each trajectory in space is associated with a family of three image trajectories as shown in Equations 2.6 through 2.9.

$$(T1) \qquad x = a(\ t), \quad y = \ b(\ t), \quad z = \ c(\ t) \tag{2.6}$$

$$(T2) \qquad x = a(-t), \quad y = -b(-t), \quad z = -c(-t) \tag{2.7}$$

$$(T3) \qquad x = a(\ t), \quad y = \ b(\ t), \quad z = -c(\ t) \tag{2.8}$$

$$(T4) \qquad x = a(-t), \quad y = -b(-t), \quad z = \ c(-t) \tag{2.9}$$

---

[1] The reader is referred to [Szebehely, 1967] for a complete analysis of the equations of motion in the restricted problem.

In other words, if trajectory ($T1$) denotes a solution to the equations of motion, trajectories ($T2$) − ($T4$) will also form solutions to this system. Proof for this theorem is provided when substituting Equations 2.7, 2.8 and 2.9 into the equations of motion presented in Equations 2.1 through 2.3. From a spatial perspective, ($T2$) marks the mirror image of ($T1$) with respect to the x-axis whereas ($T3$) and ($T4$) signify the symmetries with respect to the orbital plane. Please note that in the planar case the symmetry with respect to the xy-plane is lost, and Equations 2.6 through 2.9 collapse into a set of two trajectories. The power of this theorem will be demonstrated in the numerical approach to invariant manifold theory in Chapter 5.

2.1.3. Dimensionless quantities in the normalised system

The quantities in which the results will be expressed have been normalised to the properties of the two primaries in the CR3BP. The dimensionless revolution time, position and velocity are adjusted to 2π, distance between P_1 and P_2 and a combination of the two respectively [Hagel, 1990]. The figures adopted for this research are documented in Appendix A along with other relevant parameters and constants.

In addition to these normalised variables, a fundamental quantity is Jacobi's constant shown in Equation 2.10. Resulting from the multiplication of Equations 2.1 through 2.3 with the three velocity components respectively, this parameter is the only known conserved quantity in the CR3BP.

$$C = 2\Omega - V^2 = -2h \tag{2.10}$$

As can be seen on the right-hand side of Equation 2.10, this integration constant (C) is directly proportional to the sum of potential (2Ω) and kinetic energy ($-V^2$) of the particle. In this way, this quantity can be utilised to characterise orbits and to verify the hyperbolic manifold trajectories as no additional energy is added to the system in the ballistic case.

2.2. Numerical methods for autonomous differential systems

The time-independence of the dynamical system (as outlined in Section 2.1) forms an Hamiltonian system which entails desirable properties that can be exploited. "A complete and rigorous integration being manifestly impossible, we must turn to the process of approximation" [Poincaré, 1967b]. With this idea in mind, this section introduces the numerical techniques to propagate, refine, analyse and verify trajectories.

2.2.1. Explicit integration using adaptive step-size control of embedded methods

Propagation of state until a next time-step t is achieved through integration of the state derivative, derived from Equations 2.1 through 2.3. Renowned for its accurate and efficient approximations, the selected *Runge-Kutta-Fehlberg 7(8)* (RK78) integration scheme is widely used by the leading researchers in this field [Parker and Anderson, 2014].

This method accomplishes consistent numerical precision though its adaptive step-size control, in which the step-size is a dependent variable determined by the local truncation error. In this way, a step-size is ensured in which "each step contributes uniformly to the total integration error" [Montenbruck and Gill, 2000]. In general, the amount of effort involved in explicit integration is driven by the number of function evaluations to achieve numerical accuracy. However, the estimate of the local truncation error requires two independent approximations. The RK78 scheme poses a solution for this problem, by adopting the same set of evaluations using different weights to provide two estimates of neighbouring order. This ensures computational efficiency and results in only s instead of $2s - 1$ function evaluations. [2]

This explicit integration method allows propagation of one phase to the next, thereby satisfying the conditions for an *initial value problem* (IVP). To have the ability to refine trajectories to periodic orbits, one is required to solve a *two-point boundary value problem* (TPBVP).[3]

---

[2]A more exhaustive analysis of this Runge-Kutta method of order 7 with an embedded 8th-order method for step-size control including error tolerances and the Butcher tableau, is provided in Appendix B.

[3]Periodicity is approached in a numerical sense, thereby continuous under the thresholds stated in Appendix A

2.2.2. The Poincaré phase portrait

Explicit integration of state can be performed for a certain integration period or until a set of stopping conditions are met. Poincaré sections, also referred to as first recurrence maps, will be exploited to examine, refine and connect trajectories.

Poincaré map: *"We consider an autonomous dynamical system defined by N simultaneous differential equations. A solution can be represented by a curve, or trajectory, in an N-dimensional phase space $(x_1, \ldots, x_N)$. A frequently used technique consists in considering the successive intersections of the trajectory with a surface of section $\sum$, which in general is an (N − 1)-dimensional subset of the phase space, defined by $S(x_1, \ldots, x_N) = 0$. The dynamical system defines then a mapping of $\sum$ on itself, known as a Poincaré map"* [Hénon, 1982].

This method is widely applicable and forms a powerful contribution to the numerical procedures for orbit and manifold generation and analysis.

2.2.3. Multi-variate Newton method

The preferred approach to generating continuous solutions in the CR3BP involves the differential correction of an initial guess. This optimisation problem boils down to satisfying a set of m scalar constraint equations **F**, by optimal arrangement of n free variables **X**. This resulting zero-objective is presented on the left-hand side of Equation 2.11.

$$\mathbf{F}(\mathbf{X}) = \begin{bmatrix} F_1(\mathbf{X}) \\ \vdots \\ F_m(\mathbf{X}) \end{bmatrix} \rightarrow \mathbf{0}, \qquad \mathbf{X} = \begin{bmatrix} X_1 \\ \vdots \\ X_n \end{bmatrix} \tag{2.11}$$

In this way, refining trajectories to periodic solutions poses a root-finding problem. There are many methods available to satisfy the objective presented in Equation 2.11. However, the smooth and continuous solution space of the CR3BP offers ideal characteristics to be exploited by a gradient technique. In particular, a higher-dimensional version of the Newton–Raphson method, referred to as the multi-variate Newton method, has proved to yield efficient and robust convergence [Gómez et al., 1998]. Like the single-variable Newton-Rhapson method, gradient information is extracted through a truncated Taylor series expansion as shown in Equation 2.12.

$$\mathbf{F}(\mathbf{X}) \approx \mathbf{F}(\mathbf{X}^0) + D\mathbf{F}(\mathbf{X}^0)(\mathbf{X} - \mathbf{X}^0) + \mathcal{O}(2) \tag{2.12}$$

This approximation is limited to linear terms only, as designated by the Bachmann–Landau notation. Rearrangement of the terms displayed in Equation 2.13, contributes to an iterative procedure for the refinement of orbits. Hence, this method is also referred to as a shooting method.

$$\mathbf{X}^{j+1} = \mathbf{X}^j - D\mathbf{F}(\mathbf{X}^j)^{-1}\mathbf{F}(\mathbf{X}^j) \tag{2.13}$$

$$\delta\mathbf{X} = -D\mathbf{F}(\mathbf{X}^j)^{-1}\mathbf{F}(\mathbf{X}^j) \tag{2.14}$$

Characteristically, the free variables **X** and constraints **F** involve the position and velocity components of the third body at the start and end of an estimated period. Along these lines, the derivative of constraints with respect to the free variables $D\mathbf{F}(\mathbf{X}^0)$ requires knowledge of the sensitivity between both states. In other words, one requires mapping of the objective at time t, back to a change in initial guess.

2.2.4. Linearisation and the state propagation matrix

To satisfy the need to relate changes in initial conditions at time t_0 to a final time t_f, the EOM are rewritten from a set of three second-order differential equations to a set of six first-order variational equations (Eq. 2.15). In this way, the state derivative is computed through the *state propagation matrix* (SPM) $\mathbf{A}(t)$.

$$\mathbf{A} = \frac{\partial \dot{\mathbf{X}}(t)}{\partial \mathbf{X}(t)}, \qquad \mathbf{A}(t) = \begin{bmatrix} 0 & 0 & 0 & 1 & 0 & 0 \\ 0 & 0 & 0 & 0 & 1 & 0 \\ 0 & 0 & 0 & 0 & 0 & 1 \\ \Omega_{xx} & \Omega_{xy} & \Omega_{xz} & 0 & 2 & 0 \\ \Omega_{yx} & \Omega_{yy} & \Omega_{yz} & -2 & 0 & 0 \\ \Omega_{zx} & \Omega_{zy} & \Omega_{zz} & 0 & 0 & 0 \end{bmatrix} \tag{2.15}$$

Please note that the third quadrant of the SPM contains the Hessian of the pseudo-potential, derived from a truncated Taylor series expansion about a reference solution. This is demonstrated in Equations 2.17 and 2.18 for offsets (ξ, η, ζ) from an equilibrium point located at (a, b, c). In essence, the Jacobian matrix $\mathbf{A}(t)$ relates changes in the vector field to changes in the states and is thereby only position dependent $(\Omega = f(\mu, x, y, z))$.[4] As a result, the SPM constitutes to a linear time-invariant system. [5]

$$x = a + \xi, \qquad y = b + \eta, \qquad z = c + \zeta \tag{2.16}$$

$$\Omega_x = \Omega_x(a, b, c) + \Omega_{xx}(a, b, c)\,\xi + \Omega_{xy}(a, b, c)\,\eta + \Omega_{xz}(a, b, c)\,\zeta + \mathcal{O}(2) \tag{2.17}$$

$$= \qquad \Omega_{xx}(a, b, c)\,\xi + \Omega_{xy}(a, b, c)\,\eta + \Omega_{xz}(a, b, c)\,\zeta + \mathcal{O}(2) \tag{2.18}$$

The solution to the variational equations presented in Equation 2.15 is the *state transition matrix* (STM), and is shown in Equation 2.19. This matrix maps variations in state at time t_0 to time t. Thereby reflecting the sensitivity of the final state at time t to perturbations in the initial state at time t_0.

$$\Phi(t, t_0) = \frac{\partial \mathbf{X}(t)}{\partial \mathbf{X}(t_0)}, \qquad \Phi(t, t_0) = \begin{bmatrix} \frac{\partial x}{\partial x_0} & \frac{\partial x}{\partial y_0} & \frac{\partial x}{\partial z_0} & \frac{\partial x}{\partial \dot{x}_0} & \frac{\partial x}{\partial \dot{y}_0} & \frac{\partial x}{\partial \dot{z}_0} \\ \frac{\partial y}{\partial x_0} & \frac{\partial y}{\partial y_0} & \frac{\partial y}{\partial z_0} & \frac{\partial y}{\partial \dot{x}_0} & \frac{\partial y}{\partial \dot{y}_0} & \frac{\partial y}{\partial \dot{z}_0} \\ \frac{\partial z}{\partial x_0} & \frac{\partial z}{\partial y_0} & \frac{\partial z}{\partial z_0} & \frac{\partial z}{\partial \dot{x}_0} & \frac{\partial z}{\partial \dot{y}_0} & \frac{\partial z}{\partial \dot{z}_0} \\ \frac{\partial \dot{x}}{\partial x_0} & \frac{\partial \dot{x}}{\partial y_0} & \frac{\partial \dot{x}}{\partial z_0} & \frac{\partial \dot{x}}{\partial \dot{x}_0} & \frac{\partial \dot{x}}{\partial \dot{y}_0} & \frac{\partial \dot{x}}{\partial \dot{z}_0} \\ \frac{\partial \dot{y}}{\partial x_0} & \frac{\partial \dot{y}}{\partial y_0} & \frac{\partial \dot{y}}{\partial z_0} & \frac{\partial \dot{y}}{\partial \dot{x}_0} & \frac{\partial \dot{y}}{\partial \dot{y}_0} & \frac{\partial \dot{y}}{\partial \dot{z}_0} \\ \frac{\partial \dot{z}}{\partial x_0} & \frac{\partial \dot{z}}{\partial y_0} & \frac{\partial \dot{z}}{\partial z_0} & \frac{\partial \dot{z}}{\partial \dot{x}_0} & \frac{\partial \dot{z}}{\partial \dot{y}_0} & \frac{\partial \dot{z}}{\partial \dot{z}_0} \end{bmatrix} \tag{2.19}$$

Propagation of the STM is ensured through explicit integration of the derivative using the previously derived SPM, as illustrated in Equation 2.20. This sequential procedure is initialised using the identity matrix.

$$\dot{\Phi}(t, t_0) = \mathbf{A}(t)\Phi(t, t_0) \qquad \forall \quad \Phi(t_0, t_0) = \mathbf{I}(6, 6) \tag{2.20}$$

The STM is a powerful tool in the refinement of periodic trajectories and contains valuable information on the path-dependent dynamics and stability. A special case of this matrix is the one for periodic trajectories, which provides exceptional insights into the eigenspace like the (un)stable modes for hyperbolic manifold trajectories.

2.2.5. Monodromy matrix and the analysis of its eigensystem

A trajectory is considered to be periodic for minimal period T if it satisfies the two criteria stated in Equation 2.21.

$$\mathbf{X}(t + T) = \mathbf{X}(t) \qquad \text{and} \qquad \mathbf{X}(t + \tau) \neq \mathbf{X}(t) \quad \forall \quad 0 < \tau < T \tag{2.21}$$

The STM evaluated for the path denoted in Equation 2.21 is referred to as the *monodromy matrix*, which follows the notation presented in Equation 2.22.

$$\mathbf{M} = \Phi(t_0 + T, t_0) \tag{2.22}$$

---

[4]A constant mass parameter is assumed throughout this thesis, corresponding to the EM-system. This value and other parameter settings adopted in this research are documented in Appendix A

[5]The validity of truncating nonlinear terms is proved in the Hartman–Grobman or linearisation theorem which states that the "local behaviour of the nonlinear system near a hyperbolic equilibrium point is qualitatively determined by the behaviour of the linear system"[Perko, 2001].

Insight into the stability of this periodic solution can be deducted from the eigenvalues of this fundamental matrix with the help of *Floquet theory*. Also designated as characteristic or Floquet multipliers, the eigenvalues of the monodromy matrix pose useful properties for the verification of orbits and generation of manifolds. Firstly, as the CR3BP is Hamiltonian in nature, the system of equations described in Equations 2.1 through 2.3 is considered symplectic. Therefore, any STM is a symplectic map in which the characteristic multipliers appear in reciprocal eigenvalue pairs. In this way, λ_i^{-1} is also an eigenvalue given λ_i. For the particular case of the (real) monodromy matrix, the complex conjugate λ_i^* is also an eigenvalue given a complex eigenvalue λ_i. Secondly, a linear mapping corresponding to a periodic solution requires at least one unity eigenvalue to ensure that "a disturbance provided along a direction tangent to the periodic orbit neither grows nor decades" [Nayfeh and Balachandran, 1995]. This requires that the determinant of the monodromy matrix equals one, which provides for a simple but useful verification test.

$$det\,(\mathbf{M}) = 1 \qquad (2.23)$$

In summary, the six-dimensional phase space in the CR3BP gives rise to six eigenvalues deduced from the monodromy matrix, forming three reciprocal pairs. As one pair equals unity, two pairs remain to offer information on stability. Following the logic presented in Equation 2.24, eigenvalues greatly exceeding one signify hyperbolic motion diverging from the reference case and is therefore associated with the unstable subspace.

$$\mathbf{M}\mathbf{v_i} = \lambda_i \mathbf{v_i} \quad \forall \quad i = 1, \ldots, 6 \qquad (2.24)$$

The symplectic property of the monodromy matrix dictates that inverse of λ_i exists, and thereby giving rise to the stable subspace. The eigenvector directions associated with these two eigenvalues provide the starting points for manifold generation to be presented in Chapter 4.

To indicate the stability of the periodic solution, a stability index is introduced for each reciprocal pair shown in Equation 2.25. As "eigenvalues on the unit circle offer no information concerning the stability of the nonlinear solution," the number of eigenvalue pairs not equalling unity yield critical knowledge [Howell and Campbell, 1999]. This gives rise to an *order of linear instability*, equalling zero, one or two when assuming periodicity.

$$v_i = \frac{1}{2}\left[|\lambda_i| + \frac{1}{|\lambda_i|} \right] \quad \forall \quad i = 1, 2, 3 \qquad (2.25)$$

The monodromy matrix and analysis of its eigensystem provides significant knowledge on the stability of solutions, which can be exploited to verify the numerical results. In addition, the behaviour of the eigenvalues in the complex plane serve as useful indicators for the connection of families of orbits. In essence, "many interesting phenomena in ODE systems can only be understood by analysing global bifurcations" [Doedel et al., 2008]. The study of these phenomena is captured in *bifurcation theory*.

2.3. Bifurcation theory and stability

The scope of bifurcation theory is vast, therefore only the aspects relevant to this research will be highlighted in this section. "The very definition of a bifurcation point varies from author to author," hence the formulation stated below can be regarded as an interpretation described as the "classical definition" by [Marsden, 1978]. Knowledge of this theory is crucial to the understanding of the phase space of periodic solutions.

Bifurcation theory: *"Bifurcation theory is a study of the branching of solutions of nonlinear equations $f(x,\lambda) = 0$ where f is a nonlinear operator, x is the solution vector and λ is a parameter. It is of particular interest in bifurcation theory to study how the solutions $x(\lambda)$ and their multiplicities change as λ varies. Thus we refer to λ as the bifurcation parameter. A bifurcation point of a solution branch $x(\lambda)$ is a point $(\lambda_0, x(\lambda_0))$ from which another solution $x_1(\lambda)$ branches. That is, $x(\lambda_0) = x_1(\lambda_0)$ and $x(\lambda) \neq x_1(\lambda)$ for all λ in an interval about λ_0"* [Matkowski and Reiss, 1977].

A bifurcation point can be observed by a distinct change in eigenstructure of the monodromy matrix. The numerical technique exploited in this thesis is to consider the point at which a reciprocal pair of Floquet multipliers leave (or enter) the unit circle in the complex plane. This indicates a qualitative change in system dynamics, giving rise to a change in order of linear instability (as described in Section 2.2.5) and can imply a connection of different families of periodic solutions in phase space. [6]

2.3.1. Principle forms of collinear libration point motion

The hyperbolic collinear libration points give rise to two principle forms of motion: the H-L and V-L orbits. If considered sufficiently close to the equilibrium point, these families of solutions consist of pure planar and out-of-plane motion respectively. The existence of these one-parameter families in the collinear libration points is implied by Lyapunov's centre theorem.

The underlying evidence for this theorem is derived from the roots of the characteristic equation of the Jacobian matrix (linearised EOM in Equation 2.15) for the collinear equilibrium points. These eigenvalues are of the form $\{\pm\lambda, \pm i\omega_2, \pm i\omega_2\}$, giving rise to local centre × centre × saddle-type dynamic behaviour [Wiggins, 2003]. The first two types reveal the two mono-parametric families H-L and V-L, whereas the latter forms the foundation for invariant hyperbolic manifolds [Meyer et al., 2008]. In other words, these properties define the center and (un)stable sub-spaces respectively.[7]

2.3.2. Additional types of periodic solutions and their connections

In addition to the two principle forms of motion, the dynamical structure in the neck region of the EM-system also gives rise to different types of periodic solutions. One of the main other types of motion is the halo orbit, as displayed in Figure 2.3.
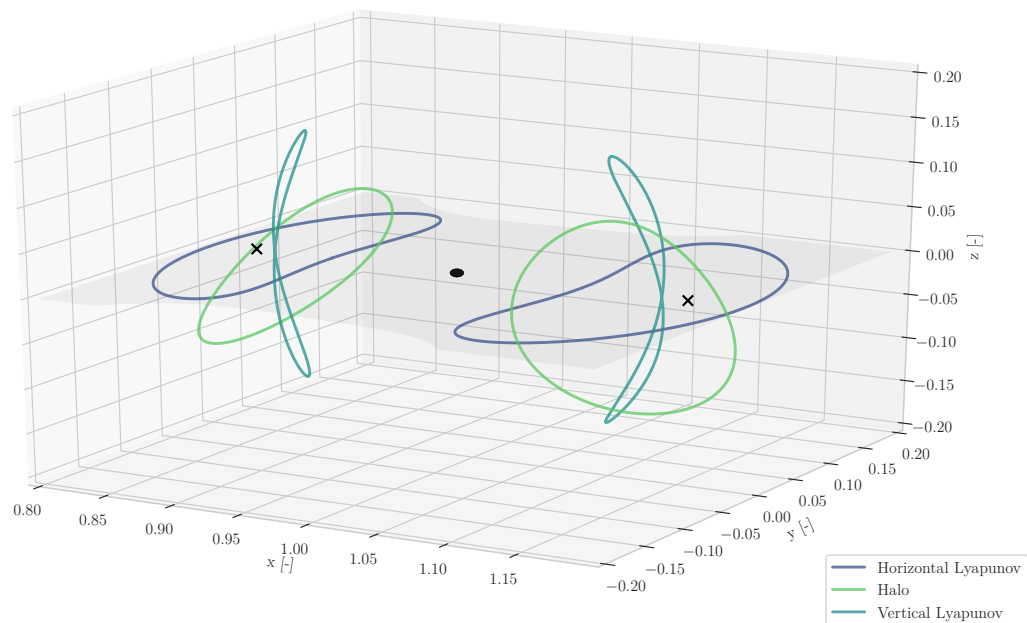
Figure 2.3: Orbits around L_1 (left cross) and L_2 (right cross) surrounding the Moon (center sphere) for $C = 3.1$. Members of the three main symmetric families are presented: horizontal Lyapunov, vertical Lyapunov and halo.

---

[6]The reader is referred to [Doedel et al., 1991a] [Doedel et al., 1991b] for a comprehensive study on the numerical approach to bifurcation theory for various types of bifurcations.

[7]The "majority of the design applications thus far are based solely on the stable and unstable manifolds," whereas the study performed by [Barden and Howell, 1998] aims to exploit the center manifold.

All orbits displayed in Figure 2.3 are members of continuous families of solutions, which cover a range of energy levels and are interconnected at bifurcation points. However, whereas the H-L and V-L emanate from the equilibrium point itself, the halo orbit requires a minimum amplitude before bifurcating from the H-L family.[8] This bifurcation is shown in Figure 2.4. Please note that according to the symmetries listed in Equations 2.6 and 2.8, both a 'northern' and 'southern' family of halo orbits with respect to the orbital plane ought to exist.

L_1 Bifurcation - Halo family connecting to horizontal Lyapunov orbits
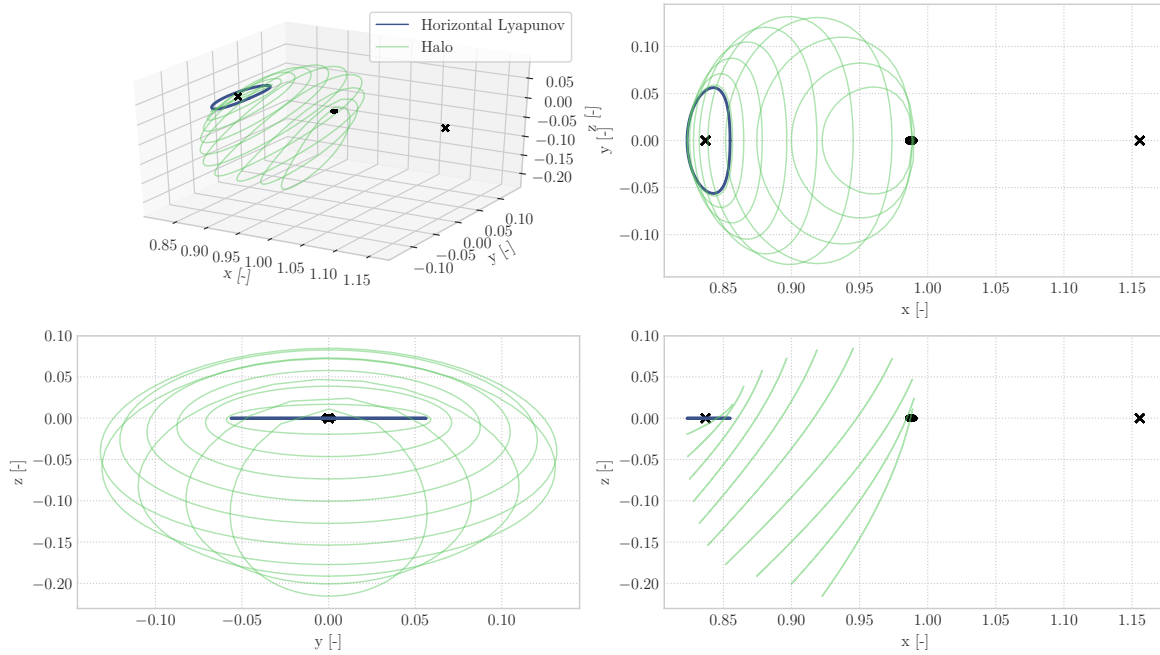
Figure 2.4: *First bifurcation of the H-L family connecting to the halo family.*

---

[8]All families treated in this research possess at least one plane of symmetry, since "relatively few results exist on asymmetric periodic solutions" [Markellos and Halioulias, 1977].

In addition to the bifurcation from H-L to halo family, the two principle forms of motion are also connected through a fourth family: the axial family. For decreasing values of C, this type of family bifurcates from the H-L for a certain amplitude into the out-of-plane direction. Continuous twisting of the axial orbit eventually results in the doubly symmetric geometry of the V-L, denoting another bifurcation point. This connection is displayed in Figure 2.5. [9]

L_1 Bifurcation - Axial family connecting horizontal and vertical Lyapunov orbits
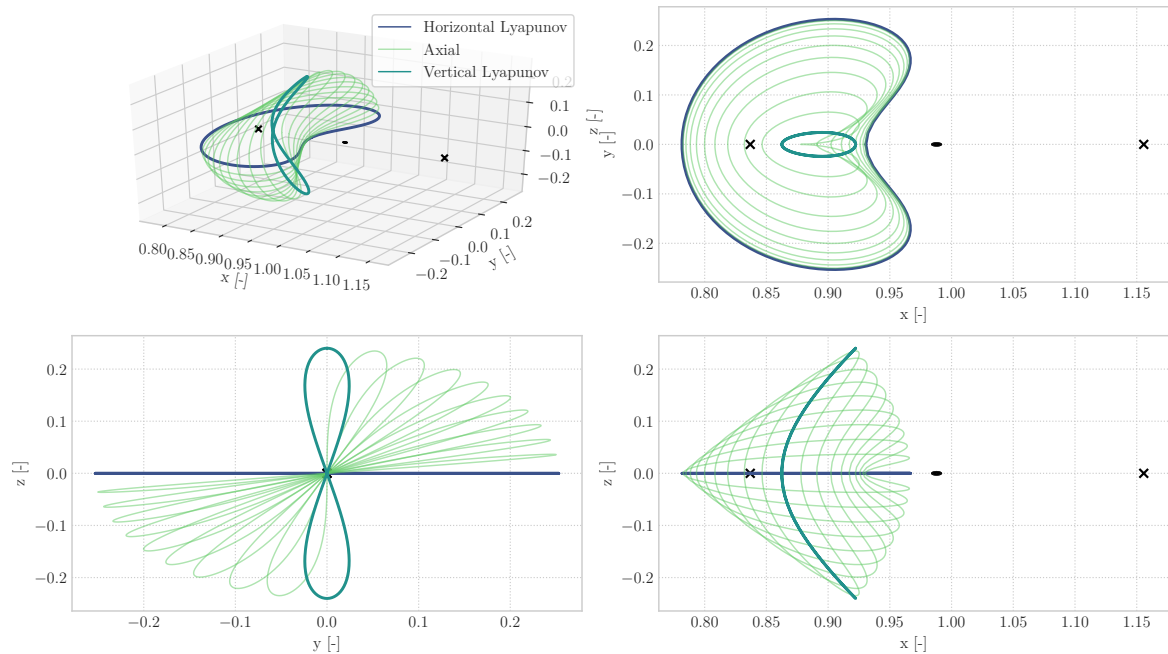
Figure 2.5: *Second bifurcation of the H-L family connecting to the axial family, which joins with the V-L family.*

When evaluating these types of periodic libration point motion with the decoupled nature of the EOM (Eq. 2.1-2.3) in mind, one can conclude that these four types possess an in-plane frequency that is equal to the out-of-plane frequency. When this constraint is weakened, a whole new set of trajectories arises called quasi-periodic orbits.

2.3.3. The existence of quasi-periodic solutions

The quasi-periodic solutions are characterised by "a periodic path in the plane of primary motion, and an uncoupled periodic out-of-plane motion" in which the "two frequencies are generally unequal" [Howell and Pernicka, 1987]. From a spatial point of view, this irrational fraction of frequencies result in multiple intersections with the Poincaré section and thereby distinguishing themselves from the periodic orbits. In this way, these quasi-periodic trajectories reside "on two-dimensional tori" around the periodic solutions [De Sousa-Silva and Terra, 2016].

"The orbital path as viewed from the Earth" corresponding to a quasi-periodic trajectory with a small amplitude "traces out a Lissajous figure" [Farquhar and Kamel, 1973]. The corresponding denomination Lissajous trajectories form the basis of the halo orbits given a minimum in-plane amplitude.[10] The existence of quasi-periodic solutions forms a useful tool when exploiting a multiple shooting technique to refine natural connections, in which relaxation of the periodicity constraints might be required to remove any discrepancy near the manifold connection.

---

[9]The existence of various types of motion as well as the location of the bifurcation points is highly dependent on the mass parameter μ. For a comprehensive numerical analysis of these phenomena as a function of the mass-ratio, the readers is referred to [Doedel et al., 2007].

[10]The procedure required to obtain this synchronised trajectory will be presented in Section 3.1.1.

2.3.4. Bifurcation theory in the numerical approach

The significance of bifurcation theory in the numerical approach of this research is demonstrated throughout the entire study. Apart from providing the reader with a critical understanding of the phase space surrounding collinear libration points L_1 and L_2, evidence of the implementation of this theory is can be observed in:

Chapter 2   Providing initial conditions for the first member of the axial family, by means of the bifurcation point from the H-L family at the second change of linear order of instability.

Chapter 3   Dynamical analysis through order of linear instability, stability indices (Eq. 2.25) and spatial representation of bifurcation points. In addition, unit tests concerning one pair of eigenvalues equalling unity and a determinant of one (Eq. 2.23) are utilised as means of verification.

Chapter 4   Sorting of the eigenvalues and corresponding selection of the (un)stable eigenvectors is critical to the correct generation of manifold structures.

The concepts presented in this chapter will form the theoretical basis for orbit generation and consecutively manifold propagation.

3

Numerical approach to orbit generation

The background theory presented in Chapter 2 will provide the basis for the numerical orbit generation scheme, which is analysed in this chapter. The aim is not to reiterate what has been done before, but to substantiate the adopted approach with respect to best practice in industry. Multiple steps are involved in producing families of orbits including analytic approximations, numerical refinement, verification, validation and continuation of solutions. As a result, one will be able to obtain a set of verified orbits (Chapter 4) from which the desired manifolds can be computed (Chapter 5).

3.1. Orbit generation scheme

The numerical approach composed in this research involves multiple steps towards generating a family of solutions, of which the operating principle is captured in the pseudocode presented in Algorithm 1. This high-level description will act as a guideline for the in-depth analysis of the various components.

Algorithm 1 Family of periodic orbits generation

Input: $\left(\text{orbitType}, L_p\right)$ **or** $\left(A_{x,z}^0, A_{x,z}^1, \text{orbitType}, L_p, \mu\right)$
Output: $\left[\mathbf{X}_0^0, T^0\right], \ldots, \left[\mathbf{X}_0^{n-1}, T^{n-1}\right]$

  1: **if** $A_{x,z}^0, A_{x,z}^1, \mu$ are unspecified **then**
  2:     $\mu, A_{x,z}^0, A_{x,z}^1 \Leftarrow$ **EM-system parameters**(orbitType, L_p)
  3: **end if**
  4: **for** $i = 0; i < 2; i + +$ **do**
  5:     $\hat{\mathbf{X}}_0^i, \hat{T}^i \Leftarrow$ **Richardson**$\left(A_{x,z}^i, \text{orbitType}, L_p, \mu\right)$ ▷ *Sec. 3.1.1*
  6:     **while** $y_{t_{\hat{T}/2}}^i, \dot{x}_{t_{\hat{T}/2}}^i, \dot{z}_{t_{\hat{T}/2}}^i > 10^{-12}$ **do**   ▷ *Sec. 3.1.3*
  7:         $\hat{\mathbf{X}}_0^i, \hat{T}^i \Leftarrow$ **DC**$\left(\hat{\mathbf{X}}_0^i, \hat{T}^i\right)$ ▷ *Sec. 3.1.2*
  8:     **end while**
  9: **end for**
10: n = 2
11: **while** $\left|Re(\lambda_p) - 1\right| < 10^{-3}$ **and** $n < n_{max}$ **do**
12:     $\hat{\mathbf{X}}_0^n, \hat{T}^n \Leftarrow$ **NC**$\left(\mathbf{X}_0^{n-2}, T^{n-2}, \mathbf{X}_0^{n-1}, T^{n-1}\right)$ ▷ *Sec. 3.1.4*
13:     **while** $y_{t_{\hat{T}/2}}^n, \dot{x}_{t_{\hat{T}/2}}^n, \dot{z}_{t_{\hat{T}/2}}^n > 10^{-12}$ **do**   ▷ *Sec. 3.1.3*
14:         $\hat{\mathbf{X}}_0^n, \hat{T}^n \Leftarrow$ **DC**$\left(\hat{\mathbf{X}}_0^n, \hat{T}^n\right)$ ▷ *Sec. 3.1.2*
15:     **end while**
16:     n += 1
17: **end while**

The algorithm is initialised by specifying five parameters: the amplitudes of the two initial guesses ($A_{x,z}^0, A_{x,z}^1$), the type of orbit, the libration point number (L_p), and mass parameter (μ). A closer look at the first few lines in Algorithm 1 reveals default settings for the EM-system. Using both amplitudes, two initial guesses

are generated using an analytic approximation and refined using differential correction (DC). This results in two periodic solutions, which give rise to a third initial guess through the process of numerical continuation (NC). The process described above is repeated until either the maximum number of members is achieved or anomalies are revealed through numerical verification.

Important to note is that techniques like DC and NC are applicable far out of the scope of periodic libration point orbits. For example, the combination of these two procedures are also relevant to the correction and continuation of a family of homo- and heteroclinic solutions [Barrabés et al., 2009][Barrabés et al., 2013].

3.1.1. Analytic approximation of initial conditions

The first step in the sequential procedure of orbit generation is the production of two initial guesses. The method selected in this research is the third-order analytic approximation described in [Richardson, 1980b][Richardson, 1980a]. As a relative of the Lindstedt-Poincaré method, this set of equations approximates periodic solutions to ordinary differential equations by eliminating secular development. This method lies in the field of *perturbation theory*, and can be used to find nonlinear oscillators. It is reliable and robust near the equilibrium points, but its accuracy reduces when increasing range through decreasing validity of the qualitatively linear behaviour.

The successive approximations leading up to the third-order estimate show the corresponding linearity, quadratic and cubic dependence on the provided amplitude in Equations 3.1 through 3.6. The derivation of these equations is a "lengthy and tedious algebraic process" involving algebraic manipulation computer programs that exploit Legendre-polynomial recursion relations [Richardson, 1980a].

$$x = - \quad A_x \cos\tau_1 \quad + a_{21}A_x^2 + a_{22}A_z^2 + (a_{23}A_x^2 - a_{24}A_z^2)\cos2\tau_1 \quad + \quad (a_{31}A_x^3 - a_{32}A_x A_z^2)\cos3\tau_1 \quad (3.1)$$

$$y = \quad k \quad A_x \sin\tau_1 \quad + (b_{21}A_x^2 - b_{22}A_z^2)\sin2\tau_1 \quad + \quad (b_{31}A_x^3 - b_{32}A_x A_z^2)\sin3\tau_1 \quad (3.2)$$

$$z = \quad \delta_n \quad A_z \cos\tau_1 \quad + \delta_n d_{21}A_x A_z(\cos2\tau_1 - 3) \quad + \delta_n \quad (d_{32}A_z A_x^2 - d_{31}A_z^3)\cos3\tau_1 \quad (3.3)$$

$$\dot{x} = \quad \lambda \quad A_x \sin\tau_1 \quad - 2\lambda(a_{23}A_x^2 - a_{24}A_z^2)\sin2\tau_1 \quad - 3\lambda \quad (a_{31}A_x^3 - a_{32}A_x A_z^2)\sin3\tau_1 \quad (3.4)$$

$$\dot{y} = \quad \lambda(k A_x \cos\tau_1 \quad + 2(b_{21}A_x^2 - b_{22}A_z^2)\cos2\tau_1 \quad + 3 \quad (b_{31}A_x^3 - b_{32}A_x A_z^2)\cos3\tau_1) \quad (3.5)$$

$$\dot{z} = -\delta_n A_z \sin\tau_1 \quad - 2\lambda\delta_n d_{21}A_x A_z\sin2\tau_1 \quad - 3\lambda\delta_n(d_{32}A_z A_x^2 - d_{31}A_z^3)\sin3\tau_1 \quad (3.6)$$

Derivation of this solution starts from the linearised form of the EOM (Eq. 2.1-2.3), shown in Equations 3.7 through 3.9.

$$\ddot{x} - 2\dot{y} - (1 + 2c_2)x = 0 \quad (3.7)$$

$$\ddot{y} + 2\dot{x} - (c_2 - 1)\ y = 0 \quad (3.8)$$

$$\ddot{z} \quad + \lambda^2 \quad z = 0 \quad (3.9)$$

As is discussed in Section 2.1.1, the motion in-plane and out-of-plane is decoupled. In an attempt to align these frequencies, a correction constant Δ is introduced in Equation 3.10.[1]

$$\Delta := \lambda^2 - c_2, \qquad \Delta \sim \mathcal{O}(A_z^n) \quad (3.10)$$

Consecutively, a new independent time-like variable is introduced (τ) in Equation 3.12 to remove secular terms. This is achieved through the specification of ω_n-terms constituting to the correction frequency (ω). These quantities relate to the solution through the definition of τ_1 in Equation 3.11.[2]

$$\tau_1 := \lambda\tau + \phi \quad (3.11)$$

$$\tau = \omega s \quad (3.12)$$

$$s = n_1 t \quad (3.13)$$

$$\omega = 1 + \sum_{n \geq 1} \omega_n, \qquad \omega_n < 1, \qquad \omega_n \sim \mathcal{O}(A_x^n) \quad (3.14)$$

---

[1]An irrational ratio of in-plane and out-of-plane frequency leads to (decoupled) quasi-periodic motion denoted as Lissajous trajectories. An example of these orbits are the quasihalos, which consist of invariant tori surrounding the halo family [Gómez et al., 1998].

[2]Important to note is the influence of amplitude A_x on the truncation error ϵ of the approximated frequency ω_n, which are chosen to remove secular terms. This underlines that the validity of the approximation is confined to the vicinity of the equilibrium point where amplitudes are small. The equivalent error related to the out-of-plane amplitude (A_z) appears in the correction constant Δ (Eq. 3.10).

To complete non-secular development in the third-order successive approximation, amplitude and phase-angle constraint relationships are defined in Equations 3.15 and 3.16 respectively.

$$l_1 A_x^2 + l_2 A_z^2 + \Delta = 0 \tag{3.15}$$

$$\psi - \phi = \frac{n\pi}{2} \quad \forall \quad n = 1, 3 \tag{3.16}$$

The scalar amplitude constraint provides interesting insights into the synchronized in- and out-of-plane motion for halo orbits. As discussed in Section 2.3.2, the halo-type orbits require a certain amplitude of H-L before bifurcating into either the northern or southern halo family.[3] This phenomenon can be expressed as the limit case of this constraint in Equation 3.17

$$A_{x_{min}} = \sqrt{\left| \frac{\Delta}{l_1} \right|} \qquad \begin{cases} A_x > 0 \\ A_z \geq 0 \end{cases} \tag{3.17}$$

This semi-analytic procedure provides the desired initial guess for the generation of pure in-plane (H-L), pure out-of-plane (V-L) and coupled (halo) motion. Without any loss of generality with respect to μ, implementation of this method forms a powerful contribution to the overall approach and concludes Line 5 of Algorithm 1.

3.1.2. Differential correction schemes

The third-order estimate resulting from Section 3.1.1 requires refinement to comply with the numerical thresholds for periodicity (Lines 7 and 14 in Algorithm 1). As the H-L, V-L and halo orbits are at least singly symmetric, their initial conditions can be fully determined by three out of six states, as shown in Equation 3.18.

$$\mathbf{X}_{t_0} = \begin{bmatrix} x_0 & 0 & z_0 & 0 & \dot{y}_0 & 0 \end{bmatrix}^T \tag{3.18}$$

Refinement is achieved through the process of differential correction (DC), which is based on a combination of the multi-variate Newton method (Section 2.2.3) and the STM (Section 2.2.4). As a first step, the third-order approximation of initial state is integrated until an estimated half-period $\hat{T}/2$.[4] Given a fully periodic trajectory, the state vector at this point should correspond to the symmetric equivalent of the initial state. However, the state vector after propagation will include deviations and is resembled by Equation 3.19.

$$\mathbf{X}_{t_{\hat{T}/2}} = \begin{bmatrix} x_{t_{\hat{T}/2}} & y_{t_{\hat{T}/2}} & z_{t_{\hat{T}/2}} & \dot{x}_{t_{\hat{T}/2}} & \dot{y}_{t_{\hat{T}/2}} & \dot{z}_{t_{\hat{T}/2}} \end{bmatrix}^T \tag{3.19}$$

In this way, the objective for DC entails Equation 3.20 to ensure numerical periodicity.

$$\{y_{t_{\hat{T}/2}}, \dot{x}_{t_{\hat{T}/2}}, \dot{z}_{t_{\hat{T}/2}}\} \to 0 \tag{3.20}$$

The iterative procedure set in place to satisfy this objective is presented in Equation 3.21. When comparing this to the equation introduced in theory of gradient techniques (Eq. 2.14), one can spot an additional term on the right-hand side. This term ensures refinement of the estimated half period.

$$\delta \mathbf{X}_{t_{\hat{T}/2}} \approx \Phi(t_{\hat{T}/2}, t_0) \delta \mathbf{X}_{t_0} \qquad\qquad + \left. \frac{\partial \mathbf{X}}{\partial t} \right|_{t_{\hat{T}/2}} \delta(\hat{T}/2) \tag{3.21}$$

$$\begin{bmatrix} \delta x \\ \delta y \\ \delta z \\ \delta \dot{x} \\ \delta \dot{y} \\ \delta \dot{z} \end{bmatrix}_{\hat{T}/2} \approx \begin{bmatrix} \Phi_{11} & \Phi_{12} & \Phi_{13} & \Phi_{14} & \Phi_{15} & \Phi_{16} \\ \Phi_{21} & \Phi_{22} & \Phi_{23} & \Phi_{24} & \Phi_{25} & \Phi_{26} \\ \Phi_{31} & \Phi_{32} & \Phi_{33} & \Phi_{34} & \Phi_{35} & \Phi_{36} \\ \Phi_{41} & \Phi_{42} & \Phi_{43} & \Phi_{44} & \Phi_{45} & \Phi_{46} \\ \Phi_{51} & \Phi_{52} & \Phi_{53} & \Phi_{54} & \Phi_{55} & \Phi_{56} \\ \Phi_{61} & \Phi_{62} & \Phi_{63} & \Phi_{64} & \Phi_{65} & \Phi_{66} \end{bmatrix}_{(\hat{T}/2, t_0)} \begin{bmatrix} \delta x \\ \delta y \\ \delta z \\ \delta \dot{x} \\ \delta \dot{y} \\ \delta \dot{z} \end{bmatrix}_{t_0} + \begin{bmatrix} \delta \dot{x} \\ \delta \dot{y} \\ \delta \dot{z} \\ \delta \ddot{x} \\ \delta \ddot{y} \\ \delta \ddot{z} \end{bmatrix}_{\hat{T}/2} \delta(\hat{T}/2) \tag{3.22}$$

---

[3] The existence of both northern and southern halo families form two solution branches and can be obtained through the switching function $\delta_n = 2 - n \ \forall \ n = 1, 3$, which is equivalent to changing the sign of A_z. These families are also referred to as halo orbits of class I or II.

[4] The preference of integrating until an estimated half period instead of the crossing of a plane of symmetry emerges from its robust convergence, especially in the case of the previously hard to obtain V-L family.

A spatial interpretation of the outlined procedure can be observed in Figure 3.1. The essence of this technique is to relate the deviations at the plane of symmetry back to a change in initial state, constituting to a single shooting algorithm. To achieve this, path dependent gradient information is required and extracted from the STM.
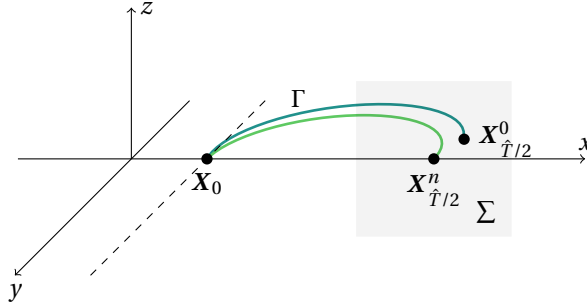
Figure 3.1: *Single shooting from initial state X_0 to $X_{\hat{T}/2}$ on Poincaré section Σ until a periodic solution is found $X_{\hat{T}/2}^n$. This method is suitable for trajectories which possess symmetries, whereas asymmetrical orbits might require multiple shooting due to the difficulty of integrating unstable orbits over longer periods of time [Gómez and Mondelo, 2001].*

The left-hand side of Equation 3.22 refers to the deviation at the estimated half period. When combining this set with the objective (Eq. 3.20), this set of equations can be reduced to the system shown in Equation 3.23.

$$\begin{bmatrix} \delta y \\ \delta \dot{x} \\ \delta \dot{z} \end{bmatrix}_{\hat{T}/2} \approx \begin{bmatrix} \Phi_{21} & \Phi_{23} & \Phi_{25} \\ \Phi_{41} & \Phi_{43} & \Phi_{45} \\ \Phi_{61} & \Phi_{63} & \Phi_{65} \end{bmatrix}_{(\hat{T}/2,\,t_0)} \begin{bmatrix} \delta x \\ \delta z \\ \delta \dot{y} \end{bmatrix}_{t_0} + \begin{bmatrix} \delta \dot{y} \\ \delta \ddot{x} \\ \delta \ddot{z} \end{bmatrix}_{\hat{T}/2} \delta(\hat{T}/2) \tag{3.23}$$

The system presented in Equation 3.23 is underdetermined. One way to overcome this issue, is by fixing one of the variables. After rearrangement of the terms, Equation 3.24 is the corresponding result of keeping the x-position constant.

$$\begin{bmatrix} \delta z_{t_0} \\ \delta \dot{y}_{t_0} \\ \delta \hat{T}/2 \end{bmatrix} \approx \begin{bmatrix} \Phi_{23} & \Phi_{25} & \delta \dot{y} \\ \Phi_{43} & \Phi_{45} & \delta \ddot{x} \\ \Phi_{63} & \Phi_{65} & \delta \ddot{z} \end{bmatrix}^{-1} \begin{bmatrix} \delta y \\ \delta \dot{x} \\ \delta \dot{z} \end{bmatrix}_{\hat{T}/2} \tag{3.24}$$

Fixing the x-position adds to the robustness of the algorithm as numerical continuation will result in a family of solution which monotonically decrease in Jacobi energy in the case of H-L, thereby preventing occurrence of turning points. The decision on which parameter is kept constant is based on a minimum norm criteria. In other words, the direction with the least error in position or velocity at $\hat{T}/2$ is kept constant over the next shooting guess.

The nature of this procedure is iterative through the truncated expansion as well as linearisation. To ensure robustness, a maximum number of iterations is set in addition to the numerical verification checks in Line 11 of Algorithm 1.

3.1.3. Periodicity verification and eigensystem validation

The periodic orbits resulting from the DC procedure need to be verified and validated for their numerical veracity. To this extent, a division is made between the periodicity verification and eigensystem validation. This analysis is based on earlier work performed by [Massarweh, 2016], which has proven to yield robust near-machine-limits accuracy for a problem which is inherently difficult to verify.[5] In contrast to the MATLAB ODE suite used in this earlier work, the platform for this analysis is based in C++ and has to cope with the challenges posed by a variable step-size integrator. Comparison of these two approaches is expected to yield interesting insights into the performance and accuracy of both schemes.

---

[5]As described in the research gap (Section 1.1.2), traditional verification techniques like visual inspection are deemed unfit due to their deceptive perception of numerical accuracy when shown in the vast scale of this system.

Periodicity verification

The aim of the periodicity verification is to ensure that the iterative DC procedure meets its intended requirements. As shown on Line 11 in Algorithm 1, this numerical test is performed for every member of the family of orbit solutions before expanding to new members through the process of NC. This check consist out of three tests:

1. The first test is performed on the norm of the position deviation at the estimated half period on whether it meets its threshold requirement.

2. Secondly, a similar test is performed on the norm of deviation in velocity.

3. Lastly, the deviation of one the eigenvalues denoting periodicity (Section 2.2.5) is checked to be within the set bounds.

Important to note is that the first two tests are numerical interpretations of Equation 2.21 and are executed at half-period, thereby ensuring periodicity through proper functioning of the DC algorithm. On the other hand, the last test is performed on the monodromy matrix at full-period which is used to assess the magnitude of over-/undershooting caused by the dependent nature of the step-size variable.

All thresholds adopted in this research are documented in Appendix A. In the case of DC with fixed x-position as posed in Equation 3.24, the norms of deviation in position and velocity can be observed in Equations 3.25 and 3.26 respectively. These values are among the most strict thresholds in literature, and have been adopted in [Cheng et al., 2017].

$$\sqrt{y_{\hat{T}/2}^2} \quad < 10^{-12} \tag{3.25}$$

$$\sqrt{\dot{x}_{\hat{T}/2}^2 + \dot{z}_{\hat{T}/2}^2} < 10^{-12} \tag{3.26}$$

The third and final test is presented in Equation 3.27.

$$\left| Re(\lambda_p) - 1 \right| \quad < 10^{-3} \tag{3.27}$$

In addition to these numerical tests to verify periodicity of every member of the computed family of solutions, the results have to satisfy an eigensystem validation. This procedure involves an extended analysis of the monodromy matrix, to ensure proper implementation of the dynamical model as well as adherence to path-dependent numerical accuracy.

Eigensystem validation

The eigensystem validation is a comprehensive process, based on the symplectic properties of the monodromy matrix described in Section 2.2.5. Whereas the periodicity verification techniques offer light checks on the results and are integrated as part of the program, the eigensystem validation is more exhaustive and requires interpretation of the results. In particular, the monodromy is analysed as follows:

1. Determinant equal to one (Eq. 2.23)

2. Smoothness of the stability indices across different members of the family (Eq. 2.25)

3. Symmetric behaviour of the norm of the set of eigenvalues, denoting three reciprocal pairs.

4. Correspondence of changes in order of linear stability to pairs of eigenvalues leaving the unit circle in the complex plane.

In addition to validating that the intended system has been computed, the analysis of the monodromy index is expected to yield insights into the performance of RK78 when computing near-machine-limits.

3.1.4. Pseudo-arclength continuation

Prior to this stage in Algorithm 1, two initial guesses have been refined and verified. Expansion of these two solutions to other members of the family is performed through the process of numerical continuation (NC). As shown on Line 12, this method requires two periodic initial conditions to approximate a third state. In the

basic case, this is achieved by addition of the difference in state to either one of the refined solutions. In this thesis, an extended version of this technique is adopted and shown in Figure 3.2.
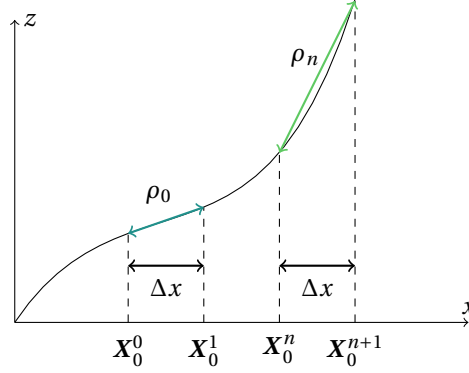
Figure 3.2: *Pseudo-Arclength $\|\rho\|$ between initial states X_0^n and X_0^{n+1} covering the distance $\sqrt{\Delta x^2 + \Delta z^2}$*

Developed by [Keller, 1977] and used by Doedel in AUTO, this variation on NC includes a scaling factor with respect to the z-position. This helps in dealing with nonlinear increments in z-direction or turning points, and enables the computation of the otherwise hard to obtain V-L family. Firstly the difference in state Δ_n (Eq. 3.28), and secondly the corresponding scaling parameter ρ_n (Eq. 3.29) is computed. Using these two variables, a third initial guess is computed as shown in Equation 3.30.

$$\Delta_n \quad = \mathbf{X}_0^{n+1} - \mathbf{X}_0^n \tag{3.28}$$

$$\rho_n \quad = \sqrt{\left(x_0^{n+1} - x_0^n\right)^2 + \left(z_0^{n+1} - z_0^n\right)^2} \tag{3.29}$$

$$\mathbf{X}_0^{n+2} = \mathbf{X}_0^{n+1} + \Delta_n \frac{10^{-4}}{\rho_n} \tag{3.30}$$

The length of adopted pseudo-arc is set at 10^{-4} which gives rise to a near-continuous set of orbits. As the increments in state vector from one energy level to the next are nonlinear, the iterative procedure of DC is repeated until also the new member is considered to be periodic.

The process of refining orbits through DC and extending the family through NC, results in the orbits which will be shown in Chapter 4. However, multiple exceptions from this procedure exists which will be reviewed prior to the analysis of results.

3.2. Extension of periodic libration point orbit solutions

Two main issues arise when implementing the orbit generation scheme outlined in Section 3.1. Firstly, the initial guess from Richardson's third order approximation requires a minimum out-of-plane amplitude for first two members of the halo orbit. In this way, the bifurcation to the H-L family is excluded from analysis. Secondly, the state vector notation as shown in Equation 3.18 has not proven to yield robust results when computing the axial family. Therefore another definition of the initial state, and corresponding DC and NC algorithms is required. Solving these two special cases leads to great insights into the extensive applicability of the presented techniques.

3.2.1. Reverse halo orbit continuation to horizontal Lyapunov tangent bifurcation

To analyse points of bifurcation, there is a need to obtain a complete set of halo orbits. Hence, one requires a backwards halo continuation scheme until the H-L family. This is achieved through reversal of the state vectors in Equation 3.28 of the pseudo-arclength. This straightforward implementation is combined with a new stopping conditions for NC. At initialisation, either the northern or southern halo family is selected. When the z-sign of the new initial guess posed by the NC is of opposite sign, the continuation procedure is stopped. This completes the computation of the halo family.

3.2.2. Axial orbit generation from horizontal Lyapunov tangent bifurcation

As introduced in Section 2.3.2, the axial family connects the H-L to the V-L family by twisting around the x-axis. A different formulation of the state vector is required for this type of family since the axial family does not posses the same symmetry with respect to the y-axis. Initial conditions for the DC-NC procedure are composed of the H-L state vector at its second change in order of linear instability, with a 'little push' in z-direction. The corresponding initial guess is presented in Equation 3.31.

$$\mathbf{X}_0 = [x_0, 0, 0, 0, \dot{y}_0, \dot{z}_0] \tag{3.31}$$

The rationale behind the idea of adding a minor increment in z-velocity is based on the continuous and smooth solution space of periodic trajectories. In other words, it is assumed that the first member of of the axial family does not vary significantly from the H-L orbit at equivalent energy level. Note that this formulation of initial conditions pose shooting conditions which depart from the x-axis, and rotate until stopped at the bifurcation to the V-L family. The corresponding DC algorithm to be employed aims to satisfy the objective shown in Equation 3.32.

$$\{y_{t_{\hat{T}/2}}, z_{t_{\hat{T}/2}}, \dot{x}_{t_{\hat{T}/2}}\} \to 0 \tag{3.32}$$

In this way, the complete set of DC equations (Eq. 3.22) reduce to the formulation shown in Equation 3.33.

$$\begin{bmatrix} \delta y \\ \delta z \\ \delta \dot{x} \end{bmatrix}_{\hat{T}/2} \approx \begin{bmatrix} \Phi_{21} & \Phi_{25} & \Phi_{26} \\ \Phi_{31} & \Phi_{35} & \Phi_{36} \\ \Phi_{41} & \Phi_{45} & \Phi_{46} \end{bmatrix}_{(\hat{T}/2, t_0)} \begin{bmatrix} \delta x \\ \delta \dot{y} \\ \delta \dot{z} \end{bmatrix}_{t_0} + \begin{bmatrix} \delta \dot{y} \\ \delta \dot{z} \\ \delta \ddot{x} \end{bmatrix}_{\hat{T}/2} \delta(\hat{T}/2) \tag{3.33}$$

Once more, this system of equations is underdetermined and is solved by fixing one of the parameters. A robust technique is to keep $\dot{z}_0$ constant to force out-of-plane motion and thereby refrain from reverting to planar motion for small off-sets of $\dot{z}$. After rearrangement of terms, this procedure constitutes to Equation 3.34.

$$\begin{bmatrix} \delta x_{t_0} \\ \delta \dot{y}_{t_0} \\ \delta \hat{T}/2 \end{bmatrix} \approx \begin{bmatrix} \Phi_{21} & \Phi_{25} & \delta \dot{y} \\ \Phi_{31} & \Phi_{35} & \delta \dot{z} \\ \Phi_{41} & \Phi_{45} & \delta \ddot{x} \end{bmatrix}^{-1} \begin{bmatrix} \delta y \\ \delta z \\ \delta \dot{x} \end{bmatrix}_{\hat{T}/2} \tag{3.34}$$

The drawback of fixing the initial guess in $\dot{z}_0$ is that one might be looking for a solution that does not exist for that parameter value. To resolve this issue, the DC switches from fixed-$\dot{z}_0$ to fixed-x_0 if the constraints for numerical periodicity are not satisfied within 10 iterations. As the initial state vector is composed of different components, the periodicity requirements in position and velocity are altered to those stated in Equations 3.35 and 3.36 in addition to the eigenvalue test.

$$\sqrt{y_{\hat{T}/2}^2 + z_{\hat{T}/2}^2} < 10^{-12} \tag{3.35}$$

$$\sqrt{\dot{x}_{\hat{T}/2}^2} \quad\quad < 10^{-12} \tag{3.36}$$

The difference in state vector does also require a different approach to pseudo-arclength continuation. As the axial family only varies slightly in x-position for consecutive members, another measure for normalising Δ is proposed in Equation 3.37.

$$\rho_n = \sqrt{\left(\dot{y}_0^{(n+1)} - \dot{y}_0^{(n)}\right)^2 + \left(\dot{z}_0^{(n+1)} - \dot{z}_0^{(n)}\right)^2} \tag{3.37}$$

Instead of using the norm of deviations in position, the vector of deviations in velocity is used as spacing between members of the axial family. This sequential procedure departs from the H-L and stops at the point of bifurcation to the V-L family. At this point another plane of symmetry is achieved, and is shown through identical velocities at start and half-period respectively ($\dot{y}_0 = \dot{y}_{T/2}$, $\dot{z}_0 = \dot{z}_{T/2}$). In the numerical case however, the probability that these values are exactly equal is not sufficient to assure robust behaviour of the stopping conditions. In this way, a set of threshold stopping conditions is derived in Equations 3.38 and 3.39.

$$|\dot{y}(T/2) - \dot{y}(0)| < 10^{-3} \tag{3.38}$$

$$|\dot{z}(T/2) - \dot{z}(0)| < 10^{-3} \tag{3.39}$$

This variant of the multi-variate Newton method including constraints as stopping conditions and verification gives an indication of the power and versatility of the introduced concepts. Including the special cases for completion of the halo family and propagation of the axial family, this Chapter provides the numerical framework for orbit generation.

4

Orbit generation results

This chapter is dedicated to the analysis and verification of families of orbits resulting from employing the numerical techniques presented in Chapter 3. The outcome of this work will be used as a basis for the manifold generation in Chapter 5. As stated in Section 1.1.2, proper verification and validation of numerical results in the CR3BP requires very demanding procedures. This is why the results in this chapter are presented in a way nearly identical to the analysis introduced in [Massarweh, 2016]. Reason for this reproduction of results is to assess the performance of the integration scheme available in Tudat (RK78) in combination with a low-level programming language (C++). The first sections are dedicated to the various types of orbits in L_1, and are succeeded by those in L_2. The sections are structured in line with the order of bifurcations from the H-L family for decreasing value of Jacobi's constant. In this way, the first bifurcation connects to the halo family and the second gives rise to the axial family, which connects to the V-L family. This chapter is concluded with a review of the generated results, including recommendations for the manifold generation.

4.1. L_1 Horizontal Lyapunov family

The first set of trajectories to be computed is the H-L family situated around L_1. As a result of the numerical procedure presented in Algorithm 1, Figure 4.1 displays the orthographic projection of every fiftieth orbit.

L_1 Horizontal Lyapunov - Orthographic projection
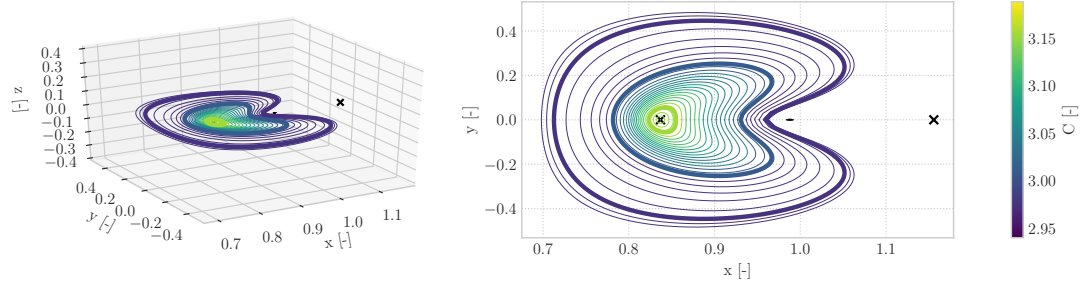
Figure 4.1: *Orthographic projection of every fiftieth member of the H-L family emanating from L_1. The thick lines highlight the orbits at which the order of linear instability changes (bifurcations). The two crosses indicate the equilibria (L_1 and L_2), whereas the sphere located at $(1 - \mu, 0, 0)$ represents the Moon at mean radius (P_2). The colour scale provides insight into the sensitivity with respect to Jacobi's constant (C).*

The trajectories presented in Figure 4.1 are instances of a near-continuous set of orbits. In this way, this family can be characterised in terms of Jacobi's constant and orbital period and is shown in Figure 4.2.

L_1 Horizontal Lyapunov - Orbital energy and period
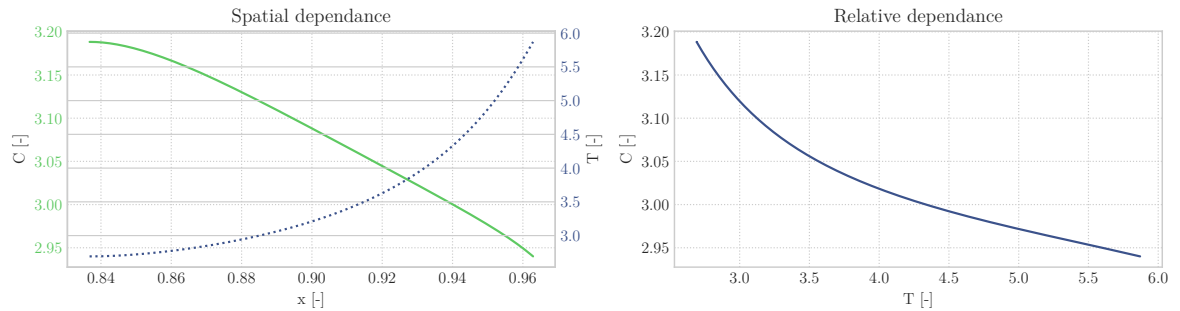
Figure 4.2: *Characterisation of the refined H-L family in L_1 in terms of the Jacobi's constant (C) and orbital period (T), as a function of the x-component of the initial conditions.*

4.1.1. Periodicity verification and eigensystem validation

To verify the numerical veracity of the results of the H-L family in L_1, Figure 4.3 shows the periodicity constraints verification. In addition to this verification procedure, the results are validated through the analysis of the monodromy matrices as presented in Figure 4.4. Please note that the six eigenvalues have been arranged in terms of their modulus.
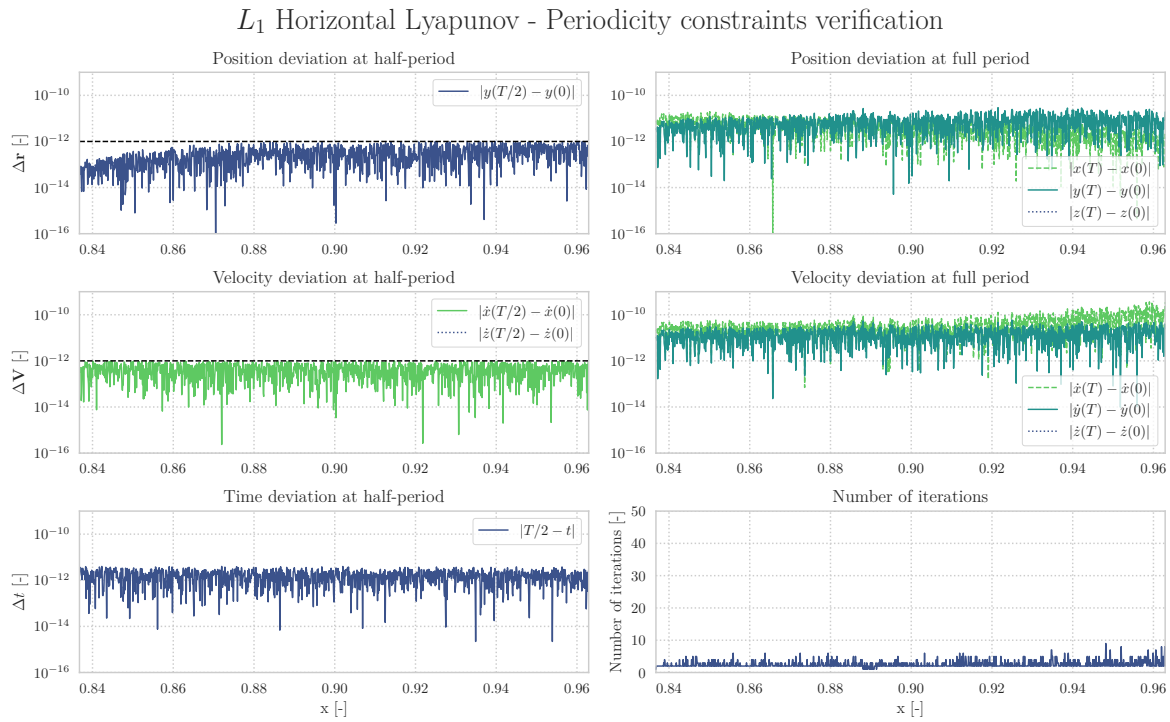
Figure 4.3: *Numerical periodicity constraints verification for all members of the H-L family in L_1. The first column displays the compliance with the thresholds set for DC in terms of position (Eq. 3.25), velocity (Eq. 3.26), and integrator overshoot. The right column indicates the periodicity at full period and the robustness of the DC algorithm through the number of iterations.*
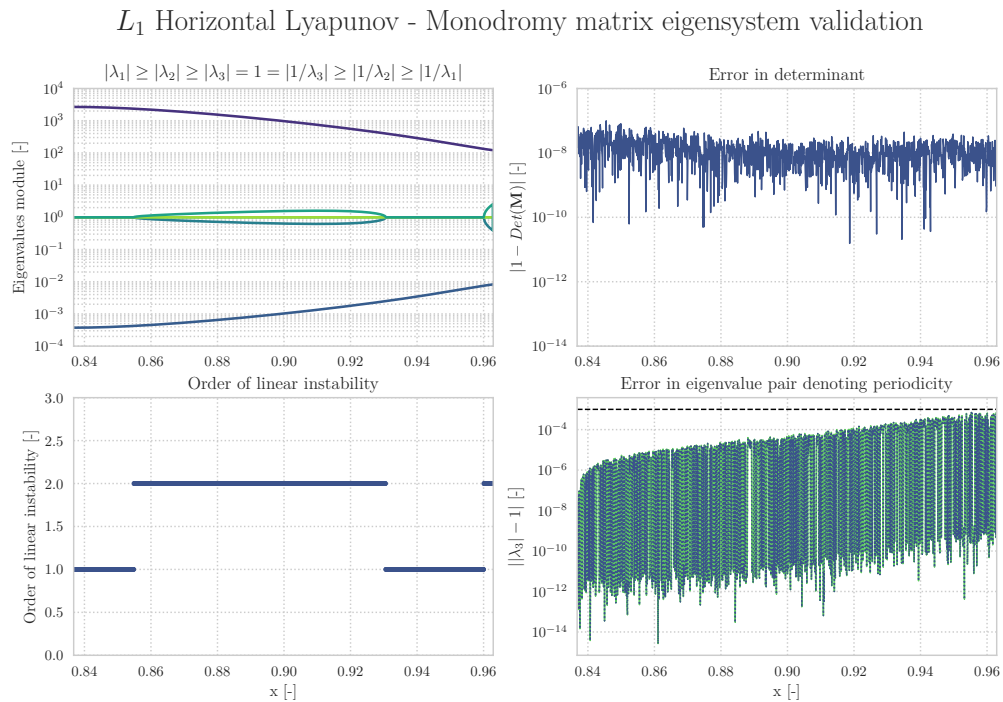
Figure 4.4: *Analysis of the monodromy matrices of the L_1 H-L family. From top to bottom, from left to right: modulus of the six eigenvalues, deviation of the determinant (Eq. 2.23), order of linear instability and error of the reciprocal pair of eigenvalues indication periodicity (Eq. 3.27). All evaluations are mapped out with respect to the x-component of the initial shooting conditions.*

As an additional insight into the stability of the members of this family, the three sets of eigenvalues extracted from the monodromy matrices are presented in Figure 4.5.
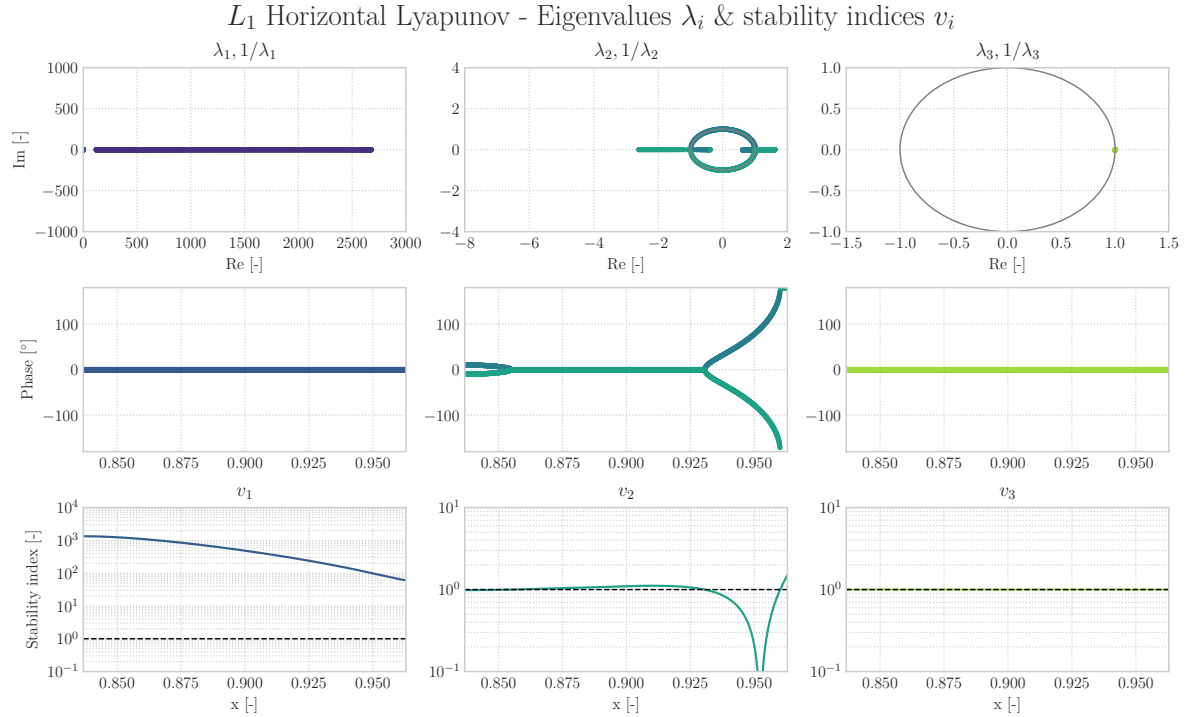
Figure 4.5: *Stability overview of the three pairs of reciprocal eigenvalues ordered in three columns, corresponding to the pair denoting the (un)stable subspace, center subspace and periodicity. The three rows indicate: the real and imaginary components, phase of the complex eigenvalues and stability index (Eq. 2.25). With the exception of the real and imaginary components, all parameters are displayed as a function of the x-component of the initial shooting conditions.*

4.1.2. Discussion of results

When analysing the 1262 H-L members from low to high orbital energy, the amplitude of the orbit geometry and the related orbital period both strictly increase. These parameters are bounded by intervals of $\langle 0, 0.48]$ in y-direction and $[2.69, 5.87]$ in time. The equivalent dimensional units are $\langle 0, 184512]$ km and $[11.70, 25.53]$ days. The tree thick lines in the spatial overview in Figure 4.1 indicate three bifurcation points and correspond to the changes in linear order of instability presented in Figure 4.4. As presented in [], these three branches are known to give rise to the halo family (Sec. 4.2), axial family (Sec. 4.3) and a period doubling bifurcation respectively.[1]

The range of small amplitude H-L orbits are characterised by a first-order linear instability and contains the maximum (minimum) unstable (stable) eigenvalue of the computed family. This characteristic facilitates a rapid unwinding of trajectories and thereby forms a desired target orbit for the computation of hyperbolic manifolds. After the first tangent bifurcation which connects this family to the halos, the linear order of instability rises from one to two. This phenomenon can be observed in the set of real eigenvalues occupying the horizontal axis for λ_2 in Figure 4.5.

The fourth quadrant of Figure 4.4 shows an increasing error in the eigenvalue pair resembling periodicity for a growing size of the orbit. Since it can be observed that the threshold value is gradually approached, it is expected that the process of continuation is stopped due to excessive error in this eigenvalue pair. Over the course of computing this family, the combination of DC and NC demonstrate great robustness as shown in the low number of iterations until the periodicity constraints are satisfied (Fig. 4.3). In addition, the undershoot of the integrator has been successfully and is of order $\sim 10^{-12}$.

---

[1] The third bifurcation is of type period-doubling and thereby does not give rise to a new family. For an extensive analysis on the types of bifurcations, the reader is referred to [Howard and MacKay, 1987][Howard and Dullin, 1998].

4.2. L_1 **Southern halo family**

The second set of trajectories to be computed is the halo family in L_1. Emanating from the first tangent or fold bifurcation of the H-L family, the resulting southern halo family is displayed in Figure 4.6. These trajectories are instances of a near-continuous set of orbits. In this way, this family can be characterised in terms of Jacobi's constant and orbital period and is shown in Figure 4.7.

L_1 Halo - Orthographic projection
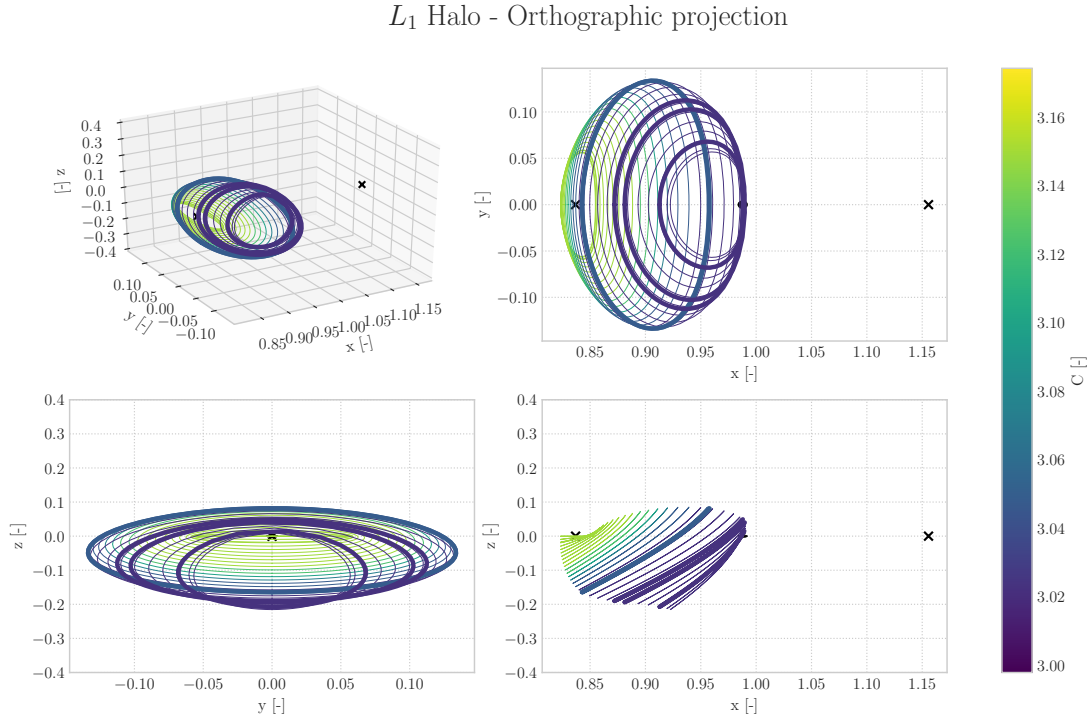
Figure 4.6: *Orthographic projection of every hundredth member of the halo family emanating from L_1. The thick lines highlight the orbits at which the order of linear instability changes (bifurcations). The two crosses indicate the equilibria (L_1 and L_2), whereas the sphere located at $(1 - \mu, 0, 0)$ represents the Moon at mean radius (P_2). The colour scale provides insight into the sensitivity with respect to Jacobi's constant (C).*

L_1 Halo - Orbital energy and period
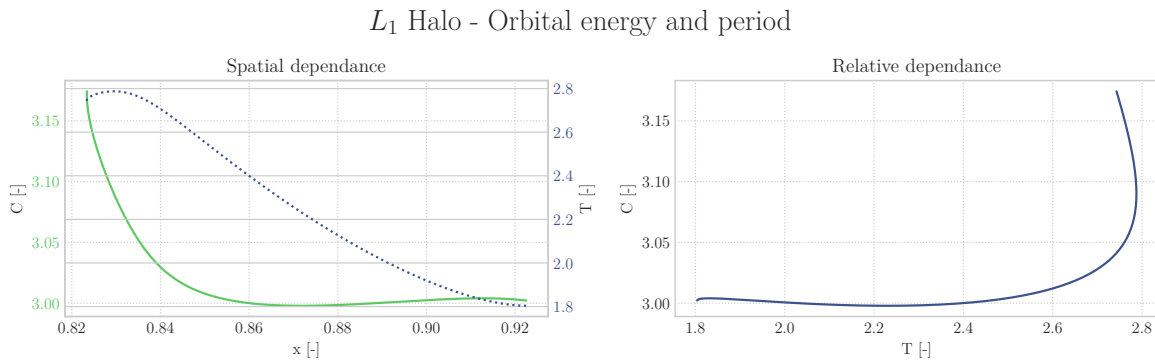
Figure 4.7: *Characterisation of the refined halo family in L_1 in terms of the Jacobi's constant (C) and orbital period (T), as a function of the x-component of the initial conditions.*

4.2.1. **Periodicity verification and eigensystem validation**

To verify the numerical veracity of the results of the halo family in L_1, Figure 4.8 shows the periodicity constraints verification. In addition to this verification procedure, the results are validated through the analysis of the monodromy matrices as presented in Figure 4.9.

L_1 Halo - Periodicity constraints verification
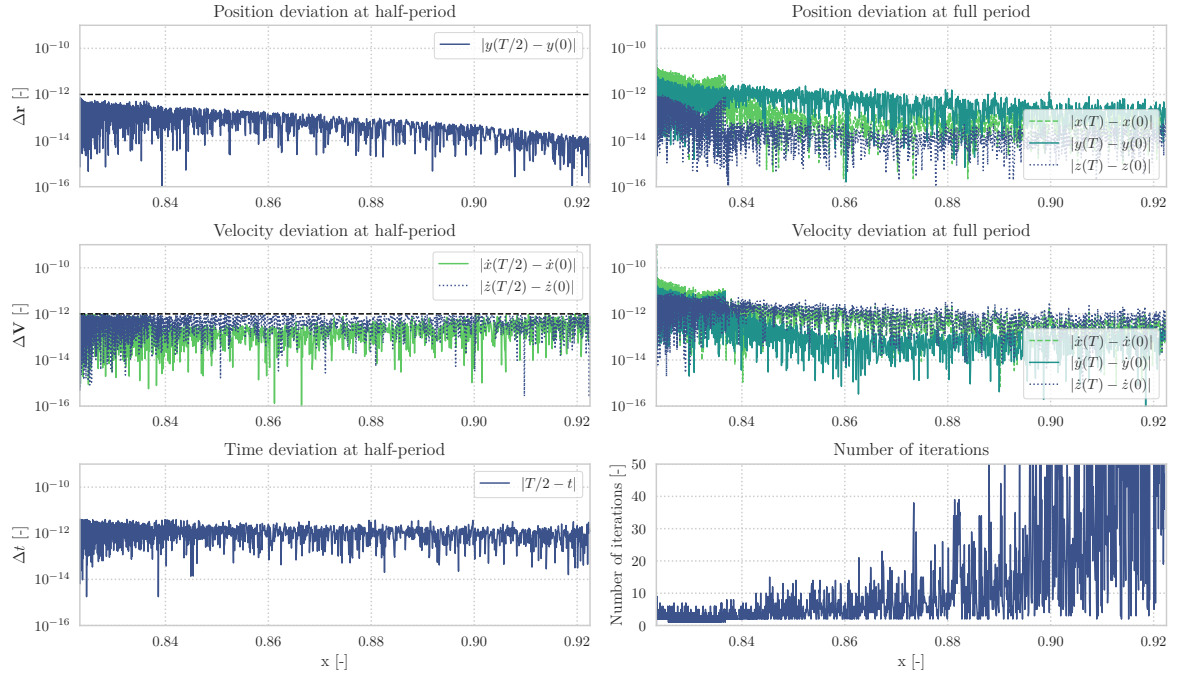
Figure 4.8: *Numerical periodicity constraints verification for all members of the halo family in L_1. The first column displays the compliance with the thresholds set for DC in terms of position (Eq. 3.25), velocity (Eq. 3.26), and integrator overshoot. The right column indicates the periodicity at full period and the robustness of the DC algorithm through the number of iterations.*

L_1 Halo - Monodromy matrix eigensystem validation
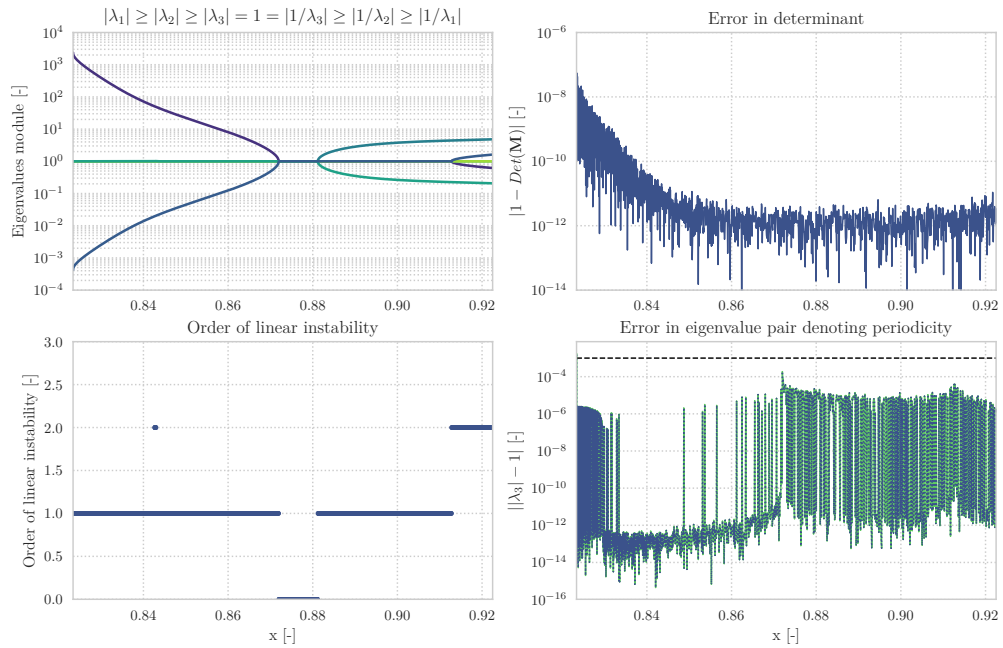
Figure 4.9: *Analysis of the monodromy matrices of the L_1 halo family. From top to bottom, from left to right: modulus of the six eigenvalues, deviation of the determinant (Eq. 2.23), order of linear instability and error of the reciprocal pair of eigenvalues indication periodicity (Eq. 3.27). All evaluations are mapped out with respect to the x-component of the initial shooting conditions.*

As an additional insight into the stability of the members of this family, the three sets of eigenvalues extracted from the monodromy matrices are presented in Figure 4.10.
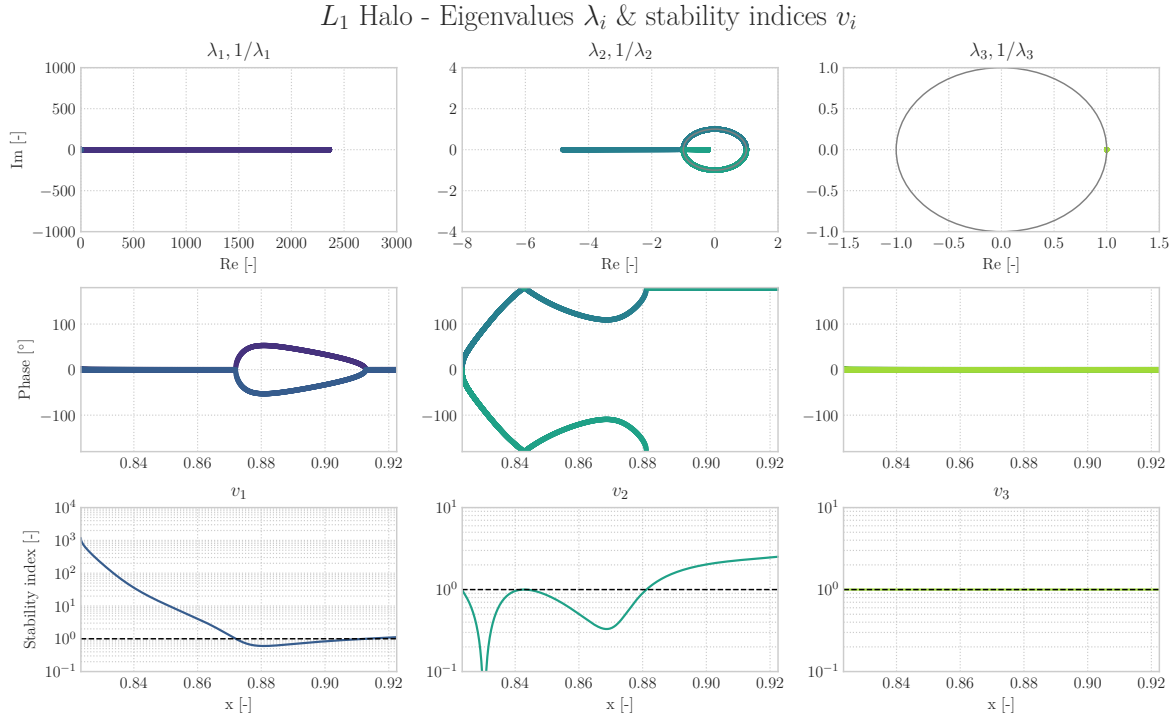
Figure 4.10: *Stability overview of the three pairs of reciprocal eigenvalues ordered in three columns, corresponding to the pair denoting the (un)stable subspace, center subspace and periodicity. The three rows indicate: the real and imaginary components, phase of the complex eigenvalues and stability index (Eq. 2.25). With the exception of the real and imaginary components, all parameters are displayed as a function of the x-component of the initial shooting conditions.*

4.2.2. Discussion of results

"The halo orbits originating in the vicinities of both L_1 and L_2 grow larger, but shorter in period, as they shift towards the Moon" [Breakwell and Brown, 1979]. This observation fits very well with the orthographic projection in Figure 4.6. The 2639 halo members are bounded in y-amplitude by $[0.05, 0.14]$ and in orbital period T by $[1.80, 2.79]$. The equivalent dimensional units are $[19220, 53816]$ km and $[7.83, 12.13]$ days.

In total, five changes in linear of instability can be observed in the analysis of the monodromy matrix in Figure 4.9. The first two branches correspond to period-doubling bifurcations [Howell and Campbell, 1999]. The third change is of type cyclic-fold bifurcation which gives rise to "a narrow band of stable orbits roughly half-way to the Moon," as can be seen observed in the first quadrant of Figure 4.9 [Breakwell and Brown, 1979]. This feature has been outside of the scope in the analysis by [Massarweh, 2016] and corresponds perfectly to the prior cited publication.[2] The last two bifurcations are also of type period-doubling and have been predicted in [Howell and Campbell, 1999]. All in all, the range of halo orbits computed in this research only possesses a single connection to another family of periodic solutions. The reveal of this branch point is enabled due to the reverse halo continuation, addressed in Section 3.2.1.

The range of halo orbits in the close vicinity of P_2 contains the maximum (minimum) unstable (stable) eigenvalue of the computed family. This characteristic facilitates a rapid unwinding of trajectories and thereby forms a desired target orbit for the computation of hyperbolic manifolds. This phenomenon is paired with an increasing error in the pair of eigenvalues denoting periodicity ($\lambda_3, 1/\lambda_3$ in the fourth quadrant of Fig. 4.9). An additional reason for this gradual increase in error is the approach of an attractor, giving rise to highly non-linear dynamics which are less well approximated by the limited-order integrator. Ultimately, the NC procedure is stopped due to breaking of the threshold for eigenvalue accuracy (Eq. 3.27).

---

[2]A possible reason for the exclusion of this phenomenon in [Massarweh, 2016] might be due to a breach of the maximum number of DC iterations, as displayed in Figure 4.3.

4.3. L_1 **North-east axial family**

The third set of trajectories to be computed is the axial family in L_1. Emanating from the second tangent or fold bifurcation of the H-L family, the resulting north-east axial family is displayed in Figure 4.11. These trajectories are instances of a near-continuous set of orbits. In this way, this family can be characterised in terms of Jacobi's constant and orbital period and is shown in Figure 4.12.

L_1 Axial - Orthographic projection
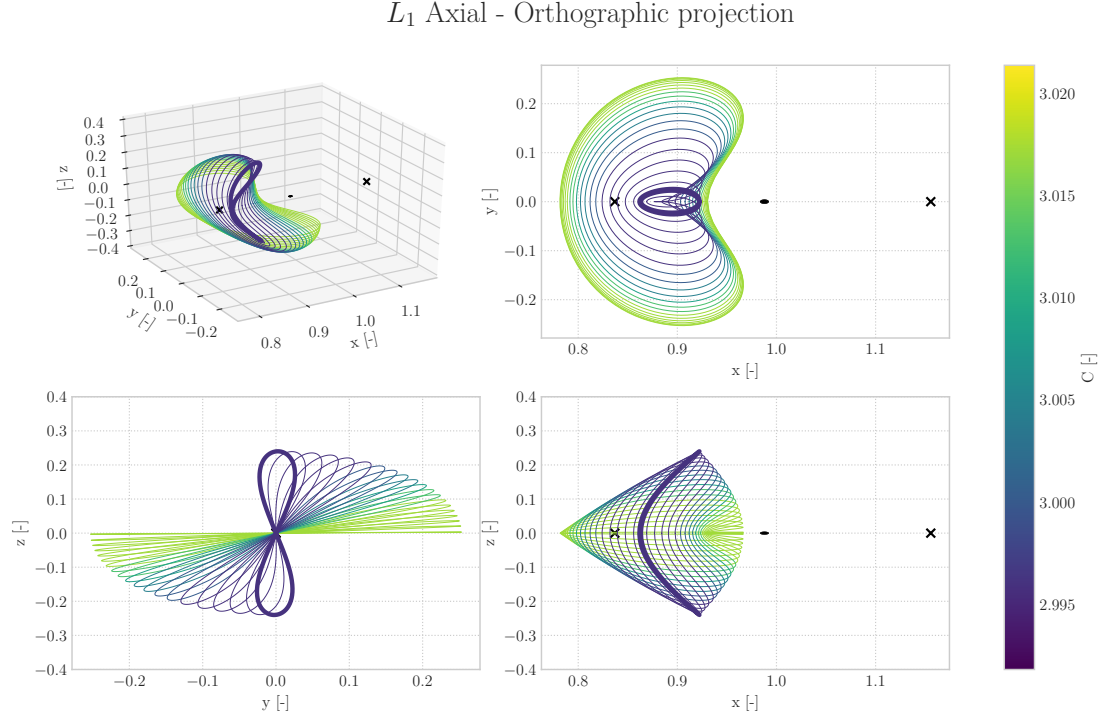
Figure 4.11: *Orthographic projection of every hundredth member of the axial family emanating from L_1. The thick lines fiftieth the orbits at which the order of linear instability changes (bifurcations). The two crosses indicate the equilibria (L_1 and L_2), whereas the sphere located at $(1 - \mu, 0, 0)$ represents the Moon at mean radius (P_2). The colour scale provides insight into the sensitivity with respect to Jacobi's constant (C).*

L_1 Axial - Orbital energy and period
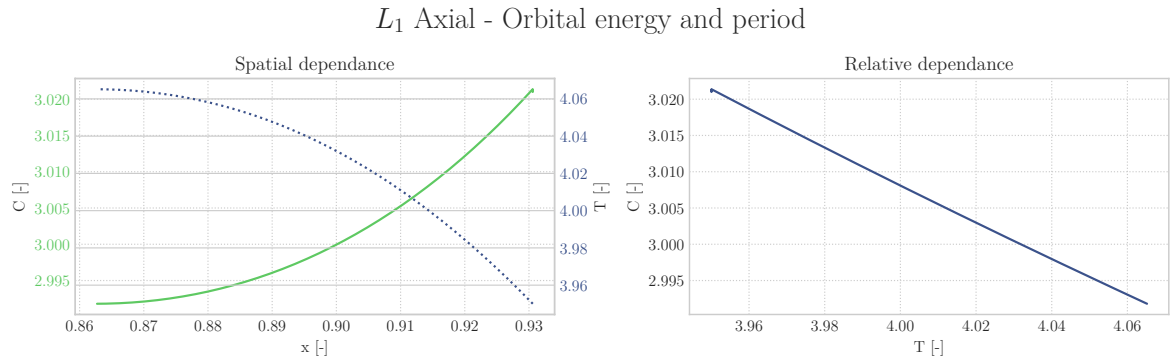
Figure 4.12: *Characterisation of the refined axial family in L_1 in terms of the Jacobi's constant (C) and orbital period (T), as a function of the x-component of the initial conditions.*

4.3.1. Periodicity verification and eigensystem validation

To verify the numerical veracity of the results of the axial family in L_1, Figure 4.13 shows the periodicity constraints verification. In addition to this verification procedure, the results are validated through the analysis of the monodromy matrices as presented in Figure 4.14.

L_1 Axial - Periodicity constraints verification
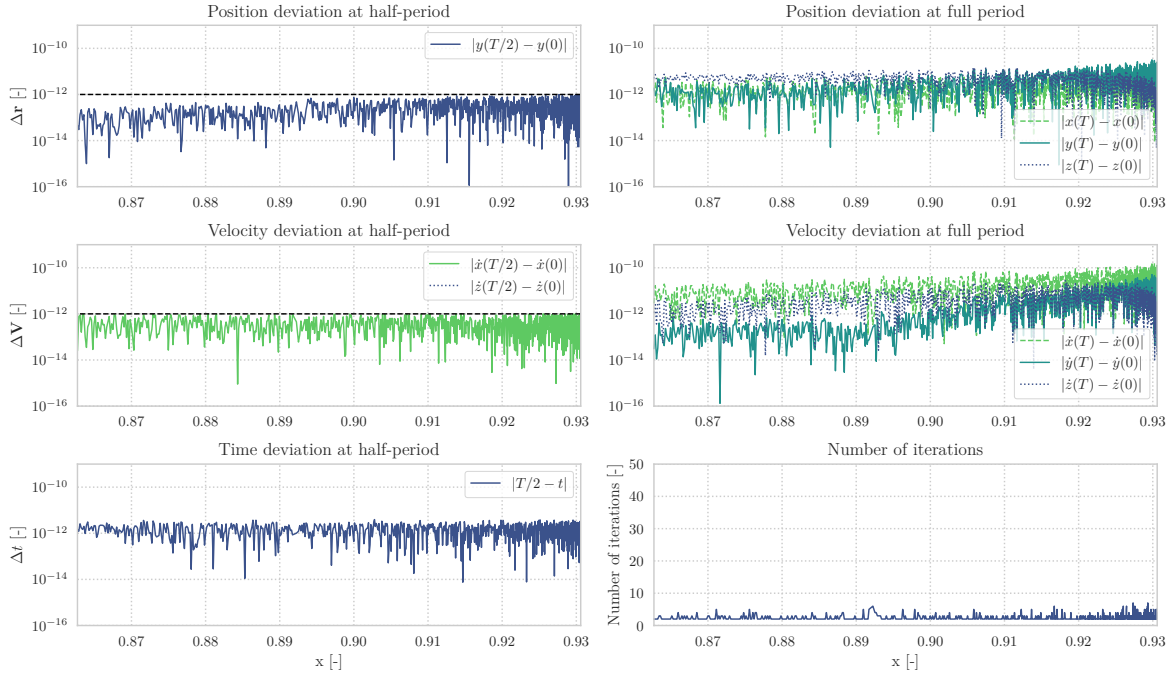
Figure 4.13: *Numerical periodicity constraints verification for all members of the axial family in L_1. The first column displays the compliance with the thresholds set for DC in terms of position (Eq. 3.25), velocity (Eq. 3.26), and integrator overshoot. The right column indicates the periodicity at full period and the robustness of the DC algorithm through the number of iterations.*

L_1 Axial - Monodromy matrix eigensystem validation
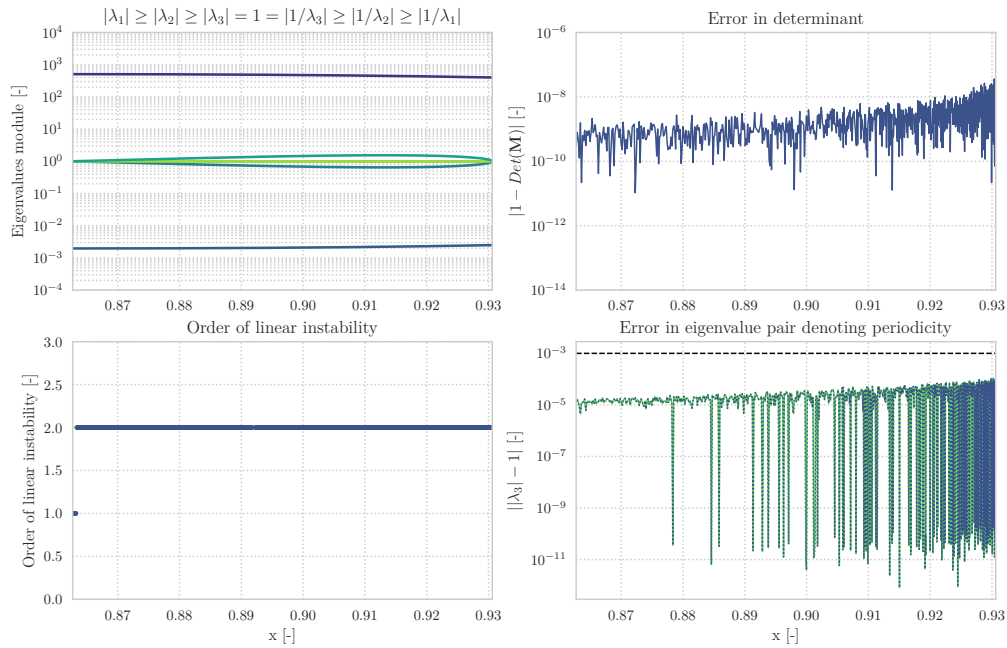
Figure 4.14: *Analysis of the monodromy matrices of the L_1 axial family. From top to bottom, from left to right: modulus of the six eigenvalues, deviation of the determinant (Eq. 2.23), order of linear instability and error of the reciprocal pair of eigenvalues indication periodicity (Eq. 3.27). All evaluations are mapped out with respect to the x-component of the initial shooting conditions.*

As an additional insight into the stability of the members of this family, the three sets of eigenvalues extracted from the monodromy matrices are presented in Figure 4.15.
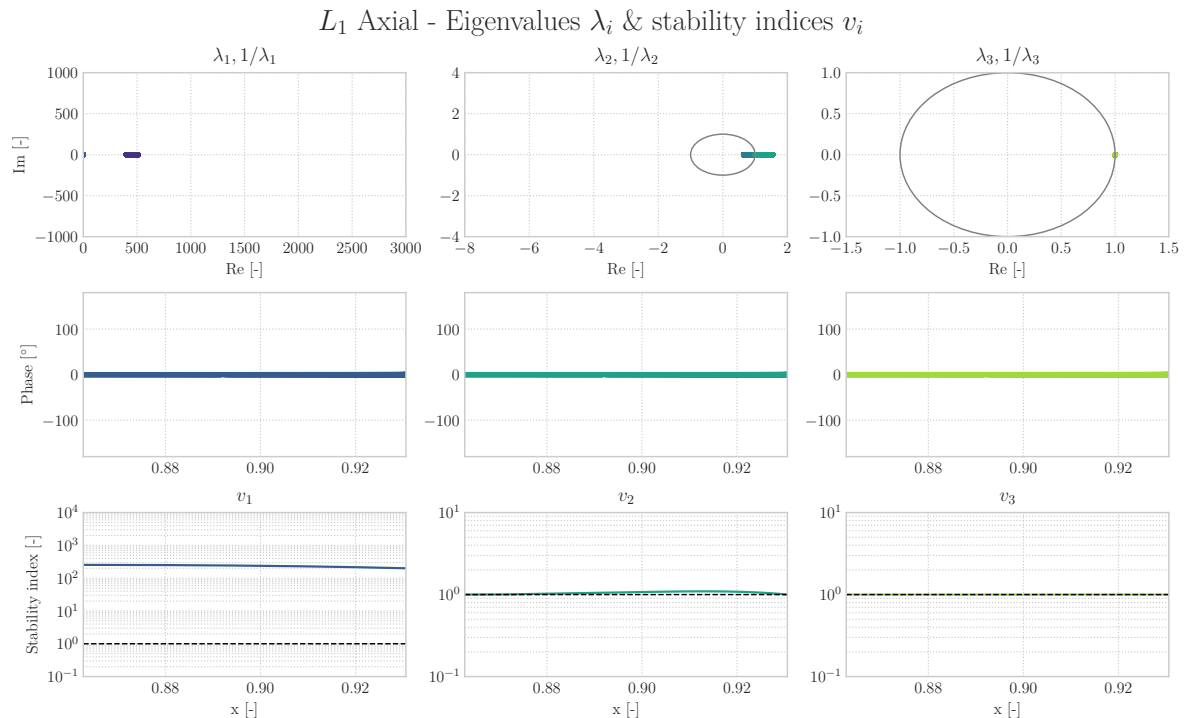
Figure 4.15: *Stability overview of the three pairs of reciprocal eigenvalues ordered in three columns, corresponding to the pair denoting the (un)stable subspace, center subspace and periodicity. The three rows indicate: the real and imaginary components, phase of the complex eigenvalues and stability index (Eq. 2.25). With the exception of the real and imaginary components, all parameters are displayed as a function of the x-component of the initial shooting conditions.*

4.3.2. Discussion of results

The 938 members of the axial family computed in this research exactly span the space between the H-L and V-L family, resulting in the bisection of the full family as shown in Figure 4.11. Hence, this family is referred to as north-east. When analysing these elements from low to high orbital energy, the consecutive orbits twists around the x-axis thereby honouring the denomination axial. The orbital period is strictly increasing and bounded by a modest interval of $[3.95, 4.07]$ in dimensionless time, corresponding to $[17.18, 17.70]$ days. The corresponding amplitude in y-direction decreases over the range $[0.02, 0.25]$, or $[7688, 96100]$ km.

Only two thick lines are shown in the spatial overview in Figure 4.11 indicating the two tangent bifurcations to H-L and V-L families of orbits. The departure of the pair of reciprocal eigenvalues at the tangent bifurcation from the H-L family gives rise to the second-order linear instability of the axial family, and greatly resembles the behaviour shown by the H-L L_1 family (Fig. 4.1 in Sec. 4.1). The location of these two branch points as well as the orthographic projections are in agreement with the results published in [Doedel et al., 2007].

The stability analysis presented in Figure 4.15 displays the two pairs of (un)stable eigenvalues in the first two columns ($\lambda_1, \lambda_1^{-1}, \lambda_2, \lambda_2^{-1}$). The magnitude of the real part of these eigenvalues is significantly smaller than those of the other families. According to Equation 2.24, this will result in a considerably slower unwinding of the corresponding hyperbolic manifolds.[3]

The robustness of the DC algorithm (Fig 4.13) and the low error in determinant of the symplectic maps (Fig. 4.14) are particularly interesting, as this family of orbits is generally not addressed in literature. In this way, the NC procedure is terminated by the stopping conditions formulated in Section 3.2.2.

---

[3]In terms of transport mechanisms, a reciprocal eigenvalue pair is desired with an extreme minimum/maximum value to provide for a time-efficient transfer.

4.4. L_1 **Vertical Lyapunov family**

The fourth and final set of trajectories computed in L_1 is the V-L. Together with the H-L family, these two families of orbits form the two principle types of motion. The resulting V-L family is displayed in Figure 4.16. These trajectories are instances of a near-continuous set of orbits. In this way, this family can be characterised in terms of Jacobi's constant and orbital period and is shown in Figure 4.17.


L_1 Vertical Lyapunov - Orthographic projection
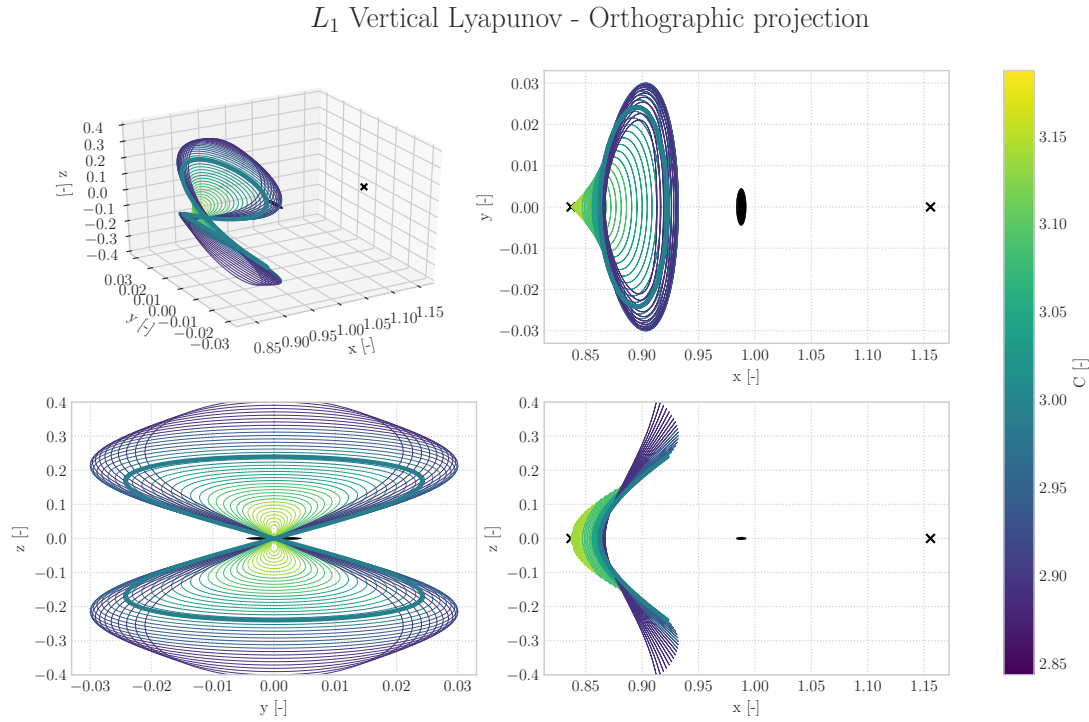
Figure 4.16: *Orthographic projection of every hundredth member of the V-L family emanating from L_1. The thick lines highlight the orbits at which the order of linear instability changes (bifurcations). The two crosses indicate the equilibria (L_1 and L_2), whereas the sphere located at $(1 − \mu, 0, 0)$ represents the Moon at mean radius (P_2). The colour scale provides insight into the sensitivity with respect to Jacobi's constant (C).*

L_1 Vertical Lyapunov - Orbital energy and period
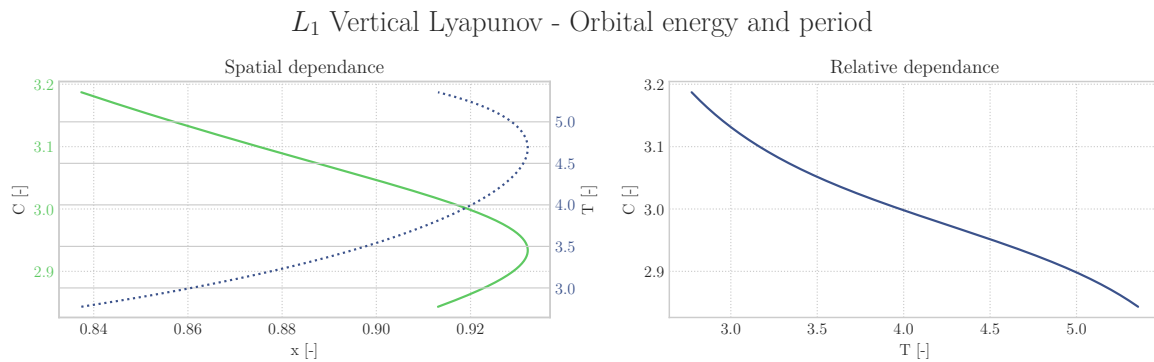
Figure 4.17: *Characterisation of the refined V-L family in L_1 in terms of the Jacobi's constant (C) and orbital period (T), as a function of the x-component of the initial conditions.*

4.4.1. Periodicity verification and eigensystem validation

To verify the numerical veracity of the results of the V-L family in L_1, Figure 4.18 shows the periodicity constraints verification. In addition to this verification procedure, the results are validated through the analysis of the monodromy matrices as presented in Figure 4.19.

L_1 Vertical Lyapunov - Periodicity constraints verification
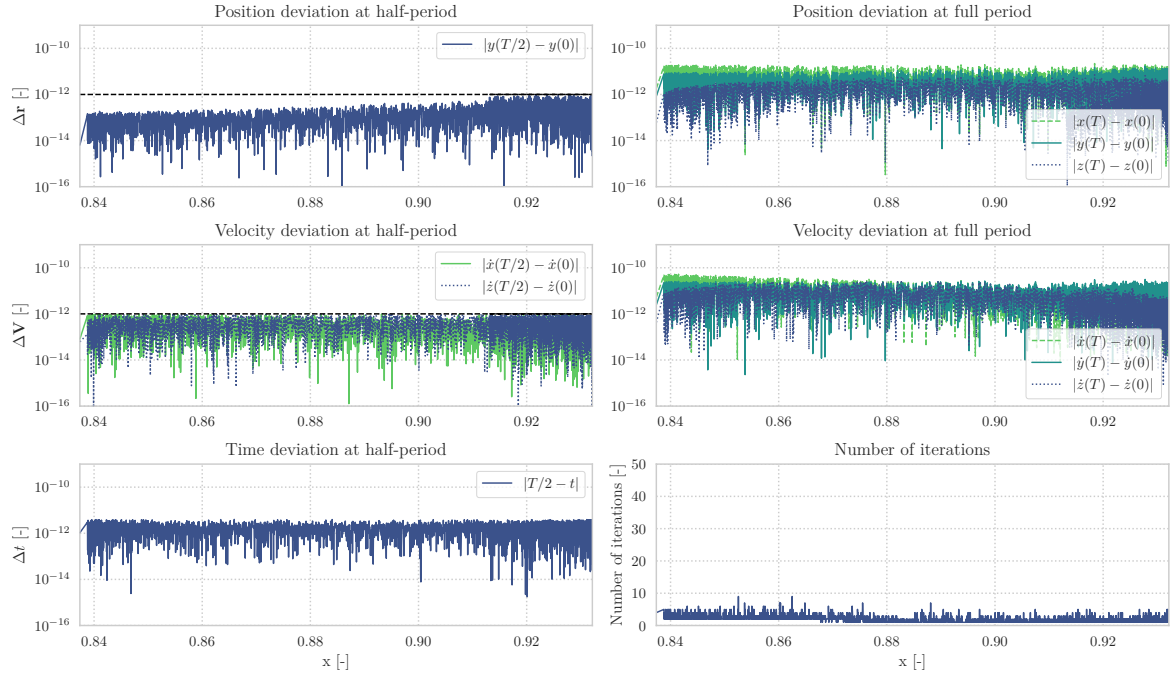
Figure 4.18: *Numerical periodicity constraints verification for all members of the V-L family in L_1. The first column displays the compliance with the thresholds set for DC in terms of position (Eq. 3.25), velocity (Eq. 3.26), and integrator overshoot. The right column indicates the periodicity at full period and the robustness of the DC algorithm through the number of iterations.*

L_1 Vertical Lyapunov - Monodromy matrix eigensystem validation
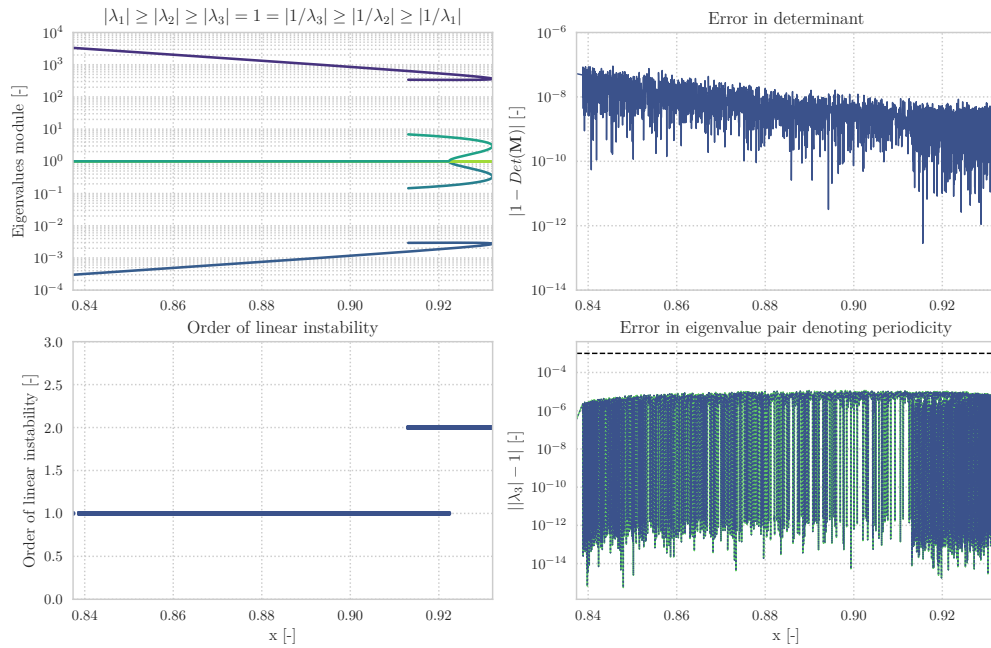
Figure 4.19: *Analysis of the monodromy matrices of the L_1 V-L family. From top to bottom, from left to right: modulus of the six eigenvalues, deviation of the determinant (Eq. 2.23), order of linear instability and error of the reciprocal pair of eigenvalues indication periodicity (Eq. 3.27). All evaluations are mapped out with respect to the x-component of the initial shooting conditions.*

As an additional insight into the stability of the members of this family, the three sets of eigenvalues extracted from the monodromy matrices are presented in Figure 4.20.
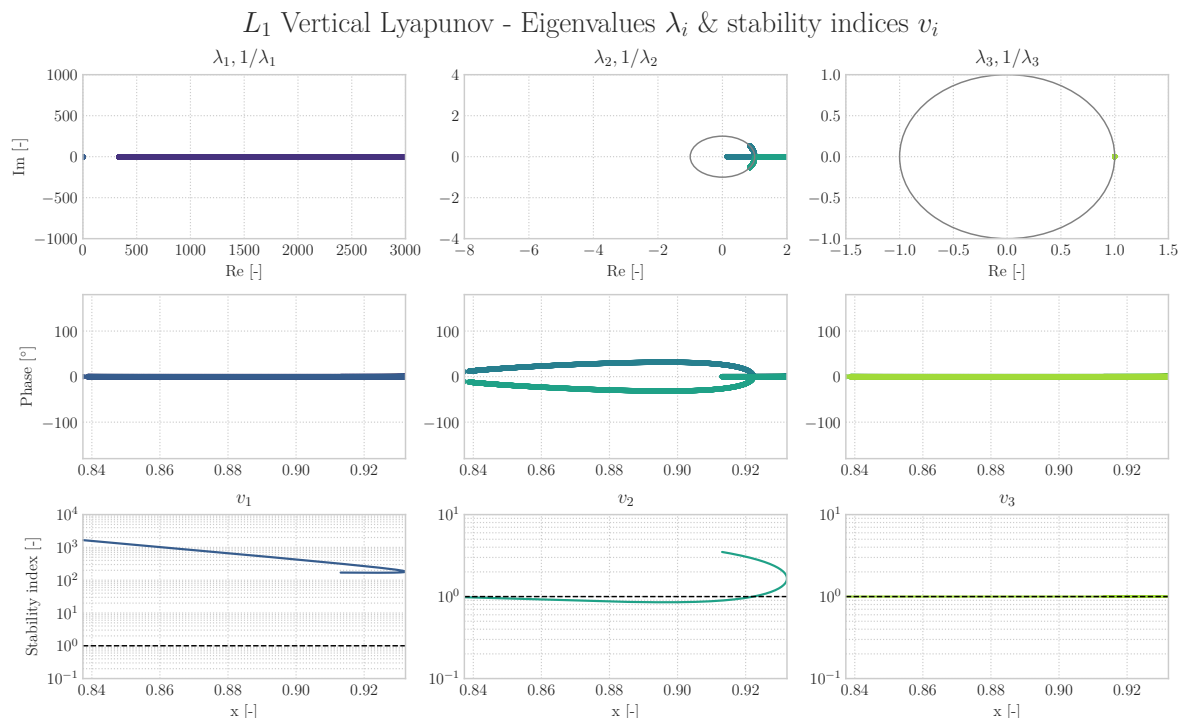
Figure 4.20: *Stability overview of the three pairs of reciprocal eigenvalues ordered in three columns, corresponding to the pair denoting the (un)stable subspace, center subspace and periodicity. The three rows indicate: the real and imaginary components, phase of the complex eigenvalues and stability index (Eq. 2.25). With the exception of the real and imaginary components, all parameters are displayed as a function of the x-component of the initial shooting conditions.*

4.4.2. Discussion of results

When analysing the 4000 V-L members from low to high orbital energy, the amplitude of the orbit geometry and the related orbital period both show a strict increase. These parameters are bounded by intervals of $\langle 0, 0.41]$ in z-direction and $[2.77, 5.36]$ in time.[4] The equivalent dimensional units are $\langle 0, 157604]$ km and $[12.05, 23.31]$ days. Only a single thick line can be observed in the spatial overview in Figure 4.16 indicating the tangent bifurcation to the axial branch and corresponds to an increase in linear order of instability from one to two (Fig. 4.19). However, the stability analysis in Figure 4.20 shows that this additional (un)stable eigenvalue pair has a relatively low real component. The first reciprocal eigenvalue pair on the the other hand, attains the most extreme maxima and minima of all computed families. This makes the V-L family highly suitable for exploitation of hyperbolic transfer mechanisms. Interestingly, the "family of the figure-of-eight orbits around L_1 consists entirely of unstable members" [Bray and Goudas, 1966].

The V-L family emanating from L_1 first embraces the second primary until a particular out of plane amplitude has been reached, after which it extends towards the larger primary. This is a unique feature of this type of family, which appears as a turning point in Jacobi's energy, orbital period (Fig. 4.17), eigenvalue modulus (Fig. 4.19), and stability indices (Fig. 4.20). Interestingly, the pseudo-arclength continuation has proven to be very robust in the handling of this reversal of x-direction (Fig. 4.18).

The second and fourth quadrants of Figure 4.19 exhibit a low error with a slight trend. The threshold value is not nearly exceeded, hence the numerical continuation is terminated due to satisfying the maximum number of members per family of orbits. Nonetheless, the results presented in this section greatly extend the work as presented by [Archambeau et al., 2011]. Together with the H-L family analysed in Section 4.1, these two types of orbits constitute to the principle forms of motion and conclude the computation of orbits in EM L_1.

---

[4]Please note that the y-scale has been significantly magnified in the orthographic projections of the family in Figure 4.16, hence the motion of the V-L orbits remains predominately in the out-of-plane direction.

## L_2 Horizontal Lyapunov - Periodicity constraints verification

Figure 4.23: *Numerical periodicity constraints verification for all members of the H-L family in L_2. The first column displays the compliance with the thresholds set for DC in terms of position (Eq. 3.25), velocity (Eq. 3.26), and integrator overshoot. The right column indicates the periodicity at full period and the robustness of the DC algorithm through the number of iterations.*

L_2 Horizontal Lyapunov - Monodromy matrix eigensystem validation

Figure 4.24: *Analysis of the monodromy matrices of the L_2 H-L family. From top to bottom, from left to right: modulus of the six eigenvalues, deviation of the determinant (Eq. 2.23), order of linear instability and error of the reciprocal pair of eigenvalues indication periodicity (Eq. 3.27). All evaluations are mapped out with respect to the x-component of the initial shooting conditions.*

As an additional insight into the stability of the members of this family, the three sets of eigenvalues extracted from the monodromy matrices are presented in Figure 4.25.
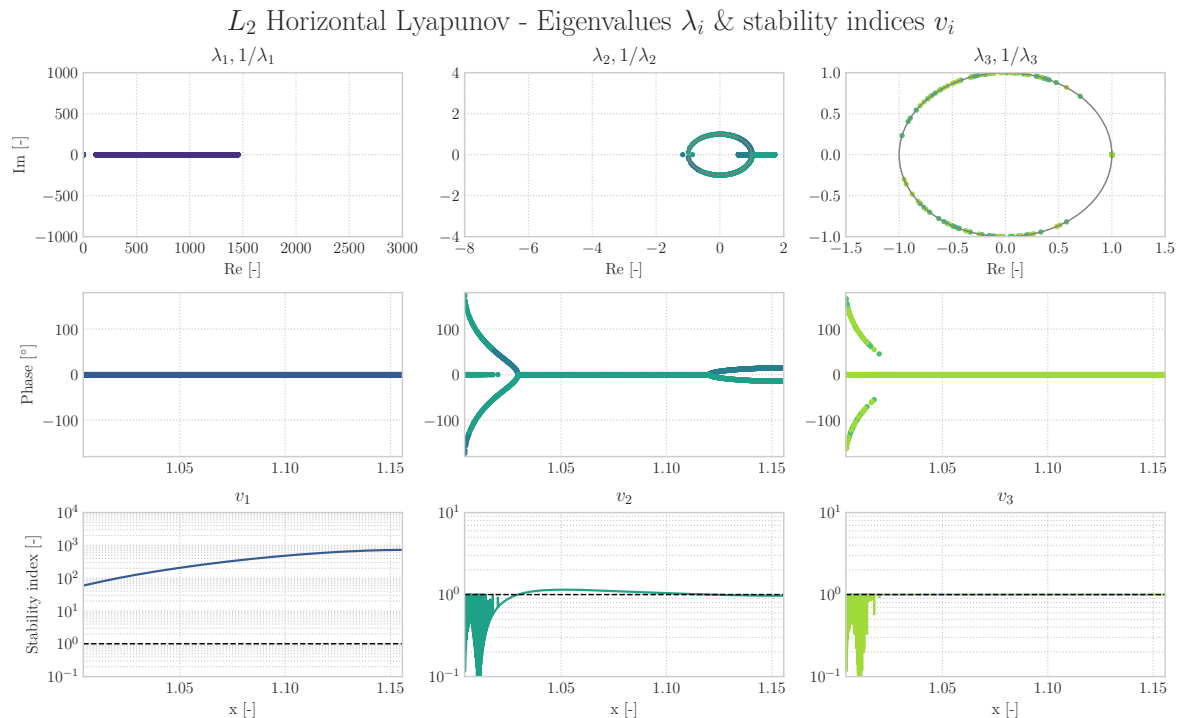
Figure 4.25: *Stability overview of the three pairs of reciprocal eigenvalues ordered in three columns, corresponding to the pair denoting the (un)stable subspace, center subspace and periodicity. The three rows indicate: the real and imaginary components, phase of the complex eigenvalues and stability index (Eq. 2.25). With the exception of the real and imaginary components, all parameters are displayed as a function of the x-component of the initial shooting conditions.*

4.5.2. Discussion of results

When analysing the 1515 H-L members from low to high orbital energy, the amplitude of the orbit geometry and the related orbital period both strictly increase. These parameters are bounded by intervals of $\langle 0, 0.43]$ in y-direction and $[3.37, 5.72]$ in time. The equivalent dimensional units are $\langle 0, 165292]$ km and $[14.65, 24.87]$ days. The tree thick lines in the spatial overview in Figure 4.21 indicate three bifurcation points and correspond to the changes in linear order of instability presented in Figure 4.24. In a similar fashion as in Section 4.1, these three branches are known to give rise to the halo family (Sec. 4.6), axial family (Sec. 4.7) and a period doubling bifurcation respectively.

Interestingly, the analysis of the symplectic properties of the monodromy matrix (Fig. 4.24) shows a near-identical mirror image to the one presented for the same family in L_1 (Fig. 4.4). The reason for this inversion is can be attributed to the reverse direction of consecutive shooting conditions, as both NC procedures advance towards P_2 for increasing energy level. When comparing the geometry of the H-L orbits in L_1 and L_2, one can observe a more distorted shape in the latter collinear point. This behaviour can be clarified with the non-inertial reference frame in mind: as one moves further away from the barycenter, the centrifugal forces grow in the rotating reference frame.

The second quadrant of Figure 4.24 shows an increasing error in the eigenvalue pair resembling periodicity for a growing size of the orbit. Distinctively different from all other computed families, it can be observed in Figure 4.25 that the requirement on a real component equal to one has been relaxed to that of a modulus. This adjustment has enabled the extension of the H-L to the amplitude shown in Figure 4.21. A possible explanation of the difficulty involved in obtaining these larger orbits, is the increase in non-linearity due to the close approach of the attractor in combination with the previously mentioned increase in centrifugal force. However, the process of NC is ultimately stopped due to an excessive error in this modulus value.[5]

---

[5]The described reduced accuracy and robustness can also be observed in the increment of noise in the stability indices (Fig. 4.25). This corresponds to the lower portion of the x-components, hence the orbits which are closest to the Moon and largest in amplitude.

4.6. L_2 **Southern halo family**

The second set of trajectories to be computed in L_2 is the halo family. In a similar manner as the one presented in Section 4.2, this family arises from the first tangent or fold bifurcation of the H-L family. The resulting southern halo family is displayed in Figure 4.26. These trajectories are instances of a near-continuous set of orbits. In this way, this family can be characterised in terms of Jacobi's constant and orbital period and is shown in Figure 4.27.

L_2 Halo - Orthographic projection
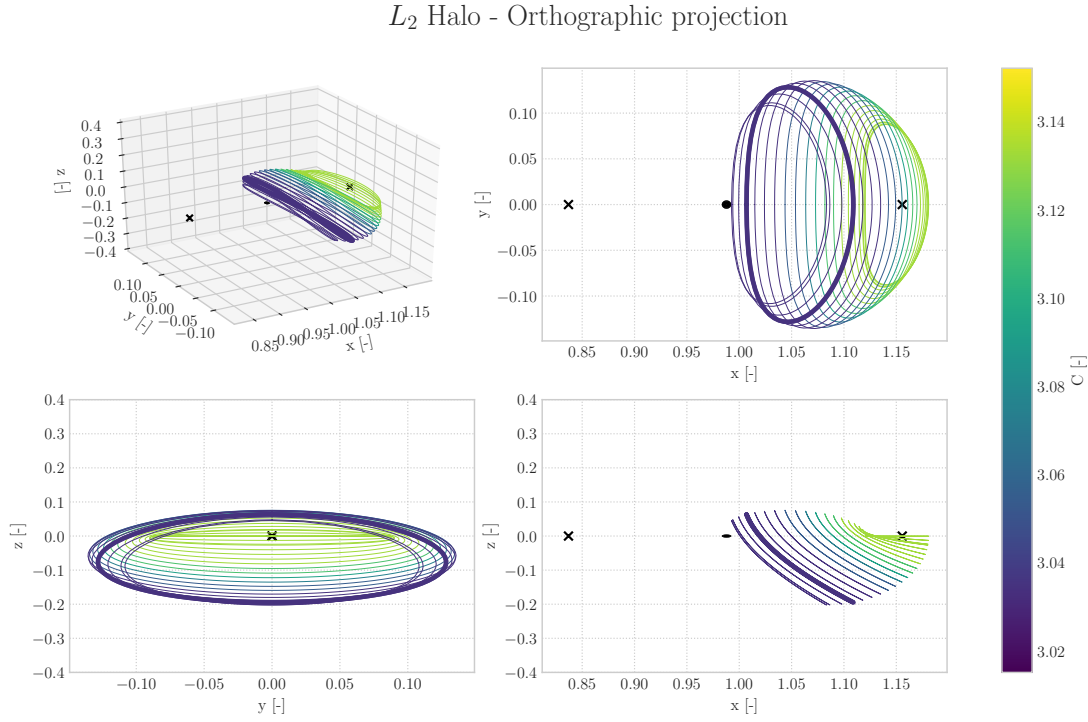
Figure 4.26: *Orthographic projection of every hundredth member of the halo family emanating from L_2. The thick lines highlight the orbits at which the order of linear instability changes (bifurcations). The two crosses indicate the equilibria (L_1 and L_2), whereas the sphere located at $(1 - \mu, 0, 0)$ represents the Moon at mean radius (P_2). The colour scale provides insight into the sensitivity with respect to Jacobi's constant (C).*

L_2 Halo - Orbital energy and period
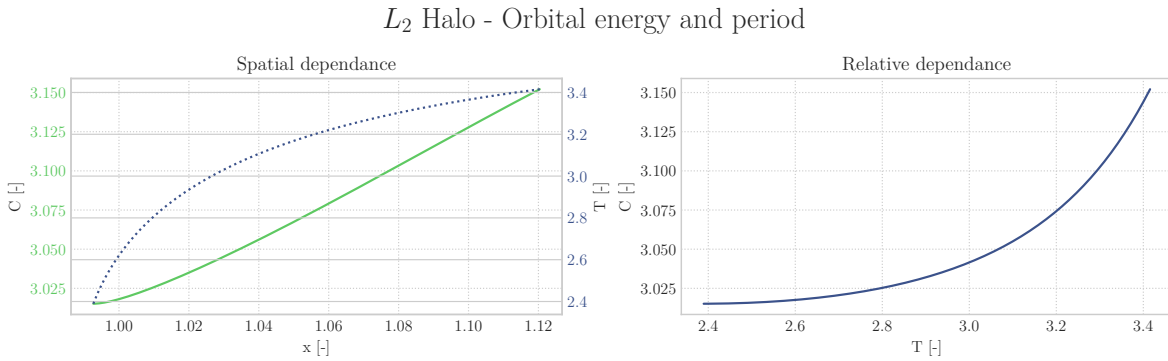
Figure 4.27: *Characterisation of the refined halo family in L_2 in terms of the Jacobi's constant (C) and orbital period (T), as a function of the x-component of the initial conditions.*

4.6.1. Periodicity verification and eigensystem validation

To verify the numerical veracity of the results of the halo family in L_2, Figure 4.28 shows the periodicity constraints verification. In addition to this verification procedure, the results are validated through the analysis of the monodromy matrices as presented in Figure 4.29.

L_2 Halo - Periodicity constraints verification
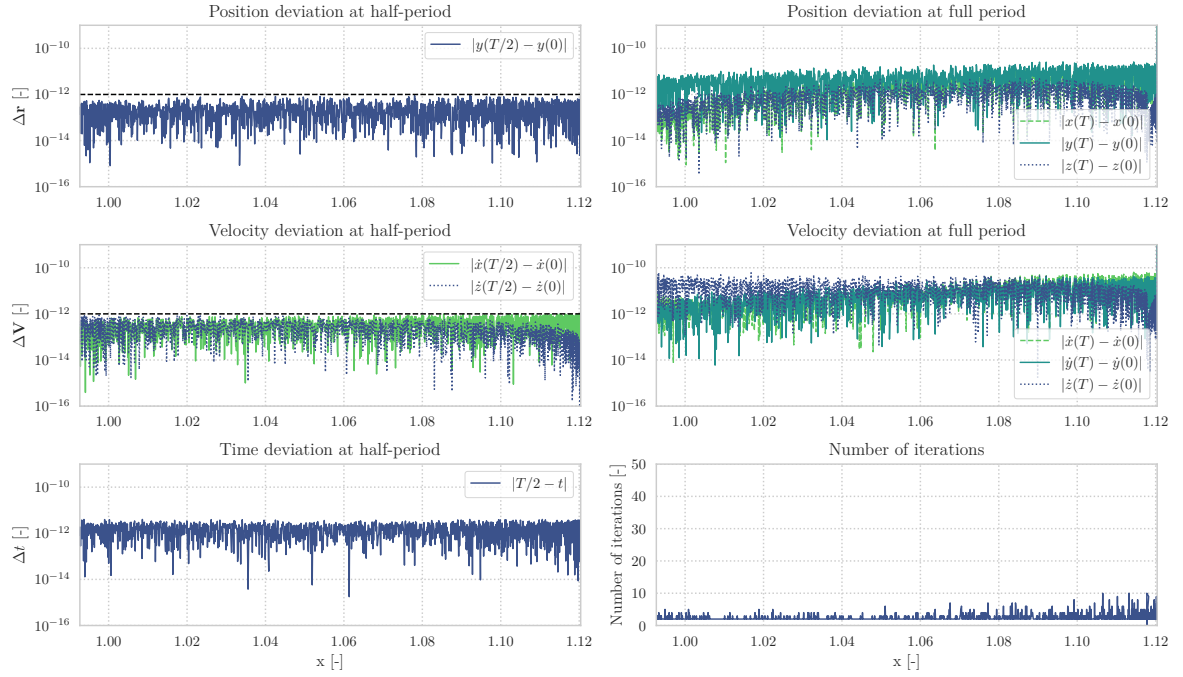
Figure 4.28: *Numerical periodicity constraints verification for all members of the halo family in L_2. The first column displays the compliance with the thresholds set for DC in terms of position (Eq. 3.25), velocity (Eq. 3.26), and integrator overshoot. The right column indicates the periodicity at full period and the robustness of the DC algorithm through the number of iterations.*

L_2 Halo - Monodromy matrix eigensystem validation
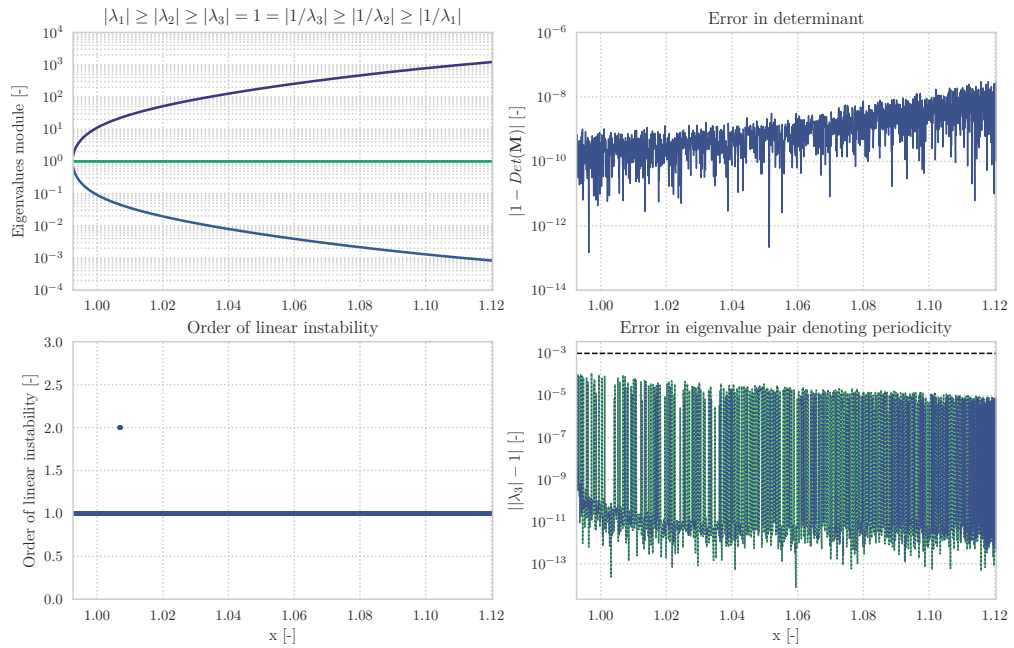
Figure 4.29: *Analysis of the monodromy matrices of the L_2 halo family. From top to bottom, from left to right: modulus of the six eigenvalues, deviation of the determinant (Eq. 2.23), order of linear instability and error of the reciprocal pair of eigenvalues indication periodicity (Eq. 3.27). All evaluations are mapped out with respect to the x-component of the initial shooting conditions.*

As an additional insight into the stability of the members of this family, the three sets of eigenvalues extracted from the monodromy matrices are presented in Figure 4.30.
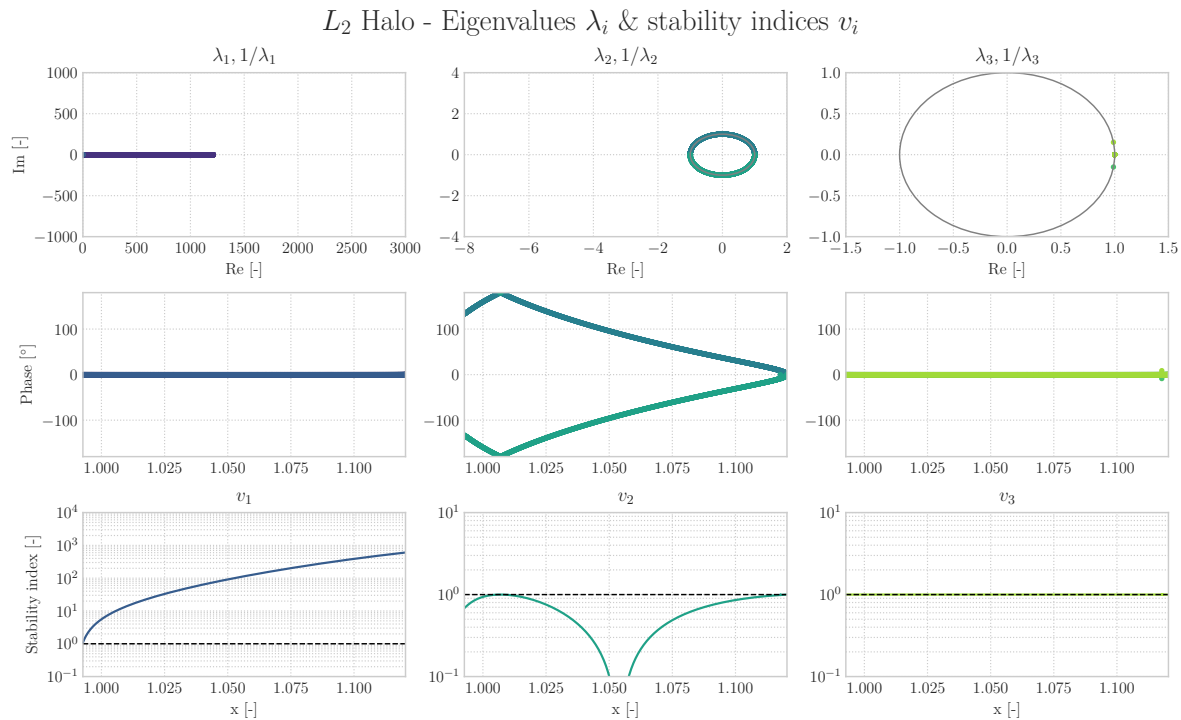
Figure 4.30: *Stability overview of the three pairs of reciprocal eigenvalues ordered in three columns, corresponding to the pair denoting the (un)stable subspace, center subspace and periodicity. The three rows indicate: the real and imaginary components, phase of the complex eigenvalues and stability index (Eq. 2.25). With the exception of the real and imaginary components, all parameters are displayed as a function of the x-component of the initial shooting conditions.*

4.6.2. Discussion of results

In a similar way to the halo family in L_1 (Fig. 4.1), the L_2 orbits grow larger in amplitude but shorter in period "as they shift towards the Moon" [Breakwell and Brown, 1979]. The 1815 halo members are bounded in y-amplitude by $[0.08, 0.14]$ and in orbital period T by $[2.39, 3.42]$. The equivalent dimensional units are $[30752, 53816]$ km and $[10.39, 14.87]$ days, which provides for a slightly larger amplitude and significantly longer orbital period.

In total, only two changes in linear of instability can be observed in the analysis of the monodromy matrix in Figure 4.9. The first branche correspond to a tangent bifurcation to the H-L family, whereas the second is of type period-doubling [Howell and Campbell, 1999]. All in all, the range of halo orbits computed in this research only possesses a single connection to another family of periodic solutions. The reveal of this branch point to the H-L family is enabled due to the reverse halo continuation, addressed in Section 3.2.1. The third change in linear order of instability caused by a bifurcation of type cyclic-fold and gives rise to "a narrow band of stable orbits roughly half-way to the Moon," as proposed in [Breakwell and Brown, 1979], is out of the scope of this analysis.

The range of halo orbits in the close vicinity of P_2 contains the maximum (minimum) unstable (stable) eigenvalue of the computed family. This characteristic facilitates a rapid unwinding of trajectories and thereby forms a desired target orbit for the computation of hyperbolic manifolds. This phenomenon is paired with an increasing error in the pair of eigenvalues denoting periodicity ($\lambda_3, 1/\lambda_3$ in the fourth quadrant of Fig. 4.9). An additional reason for this gradual increase in error is the approach of an attractor, giving rise to highly non-linear dynamics which are less well approximated by the limited-order integrator. Ultimately, the NC procedure is stopped due to breaking of the threshold for eigenvalue accuracy (Eq. 3.27.[6]

---

[6]Please note that the requirement on the pair of eigenvalues denoting periodicity (Fig 4.28) has been relaxed from a one in the real-component to the complex plane. This method is identical to the one adopted for the H-L family in L_2 (Sec. 4.5).

4.7. L_2 **North-west axial family**

The third set of trajectories to be computed in L_2 is the axial family. Emanating from the second tangent or fold bifurcation of the H-L family, the resulting north-east axial family is displayed in Figure 4.31. These trajectories are instances of a near-continuous set of orbits. In this way, this family can be characterised in terms of Jacobi's constant and orbital period and is shown in Figure 4.32.

L_2 Axial - Orthographic projection
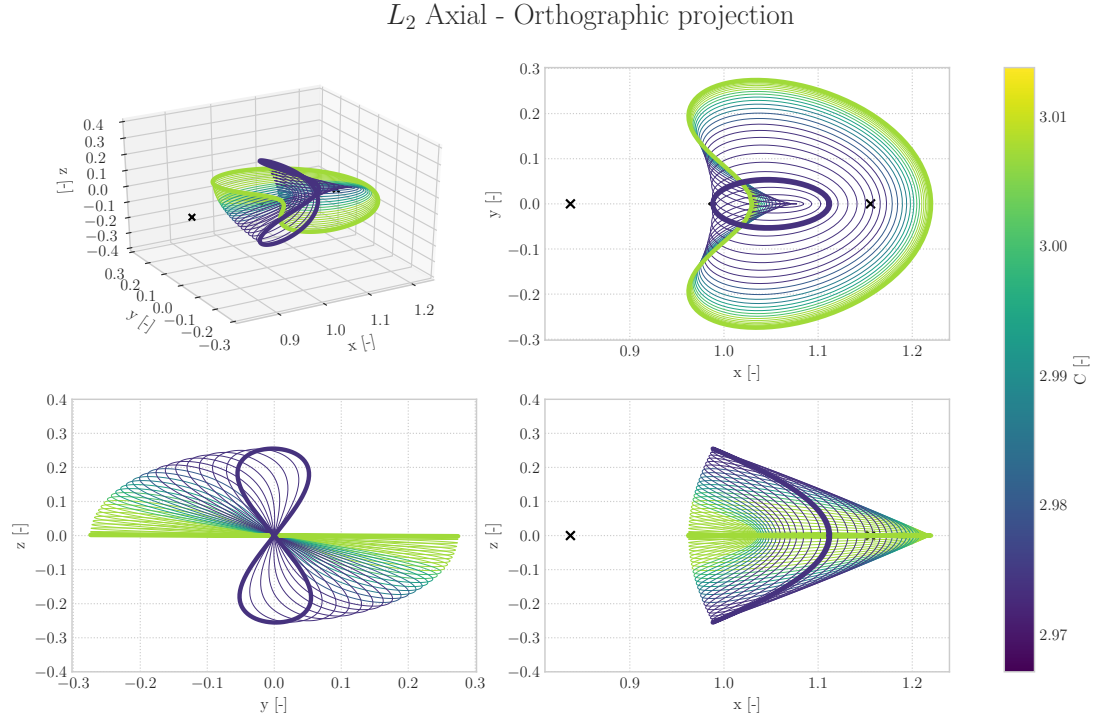
Figure 4.31: *Orthographic projection of every fiftieth member of the axial family emanating from L_2. The thick lines highlight the orbits at which the order of linear instability changes (bifurcations). The two crosses indicate the equilibria (L_1 and L_2), whereas the sphere located at $(1-\mu, 0, 0)$ represents the Moon at mean radius (P_2). The colour scale provides insight into the sensitivity with respect to Jacobi's constant (C).*

L_2 Axial - Orbital energy and period
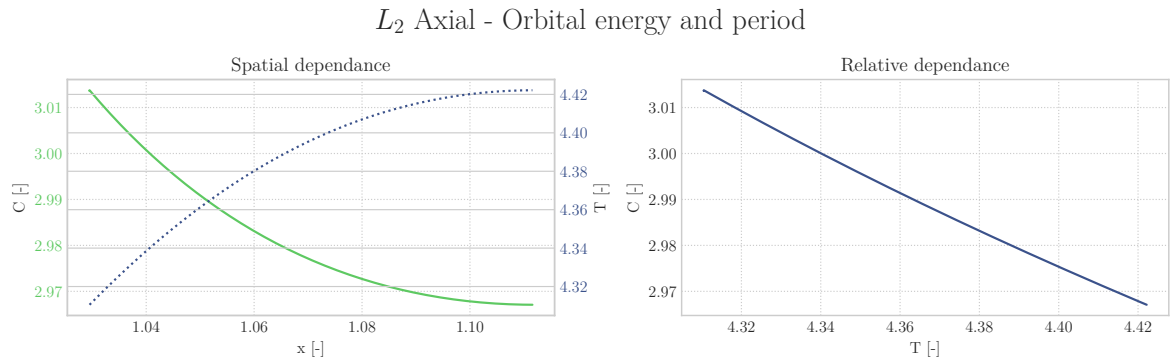
Figure 4.32: *Characterisation of the refined axial family in L_2 in terms of the Jacobi's constant (C) and orbital period (T), as a function of the x-component of the initial conditions.*

4.7.1. Periodicity verification and eigensystem validation

To verify the numerical veracity of the results of the axial family in L_2, Figure 4.33 shows the periodicity constraints verification. In addition to this verification procedure, the results are validated through the analysis of the monodromy matrices as presented in Figure 4.34.

L_2 Axial - Periodicity constraints verification
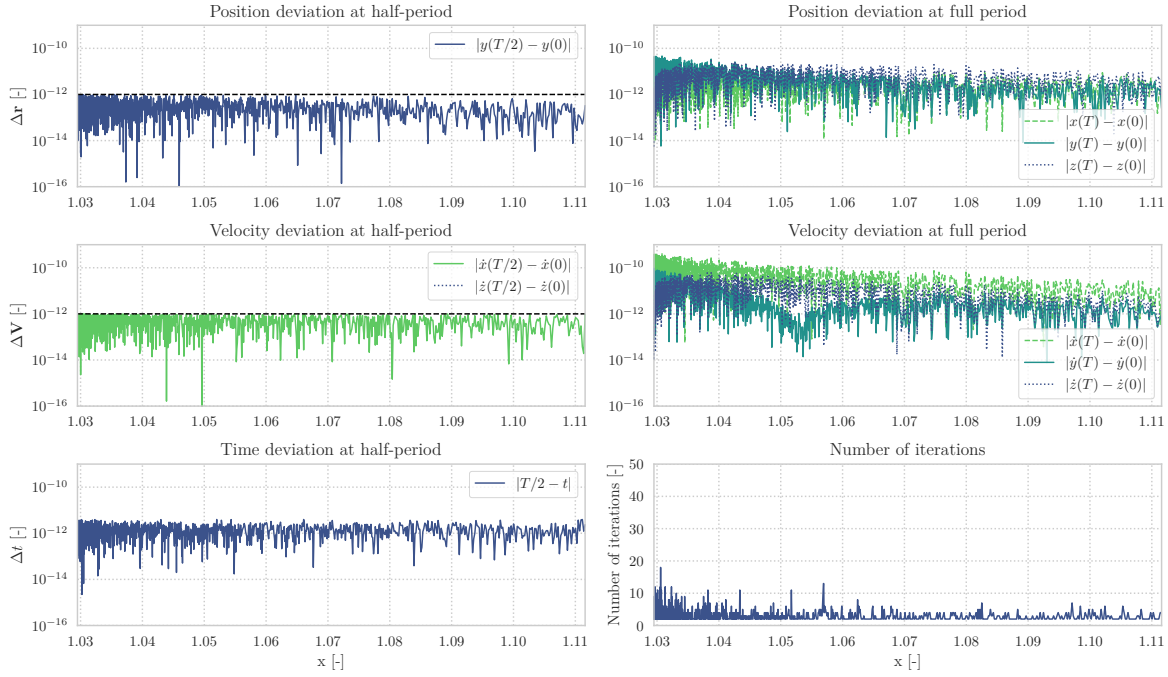
Figure 4.33: *Numerical periodicity constraints verification for all members of the axial family in L_2. The first column displays the compliance with the thresholds set for DC in terms of position (Eq. 3.25), velocity (Eq. 3.26), and integrator overshoot. The right column indicates the periodicity at full period and the robustness of the DC algorithm through the number of iterations.*

L_2 Axial - Monodromy matrix eigensystem validation
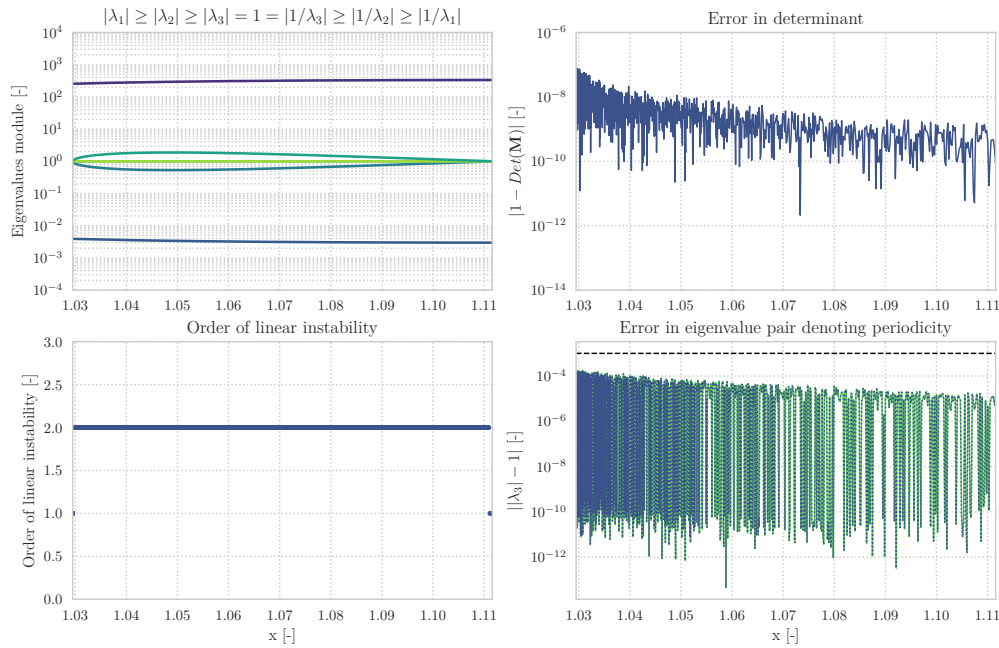
Figure 4.34: *Analysis of the monodromy matrices of the L_2 axial family. From top to bottom, from left to right: modulus of the six eigenvalues, deviation of the determinant (Eq. 2.23), order of linear instability and error of the reciprocal pair of eigenvalues indication periodicity (Eq. 3.27). All evaluations are mapped out with respect to the x-component of the initial shooting conditions.*

As an additional insight into the stability of the members of this family, the three sets of eigenvalues extracted from the monodromy matrices are presented in Figure 4.35.
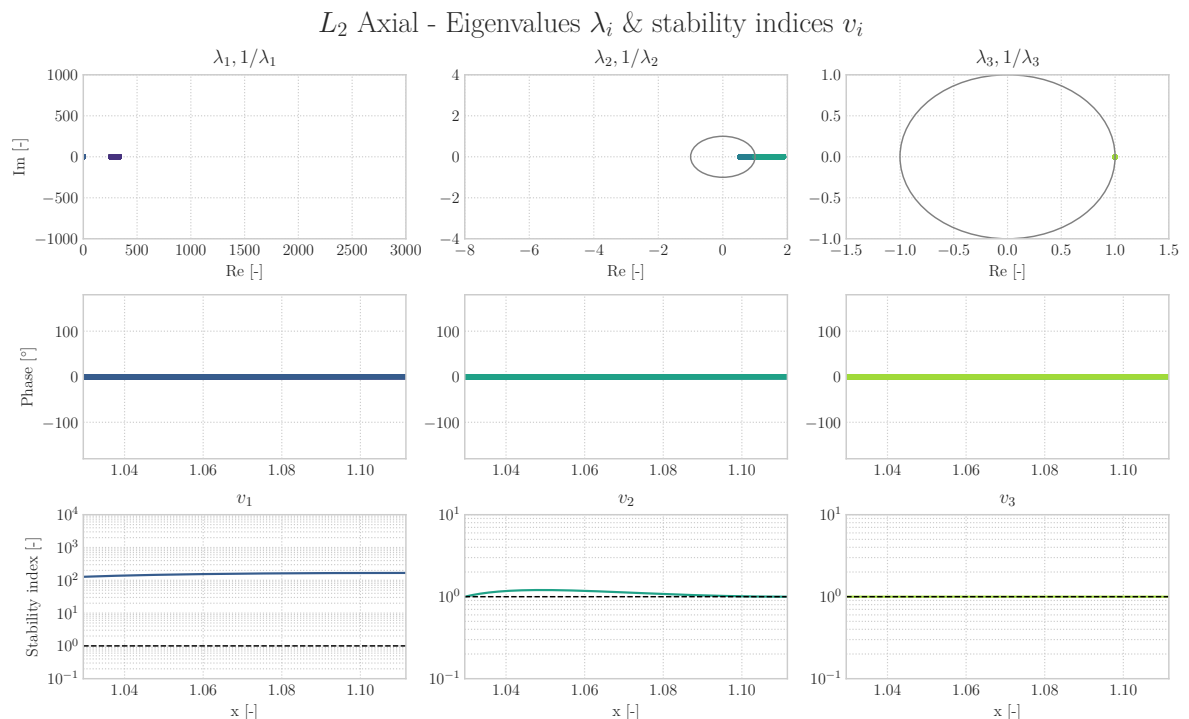
Figure 4.35: *Stability overview of the three pairs of reciprocal eigenvalues ordered in three columns, corresponding to the pair denoting the (un)stable subspace, center subspace and periodicity. The three rows indicate: the real and imaginary components, phase of the complex eigenvalues and stability index (Eq. 2.25). With the exception of the real and imaginary components, all parameters are displayed as a function of the x-component of the initial shooting conditions.*

4.7.2. Discussion of results

The 1242 members of the axial family computed in this research exactly span the space between the H-L and V-L family, resulting in the bisection of the full family as shown in Figure 4.31. In contrast to axial family presented in Section 4.3, the computed family in L_2 is the north-west segment. When analysing these elements from low to high orbital energy, the consecutive orbits twists around the x-axis thereby honouring the denomination axial. The orbital period is strictly increasing and bounded by a modest interval of $[4.31, 4.42]$ in dimensionless time, corresponding to $[18.74, 19.22]$ days. The corresponding amplitude in y-direction decreases over the range $[0.05, 0.28]$, or $[19220, 107632]$ km. In this way, the L_2 family attains a slightly larger in-plane amplitude than its related set of orbits in L_1.

Only two thick lines are shown in the spatial overview in Figure 4.31 indicating the two tangent bifurcations to H-L and V-L families of orbits. The departure of the pair of reciprocal eigenvalues at the tangent bifurcation from the H-L family gives rise to the second-order linear instability of the axial family, and greatly resembles the behaviour shown by the H-L L_2 family (Fig. 4.21 in Sec. 4.5). The location of these two branch points as well as the orthographic projections are in agreement with the results published in [Doedel et al., 2007]. In addition, the analysis of the monodromy matrix is very similar to the mirror image of the equivalent study performed in L_1 (Fig. 4.14 and 4.34). This behaviour is observed for all computed families of periodic libration point orbits.

The stability analysis presented in Figure 4.35 displays the two pairs of (un)stable eigenvalues in the first two columns $(\lambda_1, \lambda_1^{-1}, \lambda_2, \lambda_2^{-1})$. The magnitude of the real part of these eigenvalues is significantly smaller than those of the other families and relates well to its equivalent in L_1. According to Equation 2.24, this will result in a considerably slower unwinding of the corresponding hyperbolic manifolds.

The robustness of the DC algorithm (Fig 4.13) and the low error in determinant of the symplectic maps (Fig. 4.14) are still exceptional, although the performance was slightly better in the case of L_1. In a similar fashion as before, the NC procedure is terminated by the stopping conditions formulated in Section 3.2.2.

4.8. L_2 **Vertical Lyapunov family**

The fourth and final set of trajectories computed in L_2 is the V-L. Together with the H-L family, these two families of orbits form the two principle types of motion. The resulting V-L family is displayed in Figure 4.36. These trajectories are instances of a near-continuous set of orbits. In this way, this family can be characterised in terms of Jacobi's constant and orbital period and is shown in Figure 4.37.
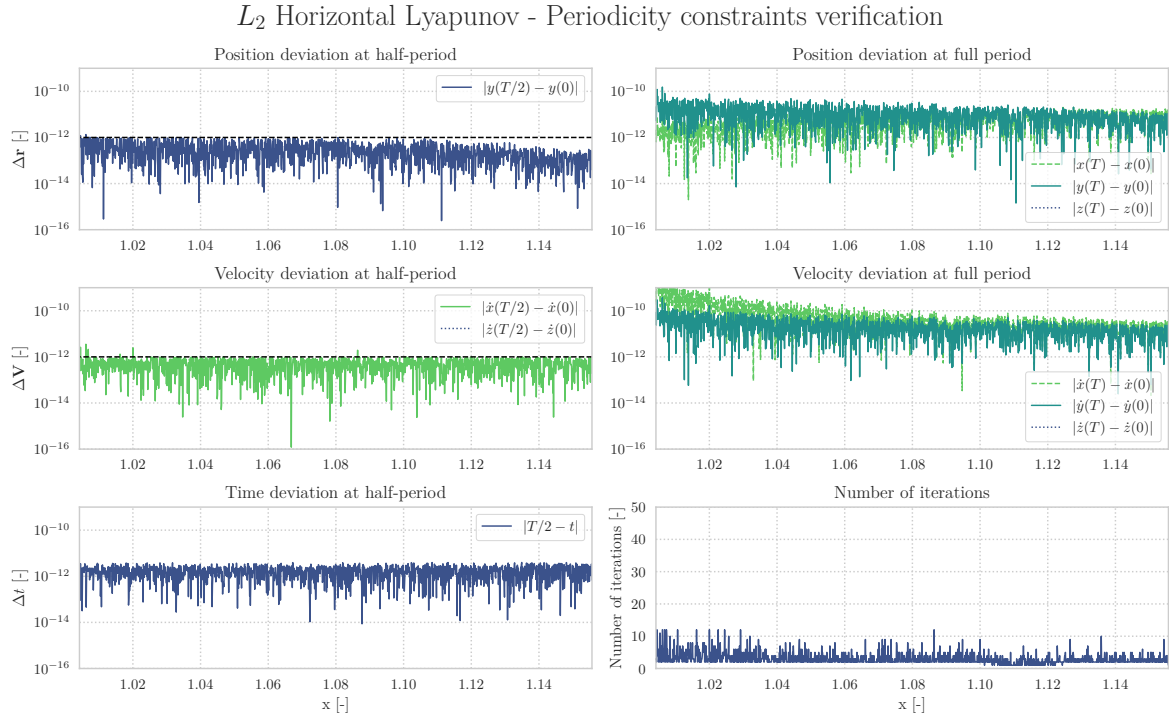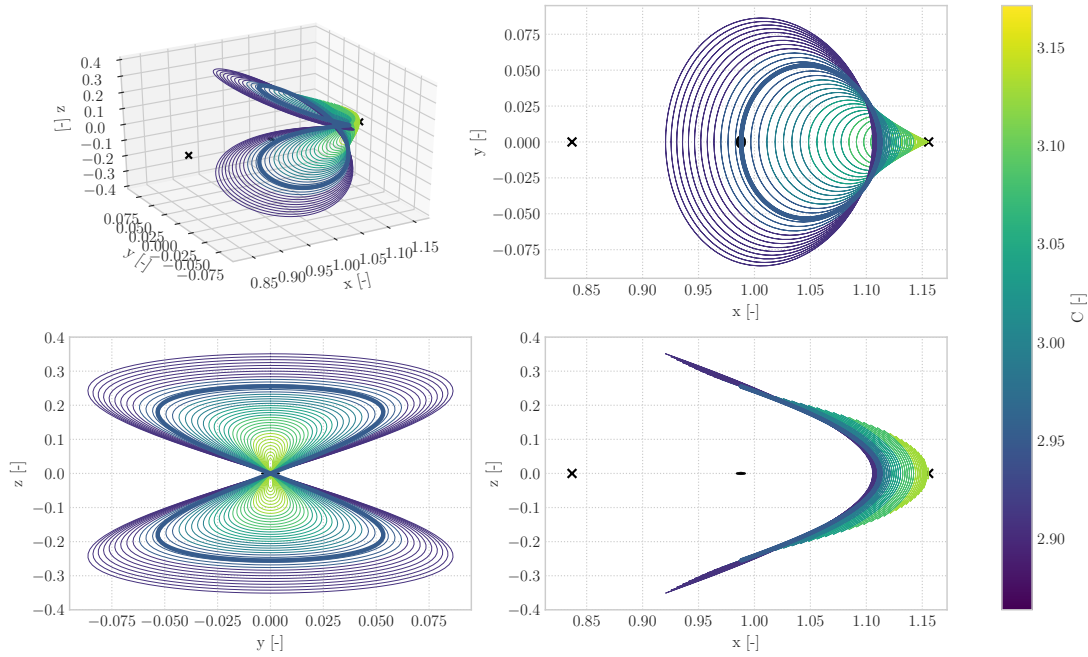

Figure 4.36: Orthographic projection of every hundredth member of the V-L family emanating from L_2. The thick lines highlight the orbits at which the order of linear instability changes (bifurcations). The two crosses indicate the equilibria (L_1 and L_2), whereas the sphere located at $(1-\mu,0,0)$ represents the Moon at mean radius (P_2). The colour scale provides insight into the sensitivity with respect to Jacobi's constant (C).
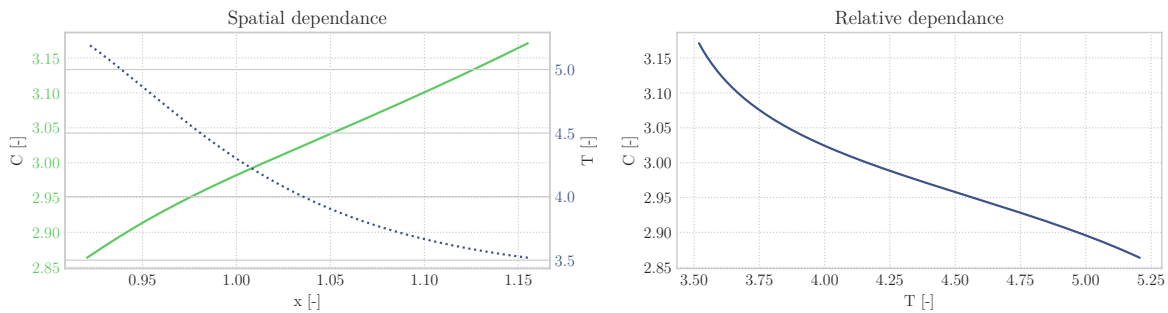
Figure 4.37: Characterisation of the refined V-L family in L_2 in terms of the Jacobi's constant (C) and orbital period (T), as a function of the x-component of the initial conditions.

4.8.1. Periodicity verification and eigensystem validation

To verify the numerical veracity of the results of the V-L family in L_2, Figure 4.38 shows the periodicity constraints verification. In addition to this verification procedure, the results are validated through the analysis of the monodromy matrices as presented in Figure 4.39.

L_2 Vertical Lyapunov - Periodicity constraints verification
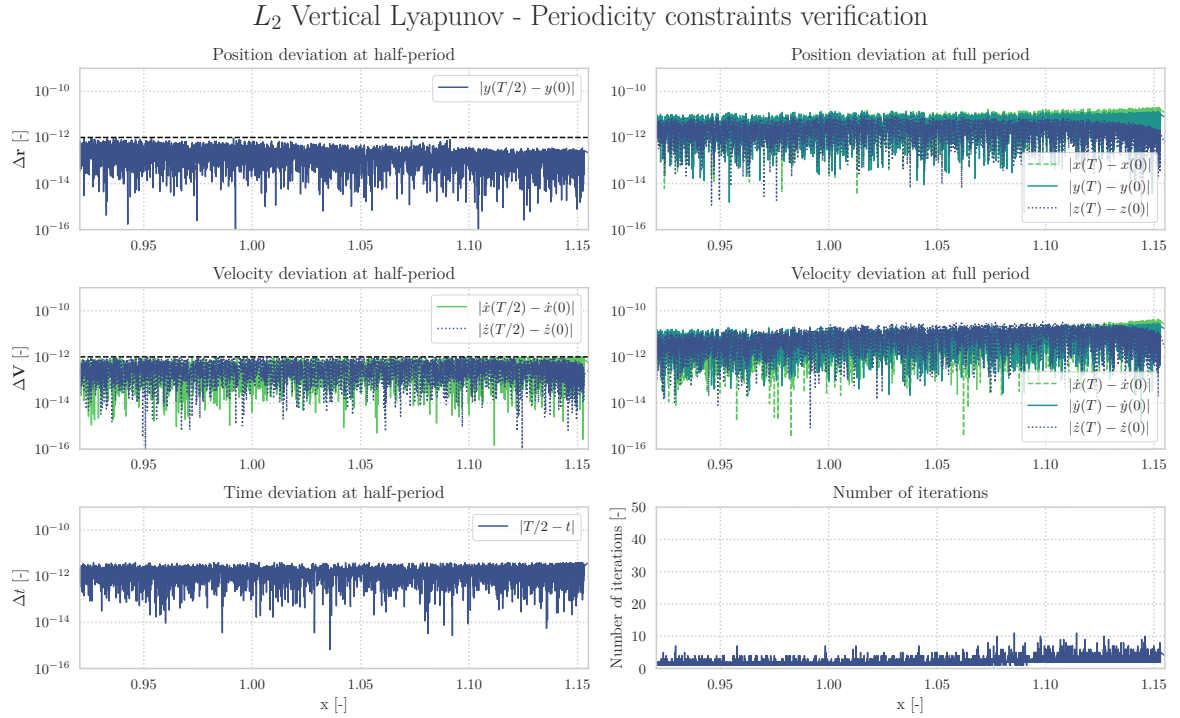
Figure 4.38: *Numerical periodicity constraints verification for all members of the V-L family in L_2. The first column displays the compliance with the thresholds set for DC in terms of position (Eq. 3.25), velocity (Eq. 3.26), and integrator overshoot. The right column indicates the periodicity at full period and the robustness of the DC algorithm through the number of iterations.*

L_2 Vertical Lyapunov - Monodromy matrix eigensystem validation
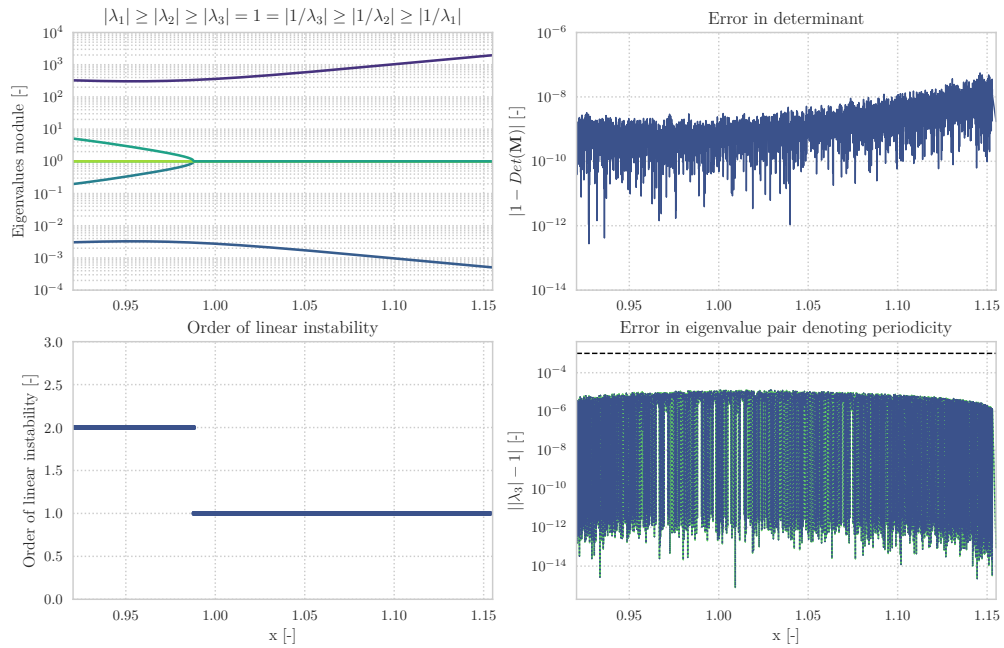
Figure 4.39: *Analysis of the monodromy matrices of the L_2 V-L family. From top to bottom, from left to right: modulus of the six eigenvalues, deviation of the determinant (Eq. 2.23), order of linear instability and error of the reciprocal pair of eigenvalues indication periodicity (Eq. 3.27). All evaluations are mapped out with respect to the x-component of the initial shooting conditions.*

As an additional insight into the stability of the members of this family, the three sets of eigenvalues extracted from the monodromy matrices are presented in Figure 4.40.
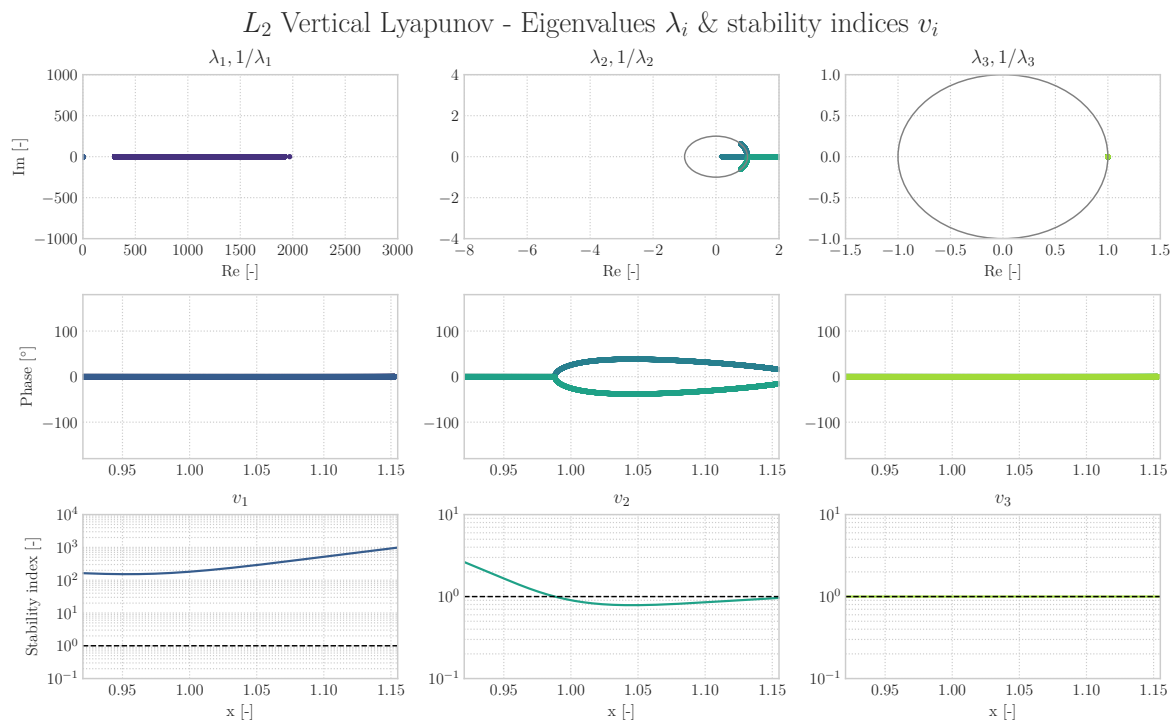
Figure 4.40: *Stability overview of the three pairs of reciprocal eigenvalues ordered in three columns, corresponding to the pair denoting the (un)stable subspace, center subspace and periodicity. The three rows indicate: the real and imaginary components, phase of the complex eigenvalues and stability index (Eq. 2.25). With the exception of the real and imaginary components, all parameters are displayed as a function of the x-component of the initial shooting conditions.*

4.8.2. Discussion of results

When analysing the 4000 V-L members from low to high orbital energy, the amplitude of the orbit geometry and the related orbital period both show a strict increase. These parameters are bounded by intervals of $\langle 0, 0.35]$ in z-direction and $[3.52, 5.21]$ in time. The equivalent dimensional units are $\langle 0, 134540]$ km and $[15.31, 22.65]$ days. Only a single thick line can be observed in the spatial overview in Figure 4.36 indicating the tangent bifurcation to the axial branch and corresponds to an increase in linear order of instability from one to two (Fig. 4.39). However, the stability analysis in Figure 4.40 shows that this additional (un)stable eigenvalue pair has a relatively low real component. The first reciprocal eigenvalue pair on the the other hand, attains the most extreme maxima and minima of all computed families in L_2 and supports that the "most unstable orbits" are those closest to "the equilibrium point" [Goudas, 1963]. This makes the V-L family highly suitable for exploitation of hyperbolic transfer mechanisms. Interestingly, also the L_2 V-L family consists entirely of unstable members.

Unlike the V-L family in L_1, there exists no turning point in x-component of the L_2 family. As both primaries are aligned in the same direction from the perspective of L_2, the set of orbits grows gradually in negative x-direction. In contrast to the first collinear equilibrium point, this orbits display a significantly larger lateral amplitude. This phenomenon is identical to the one observed for the axial family (Sec. 4.3 and 4.7). Also in the case of L_2, the pseudo-arclength continuation has proven to be very robust in the handling of this highly unstable orbit type.

The second and fourth quadrant of Figure 4.39 show a low error with a slight trend. The threshold value is not nearly exceeded, hence the numerical continuation is terminated due to satisfying the maximum number of members per family of orbits. Nonetheless, the results presented in this section greatly extend the work as presented by [Archambeau et al., 2011]. Together with the H-L family analysed in Section 4.5, these two types of orbits constitute to the principle forms of motion and conclude the computation of orbits in EM L_1.

4.9. Review of orbit generation results

The results presented in this chapter have been achieved using the RK78 integrator in combination with the high-performance C++ coding language. Using this combination, the author has independently generated periodic orbits that can be compared to the earlier work presented by [Massarweh, 2016]. The corresponding conclusions provide insight into the relative performance. In addition, the lessons learned from the numerical set-up for orbit generation provide crucial insights into the process of manifold generation.

4.9.1. Concluding statements on the results of orbit generation

In general, the results indicate the same phenomena in terms of spatial shape of the orbits, eigenvalues of monodromy matrices and energy ranges per family. However, there are also important dissimilarities that can be observed:

1. The accuracy of the RK78 seems to be very close to that of ode113, which is most likely due to the identical settings of strict error tolerances. However, the determinants of the monodromy matrices show a slightly higher error than those presented in [Massarweh, 2016]. A possible explanation for this fact is the higher order of accuracy of MATLAB's ode113 solver.

2. The location of the bifurcation points differs very slightly, which is most likely due to the minute difference in the adopted mass parameter. In Tudat, the value for μ is selected based on the fraction of gravitational parameters whereas the one adhered to by [Massarweh, 2016] has been rounded off at seven decimal numbers.

3. Due to the high performance induced by the C++ language, a higher resolution of results was achieved through an extended number of members per family of libration point orbits (17411 versus 8008 periodic solutions). In particular for the V-L family in L_1, this revealed the curving of the figure-eight shape towards the first primary. In addition, extension of the halo family in L_1 revealed additional bifurcations.

4. One of the challenges of using the RK78 scheme in a compiled language, is the emergence of overshooting. Since the step-size is not an independent variable, it is highly unlikely that the integration stop-time equals the desired period. A solution adopted in this research consists of a roll-back of state whenever overshooting occurs. This is followed by a decrease in order of initial step-size until the machine limits are reached. This has resulted in a characteristic overshoot of $\sim 10^{-12}$ and proved to be of critical importance to acquiring smooth lines of eigenvalues in the monodromy eigensystem validation.

In addition to the added performance using C++ and future synergies through the publication of generic open-source code, the results of the computation of orbits have also provided inspiration for manifold propagation.

4.9.2. Recommendations for the experimental set-up for manifold propagation

The recommendations for the approach to manifold propagation can be divided into two main parts. Firstly, proposals with respect to the orbital characteristics will be presented. This is followed by a suggestions from a numerical perspective.

Orbit selection proposal

In summary, the orbits generated using the procedure outlined in Algorithm 1 cover the ranges of Jacobi's constant and orbital period shown in Figure 4.41. The combined view of these characteristics provides for an interesting comparison:

1. Whereas both Lyapunov families monotonically increase in orbital period (T) given a reduction in Jacobi's constant (C), the halo families appear to adhere to an inverse behaviour. This phenomenon can be explained based on the geometry of the respective trajectories. Whereas both principle forms of motion increase in amplitude for an increase in orbital energy, the geometry of the halo family remains within bounds and even decreases when approaching the second primary (P_2).

2. In addition to the inverse relation of the orbital period with respect to the orbital energy, one can also observe that the Lyapunov families cover a more extended range than the halo family. There are two possible explanations for this behaviour. Firstly, halo orbits are not a principle form of motion and thereby require a minimal amplitude to exist. In this way, the minimum energy level is bounded. Secondly, the halo orbits remain restricted in both size and spatial location. On the other hand, the H-L and V-L families extend to achieve vast sizes. Especially the vertical members cover an immense range, and can even be extended beyond the shooting conditions presented in this research. Evidence for this statement can be found in Figure 4.42 and Table 4.1. These elements present the range of shooting conditions for refined trajectories and the active constraint on the maximum number of members in the V-L family respectively.[7]

3. Lastly, it is very intriguing that the most powerful hyperbolic behaviour can be observed for the orbits with the lowest energy level across all families. In other words, the pair of eigenvalues denoting the (un)stable subspace attain their highest maximum and lowest minimum near the collinear equilibrium points. A possible explanation for this phenomenon is that the local centre × centre × saddle-type dynamic behaviour reduces in strength for orbits located further away from $L_i \forall i = 1, 2, 3$.

Families overview - Orbital energy and period
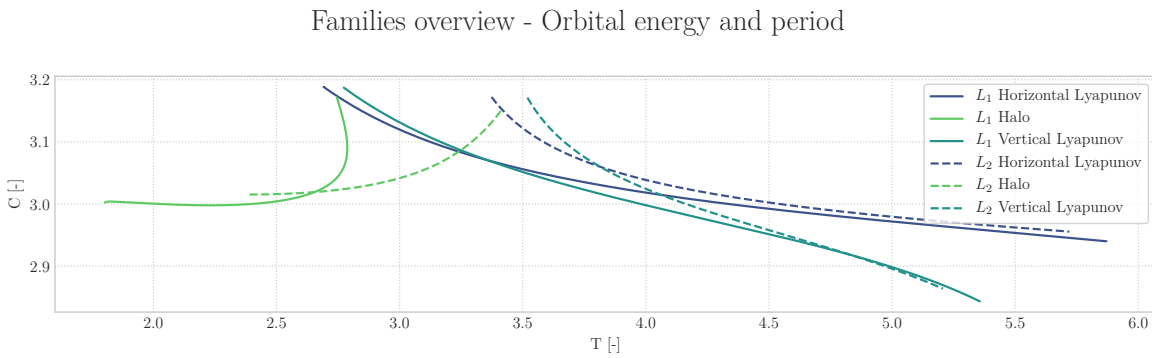
Figure 4.41: *Overview of the orbital period (T) and Jacobi's constant (C) for the various types of families of periodic libration point orbits emanating from L_1 (full) and L_2 (dashed) respectively.*

For an unbiased comparison of the manifolds emanating from different types of orbits, an equal energy level is required. In this way, a suitable range of Jacobi's constant can be selected in which all three types of families in both equilibria are known to exist.[8] This spectrum boils down to Equation 4.1.

$$3.0 < C < 3.15 \tag{4.1}$$

The distribution of the sequential energy levels corresponding to the shooting conditions for periodic trajectories is presented in Figure 4.42. Please note that due to the formulation of the initial conditions in Equation 3.18, the vertical axis indicates the z-component. This projection of the families of orbits provides constraints for the process of manifold generation, in addition to the desired energy range (Eq. 4.1). In particular for the V-L family, one would like to adhere to moderate values of C to have a significant separation between the L_1 and L_2 orbits and thereby resembling a realistic case.

---

[7]A further extension of the V-L family is documented in Appendix C and has validated that these doubly symmetric orbits completely embrace the first primary for sufficiently large energy values as presented in [Bray and Gouclas, 1967].

[8]Please note that the aim of this research is to expose novel connections for V-L orbits. In this way, the H-L and halo family serve as means of validation as those types have been investigated extensively in literature. The goal of computing the axial family is to provide a complete view of the connections between the continuous families of orbits. Since this family only covers a small energy range ([2.992, 3.021] and [2.967, 3.014] for L_1 and L_2 respectively) and possesses a very constrained set of (un)stable eigenvalues, this type of orbit is not included in the manifold analysis.

L_1, L_2 - Shooting conditions for H-L, halo, and V-L
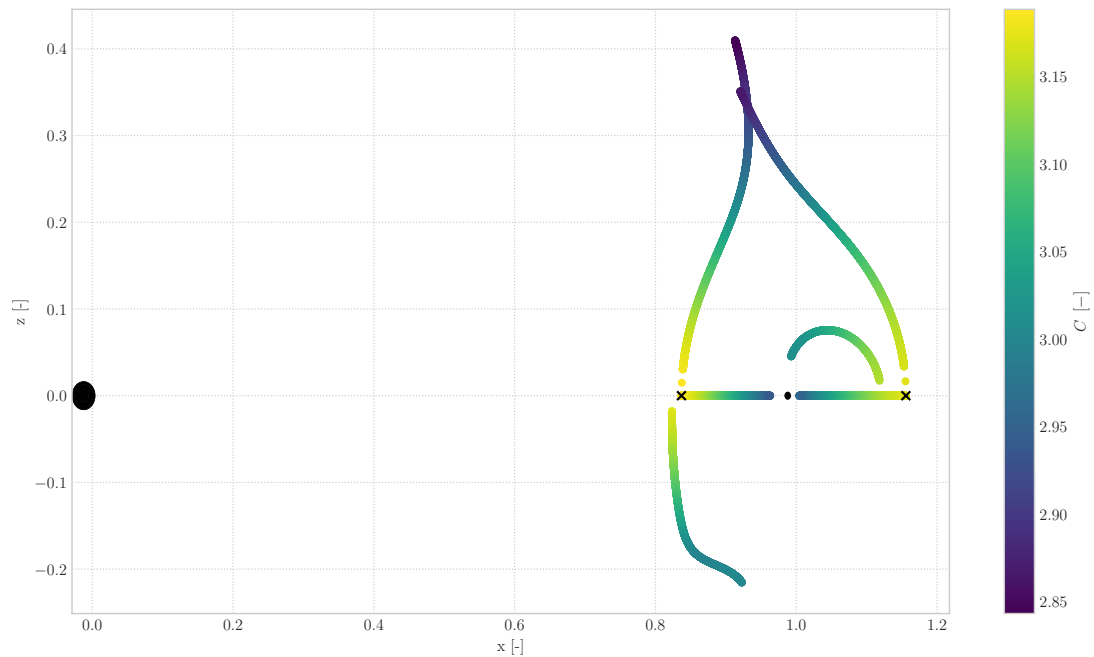
Figure 4.42: *Overview of position components of shooting conditions as a function of Jacobi's constant. The two crosses indicate L_1 and L_2 respectively. The H-L families are limited to planar shooting conditions ($z = 0$), whereas the V-L families grow quickly in positive z-direction. The halos are characterised by the two curves emanating from the horizontal plane and extending below and above the orbital plane for L_1 and L_2 respectively.*

In addition to these recommendations for target orbit selection, the process of orbit generation has improved the understanding of the numerical performance and constraints. Recommendations on both aspects are vital to a successful analysis of manifold structures.

Recommendations on computational effort, efficient memory usage and integrator settings

As described in the research frame definition in Section 1.2, this research aims to contribute to future research by producing a generic, high-performance, and tested tool for both orbit and manifold generation. The use of a compiled language has greatly increased the scope of the ranges of orbits that can be analysed, as can be observed from Table 4.1.

Table 4.1: *Number of refined trajectories per family of orbits after termination of the NC algorithm. Whereas the propagation of the H-L and halo families are stopped due to exceeding the error thresholds, the axial and V-L families are restricted by the bifurcation to the V-L family and maximum number of members respectively.*

	Number of members in L_1	Number of members in L_2
H-L	1262	1515
Halo	2639	1815
Axial	938	1242
V-L	4000	4000

However, the employment of C++ also yields a number of demanding problems which adds to the overall project risk. All in all, the following can be concluded from a numerical perspective on the results of orbit generation:

Coding effort: First of all, the effort required in writing the code greatly exceeds those by higher-level languages like Python and MATLAB. This poses a significant planning and technical risk. However, the scale of the desired scale of this project requires these high performance tools.

Computational effort: The considerable computational effort involved in orbit generation can be mainly attributed to integration with strict error tolerances. As the propagation of manifolds both greatly increases the number of orbits as well as the integration time, the corresponding computation effort is expected to increase exponentially. To aid in solving this problem, the high-performance C++ language was adopted which can be multithreaded in a very elegant way using OpenMP. [9] However, the sheer size of this operation requires additional measures.

Memory usage: Table 4.1 indicates that 17411 orbits have been refined and written into static memory. Each of these orbits correspond to four manifolds, approximated by at least 100 orbits each and propagated over characteristic timescales of $t_f = 6 - 16$ with strict error tolerances. In conclusion, an unfeasible amount of memory would be required in the case that no preventive measures are taken. As a first step, only an independent set of variable is saved at every thousandth integration step. This still produces sufficient resolution for the orthographic projections, whereas it significantly diminishes the memory size. In addition, the size of variables is initialised and passed by reference where possible and writing to static memory is performed at the end of each function. Both these approaches are adopted to relieve the effort required by this computationally intensive task.

Integrator settings: The strict error tolerances documented in Appendix B have proven to be vital to producing validated results. The significance of this near-machine-limits accuracy cannot be understated, as only extensive verification and validation procedures shown in this research can show the deficiencies in the results. In addition, the overshoot produced by the variable step-size integrator needed to be minimised to provide an accurate approximation of the monodromy matrix. This is not only important to the validation of orbits through eigensystem analysis, but will also provide the foundation for manifold generation. A minimal under-/shoot is achieved through roll-back of state whenever the stopping conditions are exceeded, and are followed by a decrease in order of the initial step-size. Following this procedure, the magnitude of the overshoot is gradually reduced until near-machine-limits whilst still adhering to strict error tolerances.

These conclusions and recommendations from orbit generation will provide the understanding required for an efficient generation of valid manifold structures. In particular, reducing the order of this system of infinitely many solutions will be required to confine the research to a feasible scope.

---

[9]The reader is referred to [Kuhn et al., 2000] for an analysis of the robustness and performance of this application programming interface (API), as well as an investigation into "how OpenMP uses threads."

This page is intentionally left blank.

<div align="right">5</div>

Numerical approach to manifold generation

Each member of the families of orbits analysed and validated in Chapter 4 inherits the saddle-type behaviour of its corresponding equilibrium point, and thereby gives rise to hyperbolic trajectories one can exploit. The propagation of these desired invariant manifolds are initiated by a 'little push' in the respective local (un)stable eigenvector direction of the orbit. Firstly, the fundamentals of *invariant manifold theory* will be discussed in Section 5.1. These methods form the basis of the numerical approach to manifold generation and are addressed in Section 5.2. In addition to the numerical propagation of these topological structures , this section will pay special attention to boundary conditions, verification, and validation. In conclusion, this chapter forms the theoretical basis and methodology for the presentation of verified and validated manifolds in Chapter 6.

5.1. Fundamentals of invariant manifold theory

A manifold "is simply a mathematical term for higher dimensional surfaces"[Koon et al., 2000a]. In this way, the invariant hyperbolic manifolds in the scope of DST are topological structures. Also referred to as *separatrices of motion*, these two-dimensional tubes separate transit orbits (located inside the tube) from non-transit trajectories (located outside of the tube). Any point on the hyperbolic manifold will asymptotically arrive at (stable) or depart from (unstable) the target orbit, hence the term hyperbolic. Like all trajectories in the scope of this research, the motion of these trajectories is completely determined by the set of differential equations governing the CR3BP.

5.1.1. Realms of hyperbolic motion

Each periodic orbit presented in Chapter 4 gives rise to a set of four hyperbolic manifolds, two of which asymptotically approach the orbit (stable) and two that asymptotically depart from this periodic trajectory (unstable). Together, these four manifolds provide the desired ballistic transfer mechanisms. The distinction between the different tubes is shown in Figure 5.1. This example shows the numerical approximation of these topological structures through a set of orbits. The asymptotic behaviour of these paths causes these trajectories to "wind on or off" its target orbit [Topputo et al., 2005].

L_2 Horizontal Lyapunov $\{\mathcal{W}^{S\pm}, \mathcal{W}^{U\pm}\}$ - Spatial overview at C = 3.15
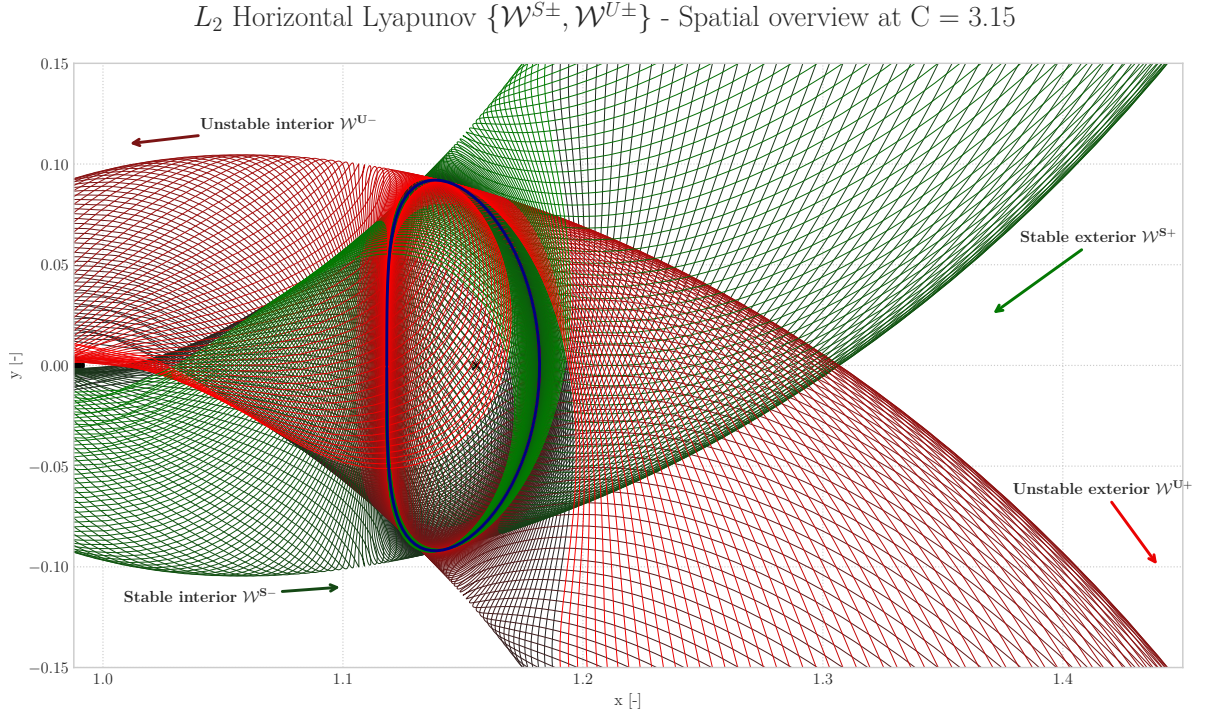
Figure 5.1: *The set of four invariant hyperbolic manifolds asymptotically arriving and departing from the H-L target orbit situated at EM-L_2 (cross at $\approx (1.156, 0)$). The sphere on the left-hand side indicates the true size of the Moon at mean radius (P_2 at $(1 - \mu, 0)$), adhering to the coordinate system presented in Figure 2.1.*

The distinction interior/exterior is attributed to the target realm of the manifold. It is "conventional to refer to the half of the manifold that moves toward the smaller body as the interior [unstable] manifold since it remains in the interior of the smaller body's influence, at least for a short while" [Parker and Anderson, 2014]. Vice versa, the unstable half that moves away from the smaller primary (P_2 in Fig. 2.1) is referred to as the unstable exterior manifold. The adopted terminology corresponding to Figure 5.1 is presented in Table 5.1.

Table 5.1: *Definition of four types of manifolds corresponding to a periodic orbit*

Symbol	Mode	Distinction for target orbit in L_1 / L_2	Integration time direction
$\mathcal{W}^{S+}$	Stable	Interior / Exterior	Negative
$\mathcal{W}^{S-}$	Stable	Exterior / Interior	Negative
$\mathcal{W}^{U+}$	Unstable	Interior / Exterior	Positive
$\mathcal{W}^{U-}$	Unstable	Exterior / Interior	Positive

Three interesting observations can be made on the basis of Table 5.1. First of all, a plus or minus sign is included in the symbol notation. This distinction separates positive from negative eigenvector offsets applied along the orbit and will be discussed in the initial conditions for manifold generation (Sec. 5.1.2). Secondly, the direction of integration time is reversed in the case of the stable manifold generation. This ensures that these hyperbolic trajectories asymptotically arrive at the target orbit. Lastly, the definitions presented in Table 5.1 indicate the dependence of the distinction exterior/interior on the collinear libration point number. This division can be clarified when expanding the scope to the manifolds emanating from an orbit around L_1. Figure 5.2 shows the result of propagating the set of four manifolds for both libration point orbits at an identical energy level.
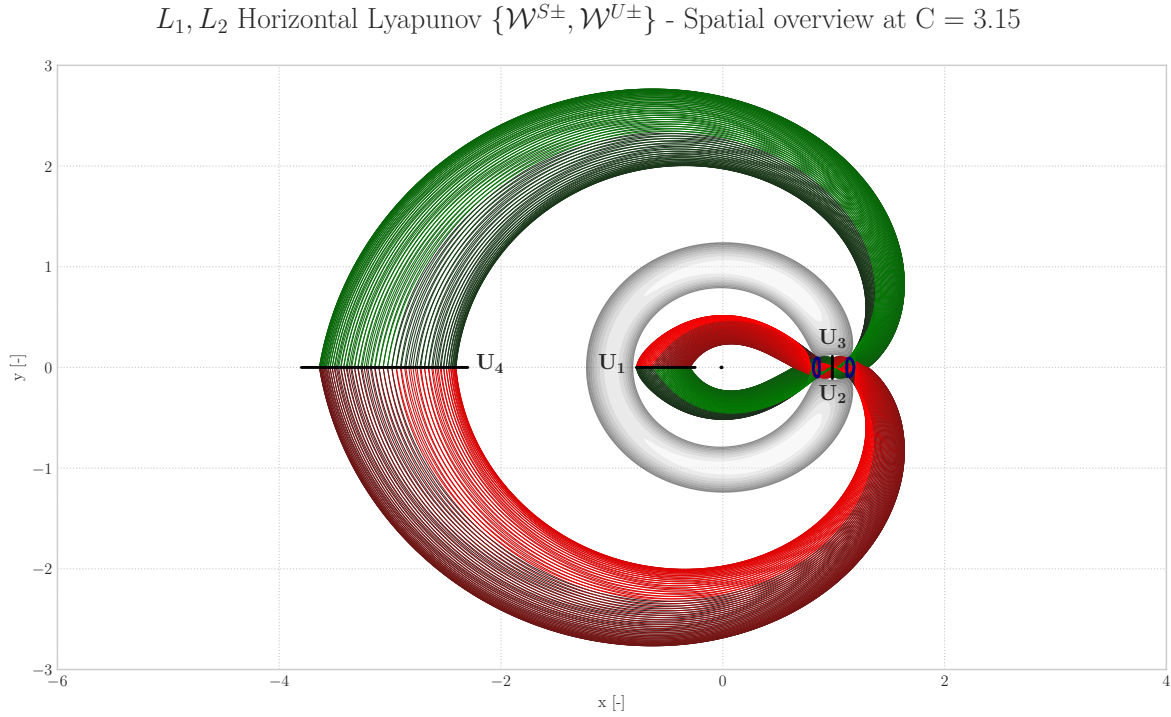
Figure 5.2: *Overview of the two sets of four invariant hyperbolic manifolds emanating from H-L orbits in L_1 and L_2 respectively. Nominal stopping conditions are indicated by predefined Poincaré sections $\mathbf{U}_i \forall i = 1,\dots,4$*

An important observation from Figure 5.2 is the definition of the stopping conditions for propagation. In theory, the eight presented manifolds can be propagated indefinitely. However, in practice the most renowned scientists in this field adopt this set of four predefined locations and orientations of the Poincaré sections as stopping conditions [Gómez et al., 2004]. [1] Hence, this set of stopping conditions ($\mathbf{U}_i \forall i = 1,\dots,4$) is referred to in this research as the nominal case. In an effort to find novel transfer solutions, variations of the orientation and position of these planes will be produced and analysed in Chapter 7.

As this research is focused on the motion near collinear libration points L_1 and L_2, a closer look is taken at the manifolds near the second primary. This interior realm is shown in Figure 5.3, along with the two Poincaré sections $\mathbf{U}_2$ and $\mathbf{U}_3$ which are separated by the x-axis. Combination of the stable and unstable interior manifolds can give rise to free transfers between the two different equilibrium points. Also described as heteroclinic connections, these trajectories define the focus of Chapter 7.

---

[1] For an in-depth derivation of invariant hyperbolic manifold structures, the reader is referred to the work of [Koon et al., 2009] or [Parker and Anderson, 2014].

L_1, L_2 Horizontal Lyapunov $\{\mathcal{W}^{S\pm}, \mathcal{W}^{U\pm}\}$ - Spatial overview at C = 3.15
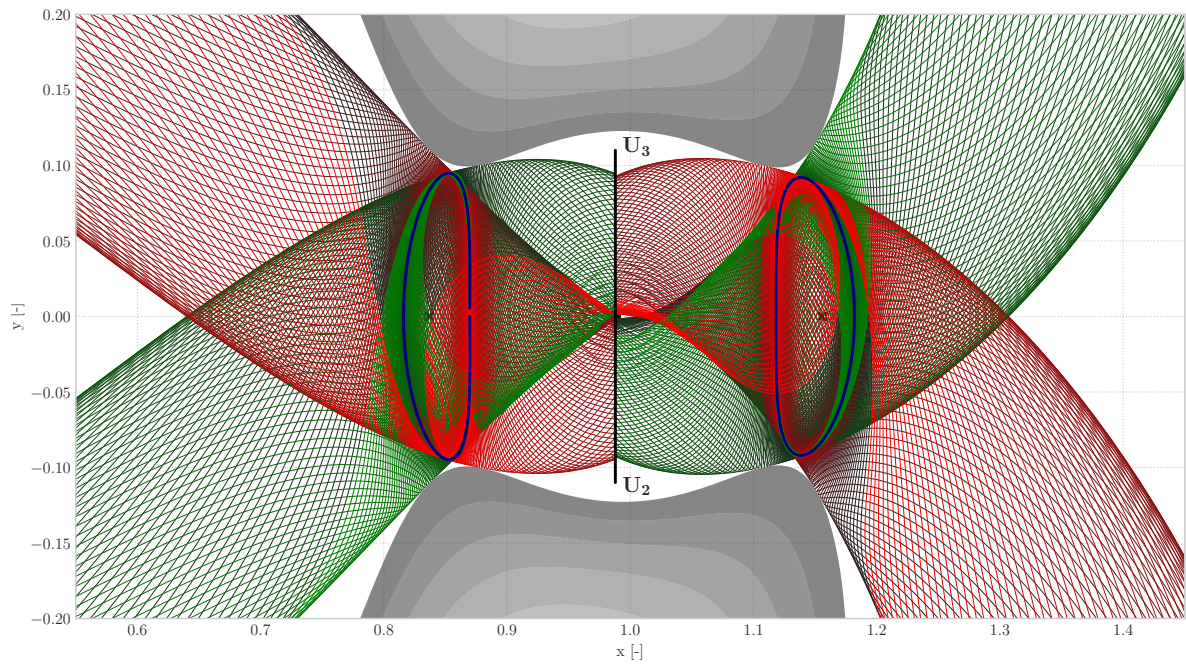
Figure 5.3: *Close-up view of the Poincaré sections $\mathbf{U}_2, \mathbf{U}_3$, which form the nominal stopping conditions for the interior manifolds emanating from H-L orbits in L_1 and L_2 respectively.*

Figures 5.2 and 5.3 already demonstrate the existence of image trajectories in the planar case (Eq. 2.6 and 2.7). In particular, it is interesting to observe the influence of reversing the direction of time that occurs for symmetries with respect to the x-axis. In the case of manifolds, this change separates the stable from unstable trajectories and complies with the direction of integration time noted in Table 5.1. This particular symmetry can also be observed in the close-up views of the two other Poincaré sections $\mathbf{U}_1$ and $\mathbf{U}_4$ in Figures 5.4 and 5.5 respectively.
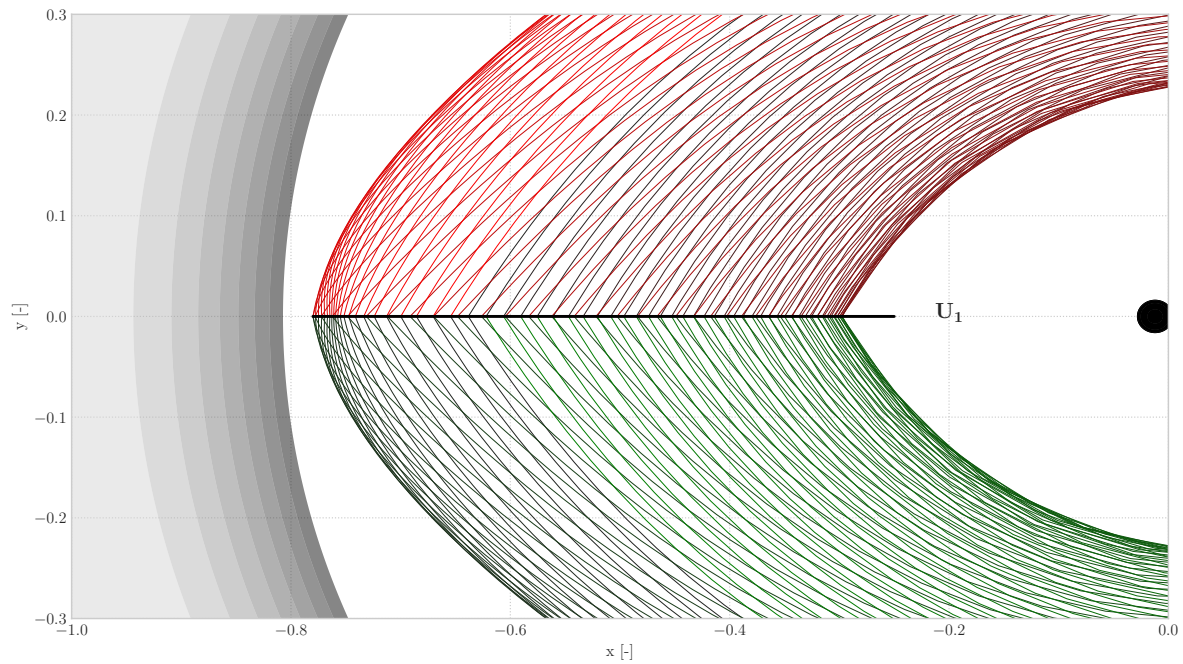
Figure 5.4: *Close-up view of the Poincaré section* $\mathbf{U}_1$*, which forms the stopping conditions for the exterior manifold arising from the H-L orbit in* L_1*.*
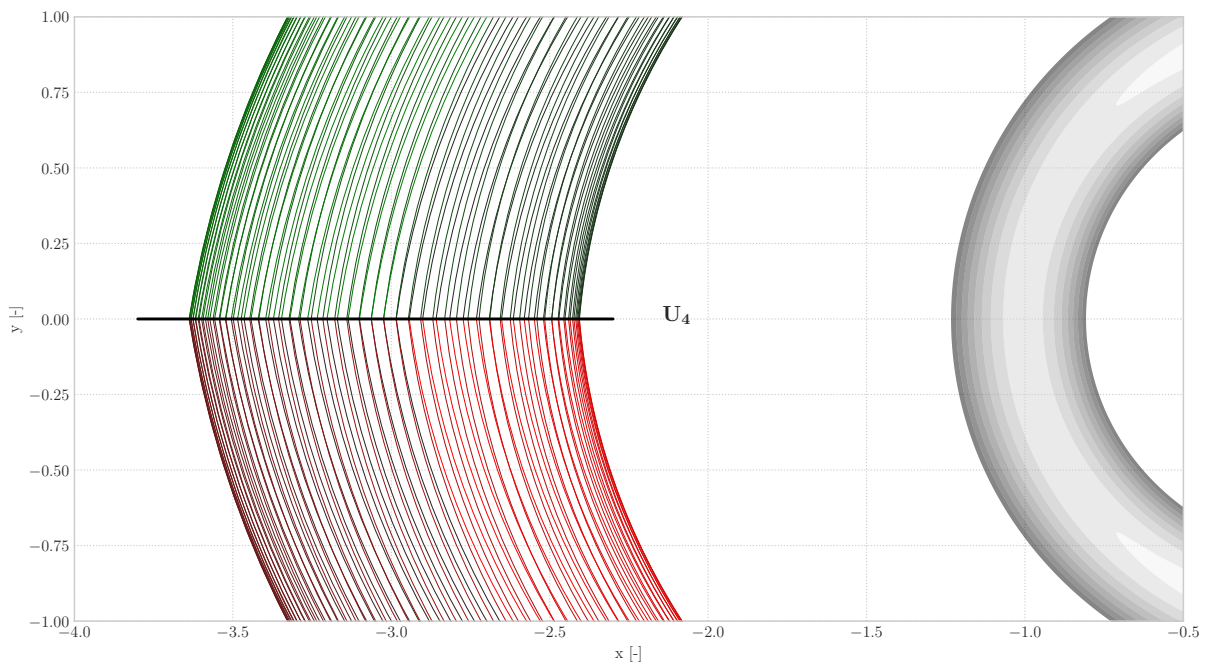
Figure 5.5: *Close-up view of the Poincaré section* $\mathbf{U}_4$*, which forms the stopping conditions for the exterior manifold arising from the H-L orbit in* L_2*.*

The mirror image with respect to the x-axis in Figures 5.4 and 5.5 show alignment in position for pairs of stable-unstable trajectories. As these trajectories have been integrated independently, comparison of

these states at $\mathbf{U}_1$ and $\mathbf{U}_4$ provide valuable insights into the trustworthiness of the results. For instance, high numerical equivalence of state indicate that the implementation of the dynamical model possesses symmetric properties. Thereby rendering syntactic mistakes in the state derivative unlikely. In addition, the extent of numerical resemblance can be used as an indicator of the relative integration error. In conclusion, the symmetric properties in the ballistic case offer valuable insights that can be exploited to test the validity of results. In a similar manner to the extensive verification and validation (V&V) of periodic trajectories presented in Chapter 4, Section 5.2.5 will introduce these novel techniques for V&V of manifold structures. The implementation of these methods aims to address the need for scientific tests of these structures.[2]

In pursuance of alignment in position of stable-unstable trajectory pairs as presented in Figures 5.4 and 5.5, the initial conditions of the manifold need to be symmetric with respect to the x-axis. Especially in the case of a variable step-size integrator, this is a challenging requirement as the time-step is not an independent variable. The solution for this process is presented in first section of the numerical approach to manifold generation in (Sec. 5.2.1).

5.1.2. Initial conditions for manifold generation

In a numerical sense, each of the four topological structures presented in Table 5.1 is approximated by a number of trajectories. As can be observed in Figure 5.6, the starting point for each of these trajectories is produced by a perturbation along the orbit. In the case of the $\mathscr{W}^{U+}$ manifold in L_2, the starting point $\left(\mathbf{X}^{U+}(t_{u0})\right)$ is created by adding an offset $(+\epsilon)$ of the local normalised eigenvector $(\hat{\mathbf{v}}^U)$ to the state $(\mathbf{X}(t_0 + \tau))$ along the periodic orbit. The unstable manifold is then propagated forward in time until the final state $\left(\mathbf{X}^{U+}(t_{u0} + T_u)\right)$.
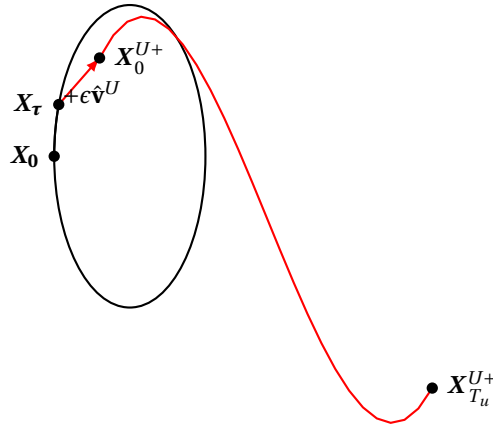
Figure 5.6: *Approach to manifold generation in the case of the unstable interior manifold ($\mathscr{W}^{U+}$) emanating from a periodic libration point orbit around L_1, in which:* $\mathbf{X}_0 = \mathbf{X}(t_0), \quad \mathbf{X}_\tau = \mathbf{X}(t_0 + \tau), \quad \mathbf{X}_0^{U+} = \mathbf{X}^{U+}(t_{u0}), \quad \mathbf{X}_{T_u}^{U+} = \mathbf{X}^{U+}(t_{u0} + T_u)$

In the case of the $\mathscr{W}^{U-}$ manifold, the sign of the offset $(+\epsilon)$ will be reversed to $(-\epsilon)$. In a similar sense, the $\mathscr{W}^{S\pm}$ manifolds are computed using the local normalised eigenvector denoting the stable subspace $(\hat{\mathbf{v}}^S)$ as offset. In addition, the stable manifold is propagated in reverse time to ensure that these trajectories asymptotically approach the orbit.

The nodes at which the eigenvector perturbation is applied are equally spaced in time along the orbit. The aim of this approach is to produce a manifold which a near-homogeneous density of trajectories. This property is critical to making robust conclusions on the results of intersection of manifolds. An example of 100 spaced perturbations is shown in Figure 5.7.

---

[2]A more extensive analysis of this research gap is presented in Section 1.1.2.

L_2 Horizontal Lyapunov $\{\mathcal{W}^{S\pm}, \mathcal{W}^{U\pm}\}$ - Orientation of (un)stable modes
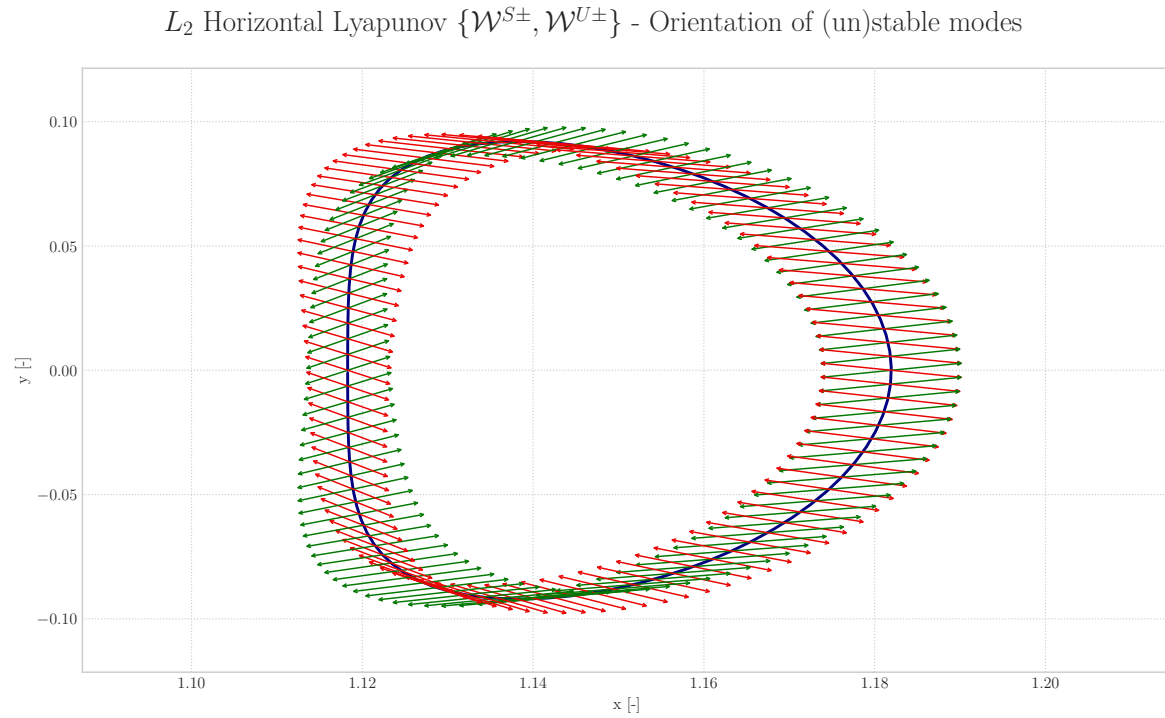
Figure 5.7: *Offset directions denoting the stable (green) and unstable (red) modes of the periodic orbit at equally spaced nodes in time.*

A detailed analysis of the eigenvector directions has proven to yield useful insights into the validity of the numerical results [Folta et al., 2014]. The analysis of the size, location and orientation of these vectors is presented in the outcome of manifold generation in Chapter 6. However, two main observations can already be made on the basis of Figure 5.7. Firstly, the positive and negative offsets generating the respective exterior and interior manifolds provide vectors of equal length and opposite orientation. This behaviour is expected since the corresponding sign is specified by the user. Secondly, the symmetry of stable versus unstable eigenvector directions with respect to the xz-plane support the theory of image solutions of the implemented EOM (Eq. 2.6 and 2.7). These symmetric pairs are related in the planar case by Equation 5.1. Both considerations add to the credibility of the results, however more techniques for verification and validation will be introduced in Section 5.2.5 to ensure a higher level of validity.

$$\tau_u = 1 - \tau_u \tag{5.1}$$

5.2. Manifold generation scheme

In a similar fashion to the orbit generation scheme in Section 3.1, this section will address the adopted approach for the construction of invariant manifolds. The fundamentals of invariant manifold theory presented in Section 5.1 are translated into a numerical scheme for the generation of manifolds. The most important components of this procedure are shown in the pseudo-code in Algorithm 2.

Algorithm 2 Generation of hyperbolic invariant manifold structures

---

Input: $\left(\mathbf{X}_0, T, \text{numberOfTrajectoriesPerManifold}, \mu\right)$
Output: $\left[\mathcal{W}^{S+}, \mathcal{W}^{S-}, \mathcal{W}^{U+}, \mathcal{W}^{U-}\right]$

1: $\Phi(t_0, t_0), \Phi(t_0 + \delta t, t_0), \ldots, \Phi(t_0 + T, t_0) \Leftarrow$ **Integrate until t_f with minimal overshoot**$(\mathbf{X}_0, T)$ ▷ *Sec. 5.2.1*
2: $(\lambda_S, \mathbf{v}_S), (\lambda_U, \mathbf{v}_U) \Leftarrow$ **Eigenanalysis**$(\Phi(t_0 + T, t_0))$ ▷ *Sec. 5.2.2*
3: **if** $|1/\lambda_S - \lambda_U| > 10^{-3}$ **then return** EXCEPTION: eigenvalues do not correspond to same reciprocal pair
4: **end if**
5: **for** $i = 0; i < 4; i + +$ **do**
6:     **Interior/exterior unstable/stable manifold selection**(i)
7:     **for** $j = 0; j < \text{numberOfTrajectoriesPerManifold}; j + +$ **do**
8:         $\mathbf{X}_0^j \Leftarrow$ **Offsetting of local eigenvector**$\left(j, \Phi(t_0 + \tau, t_0), \mathbf{v}(t_0)\right)$ ▷ *Sec. 5.2.3*
9:         **while not** fullManifoldComputed **and** $t < t_{max}$ **do**   ▷ *Sec. 5.2.4*
10:             $\mathbf{X}_{m+1}^j \Leftarrow$ **Integrate state derivative**$\left(\mathbf{X}_m^j, \delta t\text{-sign}\right)$
11:             fullManifoldComputed $\Leftarrow$ **Check stopping conditions**$\left(\mathbf{X}_{m+1}^j\right)$ ▷ *Sec. 5.2.5*
12:             m++
13:         **end while**
14:         $\mathcal{W}^i = \left[\left[\mathbf{X}_0^0, \ldots \mathbf{X}_m^0\right], \ldots, \left[\mathbf{X}_0^j, \ldots \mathbf{X}_m^j\right]\right]$
15:     **end for**
16: **end for**

The subsequent logical steps of Algorithm 2 apply the theory of creating initial conditions for manifold generation (Sec. 5.1.2). The program is initiated using any of the refined periodic orbits resulting from Algorithm 1 of which the manifolds are to be obtained.[3] Firstly, the selected trajectory is propagated for one period using a near-fixed step-size. This requires modifications to the integrator and will be presented in Section 5.2.1. Secondly, the eigenvectors are selected and ordered in Section 5.2.2 before propagation, normalisation and local offsetting along the orbit in Section 5.2.3. This forms the initial conditions for the propagation of the hyperbolic manifold, of which the stopping conditions are defined in Section 5.2.4. Lastly, novel verification and validation techniques are presented in Section 5.2.5 to ensure that the results presented in Chapter 6 are scientifically valid.

5.2.1. Variable step-size integration with minimal overshoot

To be able to exploit the symmetry between stable and unstable trajectories for manifold verification, as discussed in Section 5.1.1, one requires symmetrically placed nodes along the orbit for the eigenvector offsets. This can be approximated by a set of points along the orbit which are equally spaced in time, as presented in Figure 5.7. Since the step-size of the selected integrator scheme is not an independent variable, this requires modifications to the integrator settings.

Near-equal time intervals are achieved through lowering the maximum step-size of the integrator significantly. In this way, the scheme is further constrained in dynamic conditions which would induce larger step-sizes in the nominal case. This allows near-equal step-sizes whilst still adhering to the same strict relative and absolute error tolerances as documented in Appendix B. This near-constant step-size is combined with the procedure for minimum overshoot, as proposed in Section 4.9.2.

In addition to the local state vectors, also the corresponding STM are saved during the process of integration. These matrices are required for the computation of the local eigenvector offsets along the orbit. The procedure which enables this calculation is presented in the next section.

---

[3]Please note that a bisection method is employed together with the differential corrector to obtain the exact required energy level from the discrete set of refined orbits analysed in Chapter 4. This provides for a fair comparison between the various target orbits.

5.2.2. Selection and ordering of eigenvectors

Section 2.3.1 introduced the local centre × centre × saddle-type dynamic behaviour near the collinear equilibrium points, of which the latter gives rise to the hyperbolic manifold trajectories. Proof of this characteristic can be found in the pairs of eigenvalues and corresponding eigenvectors derived from the monodromy matrix. The ordering, selection and propagation of local eigenvectors will form the departure point for propagation of these transfer mechanisms and will be introduced in this section.

The stable and unstable modes of a periodic orbit can be derived from the eigenspace of the monodromy matrix. As discussed in Section 2.2.5 and presented in the orbit generation results in Chapter 4, this fundamental matrix gives rise to six eigenvalues forming three reciprocal pairs and can be ordered as shown in Equation 5.2. Arrangement of the eigenvector/-value pairs (Eq. 2.24) is required for proper selection of the (un)stable subspace, as the order of these vectors is dependent on the numerical solver employed.

$$|\lambda_1| \geq |\lambda_2| \geq |\lambda_3| = 1 = |1/\lambda_3| \geq |1/\lambda_2| \geq |1/\lambda_1| \tag{5.2}$$

The largest real eigenvalue in this sequence (λ_1) denotes a powerful deviation from the reference state for the corresponding eigenvector of this linear mapping, hence corresponds to the unstable subspace. Vice versa, the smallest real eigenvalue denotes motion which asymptotically approach the state and thereby gives rise to the stable subspace. In other words, the eigenvalues which are of interest to hyperbolic manifold propagation satisfy Equations 5.3 and 5.4.

$$Re(\lambda_U) >> 1, \quad Im(\lambda_U) = 0 \tag{5.3}$$

$$Re\left(\frac{1}{\lambda_U}\right) = Re(\lambda_S) << 1, \quad Im(\lambda_S) = 0 \tag{5.4}$$

5.2.3. Eigenvector propagation, normalisation and offsetting along the orbit

The selection of the eigenvalues provides the (un)stable eigenvectors of the monodromy matrix. However, these vectors only correspond to the state at time t_0 or $t_0 + T$. To solve this, the STM for each state along the orbit can be used to map this eigenvector to the correct local orientation. This is denoted in Equation 5.5.

$$\mathbf{v}_i^S = \Phi(t_i, t_0)\mathbf{v}^S \tag{5.5}$$

The propagation of the eigenvectors along the orbit changes the length of the eigenvector. To yield a constant perturbing offset from the orbit, this local eigenvector is normalised before it is added to the state along the orbit. In this way, the normalised local eigenvector is scaled by a factor ϵ to provide a consistent offset.

$$\mathbf{X}_i^S = \mathbf{X}_i \pm \epsilon \frac{\mathbf{v}_i^S}{\|\mathbf{v}_i^S\|} = \mathbf{X}_i \pm \epsilon \hat{\mathbf{v}}_i^S \tag{5.6}$$

A non-dimensional offset of magnitude $\epsilon = 10^{-6}$ is adopted as recommended by [Gómez et al., 1991]. The logic behind this number originates from the idea that one would like this offset to be sufficiently small in order that the manifold corresponds to nearly the same Jacobi's constant as the orbit. However, the value for ϵ also should not be too small as this would significantly increase the time before untangling from the orbit and thereby accumulating error.

In addition to the magnitude of the scaling parameter ϵ, the sign of this offset is used to distinguish between the interior and exterior realm. To make a robust division, one has to determine the sign of the x-position of the eigenvector. The reason for this is that one needs to compensate when adding an eigenvector $\mathbf{v}$ with a negative x-position. This procedure ensures that the desired manifold is computed and provides for consistent file naming of the output produced in C++.

5.2.4. Integrator stopping conditions for Poincaré sections

The procedures leading up to Line 11 in Algorithm 2 have provided a set of accurate starting conditions for the propagation of the hyperbolic manifolds. This integration process is stopped at the predefined Poincaré sections ($\mathbf{U}_i \forall i = 1, \dots, 4$), referred to as the nominal case in Section 5.1.1. The translation of these spatial locations to robust numerical rules is presented in this section.

Numerical boundary conditions for $\mathbf{U}_1, \mathbf{U}_4$

As depicted in Figures 5.4 and 5.5, the sections $\mathbf{U}_1$ and $\mathbf{U}_4$ are aligned with the collinear libration points with an orthogonal orientation relative to the orbital plane. In this way, crossing of these planes becomes apparent when the y-component of the last state vector changes sign. As the trajectory might cross the xz-plane multiple times while untangling from its target orbit in either L_1 or L_2, this procedure is solely initiated after crossing of yz-plane (Eq. 5.7). This formulation of the stopping conditions has proven to be a robust and efficient solution for the exterior hyperbolic manifolds.

$$c_{\text{y-sign}} = \text{sign}(y) \quad \text{when} \quad x < 0 \tag{5.7}$$

Numerical boundary conditions for $\mathbf{U}_2, \mathbf{U}_3$

The stable and unstable interior manifolds are stopped in the nominal case at the sections $\mathbf{U}_2$ and $\mathbf{U}_3$. Located orthogonal to the x-axis at the location of the second primary (P_2), these sections are also oriented perpendicular to the orbital plane. In this way, these stopping conditions can also be indicated by a change of sign (Eq. 5.8).

$$c_{\text{x-sign}} = \text{sign}(x - (1 - \mu)) \quad \forall \quad (L_1, +\epsilon), (L_2, -\epsilon) \tag{5.8}$$

Since the sole adoption of this change of sign would imply premature termination of the exterior manifolds emanating from L_2, this rule is enriched with the heritage of the trajectory it is meant to review. In this way, this stopping condition is only applied for the interior manifolds ($f(L_p, \text{sign}(\epsilon))$.[4]

Once changes in signs of either Equation 5.7 or 5.8 imply that the propagation of the trajectory should be terminated, a procedure to reduce the overshoot is initiated. The adopted method is similar to the one expressed in the conclusions and recommendations from orbit generation in Section 4.9.2. This process of manifold generation is concluded by an extensive analysis on the validity of the results.

5.2.5. Jacobi verification and symmetry validation

Similar to the division between the periodicity verification and eigensystem validation for the process of orbit generation, the V&V procedure for manifolds is divided into two main parts:

1. Jacobi verification

2. Symmetry validation

The first technique aims to reveal any deviations in the Jacobi's constant and is employed at every integration step. This provides for a very inexpensive but nonetheless effective test on this conserved quantity. On the other hand, the symmetry validation technique is a novel procedure which aims to provide a more encompassing assessment of the validity of results. This method is employed after completion of the integration process.

Jacobi verification

The rationale behind the Jacobi verification is twofold. A deviation in this constant could either denote a mismatch between the manifold and the desired target orbit or an excessive aggregation of error on the computed trajectory. The first deficiency is most likely caused by an incorrect offset along the periodic trajectory. However, the second type of difference in Jacobi's constant is expected to be caused by two factors:

1. Significant build-up of truncation error over extended integration periods, especially in the case of the exterior manifolds emanating from L_2.

2. Insufficient order of approximation of the selected integration scheme in highly non-linear dynamic circumstances. In practise, this resembles approaching the second primary.[5]

---

[4] Please note the use of the lowercase c in both Equations 5.7 and 5.8, signifying the fact that these values remain constant over the course of integration. Whereas the value for Equation 5.8 is set at the initiation of the propagation procedure, Equation 5.7 is only determined after crossing of the yz-plane.

[5] Please note that trajectories in the close vicinity of the Moon would be heavily perturbed in a full fidelity model, due to the non-homogeneous mass distribution of this body [Rahoma and Abd El-Salam, 2014]. However, these perturbations are neglected in this approach.

A posteriori, comparison of the deviation in Jacobi constant is more complex as each trajectory is associated with a unique time vector due to the slightly different dynamic conditions encountered by the variable step-size integrator. In this way, linear interpolation has to be employed to compare deviations in Jacobi's constant per manifold in absolute normalised time.

Symmetry validation

The novel validation process presented in this research gives a more encompassing assessment of the validity of the results. The inspiration for this new technique originates from the theorem on image trajectories, and aims to exploit the powerful notions of symmetry in the ballistic case. In essence, this method compares the difference in state between the stable and unstable manifolds at the end of integration. A spatial view on this symmetric property is presented in Figure 5.2 at Poincaré sections $\mathbf{U}_i \forall i = 1, \ldots, 4$. The implementation of this procedure aims to make a significant contribution the to the trustworthiness of results in the following four ways:

1. Indication of the integrator accuracy over the manifold integration period.

2. Validation of the symmetric properties in the implemented dynamical model.

3. Validation of the symmetric behaviour of STM along the orbit in the process of propagating eigenvectors to their local orientations.

4. Validation of the normalisation and sizing of the local eigenvector offset.

The outcome of this proposed validation technique will be presented in Chapter 6. After confirmation of the effectiveness of this procedure, the need for a novel method for ballistic manifold trajectory verification has been fully addressed (Section 1.2.2). In this way, the V&V procedure ensures the mathematical precision of the numerical approximation and concludes the overview of techniques employed in the adopted approach to manifold generation.

This page is intentionally left blank.

6

Manifold generation results

This chapter is dedicated to the analysis and verification of families of hyperbolic manifolds resulting from employing the novel numerical techniques presented in Chapter 5, thereby addressing the need as expressed in Section 1.1.2. The outcome of this work will form the foundation for variations on the orientation of the Poincaré section in Chapter 7. A significant portion of this analysis is dedicated to the demanding verification and validation techniques. Apart from ensuring the validity of the approximations, these tools will help in the assessment of the performance of the integration scheme available in Tudat (RK78) in combination with a low-level programming language (C++). The first sections are dedicated to the various types of manifolds emanating from the target orbits located in L_1, and are followed by those in L_2. The sections are structured in line with Chapter 4, with the exception of the axial family due to its weak hyperbolic dynamics (Sec. 4.3 and 4.7). To provide additional insight into the sensitivity with respect to the conserved energy value, this analysis is performed on a set of discrete values of the Jacobi's constant.[1] This chapter is concluded with a review of the generated results, including recommendations for the manifold generation.

---

[1] Please note that the adopted energy level range is based on the recommendations for orbit selection presented in Section 4.9.2, in addition to the implementation of the suggestions for the numerical set-up.

6.1. L_1 **Horizontal Lyapunov**

The first set of manifolds to be computed are those emanating from the H-L family situated around L_1. As a result of the numerical procedure presented in Algorithm 2, Figure 6.1 displays the orthographic projections of the four manifolds at three equally spaced energy levels and consisting of 100 trajectories each. The axis limits are equivalent for every row, thereby providing for a consistent comparison.

L_1 Horizontal Lyapunov $\{\mathcal{W}^{S\pm}, \mathcal{W}^{U\pm}\}$ - Spatial comparison
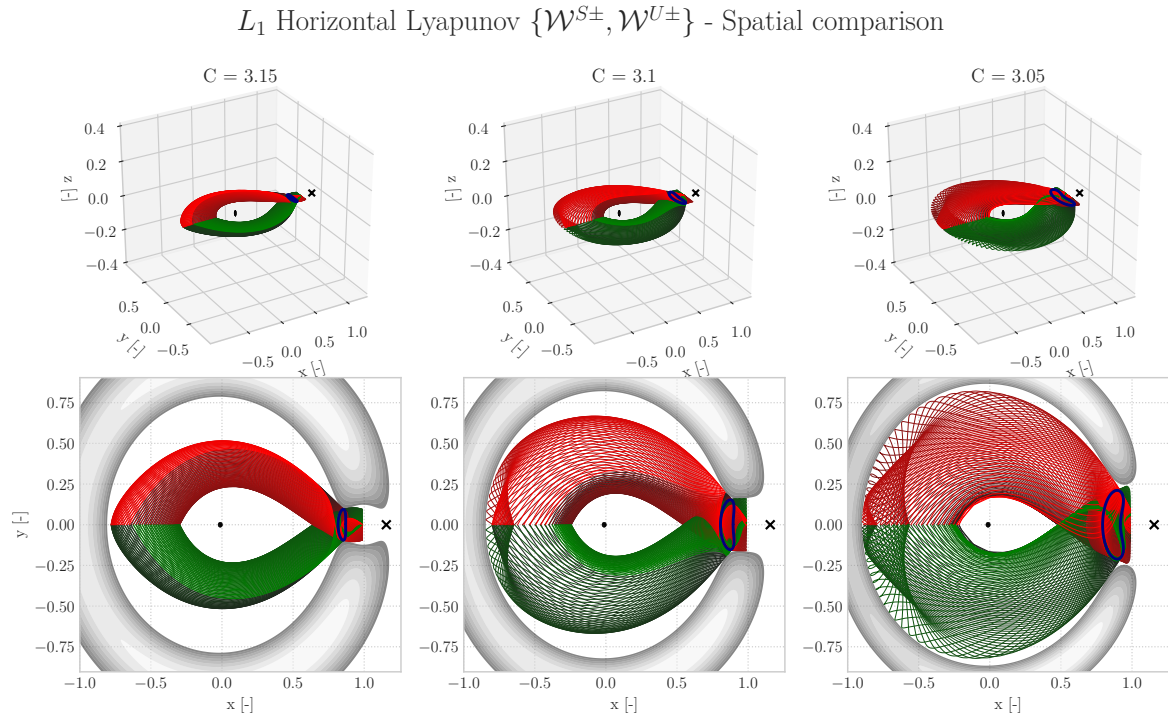
Figure 6.1: *Orthographic projection of the four (un)stable manifolds approximated by 100 trajectories which correspond to the H-L target orbit in L_1, given a set of three discrete energy levels (C = 3.05, 3.1, 3.15). The blue lines highlight the orbits from which these hyperbolic trajectories unwind. The two crosses indicate the equilibria (L_1 and L_2), of which the one denoting L_1 is covered by the set of manifold trajectories. The spheres located at $(-\mu, 0, 0)$ and $(1-\mu, 0, 0)$ represent the Earth (P_1) and Moon (P_2) at mean radius respectively. As these bodies are modelled as point masses, their shape does not influence the presented dynamics.*

Each set of manifolds presented in Figure 6.1 requires verification and validation to ensure their mathematical veracity. However, the analysis in this section is confined to a single energy level to reduce the order of the system. In this way, an energy level is selected which possesses the strongest hyperbolic characteristics and thereby is attributed with the most vocal display of the particular qualitative and quantitative traits. As recommended in Section 4.9.2, this behaviour is shown best in those members which are closest to the hyperbolic equilibrium point. This corresponds to the lower range of energy values, and hence is the reason for the selection of $C = 3.15$ for further research.

6.1.1. Local eigenvector directions

The trajectories presented in Figure 6.1 originate from a set of local normalised eigenvector offsets (Eq. 5.5).
Figure 6.2 illustrates the spatial dependence of these local orientations, in which the adopted offset has been
enlarged by a scaling factor of magnitude $20,000$ for the purpose of visualisation. The qualitative behaviour
of these eigenvector directions corresponds to those presented in [Folta et al., 2014].

L_1 Horizontal Lyapunov $\{\mathcal{W}^{S\pm}, \mathcal{W}^{U\pm}\}$ - Orientation of (un)stable modes at C = 3.15
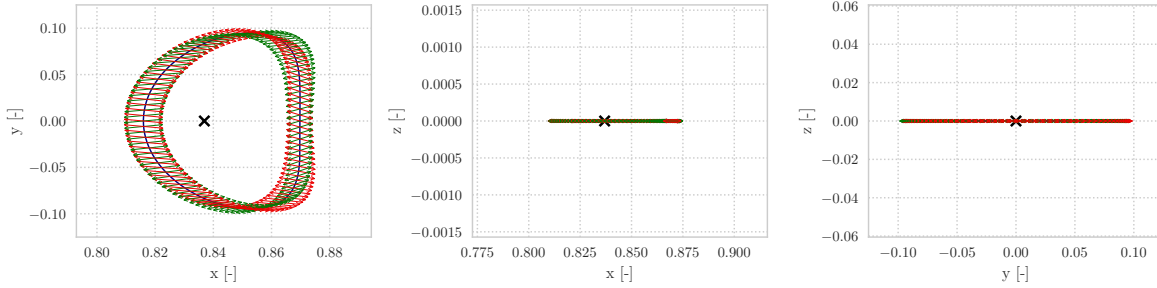
Figure 6.2: *Stable and unstable mode directions related to an horizontal Lyapunov orbit (blue) at C = 3.15. The eigenvector offset has been
magnified by a factor 20,000 and denotes the orientation with respect to the stable (green) and unstable (red) subspace. The cross displays
the location of the collinear equilibrium L_1 and serves as a point of reference.*

6.1.2. Jacobi's integral verification

To verify the numerical veracity of the hyperbolic manifold trajectories which unwind from the H-L family in
L_1, Figure 6.3 shows the study on Jacobi's integral. As described in Section 5.2.5, the 100 uniquely spaced time
vectors associated with the individual manifold trajectories require the employment of linear interpolation
to provide an all-encompassing overview.

L_1 Horizontal Lyapunov $\{\mathcal{W}^{S\pm}, \mathcal{W}^{U\pm}\}$ - Jacobi verification at C = 3.15
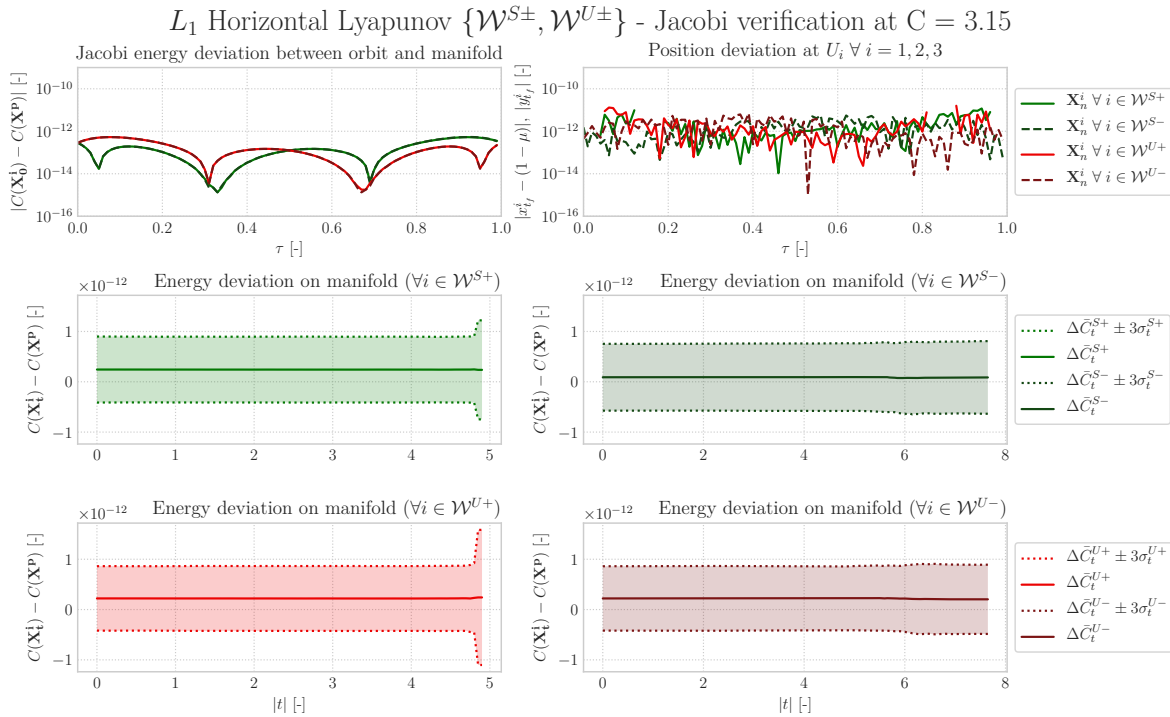
Figure 6.3: *Jacobi verification for all individual trajectories in the four sets of hyperbolic manifolds emanating from the H-L orbit in L_1.
From top to bottom, from left to right: difference in Jacobi's constant between the orbit and the corresponding first state on the manifold
(Fig. 6.2), Euclidean distance between the last integration step and the desired stopping conditions (Eq. 5.7 and 5.8), and the difference
in average local energy along the four manifolds with respect to the target orbit. Whereas the first two evaluations are mapped out with
respect to the on-orbit phase, the latter are presented as a function of absolute normalised time. The confidence bands surrounding the
deviation in C include 99.73% of all observations.*

6.1.3. Numerical validation through symmetry

In addition to the Jacobi verification procedure, the results are validated through the analysis of the symmetries as presented in Figure 6.4.
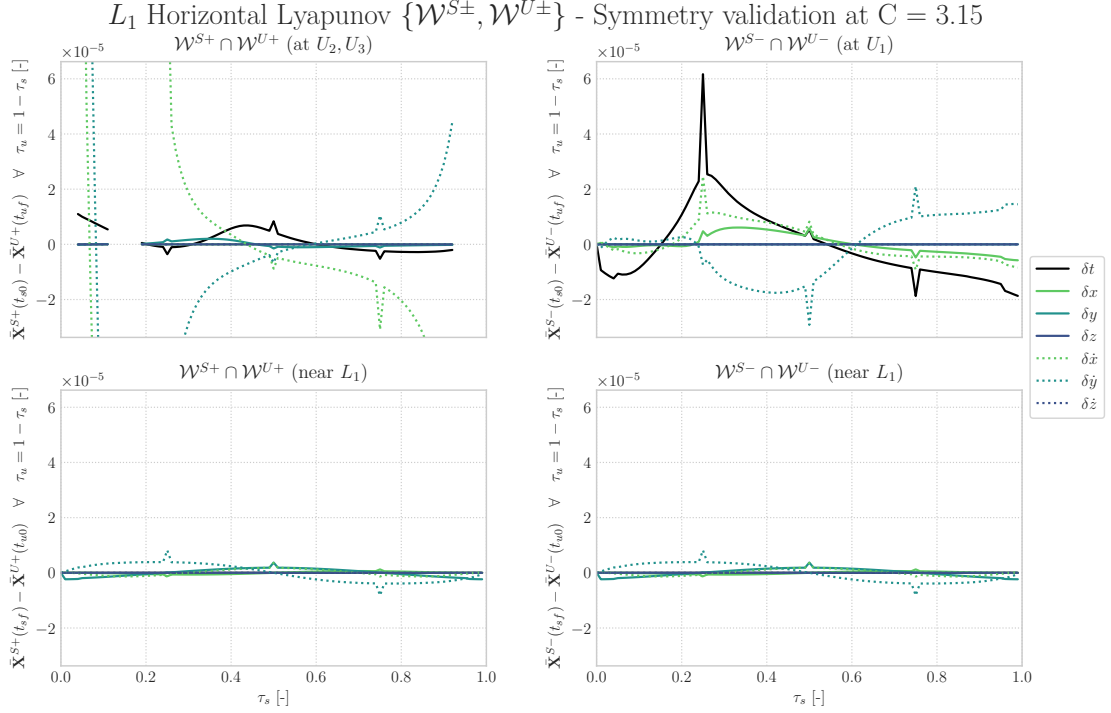
Figure 6.4: *Analysis of the pairs of symmetric (un)stable manifold trajectories associated with the H-L orbit in L_1, based on the theorem of image trajectories with respect to the x-axis (Eq. 2.6 and 2.7). The first column portrays the individual components of the discrepancy in state at the start and end of propagation, corresponding to an addition of local eigenvector. The right column adheres to the same format in case of a negative offset. Discontinuities in state discrepancies are caused by premature termination of propagation, due to violating the threshold set for the accuracy of Jacobi's constant.*

6.1.4. Discussion of results

When analysing the sets of four manifolds emanating from H-L target orbits in L_1 consisting of 100 trajectories each, many peculiarities arise. The time until approach of the nominal stopping conditions ranges from $T_{\mathcal{W}^+} = 4.9$ for the interior manifold to $T_{\mathcal{W}^-} = 7.65$ for the exterior one. The equivalent dimensional units are 21.31 and 33.26 days respectively. This disparity is expected due to the difference in distance travelled, however it does also denote that a significant portion of time is spent in untangling from the target orbit. For increasing energy levels, one can observe that the manifolds do not retain the shape of the target orbit (Fig. 6.1). Characteristically, the trajectories fan out and start to bounce off the zero-velocity surface as described in [Wakker, 2015]. This creates concentrations of trajectories within the manifold near $\mathbf{U}_4$ and provides for an efficient transfer from LEO due to close approach of the stable manifold [Alessi et al., 2010]. Similar behaviour can be observed in the planar Sun-Jupiter case as presented in [Onozaki and Yoshimura, 2014].

The (un)stable manifolds of planar Lyapunov are two-dimensional and reveal an abundance of symmetries in Figures 6.1 through 6.4 [Canalias et al., 2006]. Interestingly, the error for all manifolds is bounded by identical margins at the start, but diverge rapidly near the end for the interior ones (Fig. 6.3). When comparing this phenomenon to the symmetry validation (Fig. 6.4), one can see that a significant portion of trajectories is discontinued due to exceeding the threshold set for deviation in Jacobi's constant. This fact remains unnoticed from the orthographic projection in 6.1. The significant build-up of error is most likely due to the high non-linear dynamics close to the point mass, thereby giving rise to an increase in truncation error. The non-zero deviation in C at $t = 0$ depicts the offset with respect to the orbit. This is also shown in the symmetric top-left graph in Figure 6.3, which adheres to the relation shown in Equation 5.1. Symmetry validation suggests that the deviation between symmetric states increases during integration. However, this discrepancy is limited to $\sim 10^{-5}$ and strongly suggests a valid implementation of symmetrical dynamics together with the symmetric propagation of local eigenvectors (Fig. 6.2).

6.2. L_1 **Southern halo**

The second set of manifolds to be computed are those emanating from the halo family situated around L_1. As a result of the numerical procedure presented in Algorithm 2, Figure 6.5 displays the orthographic projections of the four manifolds at three equally spaced energy levels and consisting of 100 trajectories each.
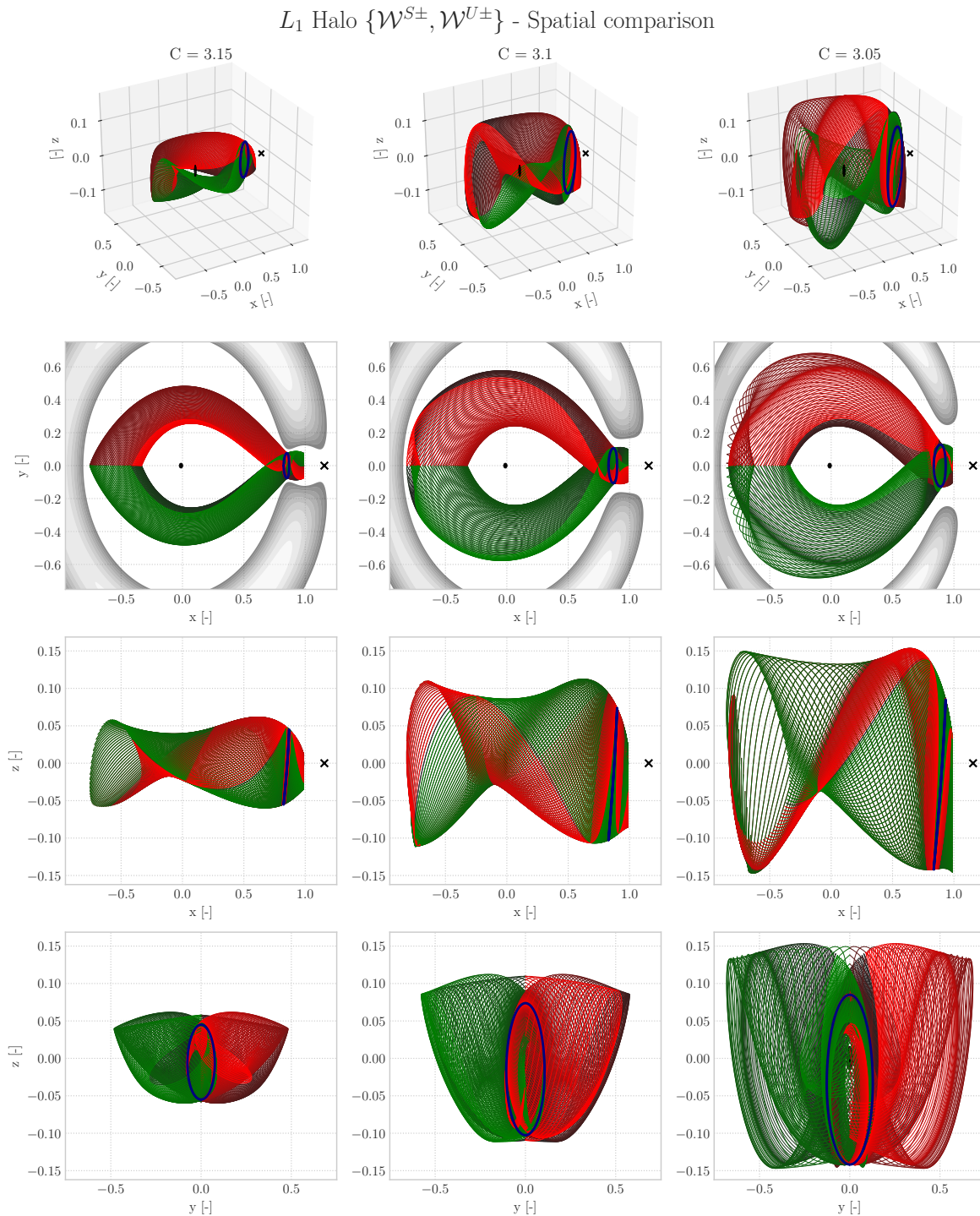
Figure 6.5: *Orthographic projection of the four (un)stable manifolds approximated by 100 trajectories which correspond to the halo target orbit in L_1, given a set of three discrete energy levels (C = 3.05, 3.1, 3.15). The blue lines highlight the orbits from which these hyperbolic trajectories unwind. The two crosses indicate the equilibria (L_1 and L_2), of which the one denoting L_1 is covered by the set of manifold trajectories. The spheres located at $(-\mu, 0, 0)$ and $(1 - \mu, 0, 0)$ represent the Earth (P_1) and Moon (P_2) at mean radius respectively. As these bodies are modelled as point masses, their shape does not influence the presented dynamics.*

6.2.1. Local eigenvector directions

The trajectories presented in Figure 6.5 originate from a set of local normalised eigenvector offsets (Eq. 5.5). Figure 6.6 illustrates the spatial dependence of these local orientations, in which the adopted offset has been enlarged by a scaling factor of magnitude 20,000 for the purpose of visualisation.
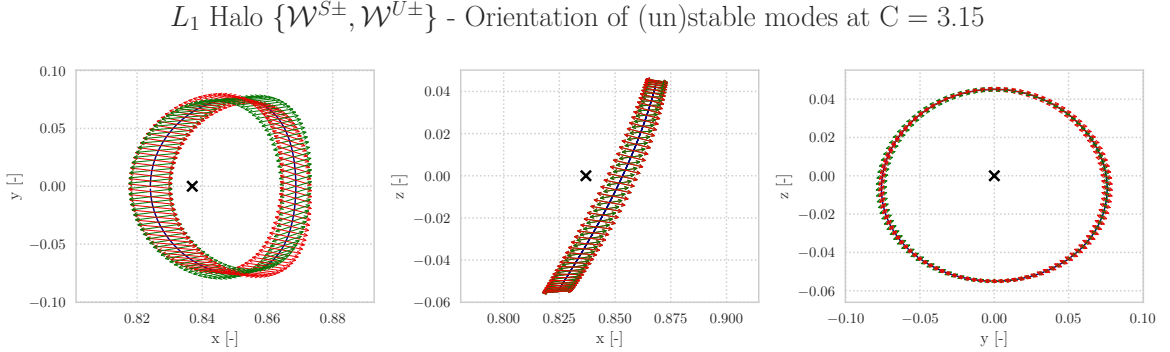
Figure 6.6: *Stable and unstable mode directions related to an halo orbit (blue) at C = 3.15. The eigenvector offset has been magnified by a factor 20,000 and denotes the orientation with respect to the stable (green) and unstable (red) subspace. The cross displays the location of the collinear equilibrium L_1 and serves as a point of reference.*

6.2.2. Jacobi integral verification

To verify the numerical veracity of the hyperbolic manifold trajectories which unwind from the halo family in L_1, Figure 6.7 shows the study on Jacobi's integral. As described in Section 5.2.5, the 100 uniquely spaced time vectors associated with the individual manifold trajectories require the employment of linear interpolation to provide an all-encompassing overview.
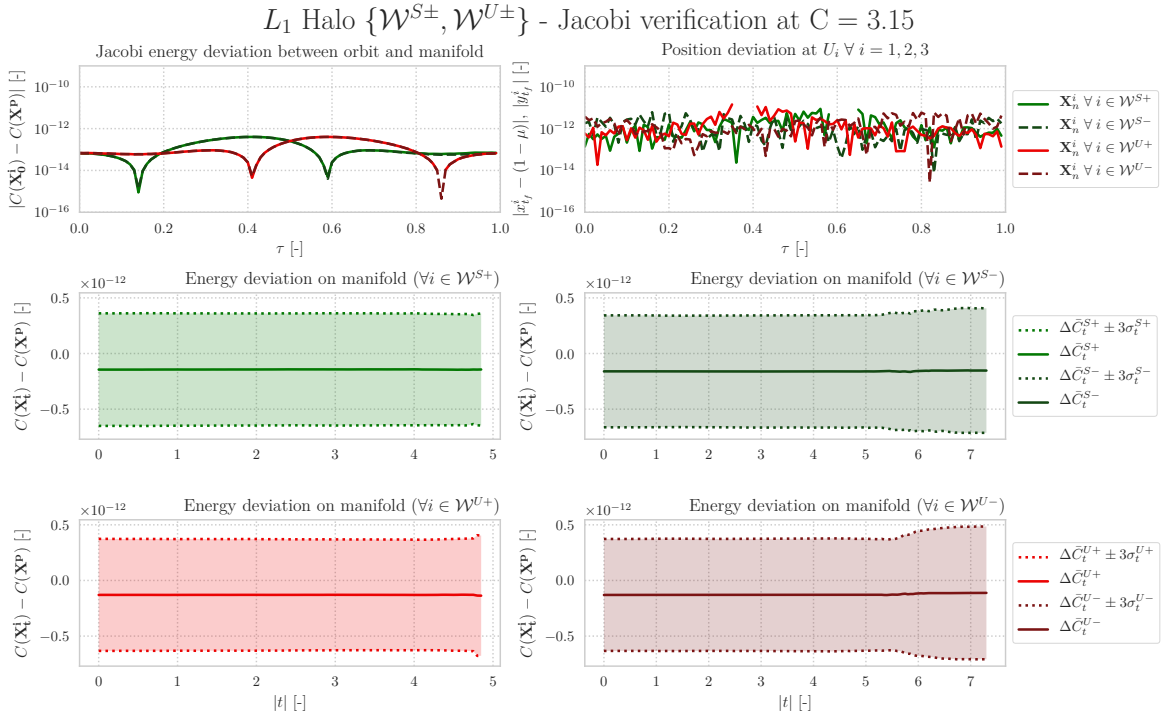
Figure 6.7: *Jacobi verification for all individual trajectories in the four sets of hyperbolic manifolds emanating from the halo orbit in L_1. From top to bottom, from left to right: difference in Jacobi's constant between the orbit and the corresponding first state on the manifold (Fig. 6.6), position deviation near stopping conditions (Eq. 5.7 and 5.8), and the difference in average local energy along the four manifolds with respect to the target orbit. Whereas the first two evaluations are mapped out with respect to the on-orbit phase, the latter are presented as a function of absolute normalised time. The confidence bands surrounding the deviation in C along the orbit include 99.73% of all observations.*

6.2.3. Numerical validation through symmetry

In addition to the Jacobi verification procedure, the results are validated through the analysis of the symmetries as presented in Figure 6.8.
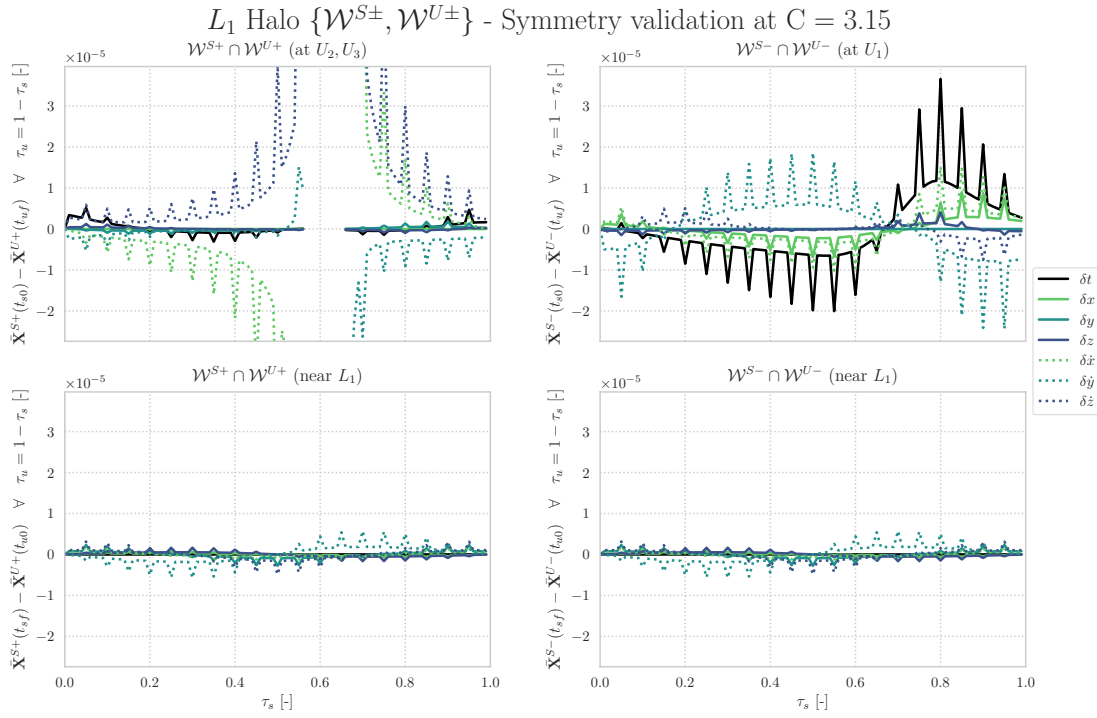
Figure 6.8: *Analysis of the pairs of symmetric (un)stable manifold trajectories associated with the halo orbit in L_1, based on the theorem of image trajectories with respect to the x-axis (Eq. 2.6 and 2.7). The first column portrays the individual components of the discrepancy in state at the start and end of propagation, corresponding to an addition of local eigenvector. The right column adheres to the same format in case of a negative offset. Discontinuities in state discrepancies are caused by premature termination of propagation, due to violating the threshold set for the accuracy of Jacobi's constant.*

6.2.4. Discussion of results

When analysing the sets of four manifolds emanating from the halo target orbits in L_1 consisting of 100 trajectories each, many peculiarities arise. The time until approach of the nominal stopping conditions ranges from $T_{\mathcal{W}^+} = 4.85$ for the interior manifold to $T_{\mathcal{W}^-} = 7.30$ for the exterior one. The equivalent dimensional units are 21.09 and 31.74 days respectively. This disparity is very similar to the behaviour observed for the H-L family in Section 6.1.4, as well as the fact that also these manifolds do not retain the shape of the target orbit (Fig. 6.1). This geometrical aspect is in strong agreement with the results presented in [Howell et al., 2006]. In addition, the notion is supported that "the stable manifold associated with the halo orbits around L_1 or L_2 does not approach the Earth" [Mingotti et al., 2007].

In a similar fashion to the (un)stable manifolds emanating from halo target orbits, Figures 6.5 through 6.8 reveal many symmetries. In terms of accuracy, a clear build-up of truncation error over time can be observed for the stable and unstable exterior manifolds in Figure 6.7. However, the magnitude of this deviation is consistently lower than the one corresponding to H-L in L_1 (Fig. 6.3). When comparing this phenomenon to the symmetry validation (Fig. 6.8), one can see that a narrow band of trajectories is prematurely terminated around $\tau_s = 0.6$ due to exceeding the threshold set for deviation in Jacobi's constant. This discontinuity is expected due to the gradual divergence between the near-symmetric states in Figure 6.8, denoting a sharp rise in highly non-linear accelerations. Symmetry validation suggests that the deviation between symmetric states increases during integration. However, this discrepancy is limited to $\sim 10^{-5}$ and strongly suggests a valid implementation of symmetrical dynamics together with the symmetric propagation of local eigenvectors (Fig. 6.6).

6.3. L_1 **Vertical Lyapunov**

The third and final set of manifolds computed in L_1 are those emanating from the V-L family. As a result of the numerical procedure presented in Algorithm 2, Figure 6.9 displays the orthographic projections of the four manifolds at three equally spaced energy levels and consisting of 100 trajectories each.
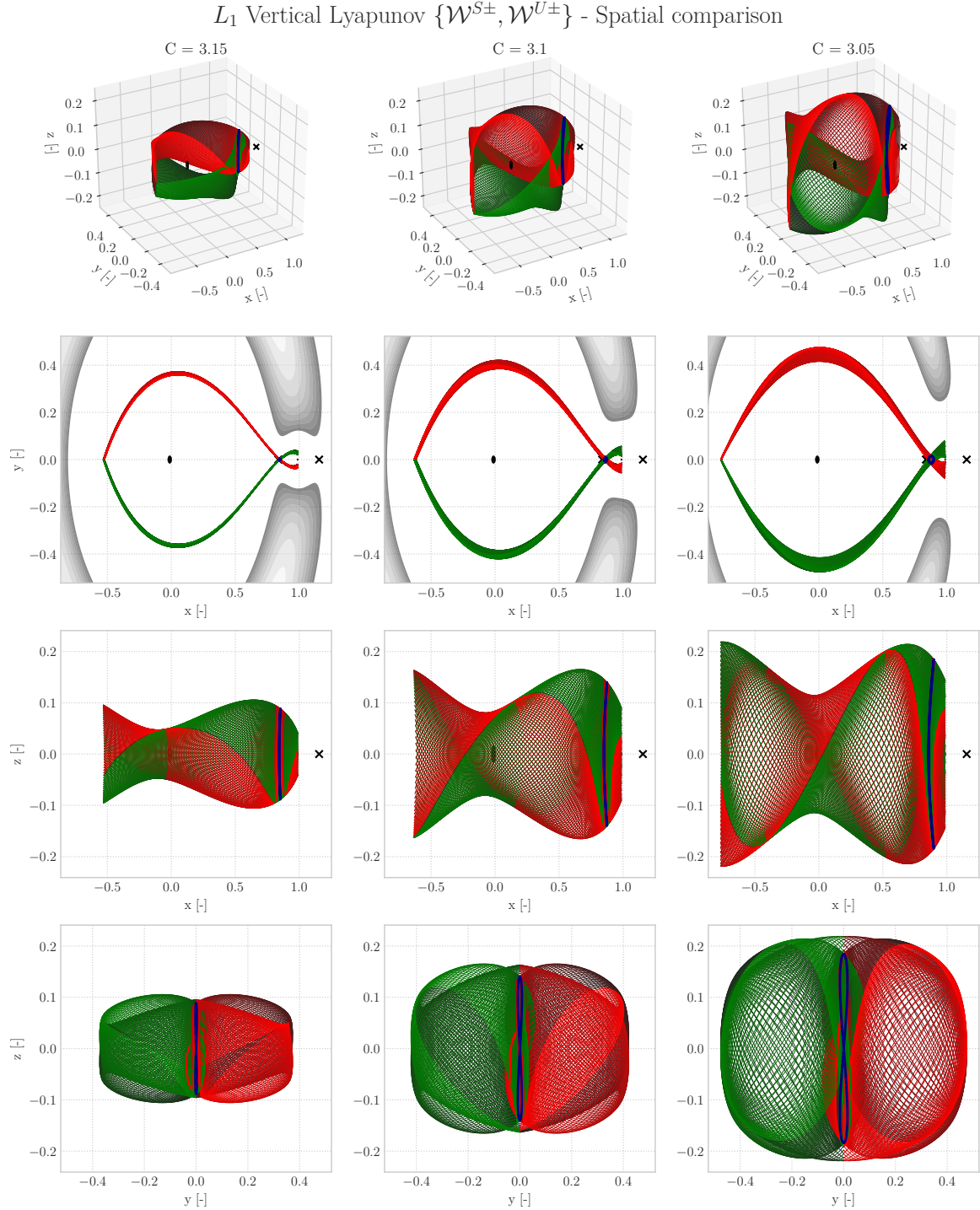
Figure 6.9: *Orthographic projection of the four (un)stable manifolds approximated by 100 trajectories which correspond to the V-L target orbit in L_1, given a set of three discrete energy levels (C = 3.05, 3.1, 3.15). The blue lines highlight the orbits from which these hyperbolic trajectories unwind. The two crosses indicate the equilibria (L_1 and L_2), of which the one denoting L_1 is covered by the set of manifold trajectories. The spheres located at $(-\mu, 0, 0)$ and $(1 - \mu, 0, 0)$ represent the Earth (P_1) and Moon (P_2) at mean radius respectively. As these bodies are modelled as point masses, their shape does not influence the presented dynamics.*

6.3.1. Local eigenvector directions

The trajectories presented in Figure 6.9 originate from a set of local normalised eigenvector offsets (Eq. 5.5). Figure 6.10 illustrates the spatial dependence of these local orientations, in which the adopted offset has been enlarged by a scaling factor of magnitude $4,000$ for the purpose of visualisation.

L_1 Vertical Lyapunov $\{\mathcal{W}^{S\pm}, \mathcal{W}^{U\pm}\}$ - Orientation of (un)stable modes at C $= 3.15$
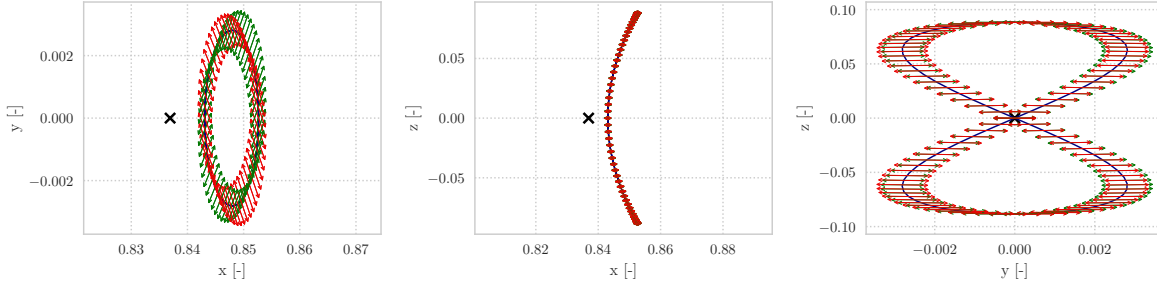
Figure 6.10: *Stable and unstable mode directions related to a vertical Lyapunov orbit (blue) at C $= 3.15$. The eigenvector offset has been magnified by a factor 4,000 and denotes the orientation with respect to the stable (green) and unstable (red) subspace. The cross displays the location of the collinear equilibrium L_1 and serves as a point of reference.*

6.3.2. Jacobi integral verification

To verify the numerical veracity of the hyperbolic manifold trajectories which unwind from the V-L family in L_1, Figure 6.11 shows the study on Jacobi's integral. As described in Section 5.2.5, the 100 uniquely spaced time vectors associated with the individual manifold trajectories require the employment of linear interpolation to provide an all-encompassing overview.

L_1 Vertical Lyapunov $\{\mathcal{W}^{S\pm}, \mathcal{W}^{U\pm}\}$ - Jacobi verification at C $= 3.15$
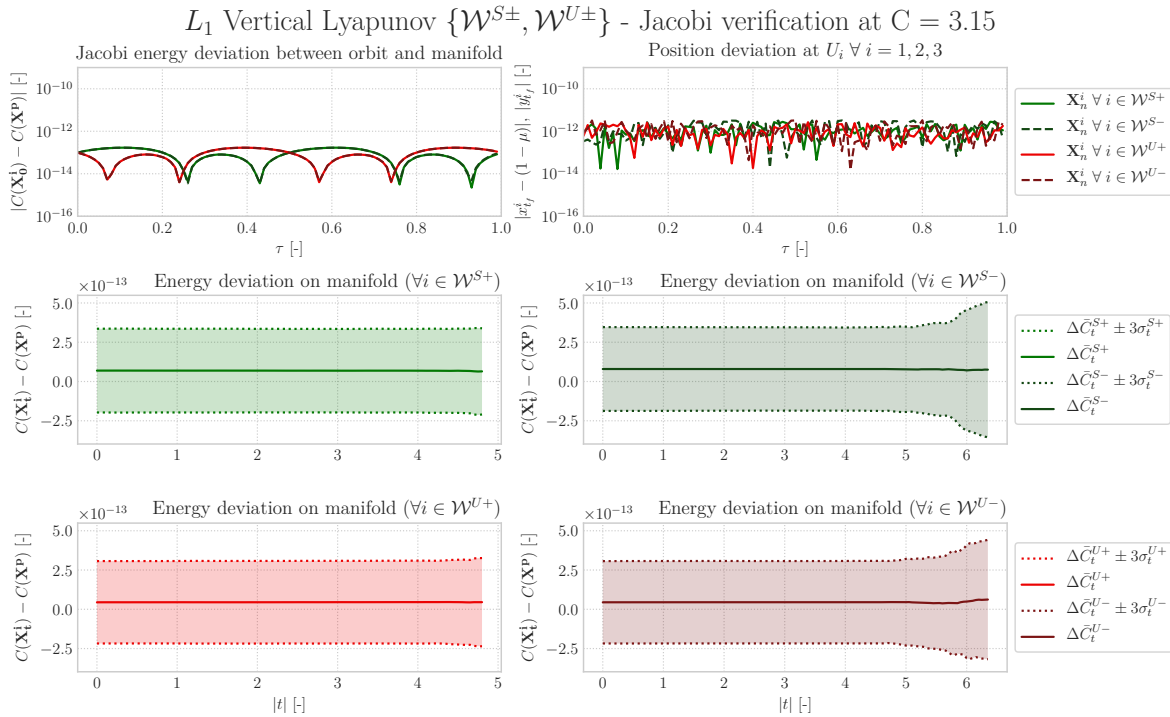
Figure 6.11: *Jacobi verification for all individual trajectories in the four sets of hyperbolic manifolds emanating from the V-L orbit in L_1. From top to bottom, from left to right: difference in Jacobi's constant between the orbit and the corresponding first state on the manifold (Fig. 6.10), position deviation near stopping conditions (Eq. 5.7 and 5.8), and the difference in average local energy along the four manifolds with respect to the target orbit. Whereas the first two evaluations are mapped out with respect to the on-orbit phase, the latter are presented as a function of absolute normalised time. The confidence bands surrounding the deviation in C along the orbit include 99.73% of all observations.*

6.3.3. Numerical validation through symmetry

In addition to the Jacobi verification procedure, the results are validated through the analysis of the symmetries as presented in Figure 6.12.
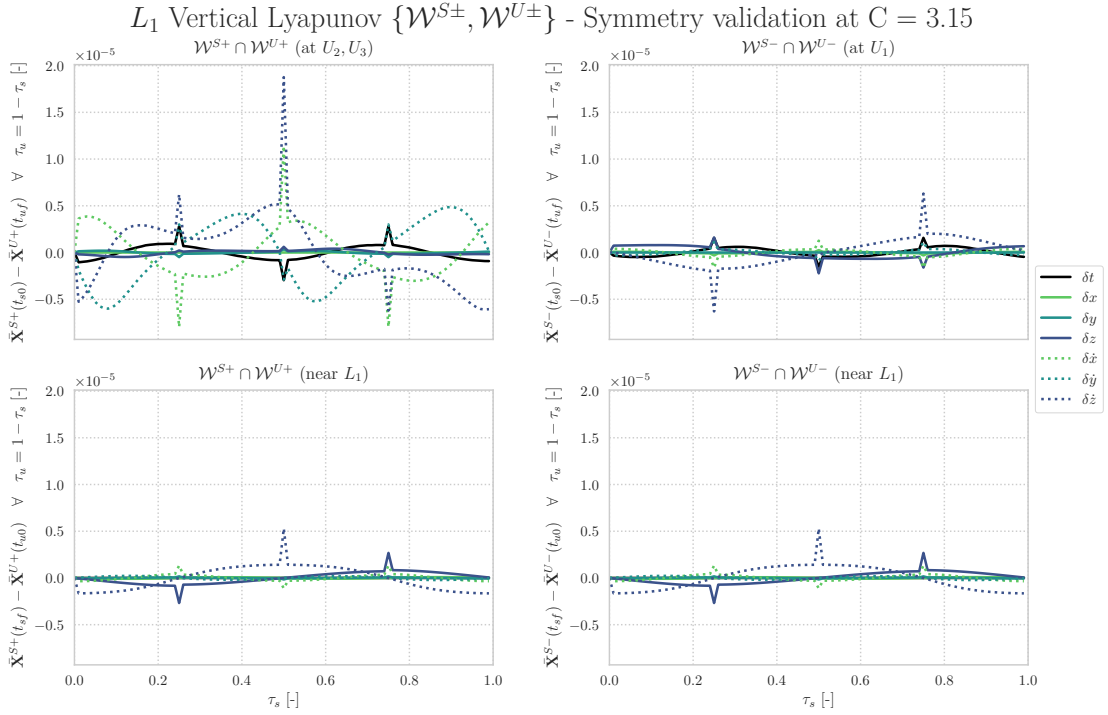
Figure 6.12: *Analysis of the pairs of symmetric (un)stable manifold trajectories associated with the V-L orbit in L_1, based on the theorem of image trajectories with respect to the x-axis (Eq. 2.6 and 2.7). The first column portrays the individual components of the discrepancy in state at the start and end of propagation, corresponding to an addition of local eigenvector. The right column adheres to the same format in case of a negative offset.*

6.3.4. Discussion of results

The hyperbolic manifolds associated with the V-L family show distinctively different behaviour than those observed for the H-L and halo types of target orbits. First and most importantly, the (un)stable manifolds retain the same structure over time, even at significant distance from primaries. This global stability property complies with the observations in [Archambeau et al., 2011], who adds that "such a stability property does not hold for halo orbits." Whereas the tubes corresponding to the halo family "behave in a chaotic way in large time," the "regular structure of invariant manifolds of eight-shaped Lissajous orbits is conserved even after a large integration time." This organised structure is well supported by the three orthographic projections at various energy levels in Figure 6.9. One possible drawback of this organised behaviour is that these tubes do not approach Earth close enough for an efficient direct departure. On the other hand, this stability does allow for robust prediction of behaviour over significant integration periods.

The maximum time until approach of the nominal stopping conditions for the four sets of 100 trajectories is the lowest across all families and ranges from $T_{\mathcal{W}^+} = 4.80$ for the interior manifold to $T_{\mathcal{W}^-} = 6.35$ for the exterior one. These dynamics are expected, based on the most powerful hyperbolic behaviour that this family possesses as concluded in Section 4.9.2. The equivalent dimensional units are 20.87 and 27.61 days respectively. The minimal time to unwind and global stability properties are accompanied with a very low error in Jacobi (Fig. 6.11) and symmetry (Fig. 6.12).

Another peculiar trait for this family is displayed in Figure 6.9 at the location of the first Poincaré section. The acute angle between the stable and unstable manifolds is persistent across the range of discrete energy levels, and suggests that a homoclinic connection does not exist for a single revolution around the first primary in the framework of nominal stopping conditions. An extended exploration on the existence of possible natural connections is presented in Chapter 7.

6.4. L_2 **Horizontal Lyapunov**

The first set of manifolds to be computed in L_2 are those emanating from the H-L family. As a result of the numerical procedure presented in Algorithm 2, Figure 6.13 displays the orthographic projections of the four manifolds at three equally spaced energy levels and consisting of 100 trajectories each. The axis limits are equivalent for every row, thereby providing for a consistent comparison.
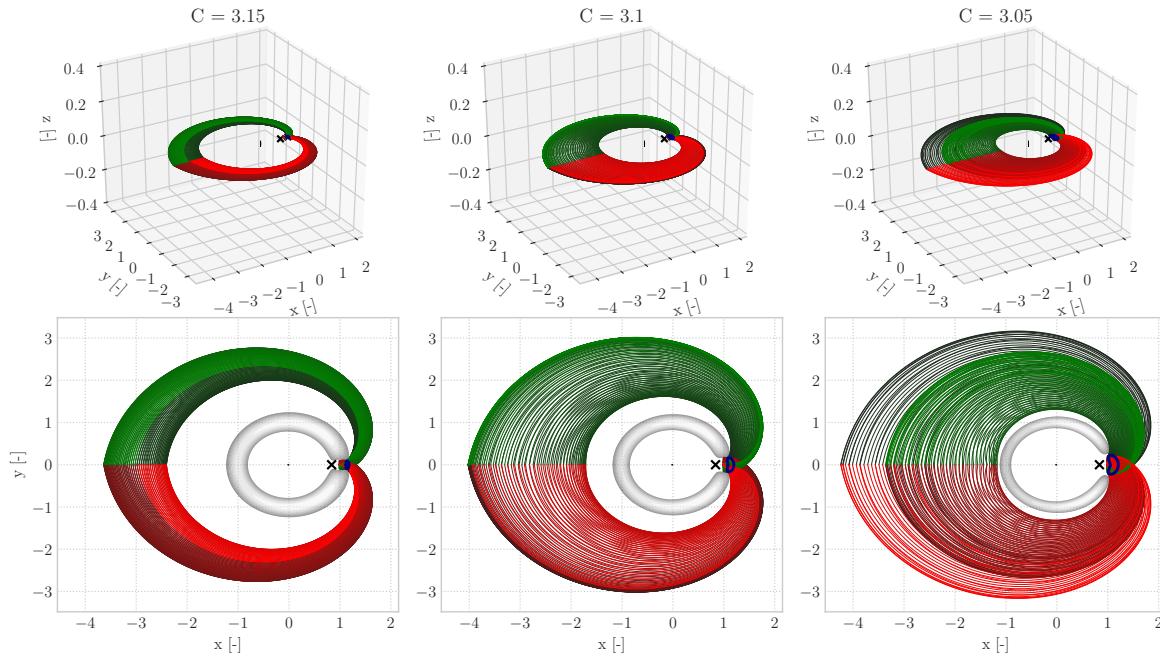
Figure 6.13: Orthographic projection of the four (un)stable manifolds approximated by 100 trajectories which correspond to the H-L target orbit in L_2, given a set of three discrete energy levels ($C = 3.05, 3.1, 3.15$). The blue lines highlight the orbits from which these hyperbolic trajectories unwind. The two crosses indicate the equilibria (L_1 and L_2), of which the one denoting L_2 is covered by the set of manifold trajectories. The spheres located at $(-\mu, 0, 0)$ and $(1 - \mu, 0, 0)$ represent the Earth (P_1) and Moon (P_2) at mean radius respectively. As these bodies are modelled as point masses, their shape does not influence the presented dynamics.

Each set of manifolds presented in Figure 6.13 requires verification and validation to ensure their mathematical veracity. However, the analysis in this section is confined to a single energy level to reduce the order of the system. In this way, an energy level is selected which possesses the strongest hyperbolic characteristics and thereby is attributed with the most vocal display of the particular qualitative and quantitative traits. As recommended in Section 4.9.2, this behaviour is shown best in those members which are closest to the hyperbolic equilibrium point. This corresponds to the lower regiment of energy values, and hence is the reason for the selection of $C = 3.15$ for further research.

6.4.1. Local eigenvector directions

The trajectories presented in Figure 6.13 originate from a set of local normalised eigenvector offsets (Eq. 5.5). Figure 6.14 illustrates the spatial dependence of these local orientations, in which the adopted offset has been enlarged by a scaling factor of magnitude 20,000 for the purpose of visualisation. The qualitative behaviour of these eigenvector directions corresponds to those presented in [Folta et al., 2014].
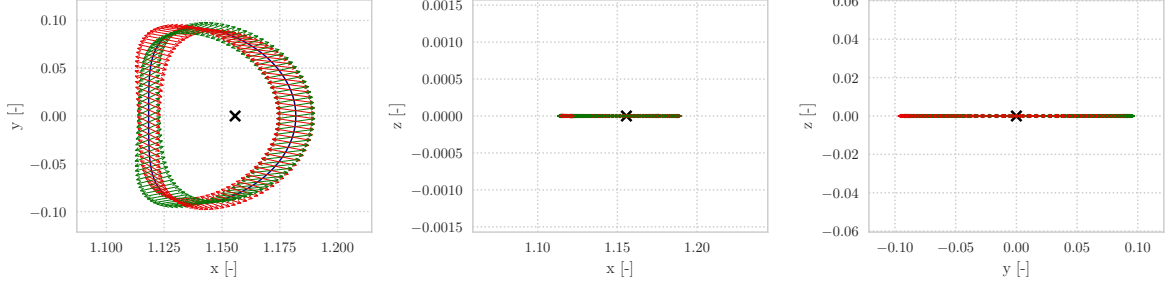
Figure 6.14: *Stable and unstable mode directions related to an horizontal Lyapunov orbit (blue) at C = 3.15. The eigenvector offset has been magnified by a factor 20,000 and denotes the orientation with respect to the stable (green) and unstable (red) subspace. The cross displays the location of the collinear equilibrium L_2 and serves as a point of reference.*

6.4.2. Jacobi integral verification

To verify the numerical veracity of the hyperbolic manifold trajectories which unwind from the H-L family in L_2, Figure 6.15 shows the study on Jacobi's integral. As described in Section 5.2.5, the 100 uniquely spaced time vectors associated with the individual manifold trajectories require the employment of linear interpolation to provide an all-encompassing overview.
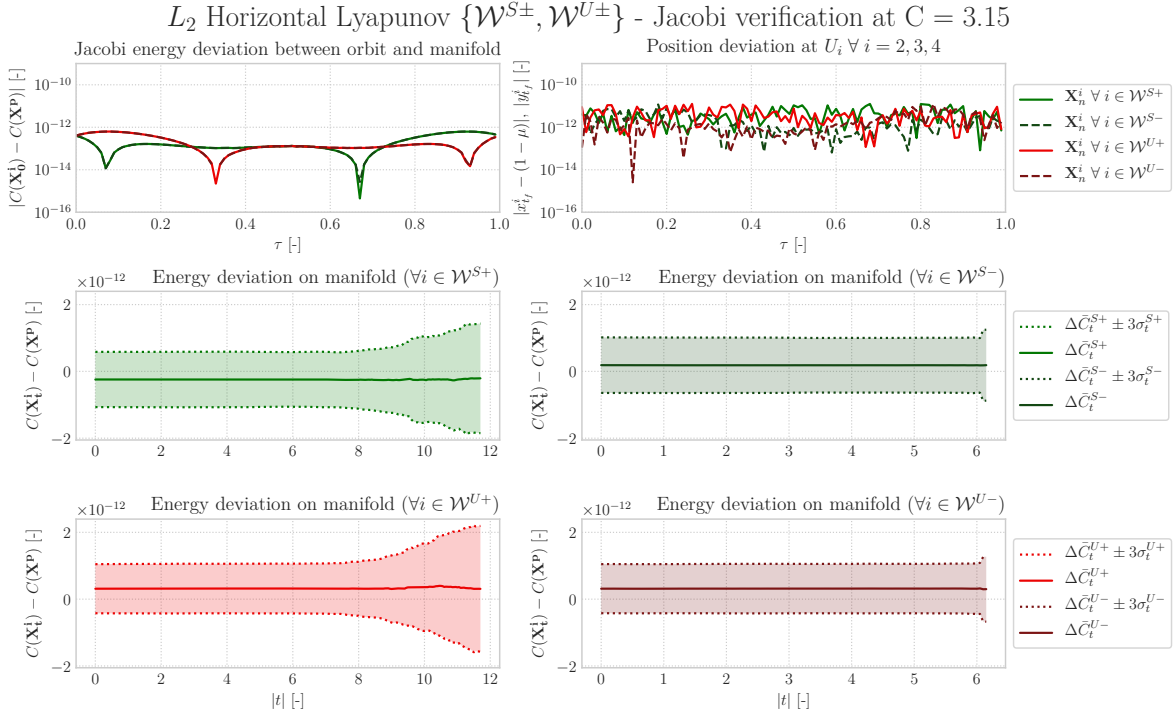
Figure 6.15: *Jacobi verification for all individual trajectories in the four sets of hyperbolic manifolds emanating from the H-L orbit in L_2. From top to bottom, from left to right: difference in Jacobi's constant between the orbit and the corresponding first state on the manifold (Fig. 6.14), position deviation near stopping conditions (Eq. 5.7 and 5.8), and the difference in average local energy along the four manifolds with respect to the target orbit. Whereas the first two evaluations are mapped out with respect to the on-orbit phase, the latter are presented as a function of absolute normalised time. The confidence bands surrounding the deviation in C along the orbit include 99.73% of all observations.*

6.4.3. Numerical validation through symmetry

In addition to the Jacobi verification procedure, the results are validated through the analysis of the symmetries as presented in Figure 6.16.
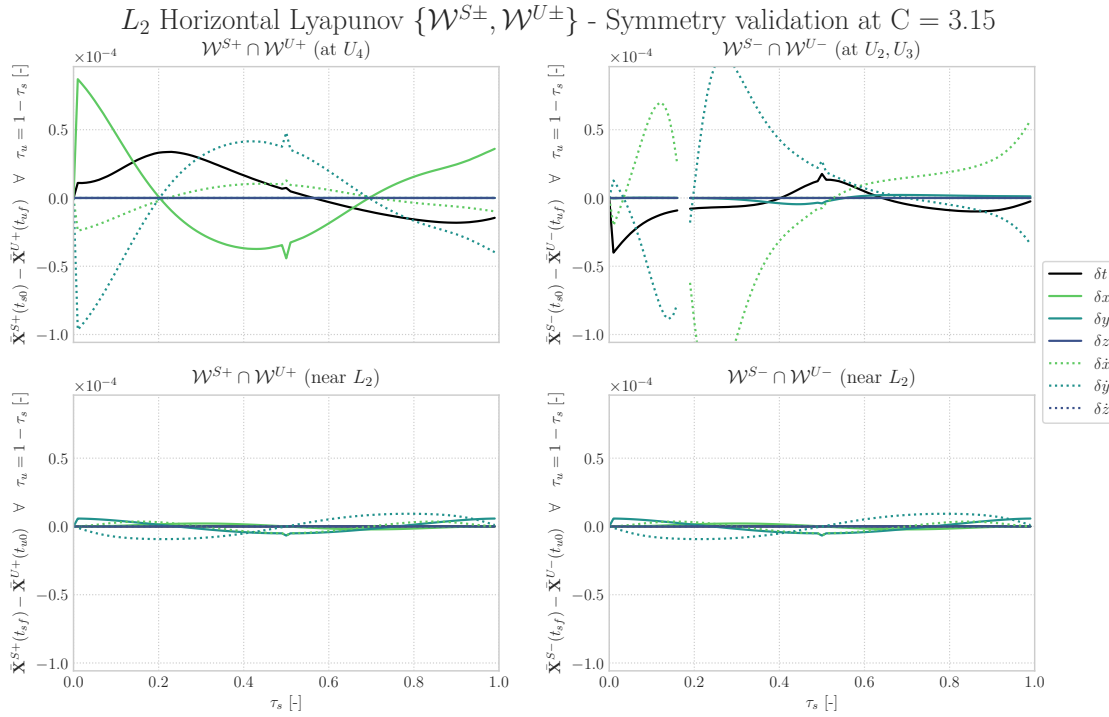
Figure 6.16: *Analysis of the pairs of symmetric (un)stable manifold trajectories associated with the H-L orbit in L_2, based on the theorem of image trajectories with respect to the x-axis (Eq. 2.6 and 2.7). The first column portrays the individual components of the discrepancy in state at the start and end of propagation, corresponding to an addition of local eigenvector. The right column adheres to the same format in case of a negative offset. Discontinuities in state discrepancies are caused by premature termination of propagation, due to violating the threshold set for the accuracy of Jacobi's constant.*

6.4.4. Discussion of results

In the comparison of the sets of four manifolds emanating from H-L target orbits in L_2 to its relative in L_1, many similarities can be observed. The fanning out of trajectories has increased over extended integration periods (Fig. 6.13), and spans a horizontal range at $\mathbf{U}_4$ of $C = \{3.15, 3.1, 3.05\} \mapsto \Delta x = \{1.25, 2.35, 3.13\}$. In dimensional units, these widths correspond to $\{480500, 903340, 1203172\}$ km respectively. For the highest orbital energy, one can observe that the orientation at $\mathbf{U}_4$ of stable and unstable trajectories changes from acute (left), to parallel (center), to obtuse (right). This behaviour suggests the existence of parallel velocity vectors at an identical spatial location, which could denote the presence of natural connections.[2]

The time until approach of the nominal stopping conditions has significantly increased with respect to L_1 and range from $T_{\mathscr{W}^-} = 6.15$ for the interior manifold to $T_{\mathscr{W}^+} = 11.70$ for the exterior one. The equivalent dimensional units are 26.74 and 50.88 days respectively. This disparity is expected due to the difference in distance travelled, however it does also denote that a significant portion of time is spent in untangling from the target orbit. The increased integration period is associated with the gradual increase in energy deviation along the exterior trajectories (Fig. 6.15).

Symmetry validation of the four sets of hyperbolic trajectories in Figure 6.16 implies the discontinuity of a set of orbits in the interior manifolds. In a similar way to the behaviour observed in Section 6.1.4, these approximations have been prematurely terminated due to exceeding the threshold set for deviation in Jacobi's constant. This fact remains unnoticed from the orthographic projection in 6.1 and is most likely due to the high non-linear dynamics close to the point mass, thereby giving rise to an increase in truncation error.

---

[2]Please note that the alignment in position of the stable and unstable members is attributed to the equal spacing of offset nodes as displayed in Figure 6.14.

6.5. L_2 **Southern halo**

The second set of manifolds to be computed around L_2 are those emanating from the halo family. As a result of the numerical procedure presented in Algorithm 2, Figure 6.17 displays the orthographic projections of the four manifolds at three equally spaced energy levels and consisting of 100 trajectories each.
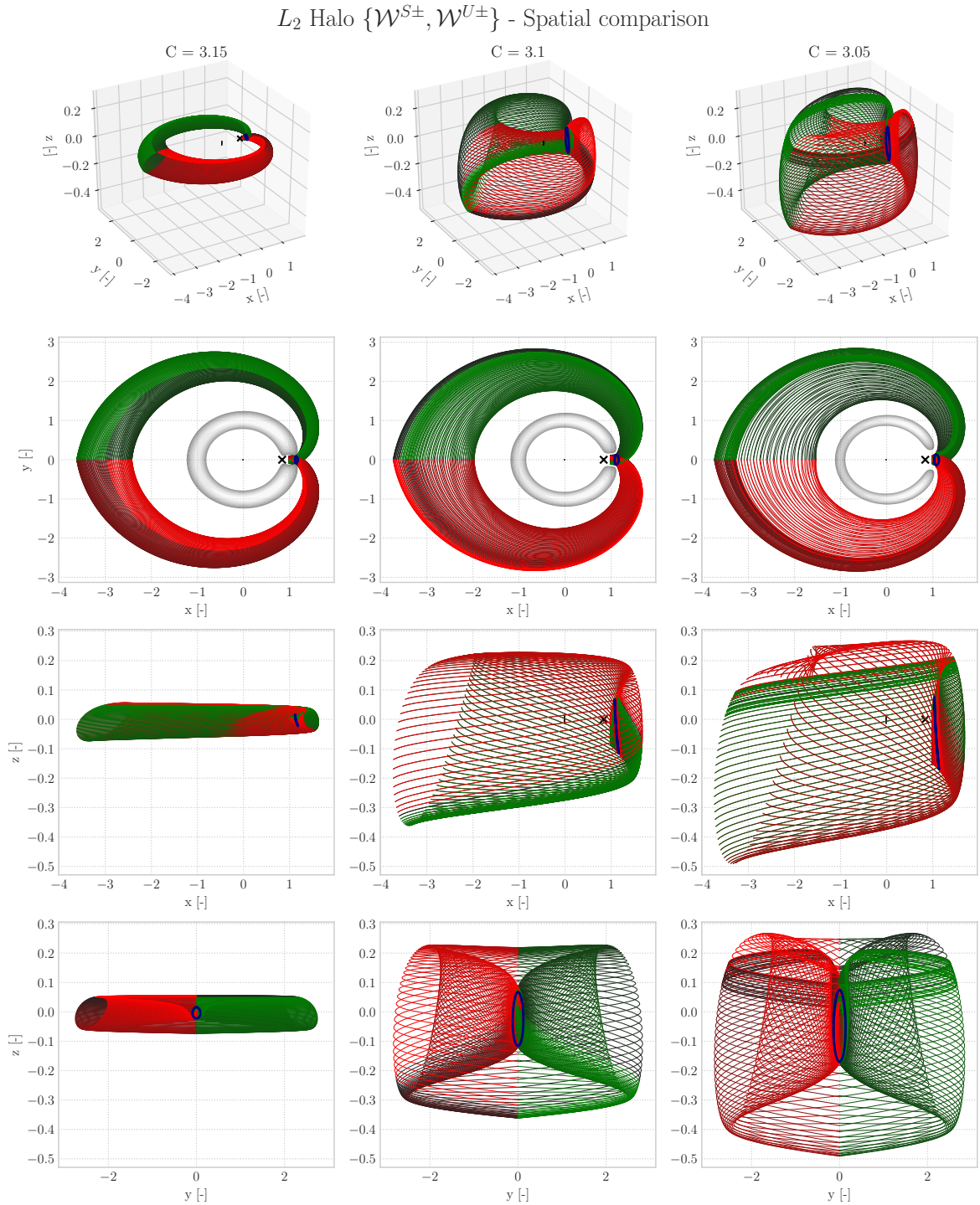

Figure 6.17: *Orthographic projection of the four (un)stable manifolds approximated by 100 trajectories which correspond to the halo target orbit in L_2, given a set of three discrete energy levels (C = 3.05, 3.1, 3.15). The blue lines highlight the orbits from which these hyperbolic trajectories unwind. The two crosses indicate the equilibria (L_1 and L_2), of which the one denoting L_2 is covered by the set of manifold trajectories. The spheres located at $(-\mu, 0, 0)$ and $(1 - \mu, 0, 0)$ represent the Earth (P_1) and Moon (P_2) at mean radius respectively. As these bodies are modelled as point masses, their shape does not influence the presented dynamics.*

6.5.1. Local eigenvector directions

The trajectories presented in Figure 6.17 originate from a set of local normalised eigenvector offsets (Eq. 5.5). Figure 6.18 illustrates the spatial dependence of these local orientations, in which the adopted offset has been enlarged by a scaling factor of magnitude 20,000 for the purpose of visualisation.
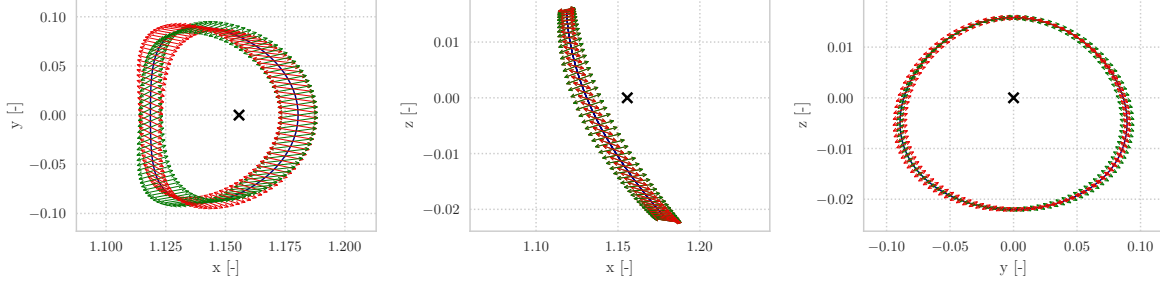
Figure 6.18: *Stable and unstable mode directions related to an halo orbit (blue) at C = 3.15. The eigenvector offset has been magnified by a factor 20,000 and denotes the orientation with respect to the stable (green) and unstable (red) subspace. The cross displays the location of the collinear equilibrium L_2 and serves as a point of reference.*

6.5.2. Jacobi integral verification

To verify the numerical veracity of the hyperbolic manifold trajectories which unwind from the halo family in L_2, Figure 6.19 shows the study on Jacobi's integral. As described in Section 5.2.5, the 100 uniquely spaced time vectors associated with the individual manifold trajectories require the employment of linear interpolation to provide an all-encompassing overview.
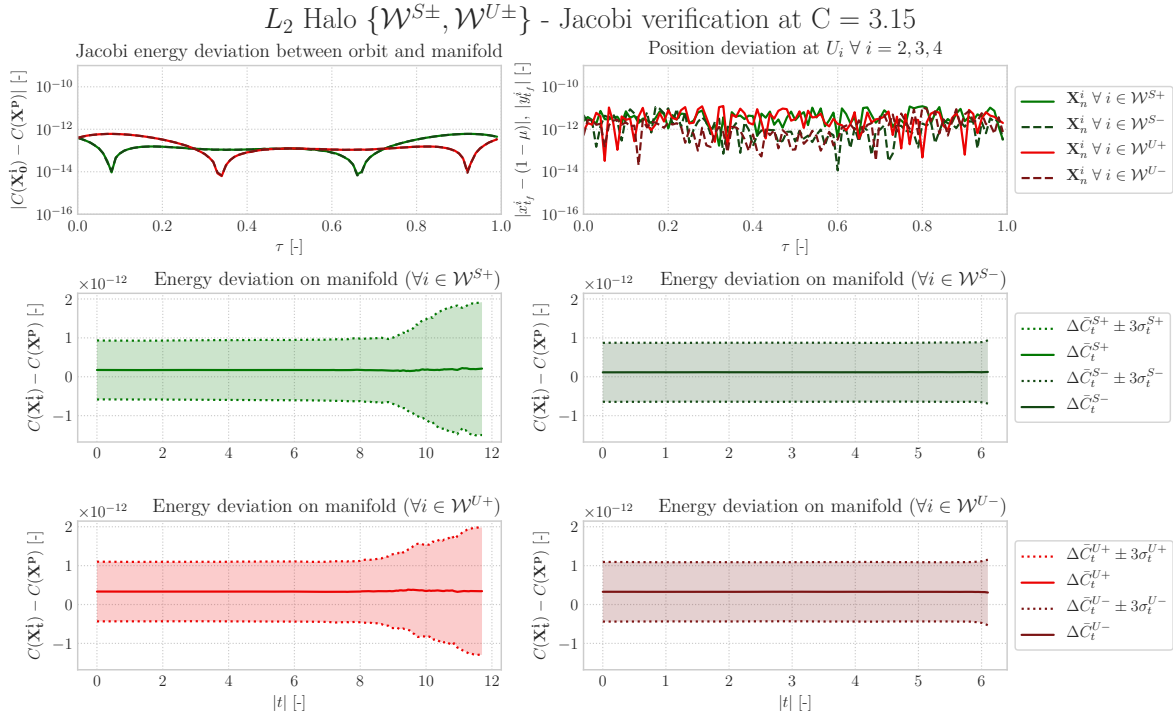
Figure 6.19: *Jacobi verification for all individual trajectories in the four sets of hyperbolic manifolds emanating from the halo orbit in L_2. From top to bottom, from left to right: difference in Jacobi's constant between the orbit and the corresponding first state on the manifold (Fig. 6.18), position deviation near stopping conditions (Eq. 5.7 and 5.8), and the difference in average local energy along the four manifolds with respect to the target orbit. Whereas the first two evaluations are mapped out with respect to the on-orbit phase, the latter are presented as a function of absolute normalised time. The confidence bands surrounding the deviation in C along the orbit include 99.73% of all observations.*

6.5.3. Numerical validation through symmetry

In addition to the Jacobi verification procedure, the results are validated through the analysis of the symmetries as presented in Figure 6.20.
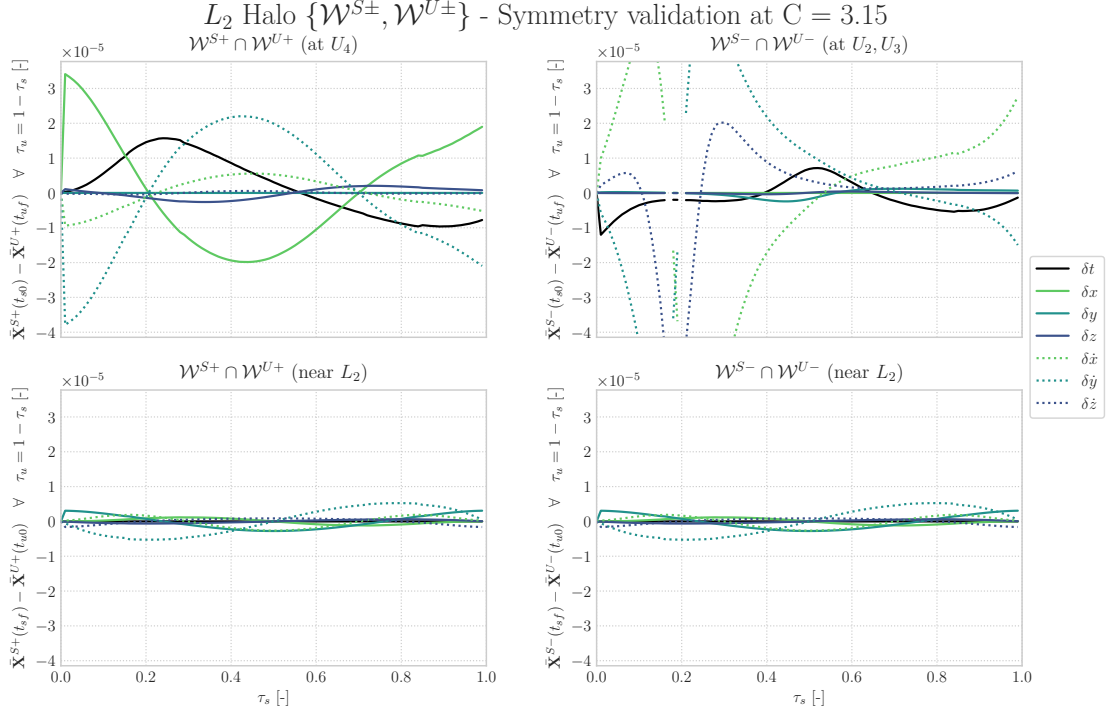
Figure 6.20: *Analysis of the pairs of symmetric (un)stable manifold trajectories associated with the halo orbit in L_2, based on the theorem of image trajectories with respect to the x-axis (Eq. 2.6 and 2.7). The first column portrays the individual components of the discrepancy in state at the start and end of propagation, corresponding to an addition of local eigenvector. The right column adheres to the same format in case of a negative offset. Discontinuities in state discrepancies are caused by premature termination of propagation, due to violating the threshold set for the accuracy of Jacobi's constant.*

6.5.4. Discussion of results

When analysing the sets of four manifolds emanating from the halo target orbits in L_2 consisting of 100 trajectories each, many peculiarities arise. The time until approach of the nominal stopping conditions ranges from $T_{\mathcal{W}^-}$ = 6.10 for the interior manifold to $T_{\mathcal{W}^+}$ = 11.70 for the exterior one. The equivalent dimensional units are 26.53 and 50.88 days respectively. This disparity is very similar to the behaviour observed for the H-L family in Section 6.4, as well as the fact that also these manifolds do not retain the shape of the target orbit (Fig. 6.13). The geometrical aspect of fanning out are observed to a lesser extent than for the ones corresponding to H-L manifolds and is in strong agreement with the results presented in [Howell et al., 2006]. In addition, these results provide an independent support to the statement that "the stable manifold associated with the halo orbits around L_1 or L_2 does not approach the Earth" [Mingotti et al., 2007].

In a similar fashion to the (un)stable manifolds emanating from halo target orbits, Figures 6.17 through 6.20 reveal many symmetries. In terms of accuracy, a clear build-up of truncation error over time can be observed for the stable and unstable exterior manifolds in Figure 6.19. The magnitude of this deviation corresponds well to the H-L manifolds in L_1 (Fig. 6.15). When comparing this phenomenon to the symmetry validation (Fig. 6.20), one can see that a narrow band of interior trajectories is prematurely terminated due to exceeding the threshold set for deviation in Jacobi's constant. This discontinuity is expected due to the gradual divergence between the near-symmetric states in Figure 6.20, denoting a sharp rise in highly non-linear accelerations. Symmetry validation suggests that the deviation between symmetric states increases during integration. However, this discrepancy is limited to $\sim 10^{-5}$ and strongly suggests a valid implementation of symmetrical dynamics together with the symmetric propagation of local eigenvectors (Fig. 6.18).

6.6. L_2 **Vertical Lyapunov**

The third and final set of manifolds computed in L_2 are those emanating from the V-L family. As a result of the numerical procedure presented in Algorithm 2, Figure 6.21 displays the orthographic projections of the four manifolds at three equally spaced energy levels and consisting of 100 trajectories each.
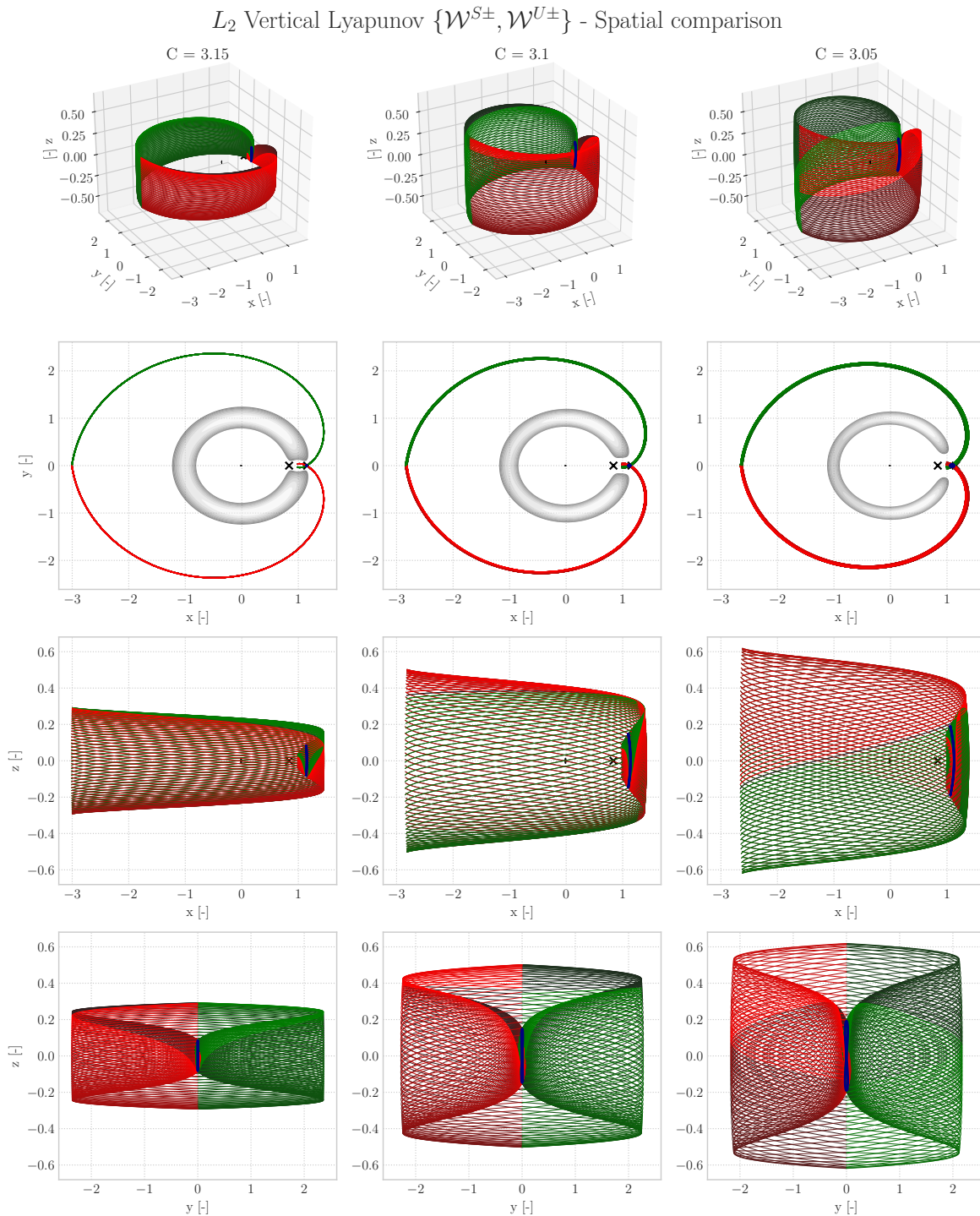

Figure 6.21: *Orthographic projection of the four (un)stable manifolds approximated by 100 trajectories which correspond to the V-L target orbit in L_2, given a set of three discrete energy levels (C = 3.05, 3.1, 3.15). The blue lines highlight the orbits from which these hyperbolic trajectories unwind. The two crosses indicate the equilibria (L_1 and L_2), of which the one denoting L_2 is covered by the set of manifold trajectories. The spheres located at ($-\mu$, 0, 0) and (1 $-\mu$, 0, 0) represent the Earth (P_1) and Moon (P_2) at mean radius respectively. As these bodies are modelled as point masses, their shape does not influence the presented dynamics.*

6.6.1. Local eigenvector directions

The trajectories presented in Figure 6.21 originate from a set of local normalised eigenvector offsets (Eq. 5.5). Figure 6.22 illustrates the spatial dependence of these local orientations, in which the adopted offset has been enlarged by a scaling factor of magnitude 4,000 for the purpose of visualisation.

L_2 Vertical Lyapunov $\{\mathcal{W}^{S\pm}, \mathcal{W}^{U\pm}\}$ - Orientation of (un)stable modes at C $= 3.15$
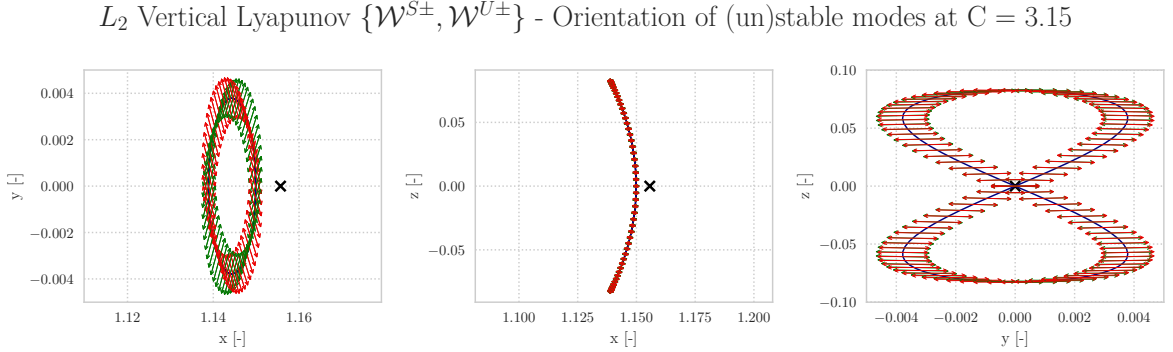
Figure 6.22: *Stable and unstable mode directions related to a vertical Lyapunov orbit (blue) at C = 3.15. The eigenvector offset has been magnified by a factor 4,000 and denotes the orientation with respect to the stable (green) and unstable (red) subspace. The cross displays the location of the collinear equilibrium L_2 and serves as a point of reference.*

6.6.2. Jacobi integral verification

To verify the numerical veracity of the hyperbolic manifold trajectories which unwind from the V-L family in L_2, Figure 6.23 shows the study on Jacobi's integral. As described in Section 5.2.5, the 100 uniquely spaced time vectors associated with the individual manifold trajectories require the employment of linear interpolation to provide an all-encompassing overview.

L_2 Vertical Lyapunov $\{\mathcal{W}^{S\pm}, \mathcal{W}^{U\pm}\}$ - Jacobi verification at C $= 3.15$
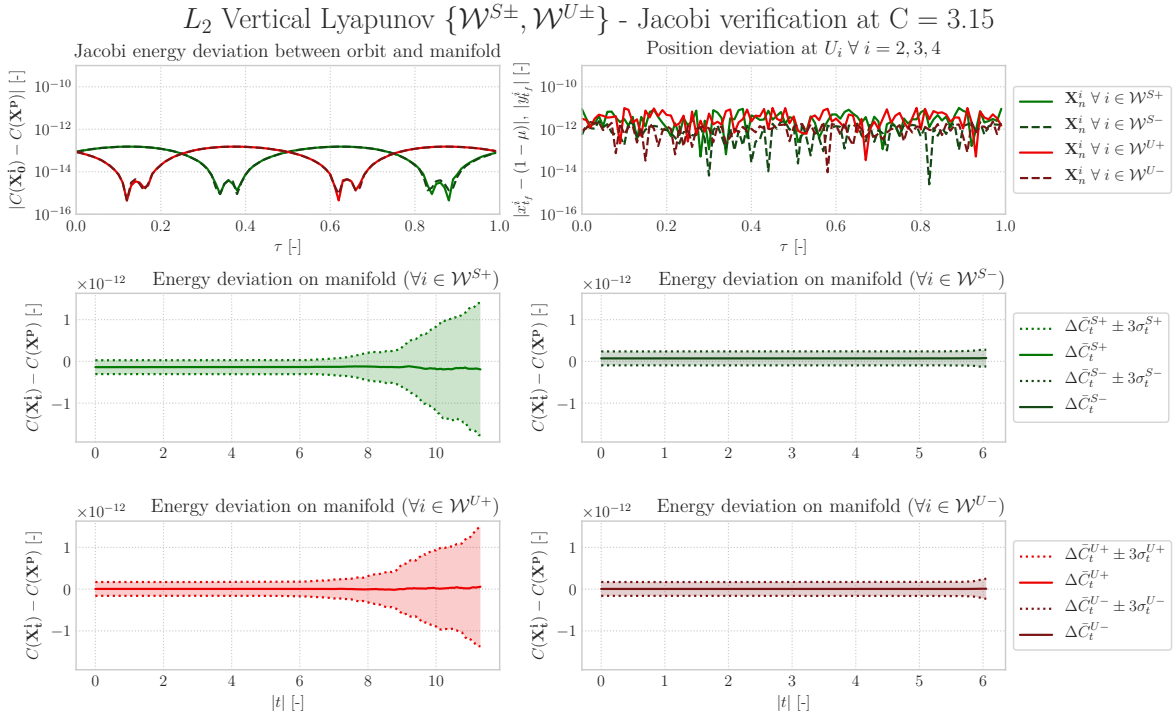
Figure 6.23: *Jacobi verification for all individual trajectories in the four sets of hyperbolic manifolds emanating from the V-L orbit in L_2. From top to bottom, from left to right: difference in Jacobi's constant between the orbit and the corresponding first state on the manifold (Fig. 6.22), position deviation near stopping conditions (Eq. 5.7 and 5.8), and the difference in average local energy along the four manifolds with respect to the target orbit. Whereas the first two evaluations are mapped out with respect to the on-orbit phase, the latter are presented as a function of absolute normalised time. The confidence bands surrounding the deviation in C along the orbit include 99.73% of all observations.*

6.6.3. Numerical validation through symmetry

In addition to the Jacobi verification procedure, the results are validated through the analysis of the symmetries as presented in Figure 6.24.
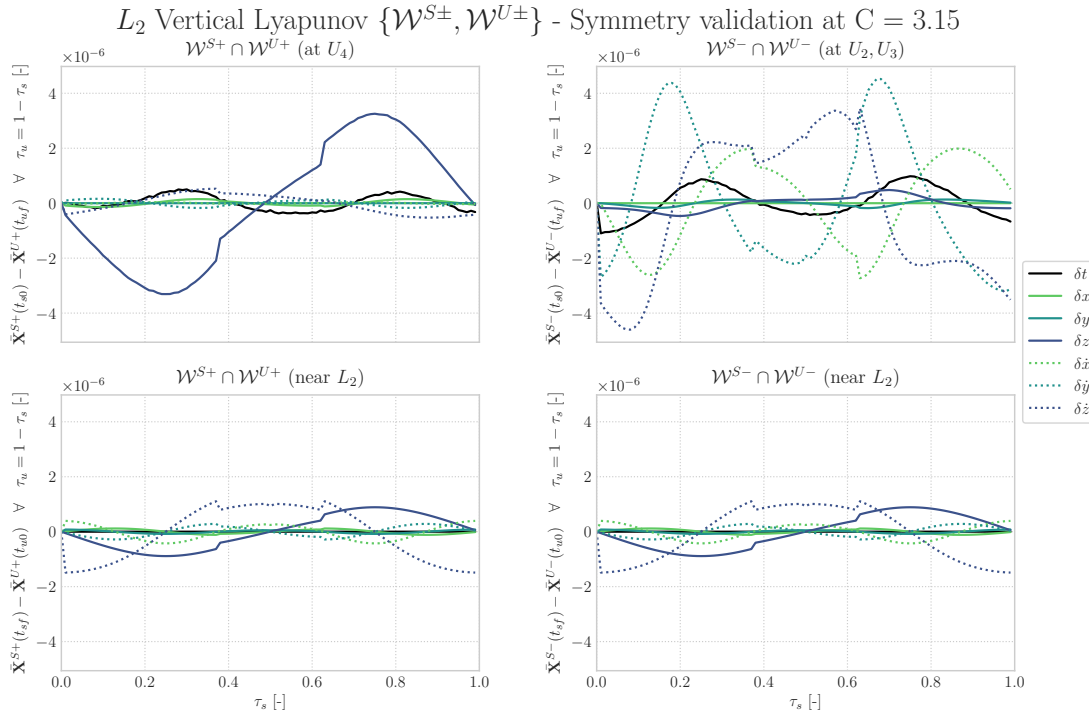
Figure 6.24: *Analysis of the pairs of symmetric (un)stable manifold trajectories associated with the V-L orbit in L_2, based on the theorem of image trajectories with respect to the x-axis (Eq. 2.6 and 2.7). The first column portrays the individual components of the discrepancy in state at the start and end of propagation, corresponding to an addition of local eigenvector. The right column adheres to the same format in case of a negative offset.*

6.6.4. Discussion of results

The final set of four hyperbolic manifolds associated with the V-L family in L_2 again show distinctively different behaviour than those observed for the H-L and halo types of target orbits. All in all, this type of manifold is truly in a class of its own. First and foremost, the (un)stable manifolds departing from L_2 also retain the same structure over time, even at significant distance from primaries. This global stability property complies with the observations in [Archambeau et al., 2011]. This "regular structure of invariant manifolds of eight-shaped Lissajous orbits is conserved even after a large integration time" and is well supported by the three orthographic projections at various energy levels in Figure 6.21. Once again, one possible drawback of this organised behaviour is that these tubes do not approach Earth close enough for an efficient direct departure. On the other hand, this stability does allow for robust prediction of behaviour over significant integration periods.

The maximum time until approach of the nominal stopping conditions for the four sets of 100 trajectories is the lowest across all families and ranges from $T_{\mathcal{W}^-} = 6.05$ for the interior manifold to $T_{\mathcal{W}^+} = 11.30$ for the exterior one. These dynamics are expected, based on the most powerful hyperbolic behaviour that this family possesses as concluded in Section 4.9.2. The equivalent dimensional units are 49.14 and 26.31 days respectively. The minimal time to unwind and global stability properties are accompanied with a very low error in Jacobi (Fig. 6.23) and symmetry (Fig. 6.24).

Another peculiar trait for this family is displayed in Figure 6.21 at the location of the first Poincaré section. The acute angle between the stable and unstable manifolds is persistent across the range of discrete energy levels, and suggests that a homoclinic connection does not exist for a single revolution around the first primary in the framework of nominal stopping conditions. An extended exploration on the existence of possible natural connections is presented in Chapter 7.

6.7. Review of manifold generation results

The results presented in this chapter have been achieved using the RK78 integrator in combination with the high-performance C++ coding language. Using this combination, the author has independently generated invariant manifolds consisting of individual hyperbolic trajectories which provide insight into the relative performance in a similar manner as presented in Section 4.9. In addition, the lessons learned from the numerical set-up for orbit generation provide crucial insights into the process of connecting manifolds at variations of Poincaré section orientation in Chapter 7.

6.7.1. Concluding statements on the novel numerical validation procedure

The numerical validation through symmetry has exposed the phases on the hyperbolic manifolds which have been prematurely terminated, due to violating the threshold set for the accuracy of Jacobi's constant. This insight is easily overlooked in the orthographic projections. In addition, the gradual divergence between the near symmetric states provides an indication as to what on-orbit phases (τ) might lead to excessive errors. In this way, the symmetry validation forms a comprehensive addition to the efficient single-parameter (C) verification check by contributing to the trustworthiness of the integrator accuracy, implemented dynamics, propagation of eigenvectors using the local STM's, and validation of the normalisation and sizing of the local eigenvector offset.

The accuracy of the adopted method adheres to very strict values ($\sim 10^{-5}$), even for extended integration periods. This is the result of a set of equally spaced nodes in time along the target orbit, as proposed in Section 5.2.1. The precision of these results could be extended further by producing sets of nodes which correspond to a greater extent in spatial symmetry. One solution to this problem could be to integrate twice, once over the interval $[0, -T/2]$ and once for $[0, T/2]$, as identical dynamics are encountered for these symmetric orbits. Another method that could aid in improving this analysis would be to select nodes based on the spatial position rather than time. However, both approaches will always retain a small error due to the finite precision inherent to this process of numerical approximation.

6.7.2. Concluding statements on the dynamical behaviour of the (un)stable manifolds

In general, the results presented in this chapter indicate the same phenomena in terms of transfer phenomena and numerical accuracy. However, there are also important dissimilarities that can be observed. As the research is not confined to the single energy level adopted in the analysis presented in this chapter, Figure 6.25 aims to increase the level of generality of conclusions.

Global stability: Whereas the hyperbolic trajectories associated with H-L and halo orbits exhibit chaotic behaviour over extended integration periods, the structure of the manifolds corresponding to V-L orbits remains preserved. This characteristic prevails for all energy levels presented in this chapter and is in agreement with [Archambeau et al., 2011]. In addition, it is noted that the "intersection curve of the manifold with the section $\sum$ has a similar shape as the figure-eight Vertical orbit from which the manifold originates" as described in [Calleja et al., 2012].

Magnitude of local eigenvectors: The (un)stable subspaces associated with the V-L orbits are significantly more powerful than those corresponding to H-L and halo orbits, which is characterised by requiring only little time to unwind from the orbit. This confirms the hypothesis stated in the results of orbit generation (Sec. 4.9.2) and shows through the fact that plots of (un)stable modes for the V-L have only been magnified with a factor 4,000. In contrast, the local eigenvector offsets for the H-L and halo families have been enlarged by $\times$ 20,000. Figure 6.25 supports this statement, as the V-L consistently attains the lowest time to unwind across all families.

Natural connections: The orthographic projections on the xy-plane reveal information on the possible existence of natural connections. The external manifolds of the V-L family meet in position at an acute angle near the collinear Poincaré sections $\mathbf{U}_1$ and $\mathbf{U}_4$. This discrepancy in orientation will require a manoeuvre to account for the difference. On the other hand, the H-L and halo manifolds fan out and seem to provide regions of velocity vector alignment in the xy-plane.

In summary, the invariant manifolds generated using the procedure outlined in Algorithm 2 adhere to the mean integration time until the nominal stopping conditions as displayed in Figure 6.25.
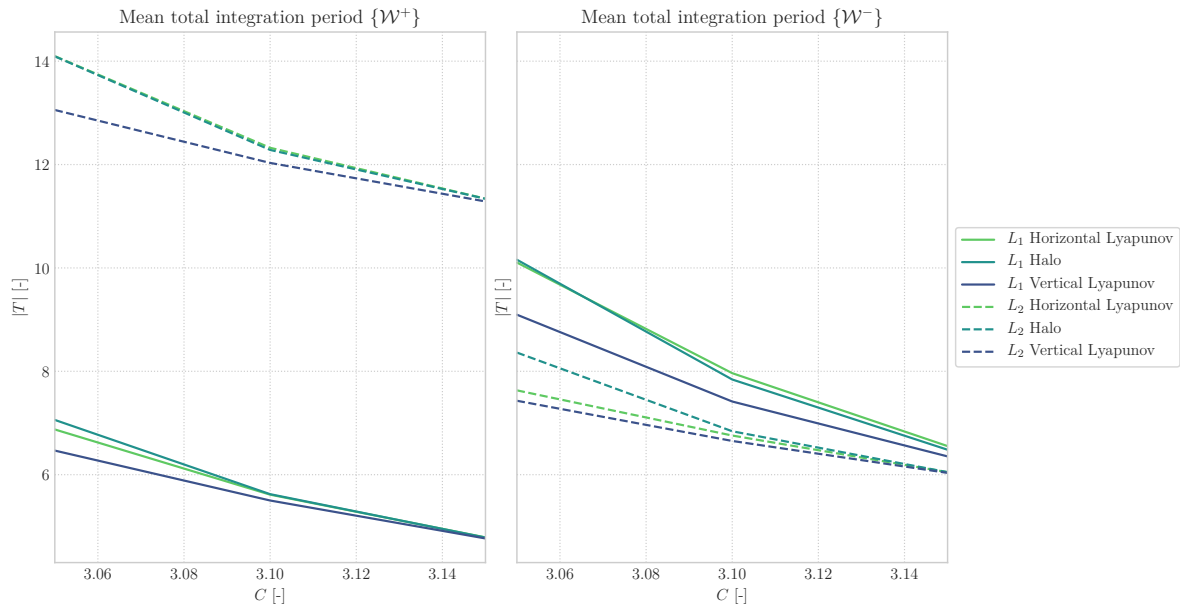
Figure 6.25: *Overview of the mean absolute time to unfold (T) and Jacobi's constant (C) for the various types of families of manifolds emanating from L_1 (full) and L_2 (dashed) respectively.*

For both collinear equilibria, the exterior manifold requires extended time to unfold. This behaviour is expected due to the increased spatial distance until approach of $\mathbf{U}_1$ and $\mathbf{U}_4$. Another interesting observation obtained from Figure 6.25 is related to the time to unwind until Poincaré sections $\mathbf{U}_2$ and $\mathbf{U}_3$. The spatial distance between these planes and the two libration points is equal, whereas the time until approach is consistently lower for the hyperbolic trajectories emanating from L_1. A possible explanation for this phenomenon can be given using the results presented in Chapter 4, in which the magnitude for the eigenvalue denoting the unstable subspace (λ_1) is consistently of higher magnitude in L_1 than for the equivalent family in L_2.

6.7.3. Recommendations for varying of Poincaré section orientation

In summary, the invariant manifolds generated using the procedure outlined in Algorithm 2 and validated in this chapter form the foundation for further investigation of the hyperbolic solution space. Based on the gained insight into the phase space, the following suggestions are proposed for Chapter 7 which considers the exploration of variable stopping conditions:

1. An equal spacing of nodes along the target orbit in time, should provide for a near-homogeneous distribution of trajectories within the orbit. This should provide for robust results in terms of discrepancies between the manifolds.

2. The computational effort can be greatly reduced by exploiting the symmetries for ballistic manifolds (Eq. 2.6 though 2.9). The H-L and halo family are characterised by a single plane of symmetry, and can therefore be reduced by a factor of two, whereas the doubly symmetric V-L orbits only require one fourth of all trajectories to be computed.[3]

3. Homoclinic connections might be found for a single revolution around the first primary in the case of exterior manifolds emanating from H-L and halo orbits. Due to the symmetry conditions with respect to the xy-plane, this natural connection requires the additional constraints of $\dot{x}, \dot{z} = 0$

4. The verification of Jacobi's constant has proven to be crucial to determine the validity of results, in combination with the diverging symmetrical states. The experience gained in this phase of the research, has yielded the threshold for the maximum deviation in C and is documented in Appendix A. The determination of this threshold is conducted via a trade-off between the highest attainable accuracy and the minimum number of discontinued trajectories over extended propagation periods.

These conclusions and recommendations from manifold generation provide the understanding required for an efficient generation of valid manifold structures at variations of stopping conditions. In particular, reducing the order of this system of infinitely many solutions will be required to confine the research to a feasible scope.

---

[3] Please note that this reduction in computations is based on the symmetry validation and adheres to the relation presented in Equation 5.1.

<div style="text-align: right; font-size: 4em;">7</div>

Connecting manifolds at variations of Poincaré section orientation

This chapter reveals the influence of the orientation of the Poincaré section on the manifold discrepancy that arises when connecting (un)stable manifolds to produce low-cost transfer mechanisms. In this manner, the final research question is addressed (Sec. 1.2.1). The numerical approach to periodic l.p.o. generation (Ch. 3) provides the trajectories (Ch. 4) that can be connected using invariant manifold theory (Ch. 5) to produce hyperbolic structures (Ch. 6). The knowledge acquired in these prior stages will form the required foundation for the efficient and robust generation of valid results. In particular the insights into the phase space of the CR3BP as well as into the behaviour of the integration scheme available in Tudat (RK78) in combination with the low-level programming language (C++) is imperative.[1] The structure of this chapter follows the similar logic as employed in Chapters 3 through 6. Firstly, the numerical approach is addressed, followed by the planar and spatial cases. Thereby the complexity of the problem will be gradually increased.

7.1. Homo- and heteroclinic connections

In the search for optimal manifold connections, one seeks the pair of trajectories with a minimal discrepancy in state to provide for a low-cost transfer mechanism. In the limit case, this disparity equals zero and a natural connection is found. The mathematical expression for this intersection of trajectories is given in Equation 7.1.

$$\mathscr{W}^{S\pm} \cap \mathscr{W}^{U\mp} \tag{7.1}$$

Two different types of natural connections can be distinguished. Firstly, an homoclinic connection forms a solution which connects an equilibrium point to itself and thereby adheres to the relation given in Equation 7.2 and presented in Figure 7.1.

$$\Phi(t) \rightarrow \mathbf{X}_0 \quad \text{as} \quad t \rightarrow \pm\infty \tag{7.2}$$

The second type of natural connection links two different equilibria to one another, as described in the set of Equations 7.3 and 7.4 and Figure 7.2.

$$\Phi(t) \rightarrow \mathbf{X}_0 \quad \text{as} \quad t \rightarrow -\infty \tag{7.3}$$

$$\Phi(t) \rightarrow \mathbf{X}_1 \quad \text{as} \quad t \rightarrow +\infty \tag{7.4}$$

A set of heteroclinic connections can be combined to form an heteroclinic cycle, as shown in Figure 7.3. Due to their qualitative dynamic behaviour, natural connections are also referred to as doubly asymptotic solutions.

---

[1]The reader is referred to [Jorba and Masdemont, 1999] for a characterisation of the phase space in the CR3BP.

Figure 7.1: *Homoclinic connection*   **Figure 7.2:** *Heteroclinic connection*   **Figure 7.3:** *Heteroclinic cycle*
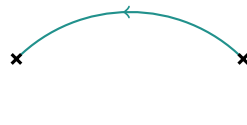
Natural connections are known to exist for H-L [Pontani and Teofilatto, 2017] in L_1 and L_2 and combinations of southern-northern halos in the same equilibrium [Haapala, 2014] at equal energy levels. These connections persist for a wide range of mass parameters, and are even known to exist for the Oterma comet in the Sun-Jupiter system at $\mu = 0.0009537$ [Wilczak and Zgliczynski, 2003][Wilczak and Zgliczyński, 2005]. However, "the chance of having a heteroclinic connection between [V-L orbits] is much less likely" which poses an intriguing research gap (Sec. 1.1.2) [Arona and Masdemont, 2007]. In this chapter the framework will presented required for the investigation of the solution space for heteroclinic connections between V-L orbits beyond the nominal stopping conditions. "As far as we can determine, if there is one of them, there is an infinite number of them" [Poincaré, 1967a].

7.2. Methodology and rationale for variations in orientation

Connecting "two-dimensional tubes in six-dimensional phase space [...] is not easy" and thereby require constraining to provide for a feasible research scope [Zazzera et al., 2004]. In this way, the analysis is confined to the trajectories connecting L_1 to L_2 for a maximum of a single revolution around P_2.[2] To establish a higher level of generality, the nominal stopping conditions set in Chapter 5 and adopted in Chapter 6 will be varied. This section addresses the definition of these parameters as well as the arguments for selection of optimal combinations of manifold trajectories.

7.2.1. Numerical definition of the Poincaré section orientation

In numerical terms, variations in the orientation of the Poincaré section boil down to the implementation of a new set of stopping conditions as well as a certain logic to find the most optimal connection. By varying the orientation, a higher level of generality is achieved with respect to the nominal stopping conditions. Figure 7.4 presents the reference frame in which the corresponding angle (θ) is established.[3]
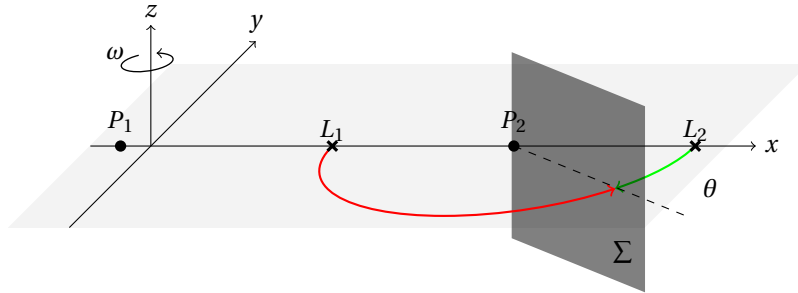
Figure 7.4: *Angle definition of variation of the Poincaré section (θ) in the rotating reference frame.*

The invariant topological tubes are approximated by a set of hyperbolic trajectories as discussed in Chapter 5. The corresponding stopping conditions need to be defined in such a way that they provide for a robust numerical test. In this way, the four quadrant arc tangent is chosen to provide for quadrature detection. This characteristic is required to distinguish between the different quadrants formed by the line connecting both

---

[2]For a classification of the geometry of homoclinic orbits "according to the number of turns about the primaries" in the planar case, the reader is referred to [Gidea and Masdemont, 2007]

[3]Poincaré maps are exploited to detect intersections of manifolds. In this way, the variations in θ form a higher dimensional version of the planar analysis presented in [Canalias et al., 2006].

primaries and the line extending the angle θ through P_2. The implemented numerical definition of this angle is stated in Equation 7.5 and is provided in the C++11 standard.

$$\theta(t_i) = \text{atan2}(y, x - 1.0 + \mu) \tag{7.5}$$

In combination with the heritage of the trajectory, including its integration time direction and libration point number, this completes the set of variables required for a robust and efficient termination procedure. Once more, the technique to reduce the overshoot is employed as stated in Section 5.2.1.

7.2.2. Arguments for selection of most optimal connection

After successful integration of the hyperbolic manifold trajectories until the desired stopping angle, the states of both manifolds are compared to find the most optimal connection. In the case that both topological structures are approximated by n equally spaced trajectories, this corresponds to n^2 combinations. A characteristic comparison for the V-L family is shown in Figure 7.5.
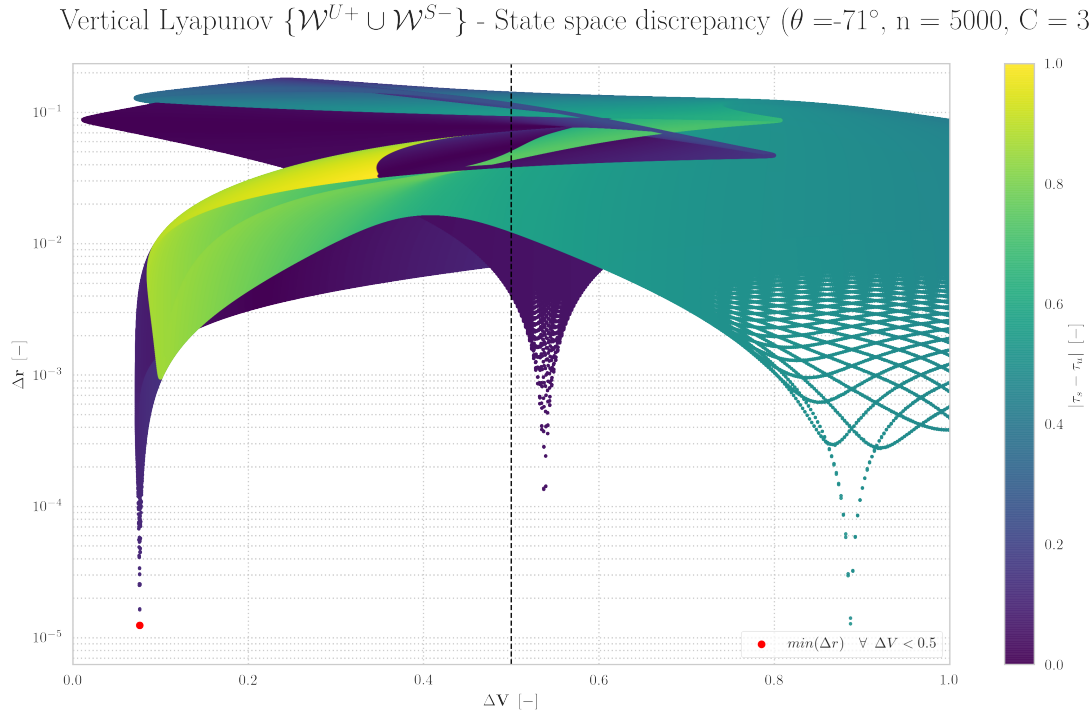
Figure 7.5: *Phase portrait of the unstable and stable manifold associated with V-L orbits in L_1 and L_2 respectively, at an identical energy level of $C = 3.1$. Both topological structures are approximated by 100 trajectories each, corresponding to 100^2 connections.*

The main focus of this research concerns bridging the research gap posed by the deficiency in knowledge regarding the phase space of V-L families. Hence, a selection criteria is formulated to suit the solution space of this particular family. Figure 7.5 shows a number of intersections gradually converging into a conical shape for minimal discrepancy in position and velocity. This trait persists across the various values of θ and is thereby provides for a robust selection criteria (Eq. 7.6).

$$min(\Delta r) \quad \forall \quad \Delta V < 0.5 \tag{7.6}$$

Using this selection criteria, one is able to produce an overview of the most optimal selection of trajectories for every angle. In this way, the sensitivity of the orientation of the Poincaré section on the state vector discrepancy that arises from the connection of hyperbolic invariant manifolds is exposed (Sec 1.2.1).

7.3. $L_1 - L_2$ Heteroclinic horizontal Lyapunov cycle

The identification of heteroclinic connections in the planar CR3BP is straightforward, due to the significant reduction in dimensions of the system. Moving from a spatial approach to the planar case reduces the phase space from six to four dimensions. In addition, the constraint on the Jacobi's constant in combination with the Poincaré map offers a two-dimensional subset of the phase space. This significant reduction in the dimensionality of the phase space enables straightforward representation, as is depicted by the characteristic curves in Figure 7.6.
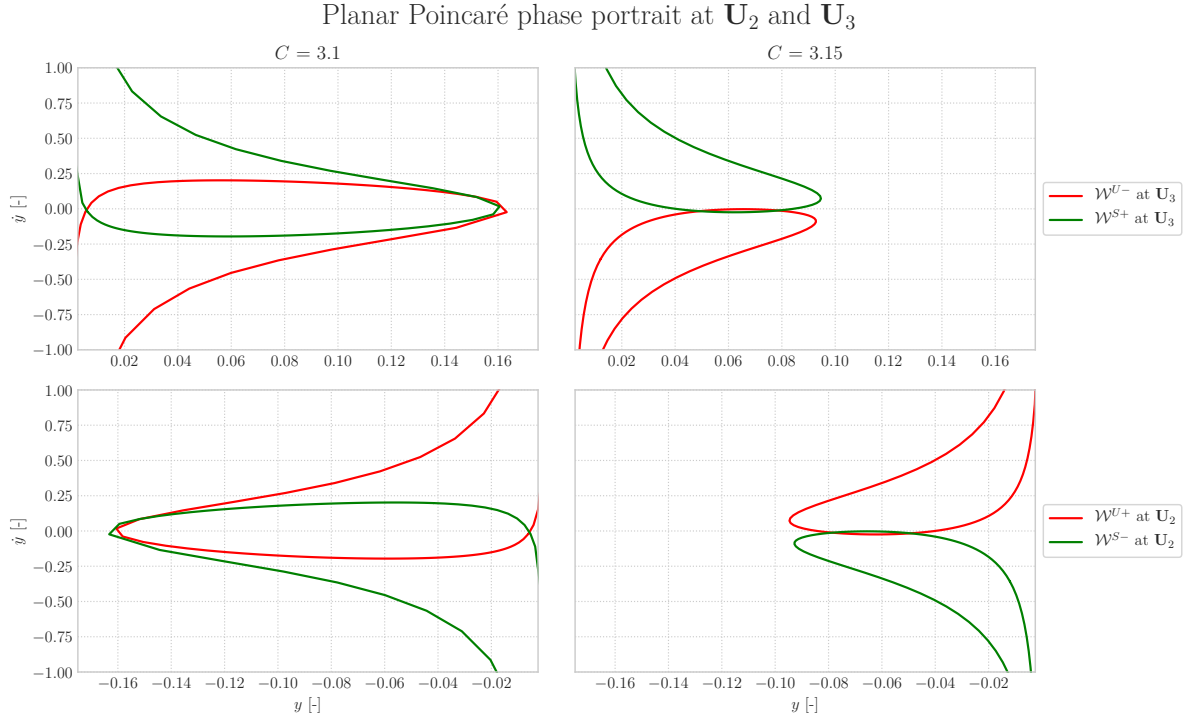
Figure 7.6: Phase portraits for the final states on the unstable and stable manifolds emanating from H-L orbits at identical energy level in L_1 and L_2 respectively. The nominal stopping conditions are located 'above' ($\mathbf{U}_3$) and 'below' ($\mathbf{U}_2$) the second primary as displayed in Figure 5.2. Two distinct cases are presented, each at a different constant energy level. Each intersection of the (un)stable contours denotes a connection in phase space and thereby proves the existence of a heteroclinic connection between the collinear libration points L_1 and L_2 in the planar case.

The transversal cuts shown in Figure 7.6 display similar qualitative behaviour to the one presented in [Koon et al., 2000b] for the planar case in the Sun-Jupiter system as well as [Canalias and Masdemont, 2006] for the Earth-Moon and Sun-Earth systems. Any intersection of these curves denotes a intersection in the full state space. In other words, a truly natural connection can be established. Figure 7.7 presents an orthographic projection of the most optimal combination of trajectories with finite numerical precision.

Horizontal Lyapunov $\{\mathcal{W}^{U+} \cup \mathcal{W}^{S-}\}$ - Near-heteroclinic connection (θ = -92°, C = 3.1)
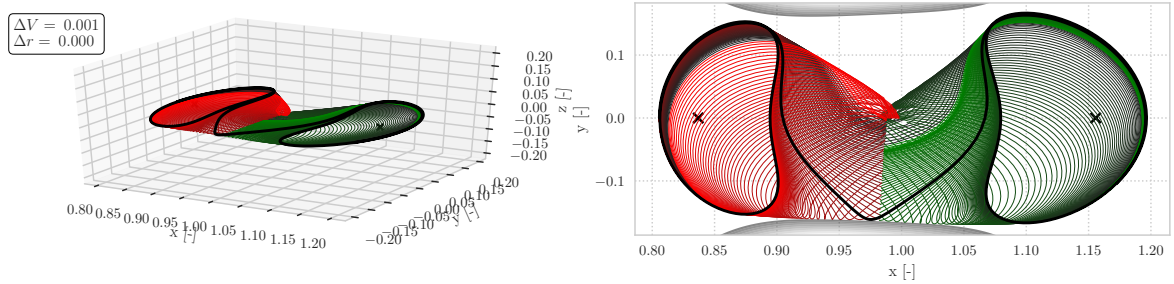
Figure 7.7: Near-heteroclinic connection between H-L orbits at identical energy level, bounded by the zero-velocity surface.

7.3.1. Discrepancy portrait in state space

The connection in Figure 7.7 corresponds to a very high extent to a true natural connection, and is the result of matching 100 equally spaced trajectories from both hyperbolic manifolds in state space. The corresponding 100^2 combinations demonstrate the similar behaviour across various stopping angles and is displayed in the case of $\theta = -92°$ in Figure 7.8.
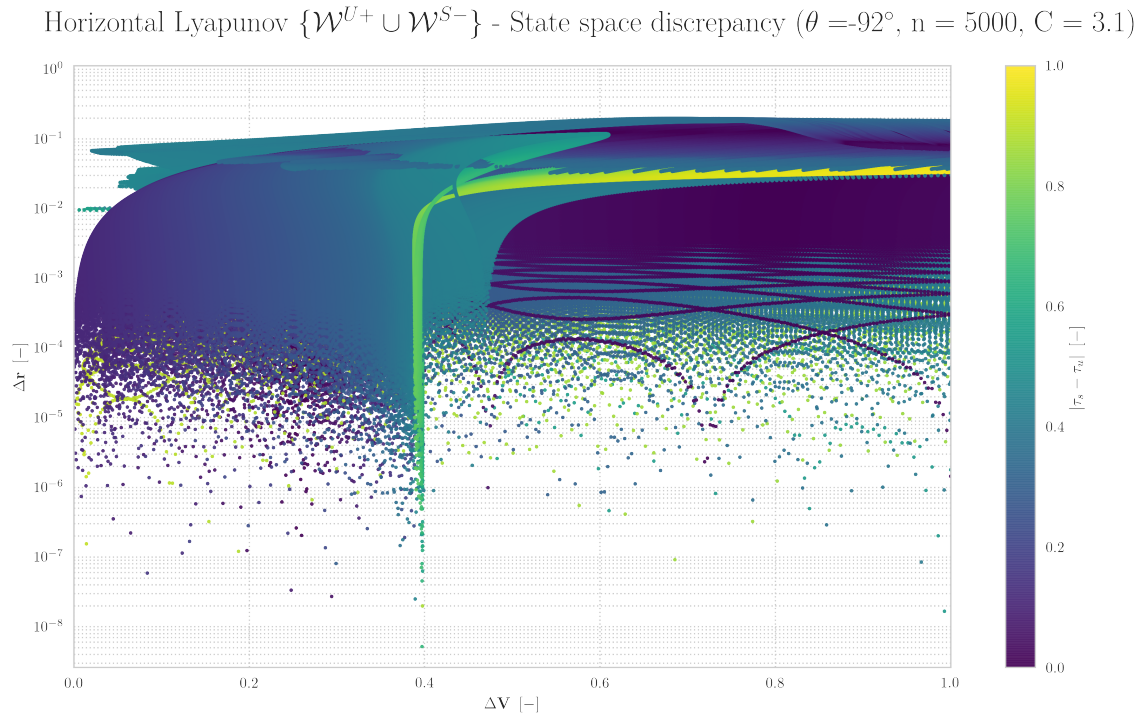
Figure 7.8: *Overview of the discrepancy in state space between the unstable and stable manifolds associated with H-L orbits in L_1 and L_2 respectively, in the case of the given stopping angle and energy level. The colour scale provides insight into the sensitivity with respect to difference in phase on the target orbits.*

The results presented in Figure 7.8 do not seem to adhere to a certain shape in the lower regimes of state discrepancy, but suggest a near stochastic distribution. In this way, the state space is not expected to be bounded, which supports the existence of natural solutions proven by the intersection of curves in Figure 7.6.

7.3.2. Near-heteroclinic cycle trajectory

The numerical approximation of this connection yields a ballistic heteroclinic cycle, given the planar symmetries with respect to the xz-plane (Eq. 2.6 and 2.7). Figure 7.9 portrays this type of connection from a spatial point of view.
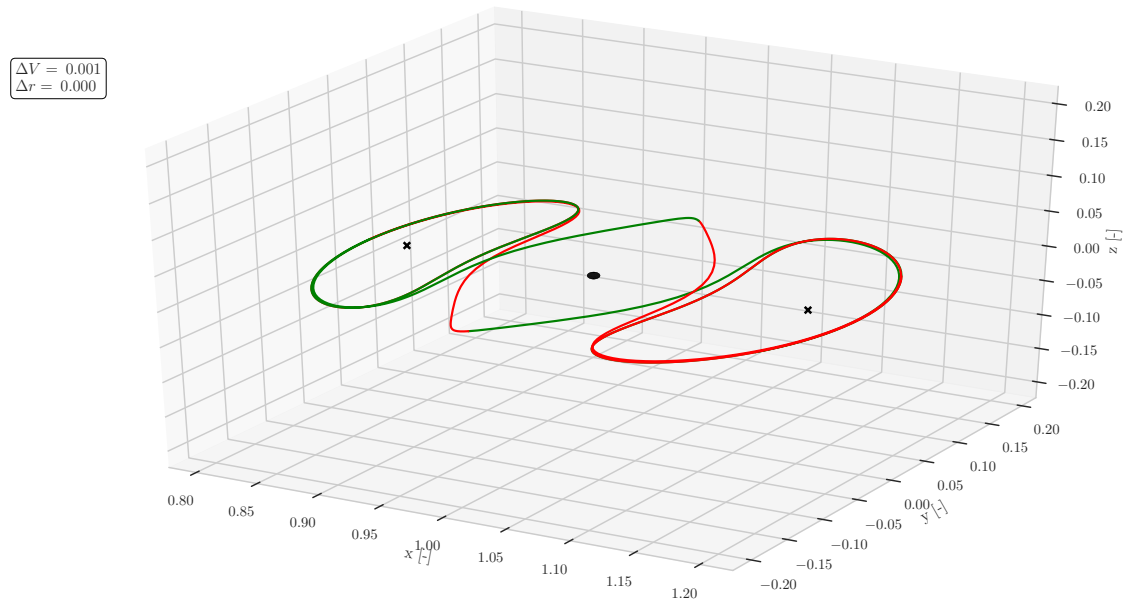
Figure 7.9: *Orthographic projection of the selected hyperbolic trajectories emanating from the H-L family. The two crosses indicate the collinear equilibria (L_1 and L_2), whereas the sphere located at $(1-\mu,0,0)$ represents the Moon at mean radius (P_2).*

The connection portrayed in Figure 7.9 can be further refined using gradient based techniques like the extended version of the multi-variate Newton method (Sec. 2.2.3), as presented in [Parker et al., 2010]. In the planar case however, one could also employ a straightforward interpolation to find the exact location of the intersecting curves shown in Figure 7.6.

"While it is straightforward to locate heteroclinic connections in the planar CR3BP, the computation of analogous solutions in the spatial problem is non-trivial" [Haapala, 2014]. The out-of-plane motion provides for a rapid increase in complexity, as the order has increased from two to four. In this way, one is unable to reduce the problem to the intersection of curves shown in Figure 7.6.

7.4. $L_1 - L_2$ **Near-heteroclinic southern halo cycle**

The first set of spatial manifold connections to be computed are those associated with southern halo orbits situated around L_1 and L_2. As a result of comparing the two hyperbolic manifolds for various stopping conditions, the discrepancies in state space are given in Figure 7.10 at 12 equally spaced values of the stopping angle.

Halo $\{\mathcal{W}^{U+} \cup \mathcal{W}^{S-}\}$ - State space discrepancies (C = 3.1, n = 5000)
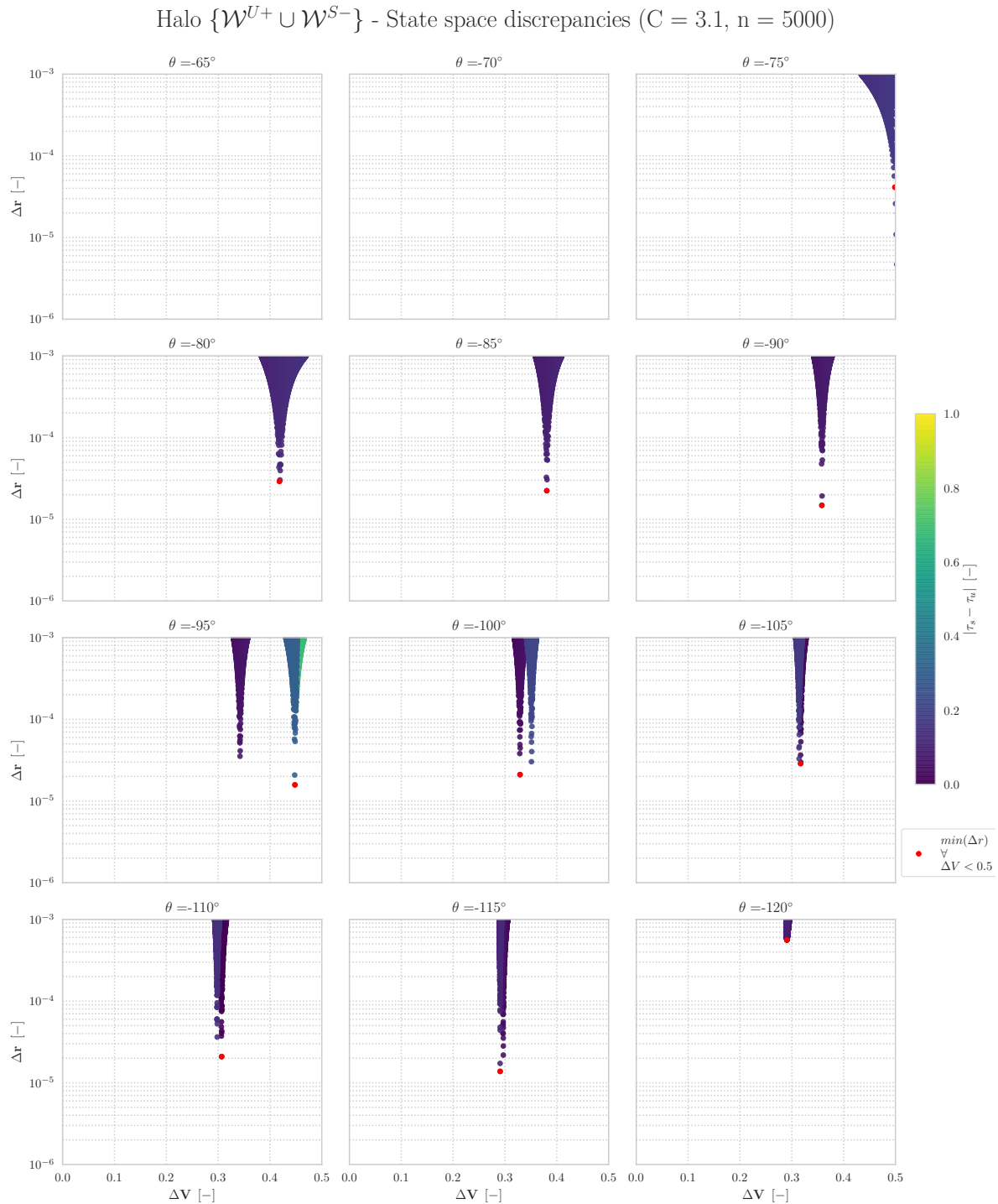
Figure 7.10: *Discrepancies between the unstable and stable hyperbolic manifold trajectories in state space for various values of the stopping angle (θ). The two hyperbolic invariant manifolds are approximated by 5000 trajectories each, associated with V-L target orbits in L_1 and L_2 for the given energy level.*

7.4.1. Minimum discrepancy in state space portraits

The state discrepancies presented in Figure 7.10 are members of a larger set of results spanning the interval $-180 \leq \theta \leq 0$. Figures 7.11 and 7.12 portray the complete and focused view of the state space corresponding to the best case for the southern halo target orbits in terms of lowest discrepancy in state.

Figure 7.11: *Overview of the discrepancy in state space between the (un)stable manifolds associated with halo orbits in L_1 and L_2 respectively, in the case of the given stopping angle and energy level. The colour scale provides insight into the sensitivity with respect to difference in phase on the target orbits.*

Figure 7.12: *Focused view of the discrepancy in state space between the (un)stable manifolds associated with halo orbits in L_1 and L_2 respectively, in the case of the given stopping angle and energy level.*

7.4.2. Near-heteroclinic cycle trajectory

The trajectories corresponding to the minimal deviation in state (Fig. 7.11 and 7.12) at the given orientation of the Poincaré section are portrayed in Figure 7.13. In addition, a cycle trajectory can be composed by exploiting the theorem on image trajectories (Eq. 2.6 through 2.9). This combination of hyperbolic trajectories is presented in Figure 7.14.

Halo $\{\mathcal{W}^{U+} \cup \mathcal{W}^{S-}\}$ - Near-heteroclinic connection (θ = -115°, C = 3.1)
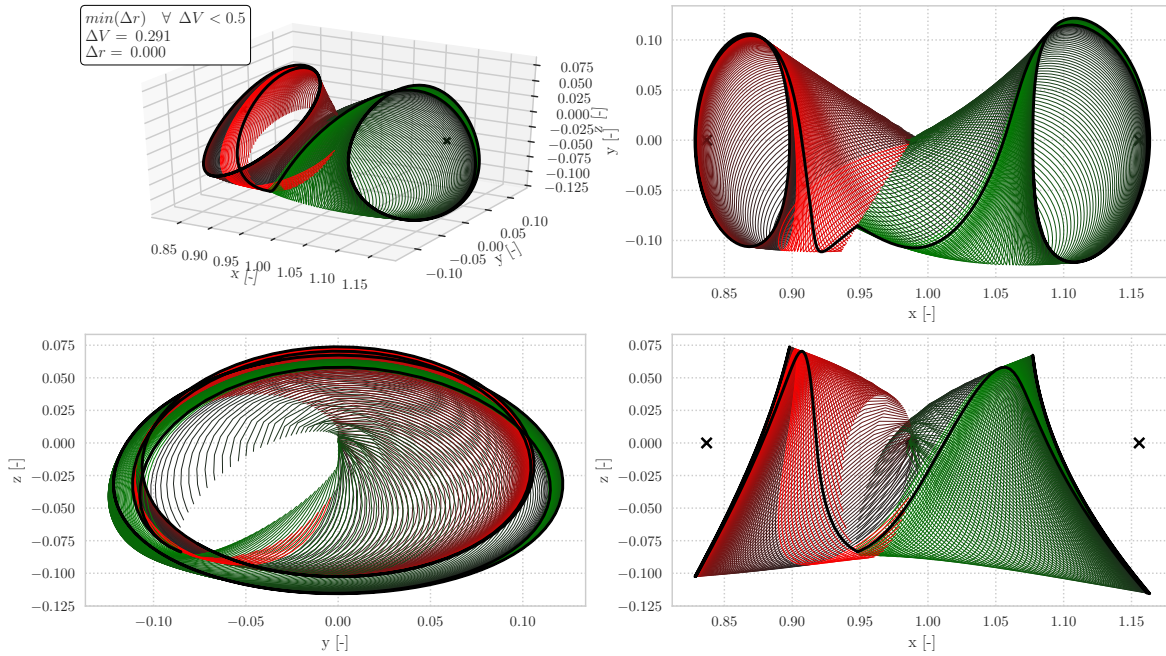
Figure 7.13: *Near-heteroclinic connection between halo orbits at identical energy level, bounded by the zero-velocity surface.*

Halo $\{\mathcal{W}^{U+} \cup \mathcal{W}^{S-}\}$ - Near-heteroclinic cycle (θ = -115°, C = 3.1)
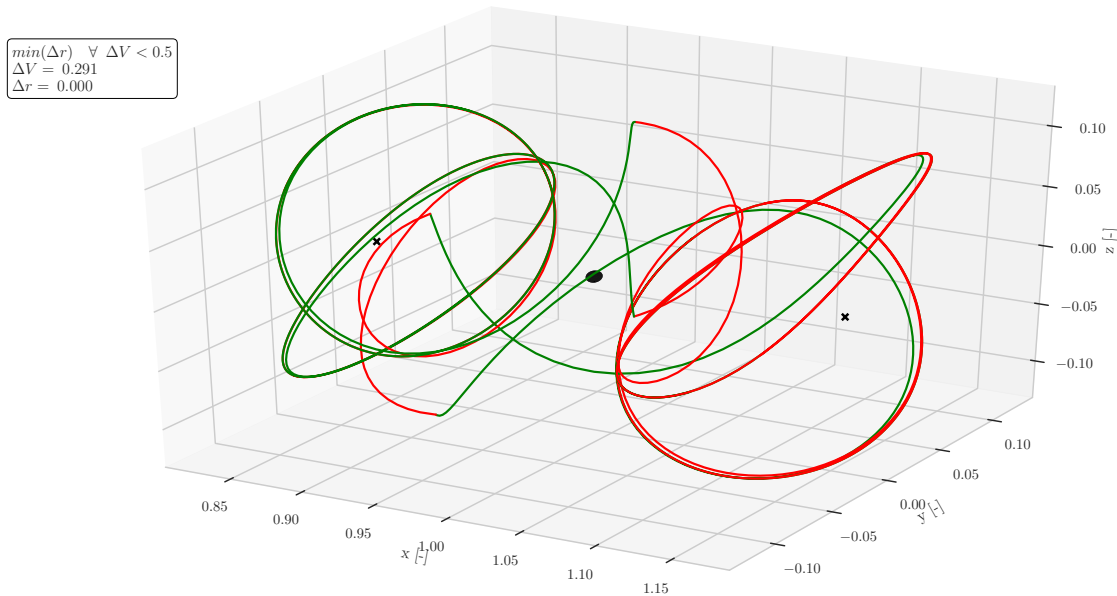
Figure 7.14: *Orthographic projection of the selected hyperbolic trajectories emanating from the halo family. The two crosses indicate the collinear equilibria (L_1 and L_2), whereas the sphere located at $(1 - \mu, 0, 0)$ represents the Moon at mean radius (P_2).*

7.4.3. Sampling validation

As stated in Section 7.4.1, the trajectories presented in Figures 7.13 and 7.14 only form a small subset of a wider range of connections. To verify that the qualitative behaviour of the presented trajectory is not singular, Figure 7.15 displays the high-level results for every stopping angle computed in this research.
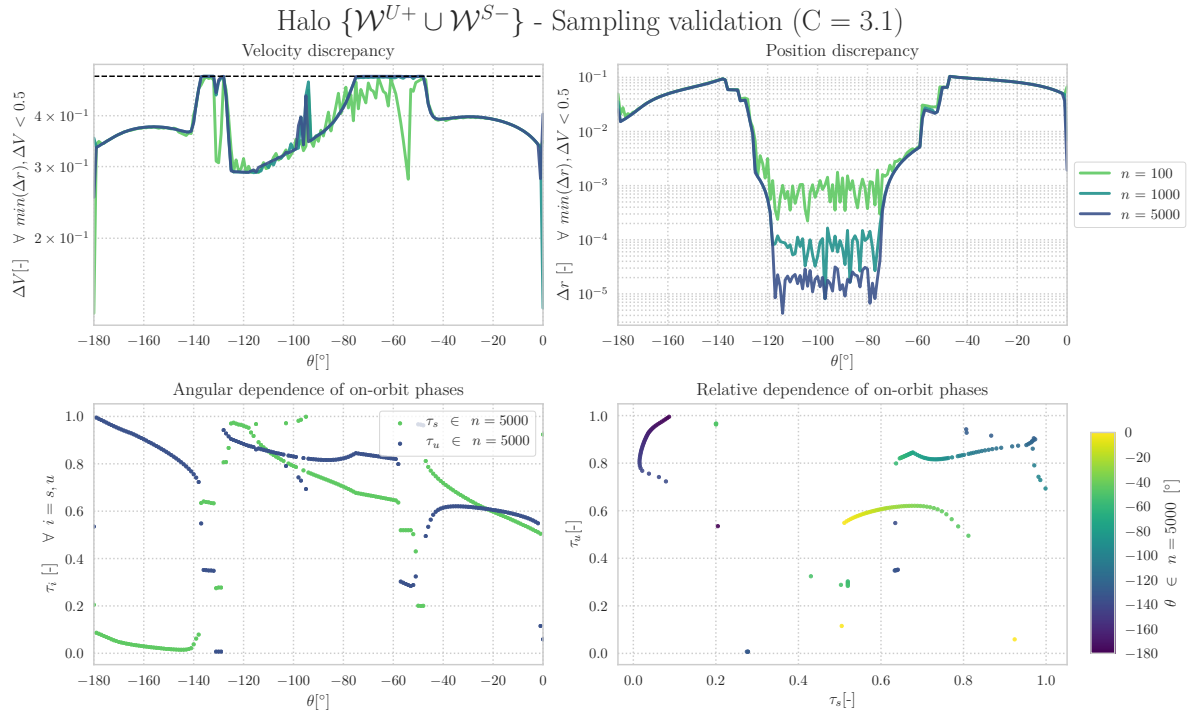
Figure 7.15: *Sampling validation of the selected connection (Eq. 7.6) for each of the 181 orientations of the Poincaré section.*

7.4.4. Discussion of results

The highlighted trajectory in Figure 7.13 exhibits a high correspondence in position and a significant discrepancy in orientation at the location of manifold connection. This corresponds to a minimal and considerable difference in position and velocity respectively. A closer look at Figures 7.11 and 7.12 reveals that the connection requires a change of $\sim 10^{-5}$ in position and 0.291 in velocity. The equivalent dimensional units are 3.844 km and 0.298 km/s.

Many conclusions can be drawn from the increase in level of generality using Figures 7.10 and 7.15. First of all, the pair of manifolds only connect in position space for a limited range of the stopping angle ($-125° \leq \theta \leq -75°$) as shown in the position discrepancy in the sampling validation (Fig. 7.15). From the orthogonal projections, it can be determined that the hyperbolic trajectories curve around second primary. Thereby significantly changing orientation and contracting in spatial spread. In addition, the sampling validation shows that the discrepancy in position and noise in the velocity deviation is reduced for an increased number of trajectories. Lastly, the most optimal connections (Fig. 7.10) seems to correspond to near equal phases on both target orbits. This is expected due to the high correspondence in symmetry around P_2 in terms of orbit geometry and orientation of local eigenvalues of all families (Ch. 6).

In conclusion, the hyperbolic manifolds associated with a pair of two northern (or southern) halo orbits situated around L_1 and L_2 do not seem to posses a natural heteroclinic connection in the EM-system at $C = 3.1$.[4] This is a very intriguing observation since both "connections from quasi-[halo L_1] to quasi-[halo L_2] orbits" [Gómez et al., 2004] and "heteroclinic connection[s] from a northern halo orbit to its southern counterpart" [Calleja et al., 2012] are known to exist.

---

[4]Please note that this research is confined to a maximum of a single revolution around P_2. Heteroclinic connections may exist over extended integration periods. However, these trajectories will most likely not resemble optimal solutions in a full fidelity model due to the close approach of the unequally distributed mass of the Moon.

7.5. $L_1 - L_2$ **Near-heteroclinic vertical Lyapunov cycle**

The second set of spatial manifold connections to be computed are those associated with V-L orbits situated around L_1 and L_2. As a result of comparing the two hyperbolic manifolds for various stopping conditions, the discrepancies in state space are given in Figure 7.16 at 12 equally spaced values of the stopping angle.
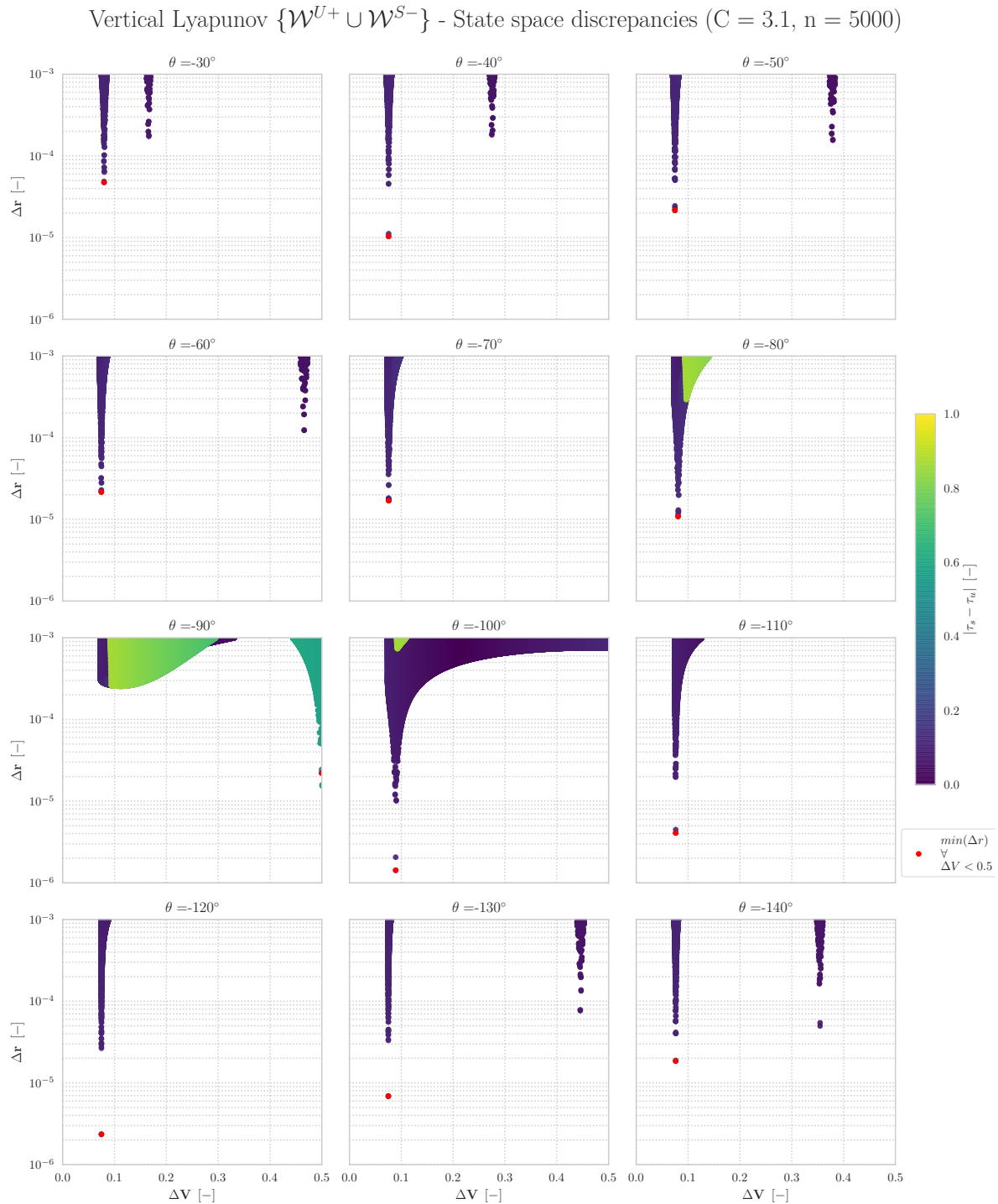
Figure 7.16: *Discrepancies between the unstable and stable hyperbolic manifold trajectories in state space for various values of the stopping angle (θ). The two hyperbolic invariant manifolds are approximated by 5000 trajectories each, associated with V-L target orbits in L_1 and L_2 for the given energy level.*

7.5.1. Minimum discrepancy in state space portraits

The state discrepancies presented in Figure 7.16 are members of a larger set of results spanning the interval $-180 \leq \theta \leq 0$. Figures 7.17 and 7.18 portray the complete and focused view of the state space corresponding to the best case for the V-L target orbits in terms of lowest discrepancy in state.
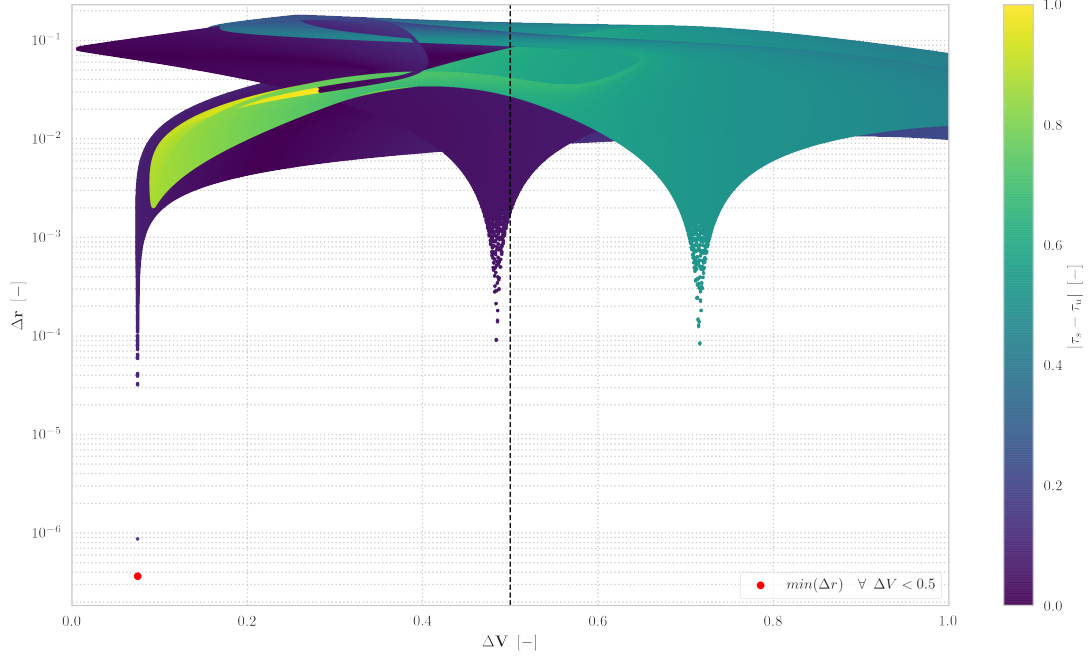
Figure 7.17: *Overview of the discrepancy in state space between the unstable and stable manifolds associated with H-L orbits in L_1 and L_2 respectively, in the case of the given stopping angle and energy level. The colour scale provides insight into the sensitivity with respect to difference in phase on the target orbits.*
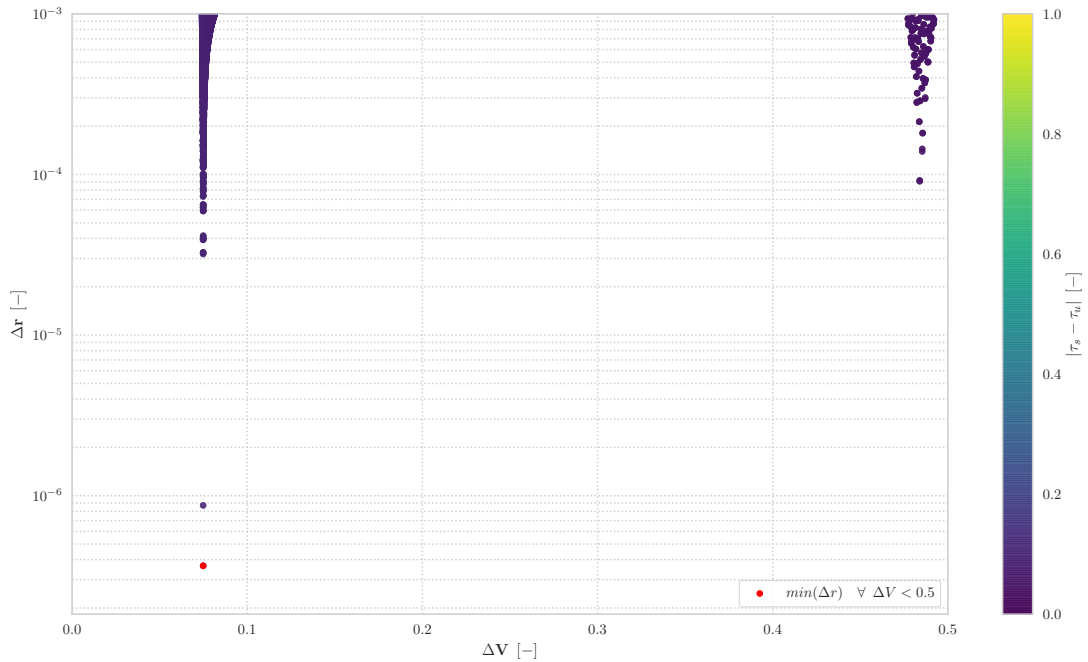
Figure 7.18: *Focused view of the discrepancy in state space between the unstable and stable manifolds associated with V-L orbits in L_1 and L_2 respectively, in the case of the given stopping angle and energy level.*

7.5.2. Near-heteroclinic cycle trajectory

The trajectories corresponding to the minimal deviation in state (Fig. 7.17 and 7.18) at the given orientation of the Poincaré section are portrayed in Figure 7.19. In addition, a cycle trajectory can be composed by exploiting the theorem on image trajectories (Eq. 2.6 through 2.9). This combination of hyperbolic trajectories is presented in Figure 7.20.

Vertical Lyapunov $\{\mathcal{W}^{U+} \cup \mathcal{W}^{S-}\}$ - Near-heteroclinic connection (θ = -125°, C = 3.1)
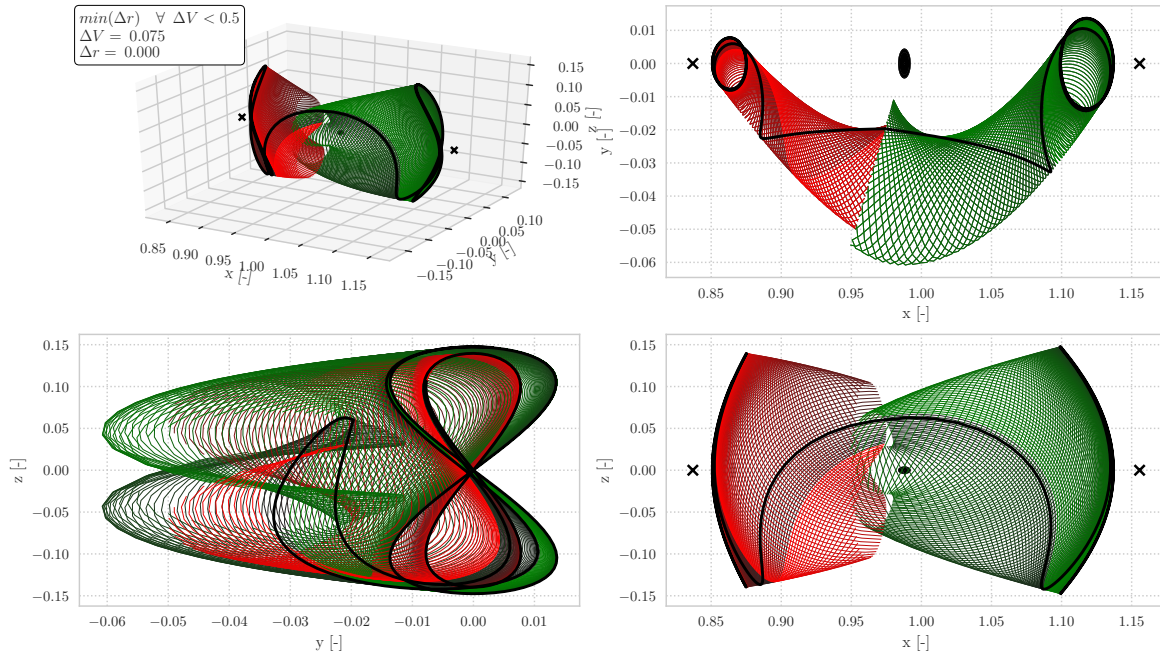
Figure 7.19: *Near-heteroclinic connection between V-L orbits at identical energy level, bounded by the zero-velocity surface.*

Vertical Lyapunov $\{\mathcal{W}^{U+} \cup \mathcal{W}^{S-}\}$ - Near-heteroclinic cycle (θ = -125°, C = 3.1)
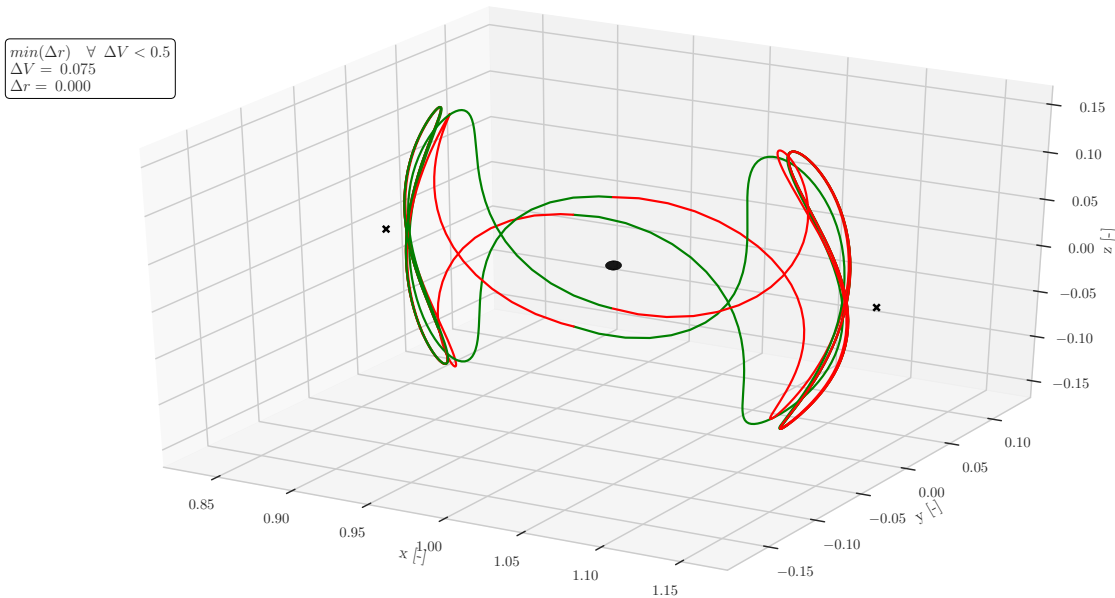

Figure 7.20: *Orthographic projection of the selected hyperbolic trajectories emanating from the V-L family. The two crosses indicate the collinear equilibria (L_1 and L_2), whereas the sphere located at $(1 - \mu, 0, 0)$ represents the Moon at mean radius (P_2).*

7.5.3. Sampling validation

As stated in Section 7.5.1, the trajectories presented in Figures 7.19 and 7.20 only form a small subset of a wider range of connections. To verify that the qualitative behaviour of the presented trajectory is not singular, Figure 7.21 displays the high-level results for every stopping angle computed in this research.
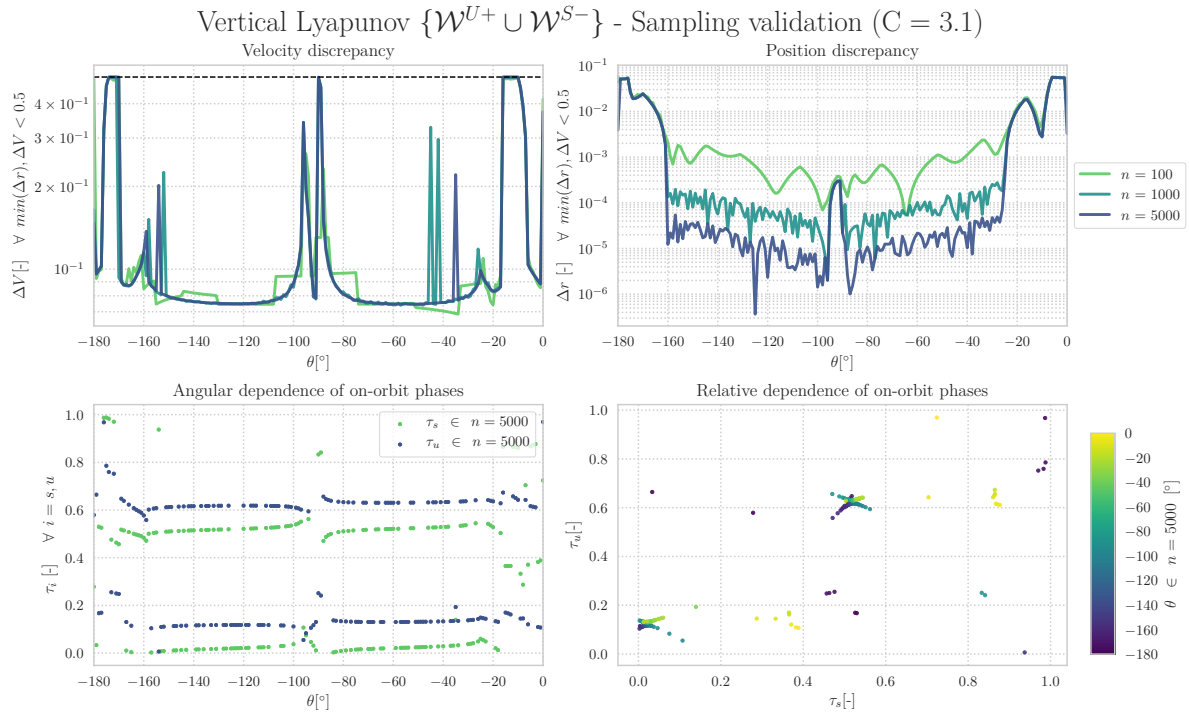
Figure 7.21: *Sampling validation of the selected connection (Eq. 7.6) for each of the 181 orientations of the Poincaré section.*

7.5.4. Discussion of results

The highlighted trajectory in Figure 7.19 exhibits a high correspondence in position and a significant discrepancy in orientation at the location of manifold connection. This corresponds to a minimal and considerable difference in position and velocity respectively. A closer look at Figures 7.17 and 7.18 reveals that the connection requires a change of $\sim 10^{-7}$ in position and 0.075 in velocity. The equivalent dimensional units are 0.038 km and 0.077 km/s.

Many conclusions can be drawn from the increase in level of generality using Figures 7.16 and 7.21. First of all, the pair of manifolds only connect in position space for an extended range of the stopping angle ($-160° \leq \theta \leq -25°$) as shown in the position discrepancy in the sampling validation (Fig. 7.21). From the orthogonal projections, it can be determined that the hyperbolic trajectories curve around second primary at a larger distance than observed for the halo family at identical energy level whilst still retaining their characteristic shape (Sec. 7.4). In addition, the sampling validation shows that the discrepancy in position and noise in the velocity deviation is reduced for an increased number of trajectories. In a similar fashion to the behaviour observed for the halos, the most optimal connections (Fig. 7.10) seems to correspond to near equal phases on both target orbits. This is expected due to the high correspondence in symmetry around P_2 in terms of orbit geometry and orientation of local eigenvalues of all families (Ch. 6).

Interestingly, optimal connections seem to appear outside the bounds set by the nominal stopping conditions. In particular, the region near $\theta = -90°$ gives rise to two sharp peaks (Fig. 7.21) as shown in the change in shape in Figure 7.16. The planar orthographic projection reveals that these hyperbolic trajectories meet under an angle near $\mathbf{U}_2$ (corresponding to $\theta = -90°$). To compensate for this change in orientation of the velocity vector, a significant impulse would be required. In conclusion, the hyperbolic manifolds associated with a pair of two V-L orbits situated around L_1 and L_2 do not seem to posses a natural heteroclinic connection in the EM-system at $C = 3.1$.[5]

---

[5]Please note that heteroclinic connections may exist over extended number of revolutions around P_2.

7.6. Review of manifold connections at variations of Poincaré section orientation

The results presented in this chapter have been achieved using the RK78 integrator in combination with the high-performance C++ coding language. Using this combination, the author has independently generated invariant manifolds connections at variations of the Poincaré section orientation which provide insight into the solution space for natural connections. This effort would not have been possible without the comprehensive verification and validation of the target orbits (Ch. 4) and their associated manifolds (Ch. 6). The lessons learned from the numerical set-up and the presented results provide crucial insights required for generating a *comprehensive understanding of the phase space of hyperbolic invariant manifolds emanating from vertical Lyapunov orbits including the potential existence of heteroclinic connections in the Earth-Moon system* (Sec. 1.1.2).

7.6.1. Contrasting characteristics exhibited by the three families

Connections of hyperbolic trajectories in phase space has revealed that different characteristics can observed across the various types of families.

H-L: The two-dimensional phase portraits (Fig. 7.6) associated with the H-L target orbits strongly supports the existence of heteroclinic connections for this family.[6] As discussed in the corresponding manifold generation results (Sec. 6.1.4), the manifolds shown in Figure 7.7 do not retain the shape of the target orbit and bounce off the zero-velocity surface. Interestingly, the latter gives rise to the most optimal alignment in state space that was found in this research. *Sec. 7.3*

Halo: The hyperbolic manifolds associated with a pair of two northern (or southern) halo orbits situated around L_1 and L_2 do not seem to posses a natural heteroclinic connection in the EM-system at $C = 3.1$, when limiting the scope to a single revolution around P_2. Heteroclinic connections may exist over extended integration periods. However, these trajectories will most likely not resemble optimal solutions in a full fidelity model due to the close approach of the unequally distributed mass of the Moon. To produce a natural doubly-asymptotic connection between two southern halo orbits, one requires a significant velocity correction at the point of manifold connection. On the other hand, the (un)stable trajectories do correspond to a very high extent ($\sim 10^{-5}$) in position space. This is a very intriguing observation since both "connections from quasi-[halo L_1] to quasi-[halo L_2] orbits" [Gómez et al., 2004] and "heteroclinic connection[s] from a northern halo orbit to its southern counterpart" [Calleja et al., 2012] are known to exist. *Sec. 7.4*

V-L: In a similar fashion as the pair of southern halo orbits, the hyperbolic manifolds associated with a pair of two northern (or southern) halo orbits situated around L_1 and L_2 do not seem to posses a natural heteroclinic connection in the scope of this research. This strongly supports the notion that "the chance of having a heteroclinic connection between [V-L orbits] is much less likely" than those for H-L [Arona and Masdemont, 2007]. Interestingly, the connection which corresponds best in position and velocity space appears at large deviations from the nominal stopping conditions. Moreover, Figure 7.21 has revealed that the best connections are found <u>outside</u> the nominal stopping conditions and require a very modest compensation in velocity (0.075). [7] *Sec. 7.5*

Apart from these contrasting characteristics that were revealed for these families, there are also observations to be noted which unite the three types of orbits.

---

[6]A comprehensive study on the refinement and continuation of heteroclinic connections between L_1 and L_2 H-L orbits is presented in [Barrabés et al., 2013].

[7]The importance of this discovery is significant, as it supports the adopted method of varying the orientation of the Poincaré section. Section 7.6.2 and Chapter 8 address this outcome in more detail.

7.6.2. General rules for connecting manifolds

The characterisation of the manifold discrepancies for the various families of orbits display interesting parallels. [8]

Phase alignment: In the case that no heteroclinic connection is suggested, the phase on the departure (τ_u) and target (τ_s) orbit is shown to be consistently close in magnitude. Especially in the case of V-L, the sampling validation (Fig. 7.21) has unveiled interesting phenomena. The selection of the most optimal pair of trajectories exhibits a near-constant offset of 0.1. From a spatial point of view, this corresponds to a little offset from the top ($\tau_u = 0.1$) or bottom ($\tau_u = 0.6$) of the departure orbit (L_1) and to the top ($\tau_s = 0$) or bottom ($\tau_s = 0.5$) of the arrival orbit (L_2). One possible explanation for this behaviour can be given through the comparison of the orientation of the (un)stable modes of both Lyapunov orbits (Fig. 6.10 and 6.22). The eigenvectors associated with the interior realm are opposite in orientation for the families in L_1 and L_2. The modest but consistent offset of 0.1 in phase might help to let the two trajectories eventually meet in phase space, after offsetting along the orbit.

Fig. 7.10, 7.16, 7.15, 7.21

Optimal orientation: Interestingly, the most optimal combination of trajectories for both the halo and V-L family have been found outside of the nominal stopping conditions ($\theta = -90°$). This cements the importance of the research question stated in Section 1.2.1.

Fig. 7.15, 7.21

Velocity asymptote The overview of the state space discrepancies for various orientations of the Poincaré section seem to adhere to an asymptote in the case of halo and V-L families. Moreover, the vertical asymptote corresponding to V-L appears to be positioned at a constant velocity deviation across various stopping angles. This suggests that employment of an optimiser might yield a very low discrepancy in position, but will always retain the deviation in velocity.

Fig. 7.10, 7.16

All in all, varying the orientation of the Poincaré section has yielded the desired insights into the attainable phase space of the hyperbolic trajectories associated with H-L, halo, and V-L orbits.

---

[8]In addition to these general rules from a scientific standpoint, it is noted that the increase in number of trajectories results in an expected decrease in position discrepancy (Fig. 7.15 and 7.21).

8
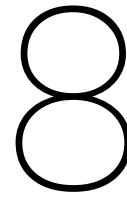
Conclusions

This research project aspires to close the scientific gap described in Section 1.1.2 and has been executed in a systematic way along the lines of the research framework. Each sub-component of this framework is aimed at solving a piece of the puzzle, which together form the answer to the main research question to be solved in reaching the project goal. This chapter is dedicated to the final concluding remarks, based on the review of orbit generation (Sec. 4.9), manifold generation (Sec. 6.7), and variations of the Poincaré section orientation (Sec. 7.6). The first section will provide answers to the research questions and is followed by the compliance with the research objectives. To conclude this research, new research proposals will be presented in the final section of this chapter.

8.1. Answers to the research questions

Answers to the research questions can be given on the basis of the results presented in the consecutive chapters of this thesis. This section captures the essence of those results, and thereby only provides concise descriptions with references to the corresponding (sub)sections in this document.

Research Question: *What is the influence of the orientation of the Poincaré section on the state vector discrepancy that arises from the connection of hyperbolic invariant manifolds emanating from Earth-Moon collinear libration points L_1 and L_2 in search of near-heteroclinic connections, after expanding the scope from the planar to the spatial case?*

A clear distinction needs to be made between the planar and spatial case to answer this question. Whereas the hyperbolic trajectories associated with H-L orbits meet in state space, the pair of two southern (or northern) halos as well as two V-L orbits do not seem to produce natural connections in the scope of this research. In the spatial case, sampling validation across all orientations of the Poincaré section has revealed that the best connections are found consistently <u>outside</u> the nominal stopping conditions for both halo and V-L families (Fig. 7.15 and 7.21). The ramifications of this behaviour are extensive and provide for a logical explanation. All manifolds presented in Chapter 6 departing from L_1 do not arrive at the L_2 location and vice versa. In contrast, these hyperbolic trajectories curve behind the Moon and therefore do not arrive perpendicular to $\mathbf{U}_2$ which would imply state vector alignment.

Sub-question 1: *How can the hyperbolic invariant manifolds for the doubly symmetric vertical Lyapunov orbits be constructed?*

The adopted procedure for V-L orbits is analogous to the one adopted for the H-L and halo families and employs the methods presented in Section 3.1. Richardson's third order approximation (Sec. 3.1.1) is consulted for the set of initial guesses. However, the doubly symmetric properties exhibited by the V-L family also enable the axial-type definition of state vector using other components (Sec. 3.2.2). Pseudo-arclength continuation (Sec. 3.1.4) has proven to be vital to the orbit generation procedure in dealing with turning points, and has successfully led to the complete computation of this family (Appendix C).

(a)   *Are any characteristics of the target orbit inherited by the stable and unstable manifolds?*   *Ch. 4*
      Certainly, through the relation stated in Equation 2.24, the eigenvalues provide an indication of
      the strength of the (un)stable modes and the corresponding saddle-type dynamic behaviour. A
      large eigenvalue module provides for rapid unwinding from the target orbit and is associated
      with a lower transfer time. Hence, this is a desired property. Across all families, the most
      powerful hyperbolic motion in each family is observed for those members which are closest to
      the collinear equilibria. Moreover, the V-L family attains the most extreme unstable eigenvalue
      moduli across all families in both equilibria and is therefore an excellent type for manifold
      transfers (Sec. 4.4 and 4.8).

(b)   *In this way, are there limitations associated to members of the family in which chaotic behaviour*   *Ch. 6*
      within the hyperbolic manifold appears?
      Characteristically, the hyperbolic trajectories associated with the H-L and halo family start
      to fan out and bounce off the zero-velocity surface. In contrast, the manifolds associated
      with the V-L family retain the same structure over time, even at significant distance from
      primaries. This global stability property complies with the observations in [Archambeau et al.,
      2011], which adds that "such a stability property does not hold for halo orbits." Whereas the
      tubes corresponding to the halo family "behave in a chaotic way in large time," the "regular
      structure of invariant manifolds of eight-shaped Lissajous orbits is conserved even after a large
      integration time." This property allows for reliable results over extended integration periods in
      case of V-L.

(c)   *How can the trajectories that numerically approximate these topological structures be verified for*   *Ch. 5*
      their mathematical fidelity?
      The procedure to ensure the validity of results is twofold. In a similar fashion as the numerical
      approach to orbit generation (Sec. 3.1), the verification part consists of efficient numerical tests
      that can be implemented in the algorithms. The conserved quantity C has proven to be a good
      indicator for this method (Sec. 5.2.5). The validation procedures on the other hand are more
      encompassing, and are performed a posteriori. In case of the manifolds, a novel validation
      technique is introduced which compares the discrepancy between symmetric states at the end
      of integration. The employment of this tool has revealed crucial insights into possible highly
      non-linear dynamics experienced along the path (Sec. 6.7).

Sub-question 2:   *How do the geometry and stability characteristics of the unstable and stable manifolds*
                       change for a range of energy levels?

The qualitative changes in dynamics due to changes in energy level are displayed in the spatial comparison
for H-L (Fig. 6.1, 6.13), halo (Fig. 6.5, 6.17), and V-L (Fig. 6.9, 6.21) in L_1 and L_2 respectively.

(a)   *Is this behaviour similar for a variety of types of orbits?*   *Ch. 6*
      No, the H-L and halo families exhibit more chaotic behaviour for increased energy levels
      whereas the V-L retains its shape.

(b)   *Can the observed dynamical behaviour be formulated into a general rule for a specific mass*   *Ch. 6*
      parameter?
      The global stability distinction does not seem to be a a function of μ, but rather of the type
      of periodic libration point motion. Only the V-L orbits is known to posses a conservation of
      structure over extended integration periods [Archambeau et al., 2011]. The hyperbolic manifold
      trajectories associated with the H-L and halo families do exhibit chaotic behaviour.

Sub-question 3:   *Do the hyperbolic manifolds emanating from different type of orbits at the collinear libration points L_1, L_2 join in phase space at the four predefined Poincaré sections for similar energy levels?*

All families have proven to meet in position space, however only the H-L family has indicated the existence of natural connections (Sec. 7.3). The qualitative dynamic behaviour as portrayed in the transversal cuts (Fig. 7.6) correspond to a very high extend to those presented in [Canalias and Masdemont, 2006]. The combination of two southern (or northern) halos, as well as V-L target orbits does not suggest to possess heteroclinic connections for the same set of restrictions.

(a)   *Is it possible to find natural connections ($\Delta V = 0$) when attempting to join the unstable and*   *Ch. 7*
        stable trajectories from L_1 and L_2 respectively at $U_{2,3}$ to form a heteroclinic connection?
        Only in the case of the H-L orbits. Both combinations of V-L orbits and southern (or
        northern) halo target orbits do not indicate that natural connections may exist. This is a very
        intriguing observation since both "connections from quasi-[halo L1] to quasi-[halo L2] orbits"
        [Gómez et al., 2004] and "heteroclinic connection[s] from a northern halo orbit to its southern
        counterpart" [Calleja et al., 2012] are known to exist. The results for the V-L family strongly
        supports the notion that "the chance of having a heteroclinic connection between [V-L orbits]
        is much less likely" than those for H-L [Arona and Masdemont, 2007].

(b)   *Can changing the orientation of the Poincaré section yield improved solutions in terms of ΔV*   *Ch. 7*
        through enhanced state vector alignment?
        Yes. Interestingly, all optima found in this research correspond to stopping angles outside the
        bounds of the nominal case. An explanation for this phenomenon is given in the answer to the
        main research question.

(c)   *How can a near-heteroclinic connection be refined to a more optimal solution in terms of*   *Ch. 8*
        minimum position and velocity discrepancy at the connection of hyperbolic trajectories?
        Multiple shooting techniques, as adopted in [Haapala, 2014], can be used to further refine these
        trajectories. However, the discrepancy overview in state space for different orientations of the
        Poincaré section has revealed an asymptote in velocity in case of the V-L family (Fig. 7.16). In
        this way, the orbit could be refined for an improved correspondence in position space, but will
        not be likely to yield heteroclinic connections.

8.2. Compliance with the research objectives

As stated in Section 1.2.2, the contribution of this thesis to solving problems outside the research itself is captured in the set of research objectives. In a similar fashion to the answers to the research questions, this section provides concise statements of compliance based on the previously presented work.

Research Objective: *To expand the current invariant manifold theory by analysing the phase space of hyperbolic manifolds emanating from vertical Lyapunov orbits for various energy levels.*

The combination of analysing the phase space for various energy levels (Ch. 6) and for variations of the Poincaré section orientation (Ch. 7) have yielded many novel insights into the dynamical behaviour of the manifolds associated with V-L orbits (Sec. 8.1), and aims to inspire new research (Sec. 8.3).

Sub-objective 1:   *Assess whether pure heteroclinic connections between vertical Lyapunov orbits might exist in the Earth-Moon system.*   *Ch. 7*
As described in the answer to the third research question (Sec. 8.1), the work presented in this thesis does not indicate that heteroclinic connections exists between the manifolds associated with V-L orbits.

Sub-objective 2:   *Develop a novel verification technique for ballistic manifold trajectories to ensure the mathematical precision of the numerical approximation.*   *Ch. 5*
Novel verification and validation techniques (Sec. 5.2.5) have been introduced based on the conserved quantity C and the symmetric properties of the EOM. The employment of these techniques have proven to be effective in assessing the numerical veracity of the trajectories (Ch. 6).

Sub-objective 3:   *Evaluate how the connection between manifolds changes for different orientations of the Poincaré section by changing these parameters one-vector-at-a-time.*   *Ch. 7*
Variations in the Poincaré section orientation have revealed fascinating phenomena for combinations northern (or southern) halo orbits as well as V-L orbits. As stated in the answer to the main research question (Sec. 8.1), sampling validation has demonstrated that the best connections for these families are found <u>outside</u> the nominal stopping conditions (Fig. 7.15 and 7.21).

Sub-objective 4:   *Lay the foundation for future manifold related research using the TU Delft Astrodynamic Toolbox (Tudat) by developing a set of generalised tools for the construction and verification of hyperbolic invariant manifolds emanating from periodic collinear libration point orbits including the generation of families of horizontal Lyapunov, vertical Lyapunov and halo orbits using semi-analytic methods for an initial guess.*   *Ch. 3, 5*
The aforementioned numerical procedures related to orbits (Ch. 3) and manifolds (Ch. 5) are implemented in C++ and have been subjected to a code refactoring to comply with the programming style adopted in Tudat. At the time of writing, this collection of files is made publicly available and requires implementation of unit tests before full integration with the Tudat repository.[1] The current implementation of these numerical techniques is expected to greatly reduce the strain on future students. In this way, even more exotic and complex problems may be feasible within the bounds of the thesis project.

Sub-objective 5: *To establish and resolve the challenges of using an explicit variable step-size*   *Ch. 3, 5*
Runge-Kutta method in the quest for an accurate numerical approximation
of periodic libration point orbits and their (un)stable subspace.
The review of orbit generation results (Sec.   4.9) has shown that the
accuracy of the RK78 scheme is very close to that of ode113, given identical
error tolerance settings. Only in the case that highly non-linear dynamics
are experienced along the trajectory, the difference in accuracy becomes
apparent. This high numerical precision is achieved by minimising the
integrator overshoot (Sec. 4.9.2) as well as a fixed step-size integration along
the orbit in case of manifold propagation (Sec. 5.2.1).

Sub-objective 6: *Provide insight into the dynamic behaviour and phase space of periodic*   *Ch. 4, 6, 7*
libration point orbits and their hyperbolic invariant manifolds by producing
animations and orthographic projections.
Orthographic projections for the orbits (Ch.   4) and manifolds (Ch.   6) are
provided for the H-L, halo and V-L families. In addition, a review of the axial
family (Sec.   4.3 and 4.7) is provided for a more comprehensive view on the
phase space in the EM-system. In this way, these chapters aim to serve as a
foundation for future investigations into the periodic libration point orbits
and their associated hyperbolic manifolds. Animations of periodic libration
point motion, unwinding of manifolds and connections between hyperbolic
trajectories have been made publicly available and can be generated using
the code provided by the author.[1]

---

[1] The reader is referred to the author's Github for the C++ implementation of the numerical techniques related to periodic libration point
orbits and their associated hyperbolic manifolds.

8.3. Recommendations for novel techniques and research topics

Following the same line of thought as presented in [Calleja et al., 2012], "our exploration shows only the tip of the iceberg of a wealth of interesting orbits." However, the exposed novel insights into the phase space of these non-planar figure-eight orbits definitely aims to inspire new research into their corresponding exotic solutions. The presented research has strong roots in both the application of numerical techniques as well as the uncovering of novel scientific phenomena. Hence, the recommendations are classified according to the two aforementioned categories.

8.3.1. Technical proposals

This research is bombarded with numerical techniques (Ch. 2, 3, and 5) which have been implemented in a highly-adjustable form to comply with the sub-objective 4 (1.2.2). The expansion of Tudat has played a major role in this research to comply with the combination of high numerical accuracy requirements and substantial integration periods. In this manner, the following suggestions have arisen over the course of the thesis project to further enhance this implementation.

Memory usage: Implementation of more efficient file types in terms of file size and quick I/O operations. In particular, the HDF5 format is highly recommended especially in the case of combining C++ with Python for post-processing. The HDF5 technology suite "supports an unlimited variety of data-types, and is designed for flexible and efficient I/O and for high-volume and complex data" [Folk et al., 2011]. Employment of this data type can significantly reduce file size and computation time.

Integrator end-time specification: An extension of the RK78 integrator implemented in Tudat to support reducing an overshoot as standard. The procedure to minimise possible under-/overshooting is discussed in the results of orbit generation (Sec. 4.9.2).

Fixed step-size integration: In addition to a minimal integrator overshoot, developing an integrator with a fixed step-size is desired for the equal-spacing of nodes along the orbit in time. The analysis of this phenomenon can be found in the numerical approach to manifold generation (Sec. 5.2.1).

Adaptive stopping criteria: Adapting the current implementation of manifold generation to suit any set of stopping criteria through *boost::functions*, thereby extending the generality of the algorithm.

Extension to other families: Addition of another semi-analytic technique to provide initial guesses for other types of libration point orbits, in addition to Richardson's third-order approximation described in the numerical approach to orbit generation (Sec. 3.1.1). The resulting state can be refined with the current implementation of the differential corrector and extended using the pseudo-arclength continuation scheme.

DC extension: Incorporate a multiple shooting option in the DC algorithm to refine the near-heteroclinic connections presented in the connections of manifolds at variations of the Poincaré section orientation (Ch. 7). When combined with the NC procedure, this forms a very powerful tool in extending the refined natural connection to a family of solutions (Sec. 3.1).

Manifold selection	Input specification in the implementation of the manifold generation tool to select which of the four hyperbolic invariant manifolds one would like to compute. Please note that for a robust distinction between exterior and interior manifolds, one should analyse the sign of the (un)stable eigenvector (Sec. 5.2.3).
Include Python in Tudat	The inclusion of generic post-processing functions into the Tudat repository can greatly improve the efficiency of reproducing work and provides for a lower threshold to adopt C++ in master theses.

In the case that a computing server is at one's disposal, please consult Appendix B.3 for additional considerations to be made in the case of extensive computational power.

8.3.2. Research proposals

The extensive analyses presented in this research has inspired many efforts which were not feasible to complete within the boundaries of this thesis project. In particular, the idea that "there is no reason that two asymptotic curves of different families cannot intersect" is hugely enticing [Poincaré, 1967a]. Following this line of thought, future research proposals are discussed.

Energy level variations	Extend the analysis on the orientation of the Poincaré to other energy levels and combinations of northern-southern halos to ascertain that the observed qualitative behaviour (Sec. 7.6) is valid across a range of energy levels.
Refinement of solutions	Exploit gradient-based techniques to refine the near-heteroclinic connections (Ch. 7) until numerical limits. The recommended technique consists of multiple shooting (Sec. 8.1) and entails an extension of the set of n free variables and m constraints employed in the multi-variate Newton method (Sec. 2.2.3). In particular, it would be very intriguing to relax the periodicity constraints and investigate whether a heteroclinic connection can be found between the quasi-periodic relative of the V-L family (Sec. 2.3.3).
Low-thrust	Investigate the use of low-thrust to connect the hyperbolic invariant manifolds associated with the V-L family to compensate for the discrepancy in state space (Sec. 7.5). In this case, the changing energy level along the orbit requires additional attention when selecting the target orbits.
Extended revolutions	Improvement of the generality of this analysis by considering the discrepancy in state space as a function of the number of revolution around the second primary, as has been performed for the homoclinic case in [Gidea and Masdemont, 2007].
Full fidelity optimization	Implementing the near-heteroclinic solutions (Ch. 7) in a full fidelity optimisation to assess to what extend the presented solutions correspond to the one in the more complex phenomena. This would significantly enhance the applicability of the scientific insights yielded by this research.

Mass parameter variations　　　A reproduction of results for different values of the mass parameter would be very interesting to analyse whether the observed dynamics (Ch. 7) persist. In particular, the Sun-Jupiter system would be an interesting suggestion due to the extensive prior research that is available [Koon et al., 2009]. This research could be performed in a similar sense as the one presented in [Doedel et al., 2007], in which the existence of the various families of orbits is assessed for "all values of the mass-ratio parameter."

Quasi-vertical orbits　　　An interesting novel approach might be to reduce the periodicity constraints and explore the solution space of quasi-vertical orbits, as has been performed for the quasi-halos and Lissajous trajectories in the Sun-Earth system [Gómez and Masdemont, 2000]. This wider range of attainable solutions might decrease the velocity discrepancy , which is restricted by an asymptote in this research as shown in 7.16. These orbits are "related to the intersections of the Lissajous type trajectories around the vertical periodic orbit" [Gómez et al., 2003].

V-L connections to different types　　　An intriguing idea that is both scientific and practical entails the connection of V-L orbits in L_2 to H-L or halo orbits in L_1. Apart from a scientific interest, this connection would significantly decrease the required velocity increment when departing from an Earth parking orbit. Evidence for this statement in provided in Sections 6.1 through 6.3, in which the V-L manifolds are proven to remain composed in geometry and do not approach Earth closely. On the other hand, the H-L and halo exterior manifolds provide for an efficient direct departure due to their minimal distance to this body. This research would extend the research presented in [Calleja et al., 2012], which has revealed a "direct connecting orbit from an L_1 halo orbit to a planar L_2 Lyapunov orbit."

The aforementioned conclusions and recommendations constitute to the final considerations presented in this thesis.

A
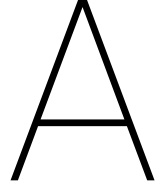
Parameters and constants

This addendum is dedicated to the settings of parameters and constants adopted in the numerical approach. Please note that the set of generalised algorithms for the construction and verification of hyperbolic invariant manifolds emanating from periodic collinear libration point orbits including the generation of families of H-L, halo, and V-L using semi-analytic methods have been made publicly available on the Tudat Github page. The values documented in this chapter constitute to the nominal settings which are highly adaptable to suit a wide variety of future applications. Any modifications required for the efficient and robust computation of particular cases are also examined in this appendix.

A.1. General constants

The parameter that defines the dynamical model with its corresponding equilibria, symmetries, and image trajectories (Sec. 2.1) is the mass ratio of the two primaries. Also referred to as the mass parameter, the adopted value for the EM-system in this research is presented in Table A.1.

Table A.1: *Parameter settings for circular restricted three-body problem [Kovalevsky and Seidelmann, 2004]*

Symbol	Value		Unit	Description	Reference
μ	1.2150581017337458	$\cdot 10^{-2}$	[-]	Mass parameter	Eq. 2.1 - 2.4
μ_{Earth}	3.986004418	$\cdot 10^{14}$	$\mathrm{m^3 s^{-2}}$	Earth standard gravitational parameter	Eq. A.1
μ_{Sun}	1.32712440018	$\cdot 10^{20}$	$\mathrm{m^3 s^{-2}}$	Sun standard gravitational parameter	Eq. A.2

It can be observed that the number of significant digits for the mass parameter greatly exceeds the commonly truncated value adopted in other studies. This is the standard in Tudat. To provide for consistency in implementation, this research also adheres to this definition which is derived from the standard gravitational parameters (Eq. A.1).

$$\mu = \frac{\mu_{Moon}}{\mu_{Earth} + \mu_{Moon}} \tag{A.1}$$

$$\mu_{Moon} = \frac{\mu_{Sun}}{328900.56 \cdot (1.0 + 81.30059)} \tag{A.2}$$

Interestingly, the mass parameter for the Moon is derived from the standard gravitational parameter of the Sun in combination of the mass ratios of Sun with respect to the combination Earth and Moon as well as the ratio of these two masses.

A.1.1. Dimensionless quantities

The definition of the equations of motion in the CR3BP have been derived in a normalised system using the computed mass parameter. These dimensionless quantities can be related to their dimensional relatives with the help of the conversion displayed in Table A.2.

Table A.2: *Conversion from normalised to dimensional quantities, resulting from the distance between Earth-Moon and the revolution period of the Moon [Kovalevsky and Seidelmann, 2004]*

Symbol	Non-dimensional value	Dimensional value	Dimensional unit	Description
x	1	384400	[km]	Position
$\dot{x}$	1	1.0231558377690937	[km/s]	Velocity
t	2π	4.3483836086738367	[days]	Time

The application of this conversion is demonstrated in the study dedicated to investigating optimal manifold connections (Ch. 7). With the help of intuitive units for discrepancies in state space, one can more easily grasp the scale of these undertakings.

A.1.2. Integrator settings

The accuracy of the trajectories resulting from the dynamical systems is hinges on the parameter settings of the adopted integration scheme. The very strict thresholds implemented in this research have proven to be crucial to achieve the high accuracy of the eigensystem validation for orbits (Ch. 4) and Jacobi verification for manifold trajectories (Ch. 6). To provide for a valid comparison with the ode113 integrator (MATLAB) presented in [Massarweh, 2016], identical error tolerance are adopted which have "been based on a trial-and-error procedure, so balancing computational time with accuracy." The corresponding quantities are presented in Table A.3.[1]

Table A.3: *Parameter settings for Runge-Kutta-Fehlberg 7(8) presented in Section 2.2.1 and extensively analysed in Appendix B.*

Symbol	Value		Unit	Description
h_0		10^{-5}	[-]	Initial step-size [2]
h_{min}	ϵ_m		[-]	Minimum step-size
h_{max}		10^{-4}	[-]	Maximum step-size
ϵ_{abs}		10^{-24}	[-]	Absolute error tolerance
ϵ_{rel}	$\epsilon_m \cdot$	10^2	[-]	Relative error tolerance

The machine epsilon (ϵ_m) stated in Table A.3 corresponds to the binary64 format adopted in C++. This double precision floating-point arithmetic has a base (β) of 2 and contains 64 bits which are assigned with the following tasks:

1 Sign

11 Exponent

53 Significand precision (t) of which one bit is implicit

As described in [Higham, 2002], "the spacing [of floating point numbers] can be characterised in terms of machine epsilon, which is the distance ϵ_m from 1.0 to the next larger floating point number." After correction for the precision of the implicit bit (ϵ_{min}), the value of the machine epsilon quantity is shown in Equation A.3.

$$\epsilon_m = \beta^{e_{min}-t} = 2^{-52} \approx 2.22044604925031 \cdot 10^{-16} \tag{A.3}$$

The integrator settings complete the set of fundamental parameters which constitute to the dynamical model.

---

[1] The reader is reffered to Appendix B for an extensive analysis of the working principles of the RK78 scheme.
[2] The initial and maximum step-sizes are reduced to 10^{-12} and 10^{-11} respectively in the case of minimising integrator overshoot as described in Section 4.9.2.

A.2. Parameter settings for orbit generation

To facilitate the process of orbit generation, additional parameter settings are adopted. As previously stated, the implementation of numerical techniques is highly flexible and can be adjusted to suit any other system of orbital bodies with minimal effort. Table A.4 displays the non-dimensional amplitudes used in Richardson's approximation, based on a trial-and-error procedure given the respective mass parameter. Please note that the in-plane amplitude (A_x) for the halo orbits is completely determined by the amplitude constraint given in Equation 3.15.

Table A.4: *Parameter settings for Richardson's third order approximation (n = 1) presented in Section 3.1.1 and adopted in Equations 3.1 through 3.6, 3.15, and 3.17.*

Symbol	Guess 1	Guess 2	Unit	Libration point number	Orbit type	Reference
A_x	10^{-3}	10^{-4}	[-]	L_1	H-L	Fig. 4.1
A_x	10^{-4}	10^{-3}	[-]	L_2	H-L	Fig. 4.21
A_z	$-1.1 \cdot 10^{-1}$	$-1.2 \cdot 10^{-1}$	[-]	L_1	Halo	Fig. 4.6
A_z	$1.5 \cdot 10^{-1}$	$1.6 \cdot 10^{-1}$	[-]	L_2	Halo	Fig. 4.26
A_z	10^{-1}	$2 \cdot 10^{-1}$	[-]	L_1	V-L	Fig. 4.16
A_z	10^{-1}	$2 \cdot 10^{-1}$	[-]	L_2	V-L	Fig. 4.36

The values presented in Table A.4 provide two initial guesses to initiate the process of refinement (DC) and extension (NC) of periodic trajectories to produce a family of verified solutions. Also this procedure is highly adjustable, as can be observed from the variety of criteria outlined in Table A.5.

Table A.5: *Parameter settings for orbit generation as outlined in Chapter 3.*

Value	Unit	Description	Reference
10^{-12}	[-]	Maximum position deviation	Eq. 3.25
10^{-12}	[-]	Maximum velocity deviation	Eq. 3.26
10^{-3}	[-]	Maximum eigenvalue deviation	Eq. 3.27
10^{-4}	[-]	Pseudo-arclength	Eq. 3.30
10^3	[-]	Save frequency	Sec. 4.9.2
10^3	[-]	Maximum number of DC iterations	
4000	[-]	Maximum number of members[3]	Sec. 4.9.2

As introduced in the review of orbit generation (Sec. 4.9, these sets of verified periodic solutions form the basis for the numerical approach to manifold generation (Ch. 5).

A.3. Parameter settings for manifold generation

In a similar fashion as the numerical approach to orbit generation, the procedure to produce hyperbolic invariant structures is highly adaptable to suit a variety of applications. The nominal values are displayed in Table A.6.

Table A.6: *Parameter settings for manifold generation as outlined in Chapter 5.*

Symbol	Value	Unit	Description	Reference
	10^{-11}	[-]	Maximum Jacobi's constant deviation	Sec. 5.2.5
ϵ	10^{-6}	[-]	Magnitude of local eigenvector offset	Eq. 5.6, Fig. 5.6
	10^2	[-]	Number of trajectories per manifold [4]	
	50	[-]	Maximum integration period	
	10^{-3}	[-]	Maximum eigenvalue deviation	Eq. 3.27
	10^3	[-]	Save frequency	Sec. 4.9.2

---

[3] The restriction on the maximum number of members per family is relieved in case of the extended V-L as presented in Appendix C.

[4] The number of trajectories per manifold is increased to 5000 to provide for an improved resolution in state discrepancy when attempting to make manifold connections at variations of the Poincaré section orientation (Ch. 7).

This page is intentionally left blank.

B

Experimental set-up of numerical approximation

Since all results obtained in this research have been acquired by integrating the equations of motion (Eq. 2.1 through 2.3), a proper understanding of the working principles behind this procedure is fundamental to the correct interpretation of the corresponding outcome. In addition, considerations involved in utilising the computational capacity of servers is shared.

B.1. TU Delft Astrodynamics Toolbox

Tudat is a "modular and robust astrodynamics toolbox" consisting of powerful C++ libraries to support astrodynamics and space research [Kumar et al., 2012]. As outlined in the research objectives (Sec. 1.2.2), one of the aims of this research is to lay the foundation for future manifold related research using the TU Delft Astrodynamic Toolbox. To this extent, the developed set of generalised tools for the construction and verification of hyperbolic invariant manifolds emanating from periodic collinear libration point orbits including the generation of those families has been implemented. This repository is publicly available on Github.

As previously stated, all algorithms are highly adjustable to suit a wide variety of applications. The integrator provided in Tudat is adopted by the most renowned researchers in this field due to a combination of high accuracy and efficiency [Koon et al., 2009].

B.2. Runge-Kutta-Fehlberg 7(8)

The adopted integration scheme has been introduced in Section 2.2.1 and will be more thoroughly analysed in this section. In essence, the procedure boils down to integrating a polynomial through a number of points to approximate the true solution. An increased number of points results in a higher-order polynomial to be integrated and hence a higher-order approximation of the true solution. As the state of the system at a later time is derived from the state at the current time, this procedure constitutes to an explicit method.[1]

The particular integration scheme adopted in this research is the Runge-Kutta-Fehlberg 7(8), which employs step-size control through the approximation of the local truncation error using two independent estimates through its embedded nature. Derived in [Fehlberg, 1968], the inner workings of this procedure are illustrated in this section. To this extent, the notation adheres to the one presented in [Enright et al., 1995].

---

[1]In contrast to explicit methods, implicit integration "require the solution of a nonlinear system of equations to obtain the increment function" [Montenbruck and Gill, 2000].

Given the explicit nature of this Runge-Kutta method, one aims to approximate a future state (y_i) situated at one step-size (h_i) from the location (x_{i-1}) of the previous state (y_{i-1}) as illustrated in Equation B.1.

$$x_i := x_{i-1} + h_i \tag{B.1}$$

To this extent, function evaluations (f) are employed at a number of stages (s) along the interval spanned by the step-size (h_i) as described in Equations B.2 and B.3. The weighted sum of these approximations constitute to the increment function, which provides the two independent estimates of the future state ($y_i, \hat{y}_i$) given a different set of external weights ($b_r, \hat{b}_r$) as presented in Equations B.4 and B.5.

$$k_1 = f(x_{i-1}, y_{i-1}) \tag{B.2}$$

$$k_r = f\left(x_{i-1} + c_r h, y_{i-1} + h \sum_{j=1}^{r-1} a_{rj} k_j\right) \quad \forall \quad r = 2, \ldots, s \tag{B.3}$$

$$y_i = y_{i-1} + h_i \sum_{r=1}^{s} b_r k_r \tag{B.4}$$

$$\hat{y}_i = y_{i-1} + h_i \sum_{r=1}^{s} \hat{b}_r k_r \tag{B.5}$$

Equations B.4 and B.5 capture the essence of this embedded method, since two independent estimates of varying order are derived from the same set of function evaluations.[2] This decreases the required computational effort significantly. The nodes $\{c_r\}_{r=1}^{s}$, the internal weights $\{a_{rj}\}_{j=1,r=2}^{r-1,s}$, and the external weights $\{b_r\}_{r=1}^{s}$ are specific constants given a particular integration scheme. In case of the RK78, in total 13 stages are employed and attain the set of constants displayed in the Butcher tableau (Tab B.1).

Table B.1: *Butcher tableau following the constants derived in [Butcher, 1963]. Please note that the set of internal weights $\{a_{rj}\}_{j=1,r=2}^{r-1,s}$ is lower-triangular, thereby stipulating the explicit nature of RK7(8).*

r	c_r	1	2	3	4	5	6	7	8	9	10	11	12	b_r	$\hat{b}_r$
1	0													41/840	0
2	2/27	2/27												0	0
3	1/9	1/36	1/12											0	0
4	1/6	1/24	0	1/8										0	0
5	5/12	5/12	0	-25/16	25/16									0	0
6	1/2	1/20	0	0	1/4	1/5								34/105	34/105
7	5/6	-25/108	0	0	125/108	-65/27	125/54							9/35	9/35
8	1/6	31/300	0	0	0	61/225	-2/9	13/900						9/35	9/35
9	2/3	2	0	0	-53/6	704/45	-107/9	67/90	3					9/280	9/280
10	1/3	-91/108	0	0	23/108	-976/135	311/54	-19/60	17/6	-1/12				9/280	9/280
11	1	2383/4100	0	0	-341/164	4496/1025	-301/82	2133/4100	45/82	45/164	18/41			41/840	0
12	0	3/205	0	0	0	0	-6/41	-3/205	-3/41	3/41	6/41	0		0	41/840
13	1	-1777/4100	0	0	-341/164	4496/1025	-289/82	2193/4100	51/82	33/164	12/41	0	1	0	41/840

The definition of internal and external weights outlined in the Butcher tableau (Tab. B.1) obey the relations shown in Equation B.6.

$$\sum_{r=1}^{s} b_r = 1, \qquad c_1 = 0, \qquad c_r = \sum_{j=1}^{r-1} a_{rj} \ \forall \ i > 1 \tag{B.6}$$

The two independent estimates of the future state ($y_i, \hat{y}_i$) are of varying order, and thereby possess information on the local truncation error (e). This approximated error of the lower order estimate is computed using Equation B.7.

$$e(h_i) = |\hat{y} - y| \tag{B.7}$$

---

[2]This phenomenon is provided by the fact that the weights are not uniquely determined by the condition of maximum order [Montenbruck and Gill, 2000].

If the magnitude of $e(h_i)$ exceeds the relative and absolute error tolerances as documented in Table A.3, the integration step is repeated for a smaller step-size (h^*). The value of this parameter is derived based on the knowledge "that $e(h_i)$ is proportional to h_i^{p+1} for the method of order p" [Montenbruck and Gill, 2000].

$$\frac{e(h_i^*)}{e(h_i)} = \left(\frac{h_i^*}{h_i}\right)^{p+1} \quad \mapsto \quad h_i^* = \sqrt[p+1]{\frac{\epsilon_{tol}}{e(h_i)}} \cdot h_i \tag{B.8}$$

Please note that the desired truncation error of the integration step ($e(h_i^*)$) is replaced by the dominating error tolerance (ϵ_{tol}). Depending on magnitude of the solution components, this is either the relative (ϵ_{rel}) or absolute (ϵ_{abs}) error tolerance.

In conclusion, every integration step adopts a step-size that provides for a consistent truncation error. By exploiting the same set of function evaluations, two independent estimates of varying order have been derived with minimal additional computational effort. Additional insights into this scheme include:

Function evaluations The employment of Runge-Kutta methods replaces the the cumbersome operation of computing derivatives, as is the case for Taylor series, with function evaluations at a number of points. In this way, the Runge-Kutta methods are "an easy to use standard technique for numerical solution of ode's" Montenbruck and Gill [2000].

Butcher barriers As can be observed from the Butcher tableau (Tab B.1), higher-order approximations of the integration procedure require exponentially more evaluations. The minimum number of stages required for a certain order is also referred to as *Butcher barriers*. Moreover, "only few methods of higher order are currently known since the derivation of appropriate coefficients becomes increasingly difficult" [Montenbruck and Gill, 2000].

Initial step-size As the desired step-size is only update in the process of integration (Eq. B.8), the initial step-size (h_0) still needs to be specified by the user. The corresponding value adopted in this research is documented in Table A.3.

Despite the efficiency and accuracy that this embedded variable step-size integrator scheme has to offer, the process of integration remains a costly process. In this manner, the next section will introduce a set of techniques which can be employed in the case that one has access to a computing server.

B.3. Computing server

Once the validity of the implementation has been ensured, a computing server can be invaluable to providing a significantly higher-level of generality with minimal additional coding effort. The result of employing this computational power is exhibited all throughout this thesis, including the high number of manifold trajectories at 181 different angles of the stopping conditions (Ch. 7). Two main recommendations related to this endeavour, are presented in this section.

B.3.1. Parallel processing

As recommended in Section 4.9.2, OpenMp is the preferred API for parallel programming in C++. Implementation is straightforward and can be as simple as feeding a for loop to the pragma omp parallel. In this way, only a wrapper function is required to call multiple instances of the expensive function for various parameter settings. As is the case for all applications of parallel processing, this implementation requires independent function evaluations.

In case that Python is employed for post-processing of the results, the reader is referred to the 'pool' class in the 'multiprocessing' package. This enables instantiating of plotting and animation classes and thereby computing these objects in parallel. Also this approach requires defining wrapper functions.

B.3.2. Terminal multiplexing

When aiming to analyse a variety of functions and parameter combinations, the list of executables rapidly expands. To solve the problem of requiring independent terminal windows for every process, a terminal multiplexer has been employed. This API enables the multiplexing of multiple virtual consoles. In this way, the output of the different processes remain separated and can be viewed after logging out and in again.

A very intuitive software application in this regard is *tmux*. In addition to the configuration file required for shortcuts that can be found on the tmux Github, the most important commands include:

tmux	Creates a new session.
tmux a	Attach to last session. In the case that multiple sessions are open, '-t' can be added combined with the name of the desired session.
tmux ls	List all sessions.
tmux det	Detaches from current session.
tmux kill-session	Delete current session.

The combination of processing in parallel and terminal multiplexing has been crucial to the success of this thesis.

C

Extended vertical Lyapunov analysis

This appendix is dedicated to the analysis of the extended family of V-L orbits, resulting from employing the numerical techniques presented in Chapter 3. The focus will lie on revealing additional features as a supplement to the variety of interesting traits discussed in the review of orbit generation results (Sec. 4.9). As the corresponding energy levels significantly exceed those of the other families, these orbits are solely appreciated for their mathematical appeal. The aim of this addendum is to provide the reader with additional insight into the remarkable geometry and stability properties this family has to offer. In a similar fashion as before, these results have been obtained using the integration scheme available in Tudat (RK78) in combination with a low-level programming language (C++). The corresponding high performance has enabled the number of family members to be refined to attain extraordinary levels, and provides insights into the robustness of the implemented scheme under extreme circumstances.

It is quite astonishing that the geometric character of these orbits was already documented in [Moulton, 1920]. In a time in which one could not resort to sheer computational power as adopted in this research, the geometric character of these orbits was described as follows:

Geometric character of V-L   *"In a general way they have the shape of the handles of ice-tongs, one of the two handles being situated on one side of the xy-plane, and the other symmetrically on the other side of this plane. The place of the hinge is where they cross the x-axis. In the case of the points L_1 and L_2 they open toward the finite mass μ, and in the case of L_3, toward the finite mass $1 - \mu$."*

Interestingly, the results presented in this appendix will reveal contrasting behaviour for the extended members of the V-L emanating from L_1.

C.1. L_1 **Vertical Lyapunov family**

The first extended set of V-L trajectories to be computed is the one associated with L_1. Together with the H-L family, these two families of orbits form the two principle types of motion. The resulting V-L family is displayed in Figure C.1. These trajectories are instances of a near-continuous set of orbits. In this way, this family can be characterised in terms of Jacobi's constant and orbital period and is shown in Figure C.2.
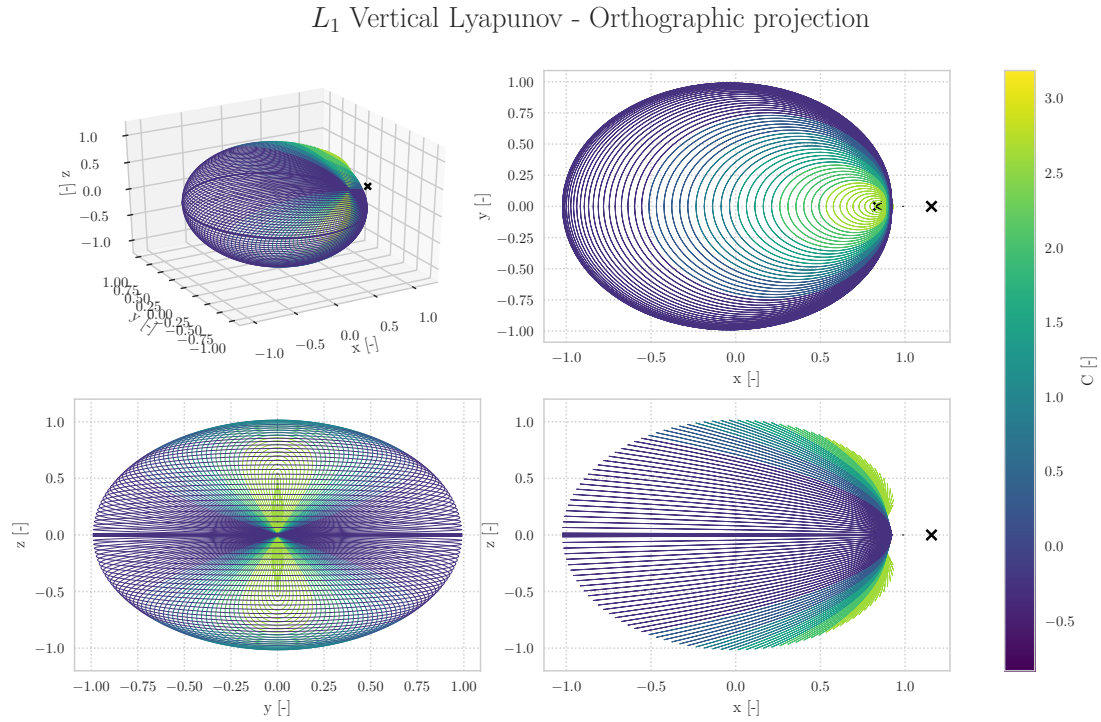
Figure C.1: Orthographic projection of every hundredth member of the V-L family emanating from L_1. The thick lines highlight the orbits at which the order of linear instability changes (bifurcations). The two crosses indicate the equilibria (L_1 and L_2), whereas the sphere located at $(1-\mu,0,0)$ represents the Moon at mean radius (P_2). The colour scale provides insight into the sensitivity with respect to Jacobi's constant (C).
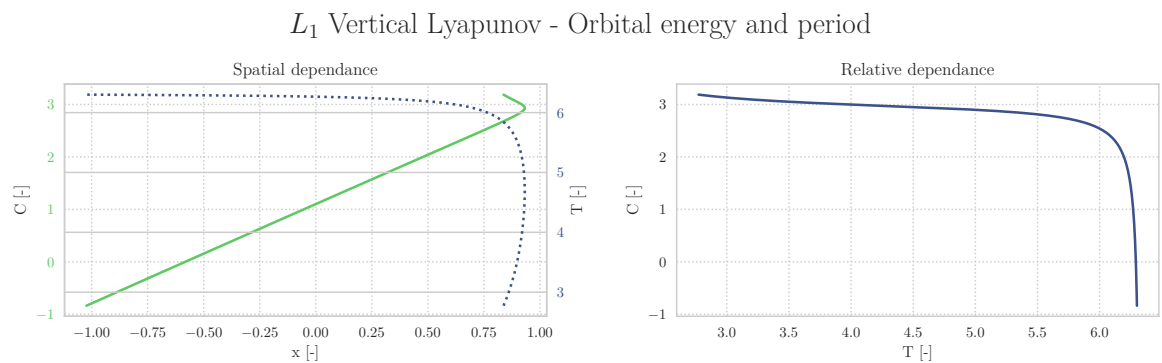
Figure C.2: Characterisation of the refined V-L family in L_1 in terms of the Jacobi's constant (C) and orbital period (T), as a function of the x-component of the initial conditions.

C.1.1. Periodicity verification and eigensystem validation

To verify the numerical veracity of the results of the V-L family in L_1, Figure C.3 shows the periodicity constraints verification. In addition to this verification procedure, the results are validated through the analysis of the monodromy matrices as presented in Figure C.4.

Figure C.3: *Numerical periodicity constraints verification for all members of the V-L family in L_1. The first column displays the compliance with the thresholds set for DC in terms of position (Eq. 3.25), velocity (Eq. 3.26), and integrator overshoot. The right column indicates the periodicity at full period and the robustness of the DC algorithm through the number of iterations.*

Figure C.4: *Analysis of the monodromy matrices of the L_1 V-L family. From top to bottom, from left to right: modulus of the six eigenvalues, deviation of the determinant (Eq. 2.23), order of linear instability and error of the reciprocal pair of eigenvalues indication periodicity (Eq. 3.27). All evaluations are mapped out with respect to the x-component of the initial shooting conditions.*

As an additional insight into the stability of the members of this family, the three sets of eigenvalues extracted from the monodromy matrices are presented in Figure C.5.

Figure C.5: *Stability overview of the three pairs of reciprocal eigenvalues ordered in three columns, corresponding to the pair denoting the (un)stable subspace, center subspace and periodicity. The three rows indicate: the real and imaginary components, phase of the complex eigenvalues and stability index (Eq. 2.25). With the exception of the real and imaginary components, all parameters are displayed as a function of the x-component of the initial shooting conditions.*

C.1.2. Discussion of results

In contrast to the V-L family in Section 4.4, the number of members has been increased significantly and now encompasses over 30,000 orbits given an equivalent pseudo-arclength. Characteristically, the relative dependence of the orbital energy and period is still strictly monotonic (Fig. C.2). These parameters are bounded by intervals of $\langle 0, 1.01]$ in z-direction and $[2.77, 6.30]$ in time.[1] The equivalent dimensional units are $\langle 0, 388244]$ km and $[12.05, 27.39]$ days, thereby exceeding the orbital period of the primaries . The orthographic projection (Fig. C.1) reveals two bifurcation regions, which supports the results presented in [Hou and Liu, 2013].

"It is notable that the vertical [...] orbits themselves can be far from the equilibrium point" [Howell, 2001]. However, the elongated members attain lower magnitudes of the first reciprocal pair of eigenvalues associated with the (un)stable subspace. Therefore, the V-L members of modest geometry are most suitable for exploitation of hyperbolic transfer mechanisms. This phenomenon supports the conclusions in the review of orbit generation (Sec. 4.9), in which the most extreme maxima and minima are experienced near the equilibrium across all families. Interestingly, the "family of the figure-of-eight orbits around L_1 consists entirely of unstable members" [Bray and Goudas, 1966].

The V-L family emanating from L_1 first embraces the second primary until a particular out of plane amplitude has been reached, after which it extends towards the larger primary. This is a unique feature of this type of family, which appears as a turning point in Jacobi's energy, orbital period (Fig. C.2), eigenvalue modulus (Fig. C.4), and stability indices (Fig. C.5). The second and fourth quadrants of Figure C.4 exhibit a low error with a slight trend. The threshold value is not nearly exceeded, hence the numerical continuation is terminated due to intersecting with the xy-plane. Moreover, the pseudo-arclength continuation has proven to be very robust in the handling of this reversal of x-direction (Fig. C.3). To conclude, the results presented in this section greatly extend the work as presented by [Archambeau et al., 2011].

---

[1]Please note that in this analysis the y-scale has <u>not</u> been significantly magnified in the orthographic projections of the family in Figure C.1. The motion of the extended V-L orbits portrays a sphere which is nearly equal in in-/out-of-plane direction.

C.2. L_2 **Vertical Lyapunov family**

The second and final extended set of V-L trajectories to be computed is the one associated with L_2. Together with the H-L family, these two families of orbits form the two principle types of motion. The resulting V-L family is displayed in Figure C.6. These trajectories are instances of a near-continuous set of orbits. In this way, this family can be characterised in terms of Jacobi's constant and orbital period and is shown in Figure C.7.
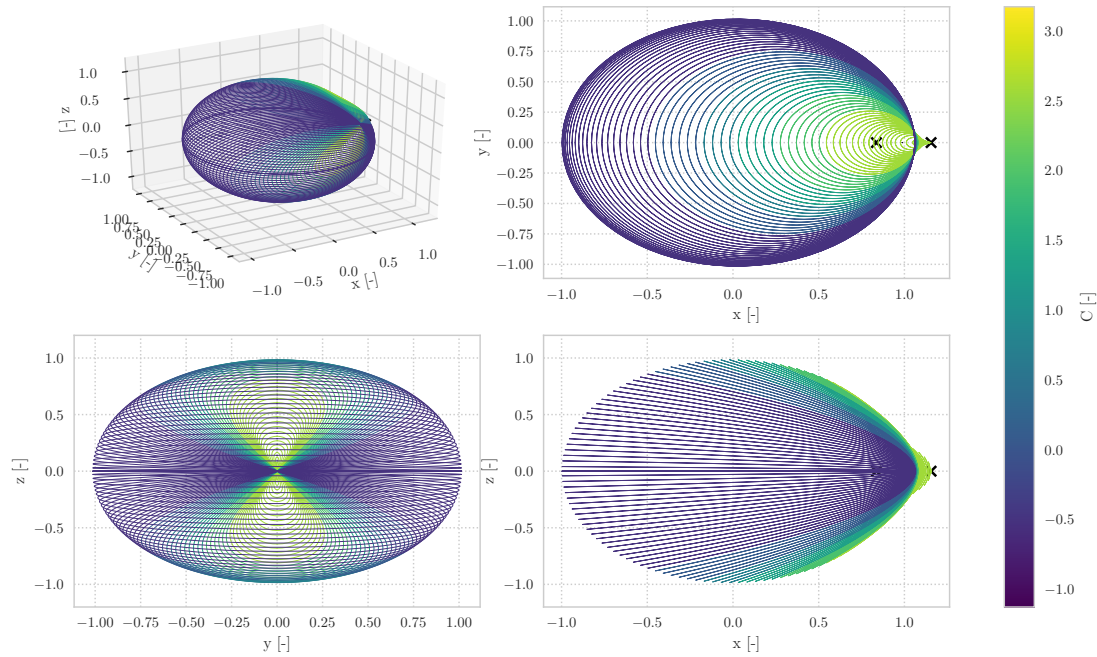
Figure C.6: *Orthographic projection of every hundredth member of the V-L family emanating from L_2. The thick lines highlight the orbits at which the order of linear instability changes (bifurcations). The two crosses indicate the equilibria (L_1 and L_2), whereas the sphere located at $(1 − μ, 0, 0)$ represents the Moon at mean radius (P_2). The colour scale provides insight into the sensitivity with respect to Jacobi's constant (C).*
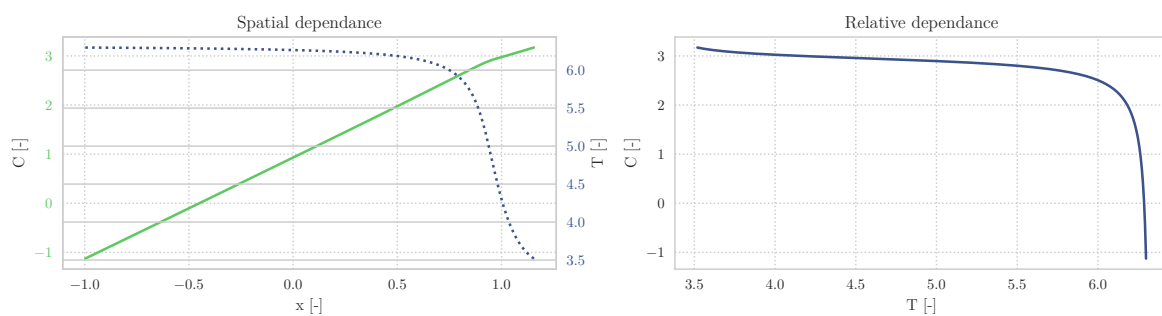
Figure C.7: *Characterisation of the refined V-L family in L_2 in terms of the Jacobi's constant (C) and orbital period (T), as a function of the x-component of the initial conditions.*

C.2.1. **Periodicity verification and eigensystem validation**

To verify the numerical veracity of the results of the V-L family in L_2, Figure C.8 shows the periodicity constraints verification. In addition to this verification procedure, the results are validated through the analysis of the monodromy matrices as presented in Figure C.9.

L_2 Vertical Lyapunov - Periodicity constraints verification
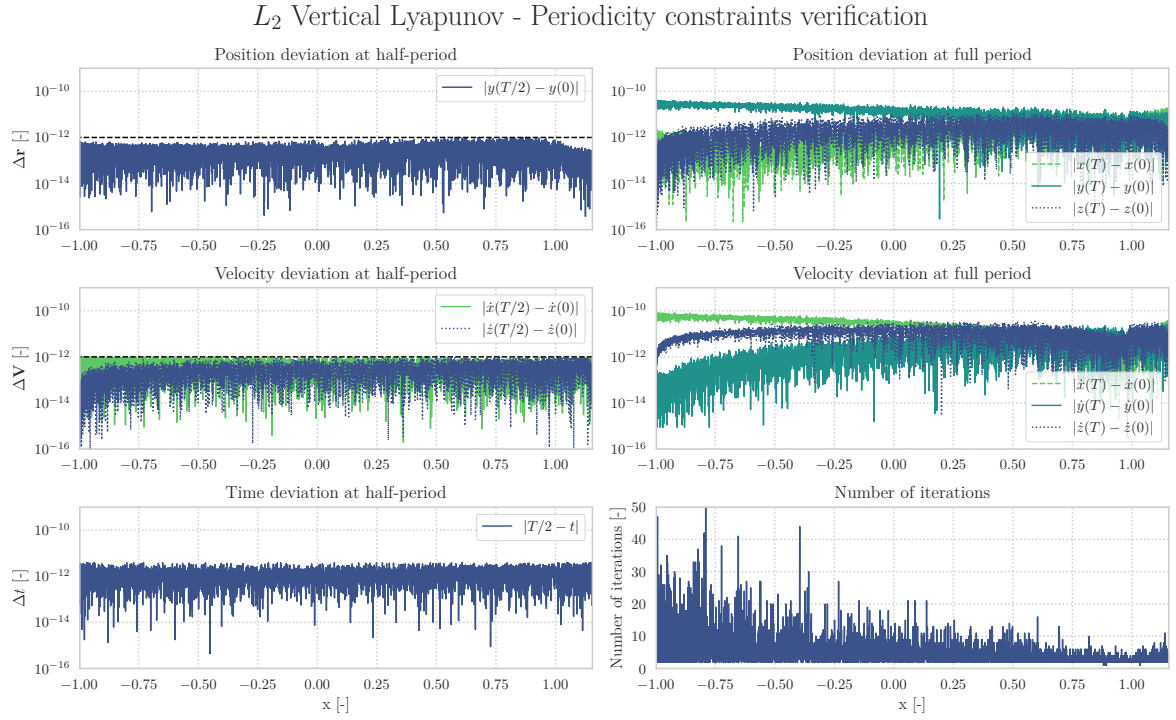
Figure C.8: *Numerical periodicity constraints verification for all members of the V-L family in L_2. The first column displays the compliance with the thresholds set for DC in terms of position (Eq. 3.25), velocity (Eq. 3.26), and integrator overshoot. The right column indicates the periodicity at full period and the robustness of the DC algorithm through the number of iterations.*

L_2 Vertical Lyapunov - Monodromy matrix eigensystem validation
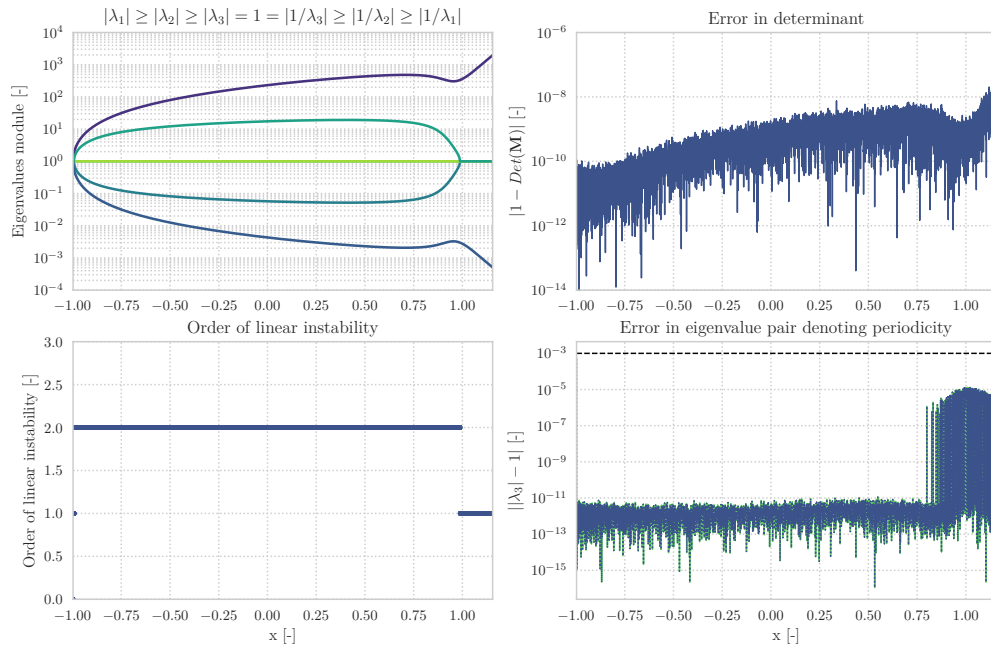
Figure C.9: *Analysis of the monodromy matrices of the L_2 V-L family. From top to bottom, from left to right: modulus of the six eigenvalues, deviation of the determinant (Eq. 2.23), order of linear instability and error of the reciprocal pair of eigenvalues indication periodicity (Eq. 3.27). All evaluations are mapped out with respect to the x-component of the initial shooting conditions.*

As an additional insight into the stability of the members of this family, the three sets of eigenvalues extracted from the monodromy matrices are presented in Figure C.10.

L_2 Vertical Lyapunov - Eigenvalues λ_i & stability indices v_i
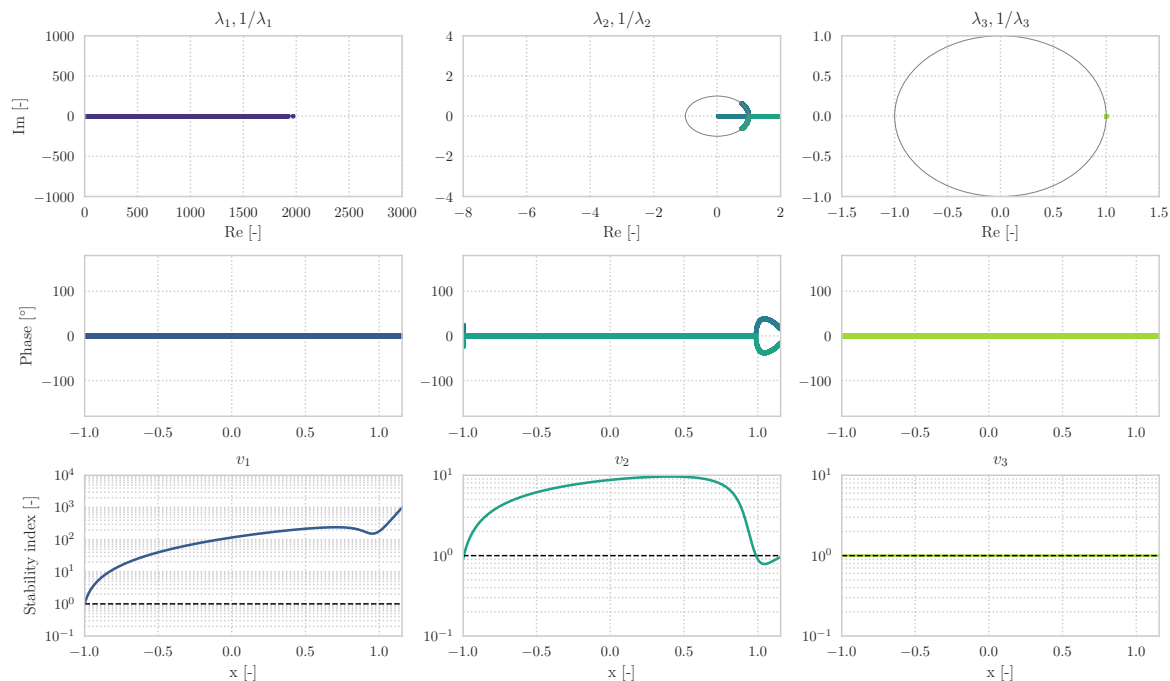
Figure C.10: *Stability overview of the three pairs of reciprocal eigenvalues ordered in three columns, corresponding to the pair denoting the (un)stable subspace, center subspace and periodicity. The three rows indicate: the real and imaginary components, phase of the complex eigenvalues and stability index (Eq. 2.25). With the exception of the real and imaginary components, all parameters are displayed as a function of the x-component of the initial shooting conditions.*

C.2.2. Discussion of results

In contrast to the V-L family in Section 4.8, the number of members has been increased significantly and now encompasses over 30,000 orbits given an equivalent pseudo-arclength. Characteristically, the relative dependence of the orbital energy and period is still strictly monotonic (Fig. C.7). These parameters are bounded by intervals of $\langle 0, 1.02]$ in z-direction and $[3.52, 6.30]$ in time.[2] The equivalent dimensional units are $\langle 0, 392088]$ km and $[15.31, 27.39]$ days, thereby exceeding the orbital period of the primaries . The orthographic projection (Fig. C.6) reveals two bifurcation regions, which supports the results presented in [Hou and Liu, 2013].

"It is notable that the vertical […] orbits themselves can be far from the equilibrium point" [Howell, 2001]. However, the elongated members attain lower magnitudes of the first reciprocal pair of eigenvalues associated with the (un)stable subspace. Therefore, the V-L members of modest geometry are most suitable for exploitation of hyperbolic transfer mechanisms. This phenomenon supports the conclusions in the review of orbit generation (Sec. 4.9), in which the most extreme maxima and minima are experienced near the equilibrium across all families. Interestingly, the "family of the figure-of-eight orbits around L_1 consists entirely of unstable members" [Bray and Goudas, 1966].

The V-L family emanating from L_2 extends towards both primaries until complete embracement of P_1. This is a unique feature of this type of family, which appears as a turning point in Jacobi's energy, orbital period (Fig. C.7), eigenvalue modulus (Fig. C.9), and stability indices (Fig. C.10). The second and fourth quadrants of Figure C.9 exhibit a low error with a slight trend. The threshold value is not nearly exceeded, hence the numerical continuation is terminated due to intersecting with the xy-plane. Moreover, the pseudo-arclength continuation has proven to be very robust in the handling of this reversal of x-direction (Fig. C.8). To conclude, the results presented in this section greatly extend the work as presented by [Archambeau et al., 2011].

---

[2]Please note that in this analysis the y-scale has <u>not</u> been significantly magnified in the orthographic projections of the family in Figure C.6. The motion of the extended V-L orbits portrays a sphere which is nearly equal in in-/out-of-plane direction.

C.3. Review of extended vertical Lyapunov analysis

The results presented in this chapter have been achieved using the RK78 integrator in combination with the high-performance C++ coding language. Using this combination, the author has independently generated periodic orbits that can be compared to the earlier work presented by [Archambeau et al., 2011].

C.3.1. Concluding statements on the numerical approach

It is remarkable that all members of both families presented in this addendum have been computed without relaxation of the periodicity (Eq. 3.25 and 3.26) or eigenvalue (Eq. 3.27) requirements. Nonetheless, a consistent increase in the number of iterations can be observed in Figures C.3 and C.8. The corresponding lack of rapid convergence might be both due to the order of the integration scheme as well as limited numerical precision. This behaviour is also portrayed in the increasing deviation in state space at full period.

The monodromy matrix eigensystem validations display a lower error in its determinants as well as the eigenvalue pairs denoting periodicity for decreasing values of x (Fig. C.4 and C.9). This behaviour is paired with a decrease (increase) of the unstable (stable) eigenvalue for these members located at a larger distance from the equilibria.

C.3.2. Concluding statements on the dynamical behaviour of V-L orbits

The orthographic projections (Fig C.1 and C.6) reveal remarkable out-of-plane amplitudes. These values attained due to the fact that "vertical instability is generally much milder than horizontal instability" [Hénon, 1973]. In this way, "instability appears first in the plane and only later in the perpendicular direction." The distribution of the sequential energy levels corresponding to the extended shooting conditions for periodic trajectories is presented in Figure C.11.
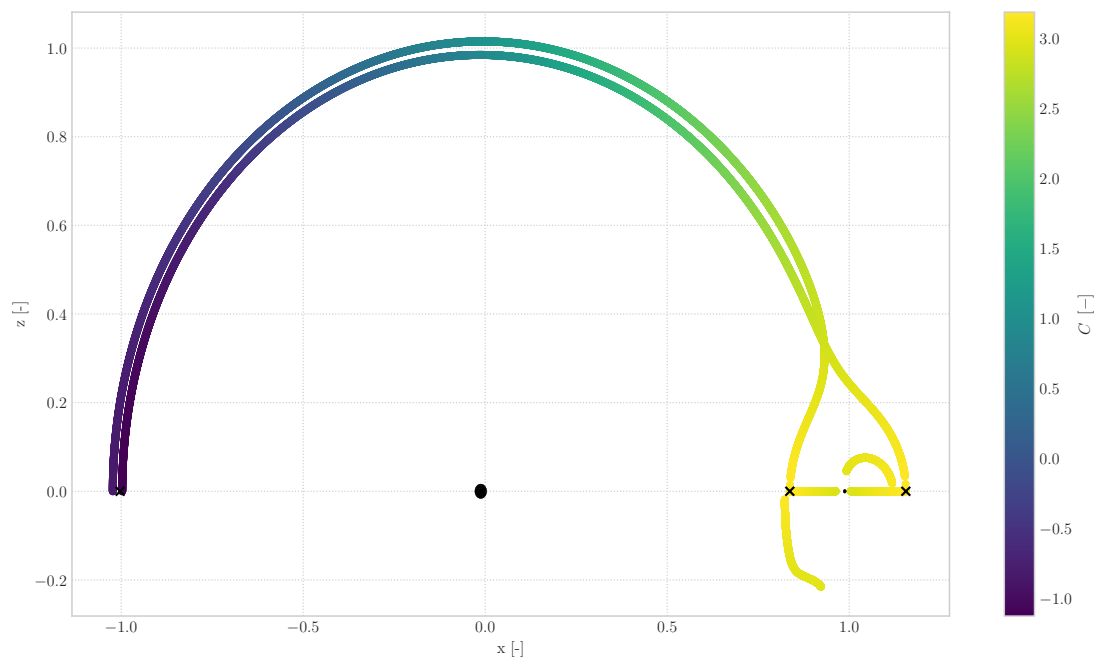
Figure C.11: *Overview of position components of shooting conditions as a function of Jacobi's constant. The two crosses indicate L_1 and L_2 respectively. The H-L families are limited to planar shooting conditions ($z = 0$), whereas the extended V-L families grow quickly in positive z-direction. The halos are characterised by the two curves emanating from the horizontal plane and extending below and above the orbital plane for L_1 and L_2 respectively.*

Please note that due to the formulation of the initial conditions (Eq. 3.18), the vertical axis indicates the z-component. In comparison to Figure 4.42, this projection of the families of orbits displays that the additional members greatly exceed the energy range of the H-L and halo families (Eq. 4.1). To conclude, the results presented in this addendum completes the analysis of the V-L family treated in Chapter 4 and extend the work presented by [Archambeau et al., 2011] considerably.

This page is intentionally left blank.

Bibliography

[Alessi et al. 2010]   ALESSI, E.M. ; GÓMEZ, G. ; MASDEMONT, J.J.:   Two-manoeuvres transfers between LEOs and Lissajous orbits in the Earth-Moon system.   In: *Advances in Space Research* 45 (2010), Nr. 10, p. 1276–1291

[Archambeau et al. 2011]   ARCHAMBEAU, G. ; AUGROS, P. ; TRÉLAT, E.:   Eight-shaped Lissajous orbits in the Earth-Moon system.   In: *MathematicS In Action* 4 (2011), Nr. 1, p. 1–23

[Arona and Masdemont 2007]   ARONA, L. ; MASDEMONT, J.J.:   Computation of heteroclinic orbits between normally hyperbolic invariant 3-spheres foliated by 2-dimensional invariant tori in hill's problem.   In: *Discrete and Continuous Dynamical Systems- Series A* (2007), Nr. SUPPL., p. 64–74

[Barden and Howell 1998]   BARDEN, B.T. ; HOWELL, K.C.:   Fundamental motions near collinear libration points and their transition.   In: *Journal of the Astronautical Sciences* 46 (1998), Nr. 4, p. 361–378

[Barrabés et al. 2009]   BARRABÉS, E. ; MONDELO, J.M. ; OLLÉ, M.:   Numerical continuation of families of homoclinic connections of periodic orbits in the RTBP.   In: *Nonlinearity* 22 (2009), Nr. 12, p. 2901–2918

[Barrabés et al. 2013]   BARRABÉS, E. ; MONDELO, J.M. ; OLLÉ, M.:   Numerical continuation of families of heteroclinic connections between periodic orbits in a Hamiltonian system.   In: *Nonlinearity* 26 (2013), Nr. 10, p. 2747–2765

[Bray and Gouclas 1967]   BRAY, T. A. ; GOUCLAS, C. L.:   Doubly symmetric orbits about the collinear Lagrangian points.   In: *Astronomical Journal* 72 (1967), Mar, p. 202–213

[Bray and Goudas 1966]   BRAY, T.A. ; GOUDAS, C.L.:   Three-dimensional Periodic Oscillations About L1, L2, and L3.   In: *Publications of the Astronomical Society of the Pacific* 78 (1966), Nr. 465, p. 440

[Breakwell and Brown 1979]   BREAKWELL, J.V. ; BROWN, J.V.:   The 'Halo' family of 3-dimensional periodic orbits in the Earth-Moon restricted 3-body problem.   In: *Celestial Mechanics* 20 (1979), Nr. 4, p. 389–404

[Butcher 1963]   BUTCHER, J.C.:   Coefficients for the study of Runge-Kutta integration processes.   In: *Journal of the Australian Mathematical Society* 3 (1963), Nr. 2, p. 185–201

[Calleja et al. 2012]   CALLEJA, R.C. ; DOEDEL, E.J. ; HUMPHRIES, A.R. ; LEMUS-RODRÍGUEZ, A. ; OLDEMAN, E.B.:   Boundary-value problem formulations for computing invariant manifolds and connecting orbits in the circular restricted three body problem.   In: *Celestial Mechanics and Dynamical Astronomy* 114 (2012), Nr. 1-2, p. 77–106

[Canalias et al. 2006]   CANALIAS, E. ; DELSHAMS, A. ; MASDEMONT, J.J. ; ROLDÁN, P.:   The scattering map in the planar restricted three body problem.   In: *Celestial Mechanics and Dynamical Astronomy* 95 (2006), Nr. 1-4, p. 155–171

[Canalias and Masdemont 2006]   CANALIAS, E. ; MASDEMONT, J.J.:   Homoclinic and heteroclinic transfer trajectories between planar Lyapunov orbits in the Sun-Earth and Earth-Moon systems.   In: *Discrete and Continuous Dynamical Systems* 14 (2006), Nr. 2, p. 261–279

[Cheng et al. 2017]   CHENG, Y. ; GÓMEZ, G. ; MASDEMONT, J.J. ; YUAN, J.:   Study of the transfer between libration point orbits and lunar orbits in Earth–Moon system.   In: *Celestial Mechanics and Dynamical Astronomy* 128 (2017), Nr. 4, p. 409–433

[De Sousa-Silva and Terra 2016]   DE SOUSA-SILVA, P.A. ; TERRA, M.O.:   A survey of different classes of Earth-to-Moon trajectories in the patched three-body approach.   In: *Acta Astronautica* 123 (2016), p. 340–349

[Dekens et al. 2014]   DEKENS, E. ; ENGELEN, S. ; NOOMEN, R.: A satellite swarm for radio astronomy. In: *Acta Astronautica* 102 (2014), p. 321–331

[Doedel et al. 1991a]   DOEDEL, E. ; KELLER, H. ; KERNEVEZ, J.: Numerical analysis and control of bifurcation problems (I): bifurcation in finite dimensions. In: *International Journal of Bifurcation and Chaos* 01 (1991), Nr. 03, p. 493–520

[Doedel et al. 1991b]   DOEDEL, E. ; KELLER, H. ; KERNEVEZ, J.: Numerical analysis and control of bifurcation problems (II): bifurcation in infinite dimensions. In: *International Journal of Bifurcation and Chaos* 01 (1991), Nr. 04, p. 745–772

[Doedel et al. 2008]   DOEDEL, E.J. ; KOOI, B.W. ; VAN VOORN, G.A.K. ; KUZNETSOV, Yu.A.: Continuation of connecting orbits in 3D-odes: (I) point-to-cycle connections. In: *International Journal of Bifurcation and Chaos* 18 (2008), Nr. 7, p. 1889–1903

[Doedel et al. 2007]   DOEDEL, E.J. ; ROMANOV, V.A. ; PAFFENROTH, R.C. ; KELLER, H.B. ; DICHMANN, D.J. ; GALÁN-VIOQUE, J. ; VANDERBAUWHEDE, A.: Elemental periodic orbits associated with the libration points in the Circular Restricted 3-Body Problem. In: *International Journal of Bifurcation and Chaos* 17 (2007), Nr. 8, p. 2625–2677

[Dunhan and Farquhar 2003]   DUNHAN, D.W. ; FARQUHAR, R.W.: Libration Point Missions, 1978-2002. (2003), p. 48 – 73. – In Libration Point Orbits and Applications, edited by Gómez, G. and Lo, M.W. and Masdemont, J.J.

[Enright et al. 1995]   ENRIGHT, W.H. ; HIGHAM, D.J. ; OWREN, B. ; SHARP, P.W.: A Survey of the Explicit Runge-Kutta Method / Department of Computer Science, University of Toronto. April 1995. – Technical Report. 291/94

[Farquhar and Kamel 1973]   FARQUHAR, Robert W. ; KAMEL, Ahmed A.: Quasi-periodic orbits about the translunar libration point. In: *Celestial mechanics* 7 (1973), Jun, Nr. 4, p. 458–473. – ISSN 1572-9478

[Farquhar 2001]   FARQUHAR, R.W.: The flight of ISEE-3/ICE: Origins, mission history, and a legacy. In: *Journal of the Astronautical Sciences* 49 (2001), Nr. 1, p. 23–73

[Farquhar et al. 2004]   FARQUHAR, R.W. ; DUNHAM, D.W. ; GUO, Y. ; MCADAMS, J.V.: Utilization of libration points for human exploration in the Sun-Earth-Moon system and beyond. In: *Acta Astronautica* 55 (2004), Nr. 3-9, p. 687–700

[Fehlberg 1968]   FEHLBERG, E.: Classical Fifth-, Sixth-, Seventh-, and Eighth-Order Runge-Kutta Formulas with Stepsize Control. 1968. – Technical report. Patent Number: NASA-TR-R-287

[Folk et al. 2011]   FOLK, M. ; HEBER, G. ; KOZIOL, Q. ; POURMAL, E. ; ROBINSON, D.: An overview of the HDF5 technology suite and its applications. In: *ACM International Conference Proceeding Series* (2011), p. 36–47

[Folta et al. 2014]   FOLTA, D.C. ; PAVLAK, T.A. ; HAAPALA, A.F. ; HOWELL, K.C. ; WOODARD, M.A.: Earth-Moon libration point orbit stationkeeping: Theory, modeling, and operations. In: *Acta Astronautica* 94 (2014), Nr. 1, p. 421–433

[Gidea and Masdemont 2007]   GIDEA, M. ; MASDEMONT, J.J.: Geometry of homoclinic connections in a planar circular restricted three-body problem. In: *International Journal of Bifurcation and Chaos* 17 (2007), Nr. 4, p. 1151–1169

[Gómez et al. 2001a]   GÓMEZ, G. ; LLIBRE, J. ; MARTÍNEZ, R. ; SIMÓ, C.: *Dynamics and Mission Design near Libration Points*. Vol. 2: *Fundamentals: The Case of Collinear Libration Points*. Singapore : World Scientific, Apr 2001. – ISBN 978-981-02-4285-5

[Gómez et al. 2001b]   GÓMEZ, G. ; LLIBRE, J. ; MARTÍNEZ, R. ; SIMÓ, C.: *Dynamics and Mission Design near Libration Points*. Vol. 3: *Fundamentals: The Case of Triangular Libration Points*. Singapore : World Scientific, Feb 2001. – ISBN 978-981-02-4274-9

[Gómez et al. 2003]   GÓMEZ, G. ; MASDEMONT, J.J. ; MONDELO, J.M.: *Libration Point Orbits and Applications*. World Scientific, May 2003 (A survey from the dynamical point of view). – 311–372 p.

[Goudas 1963]   GOUDAS, C.L.: Three-dimensional periodic orbits and their stability. In: *Icarus* 2 (1963), Nr. C, p. 1–18

[Grebow et al. 2008]   GREBOW, D.J. ; OZIMEK, M.T. ; HOWELL, K.C. ; FOLTA, D.C.: Multibody orbit architectures for lunar south pole coverage. In: *Journal of Spacecraft and Rockets* 45 (2008), Nr. 2, p. 344–358

[Gómez et al. 1991]   GÓMEZ, G. ; JORBA, A. ; MASDEMONT, J.J.: Study Refinement of Semi-Analytical Halo Orbit Theory. 1991. – Technical Report. ESOC Contract No.: 8625/89/D/MD(SC)

[Gómez et al. 2004]   GÓMEZ, G. ; KOON, W.S. ; LO, M.W. ; MARSDEN, J.E. ; MASDEMONT, J. ; ROSS, S.D.: Connecting orbits and invariant manifolds in the spatial restricted three-body problem. In: *Nonlinearity* 17 (2004), Nr. 5, p. 1571–1606

[Gómez and Masdemont 2000]   GÓMEZ, G. ; MASDEMONT, J.: Some zero cost transfers between libration point orbits. In: *Advances in the Astronautical Sciences* 105 II (2000), p. 1199–1216

[Gómez et al. 1998]   GÓMEZ, G. ; MASDEMONT, J. ; SIMÓ, C.: Quasihalo orbits associated with libration points. In: *Journal of the Astronautical Sciences* 46 (1998), Nr. 2, p. 135–176

[Gómez and Mondelo 2001]   GÓMEZ, G. ; MONDELO, J.M.: The dynamics around the collinear equilibrium points of the RTBP. In: *Physica D: Nonlinear Phenomena* 157 (2001), Nr. 4, p. 283–321

[Haapala 2014]   HAAPALA, C.: Representations of higher-dimensional Poincaré maps with applications to spacecraft trajectory design. In: *Acta Astronautica* 96 (2014), p. 23 – 41. – ISSN 0094-5765

[Hagel 1990]   HAGEL, J.: An approximate integral and solution for eccentric planetary type orbits in the restricted problem of three bodies. In: *Celestial Mechanics and Dynamical Astronomy* 50 (1990), Nr. 3, p. 209–230

[Higham 2002]   HIGHAM, Nicholas J.: *Accuracy and Stability of Numerical Algorithms*. Second. Philadelphia, PA, USA : Society for Industrial and Applied Mathematics, 2002. – ISBN 0-89871-521-0

[Hou and Liu 2013]   HOU, X.Y. ; LIU, L.: Bifurcating families around collinear libration points. In: *Celestial Mechanics and Dynamical Astronomy* 116 (2013), Nr. 3, p. 241–263

[Howard and Dullin 1998]   HOWARD, J.E. ; DULLIN, H.R.: Linear stability of natural symplectic maps. In: *Physics Letters, Section A: General, Atomic and Solid State Physics* 246 (1998), Nr. 3-4, p. 273–283

[Howard and MacKay 1987]   HOWARD, J.E. ; MACKAY, R.S.: Linear stability of symplectic maps. In: *Journal of Mathematical Physics* 28 (1987), Nr. 5, p. 1036–1051

[Howell and Pernicka 1987]   HOWELL, K. C. ; PERNICKA, H. J.: Numerical determination of Lissajous trajectories in the restricted three-body problem. In: *Celestial mechanics* 41 (1987), Mar, Nr. 1, p. 107–124. – ISSN 1572-9478

[Howell 2001]   HOWELL, K.C.: Families of orbits in the vicinity of the collinear libration points. In: *Journal of the Astronautical Sciences* 49 (2001), Nr. 1, p. 107–125

[Howell et al. 1997]   HOWELL, K.C. ; BARDEN, B.T. ; LO, M.W.: Application of dynamical systems theory to trajectory design for a libration point mission. In: *Journal of the Astronautical Sciences* 45 (1997), Nr. 2, p. 161–178

[Howell et al. 2006]   HOWELL, K.C. ; BECKMAN, M. ; PATTERSON, C. ; FOLTA, D.: Representations of invariant manifolds for applications in three-body systems. In: *Journal of the Astronautical Sciences* 54 (2006), Nr. 1, p. 69–93

[Howell and Campbell 1999]   HOWELL, K.C. ; CAMPBELL, E.T.: Three-dimensional periodic solutions that bifurcate from halo families in the circular restricted three-body problem. In: *Advances in the Astronautical Sciences* 102 II (1999), p. 891–910

[Hénon 1973]   HÉNON, M.: Vertical stability of periodic orbits in the restricted problem. In: *Celestial Mechanics* 8 (1973), Nr. 2, p. 269–272

[Hénon 1982] HÉNON, M.: On the numerical computation of Poincaré maps. In: *Physica D: Nonlinear Phenomena* 5 (1982), Nr. 2, p. 412 – 414. – ISSN 0167-2789

[Jorba and Masdemont 1999] JORBA, A. ; MASDEMONT, J.: Dynamics in the center manifold of the collinear points of the restricted three body problem. In: *Physica D: Nonlinear Phenomena* 132 (1999), Nr. 1-2, p. 189–213

[Jorba and Masdemont 1996] JORBA, A. ; MASDEMONT, J.J.: *Nonlinear Dynamics in an Extended Neighbourhood of the Translunar Equilibrium Point.* Kluwer Academic Publishers, 1996 (Hamiltonian Systems with Three or More Degrees of Freedom). – 430–434 p.

[Keller 1977] KELLER, H.B.: *Numerical solution of bifurcation and nonlinear eigenvalue problems.* New York : Academic Press, New York, 1977 (Applications of Bifurcation Theory)

[Koon et al. 2009] KOON, W. ; LO, M. ; MARSDEN, J. ; ROSS, S.: *Dynamical Systems, the Three-Body Problem, and Space Mission Design.* New York : Springer-Verlag New York Inc., Jun 2009. – ISBN 978-0387495156

[Koon et al. 2000a] KOON, W.S. ; LO, M.W. ; MARSDEN, J.E. ; ROSS, S.D.: The genesis trajectory and heteroclinic connections. In: *Advances in the Astronautical Sciences* 103 (2000), Nr. 3, p. 2327–2343

[Koon et al. 2000b] KOON, W.S. ; MARTIN W, L. ; MARSDEN, J.E. ; ROSS, S.D.: Heteroclinic connections between periodic orbits and resonance transitions in celestial mechanics. In: *Chaos* 10 (2000), Nr. 2, p. 427–461

[Kovalevsky and Seidelmann 2004] KOVALEVSKY, J. ; SEIDELMANN, P.K.: *Fundamentals of Astrometry.* First. Cambridge University Press, July 2004. – 363–369 p.. – ISBN 978-0521642163

[Kuhn et al. 2000] KUHN, B. ; PETERSEN, P. ; O'TOOLE, E.: OpenMP versus threading in C/C++. In: *Concurrency Practice and Experience* 12 (2000), Nr. 12, p. 1165–1176

[Kumar et al. 2012] KUMAR, K. ; ABDULKADIR, Y. ; BARNEVELD, P.W.L. van ; BELIEN, F. ; BILLEMONT, S. ; BRANDON, E. ; DIJKSTRA, M. ; DIRKX, D. ; ENGELEN, F. ; GONDELACH, D. ; HAM, L. van der ; HEEREN, E. ; IORFIDA, E. ; LELOUX, J. ; MELMAN, J. ; MOOIJ, E. ; MUSEGAAS, P. ; NOOMEN, R. ; RÖMGENS, B. ; RONSE, A. ; LEITE PINTO SECRETIN, T.A. ; TONG MINH, B. ; VANDAMME, J. ; PERSSON, S.M.: Tudat: a modular and robust astrodynamics Toolbox. In: *Fifth International Conference on Astro- dynamics Tools and Techniques (ICATT)* (2012), p. 1–9

[Markellos and Halioulias 1977] MARKELLOS, V. V. ; HALIOULIAS, A. A.: Numerical determination of asymmetric periodic solutions. In: *Astrophysics and Space Science* 46 (1977), Jan, Nr. 1, p. 183–193. – ISSN 1572-946X

[Marsden 1978] MARSDEN, J.: Qualitative methods in bifurcation theory. In: *Bulletin of the American mathematical society* 84 (1978), Nr. 06

[Massarweh 2016] MASSARWEH, L.: *Linear stability and bifurcations of periodic Lagrange orbits in the Elliptic Restricted 3-Body Problem: An investigation at L1/L2 in the Earth-Moon system,* Delft University of Technology, Master's thesis, 2016

[Matkowski and Reiss 1977] MATKOWSKI, B. ; REISS, E.: Some iteractions between bifurcation theory and catastrophe theory. In: *American Mathematical Society* (1977)

[Meyer et al. 2008] MEYER, K. ; HALL, G. ; OFFIN, D.: *Applied Mathematical Sciences.* Vol. 90: *Introduction to Hamiltonian Dynamical Systems and the N-Body Problem.* New York : Springer-Verlag, Dec 2008. – ISBN 978-3-319-53690-3

[Miele 2010] MIELE, A.: Revisit of the Theorem of Image Trajectories in the Earth-Moon Space. In: *Journal of Optimization Theory and Applications* 147 (2010), Dec, Nr. 3, p. 483–490. – ISSN 1573-2878

[Mingotti et al. 2007] MINGOTTI, G. ; TOPPUTO, F. ; BERNELLI-ZAZZERA, F.: Combined optimal low-thrust and stable-manifold trajectories to the earth-moon halo orbits. In: *AIP Conference Proceedings* 886 (2007), p. 100–112

[Montenbruck and Gill 2000]   MONTENBRUCK, O. ; GILL, E.:   *Satellite Orbits - Models, Methods, and Applications.* Berlin Heidelberg : Springer-Verlag, 2000. – ISBN 3-540-67280-X

[Moulton 1920]   MOULTON, F.R.: *New methods of celestial mechanics.* Vol. 3: *Periodic orbits.* Washington, D.C. : Carnegie Institution of Washington, Dec 1920. – In collaboration with Danial Buchanan, Thomas Buck, Frank L. Griffin, William R. Longley and William D. MacMillan

[Nayfeh and Balachandran 1995]   NAYFEH, A. H. ; BALACHANDRAN, B.:   *Applied Nonlinear Dynamics: Analytical, Computational, and Experimental Methods.* Wiley-VCH Verlag GmbH, Mar 1995 (Wiley Series in Nonlinear Science). – ISBN 978-0-471-59348-5

[Onozaki and Yoshimura 2014]   ONOZAKI, K. ; YOSHIMURA, H.:   Invariant manifolds and Lagrangian coherent structures in the planar circular restricted three-body problem.   In: *Theoretical and Applied Mechanics Japan* 62 (2014), p. 119–128

[Parker and Anderson 2014]   PARKER, J. S. ; ANDERSON, R. L.: *Low-Energy Lunar Trajectory Design.* Pasadena, California : Jet Propulsion Laboratory, Jul 2014 (JPL deep-space communications and navigations series)

[Parker et al. 2010]   PARKER, J.S. ; DAVIS, K.E. ; BORN, G.H.:   Chaining periodic three-body orbits in the EarthMoon system. In: *Acta Astronautica* 67 (2010), Nr. 5-6, p. 623–638

[Perko 2001]   PERKO, L.: *Texts in Applied Mathematics.* Vol. 7: *Differential Equations and Dynamical Systems.* New York : Springer-Verlag, Feb 2001. – ISBN 978-0-387-95116-4

[Poincaré 1967a]   POINCARÉ, H.:   *New methods of celestial mechanics.* Vol. 3: *Integral invariants periodic solutions of the second type doubly asymptotic solutions.* Washington, D.C. : National Aeronautics and Space Administration, Jun 1967. – NASA technical translation

[Poincaré 1967b]   POINCARÉ, H.:   *New methods of celestial mechanics.* Vol. 1: *Periodic solutions, the non-existence of integral invariants, asymptotic solutions.* Washington, D.C. : National Aeronautics and Space Administration, Apr 1967. – NASA technical translation

[Pontani and Teofilatto 2017]   PONTANI, M. ; TEOFILATTO, P.: Invariant manifold connections via polyhedral representation. In: *Acta Astronautica* 137 (2017), p. 512–521

[Rahoma and Abd El-Salam 2014]   RAHOMA, W.A. ; ABD EL-SALAM, F.A.: The effects of Moon's uneven mass distribution on the critical inclinations of a lunar orbiter. In: *Journal of Astronomy and Space Science* 31 (2014), Nr. 4, p. 285–294

[Richardson 1980a]   RICHARDSON, D.L.: Analytic construction of periodic orbits about the collinear points. In: *Celestial Mechanics* 22 (1980), Nr. 3, p. 241–253

[Richardson 1980b]   RICHARDSON, D.L.: A note on a Lagrangian formulation for motion about the collinear points. In: *Celestial Mechanics* 22 (1980), Nr. 3, p. 231–236

[Szebehely 1967]   SZEBEHELY, V.: *Theory of Orbits: The Restricted Problem of Three Bodies.* New York : Academic Press Inc., Jan 1967. – ISBN 978-0-12-395732-0

[Topputo et al. 2005]   TOPPUTO, F. ; VASILE, M. ; BERNELLI-ZAZZERA, F.: Low energy interplanetary transfers exploiting invariant manifolds of the restricted three-body problem.   In: *Journal of the Astronautical Sciences* 53 (2005), Nr. 4, p. 353–372

[Wakker 2015]   WAKKER, Karel F.: *Fundamentals of Astrodynamics.* Delft : Institutional Repository Library Delft University of Technology, Jan 2015. – ISBN 978-94-6186-419-2

[Wiggins 2003]   WIGGINS, S.: *Texts in Applied Mathematics.* Vol. 2: *Introduction to Applied Nonlinear Dynamical Systems and Chaos.* New York : Springer-Verlag, Oct 2003. – ISBN 978-0-387-00177-7

[Wilczak and Zgliczynski 2003]   WILCZAK, D. ; ZGLICZYNSKI, P.: Heteroclinic connections between periodic orbits in planar restricted circular three-body problem - A computer assisted proof. In: *Communications in Mathematical Physics* 234 (2003), Nr. 1, p. 37–75

[Wilczak and Zgliczyński 2005] Wilczak, D. ; Zgliczyński, P.: Heteroclinic connections between periodic orbits in planar restricted circular three body problem. Part II. In: *Communications in Mathematical Physics* 259 (2005), Nr. 3, p. 561–576

[Zazzera et al. 2004] Zazzera, F.B. ; Topputo, F. ; Massari, M.: Assessment of Mission Design Including Utilization of Libration Points and Weak Stability Boundaries. In: *Advanced Concepts Team (ESTEC), Contract Number: 18147/04/NL/MV* (2004)